POROUS GRAIN MODEL AND EQUIVALENT ELASTIC MEDIUM APPROACH FOR PREDICTING EFFECTIVE ELASTIC PROPERTIES OF SEDIMENTARY ROCKS

A DISSERTATION

SUBMITTED TO THE DEPARTMENT OF GEOPHYSICS

AND THE COMMITTEE ON GRADUATE STUDIES

OF STANFORD UNIVERSITY

IN PARTIAL FULFILLMENT OF THE REQUIREMENTS

FOR THE DEGREE OF

DOCTOR OF PHILOSOPHY

Franklin J. Ruiz

August 2009

I certify that I have read this dissertation and that, in my opinion, it is fully adequate in scope of and quality as a dissertation for the degree of Doctor of Philosophy.

Gary Mavko (Principal Adviser)

I certify that I have read this dissertation and that, in my opinion, it is fully adequate in scope of and quality as a dissertation for the degree of Doctor of Philosophy.

Jack Dvorkin

I certify that I have read this dissertation and that, in my opinion, it is fully adequate in scope of and quality as a dissertation for the degree of Doctor of Philosophy.

Mark Zoback

I certify that I have read this dissertation and that, in my opinion, it is fully adequate in scope of and quality as a dissertation for the degree of Doctor of Philosophy.

Tapan Mukerji

Approved for the University Committee on Graduate Studies:

Abstract

This dissertation presents the results of using different inclusion and granular effective medium models and poroelasticity to predict the elastic properties of rocks with complex microstructures. Effective medium models account for the microstructure and texture of rocks, and can be used to predict the type of rock and microstructure from seismic velocities and densities. We show that if enough information regarding the rock microstructure is available, effective-medium models produce better estimates of the elastic properties of the rock matrix than the average of Hashin-Shtrikman (1963). We introduce the *elastic equivalency* approach, using the differential effective medium model, to predict the effective elastic moduli of rocks and attenuation. We introduce the *porous grain concept* and develop rock physics models for rocks with microporosity. We exploit the porous grain concept to describe a variety of arrangements of uncemented and cemented grains with different degrees of hydraulic connectivity in the pore space.

We first investigate the accuracy of the differential effective medium and self-consistent estimations of elastic properties of complex rock matrix using composites as analogs. At low porosity, the elastic moduli of the rock mineral matrix often dominate those of the whole rock. A sedimentary rock matrix may be considered as a composite and may include mineral constituents with very different moduli and shapes. To describe the fabric of these rocks, an unmanageable number of parameters may be needed. We test whether the differential effective-medium (DEM) and self-consistent (SC) models can accurately estimate the elastic moduli of a complex rock

matrix and compare the results with the average of upper and lower Hashin-Shtrikman bounds. The testing was conducted using data from the literature on particulate-filled composites, covering a wide range of inclusion concentrations, inclusion shapes, and elastic modulus contrasts. We find that when the material microstructure is consistent with DEM, this model is more accurate than both SC and the bound-average method for a variety of inclusion aspect ratios, concentrations, and modulus contrasts. If relatively little information is known about the rock microstructure, the differential effective-medium approximation can estimate the elastic properties of complex mixtures of minerals more accurately than heuristic estimates, such as the arithmetic average of the upper and lower elastic bounds.

Based on these results, we next pose a question: can a theoretical inclusion model, specifically, the differential effective-medium model (DEM), be used to match experimental velocity data in rocks that are not necessarily made of inclusions (such as clastics)? We first approach this question by using empirical velocity-porosity equations as proxies for data. By finding a DEM inclusion aspect ratio (AR) to match these equations, we find that the required range of AR is remarkably narrow. Moreover, a constant AR of about 0.13 can be used to accurately match empirical relations in competent sand, shale, and quartz/calcite mixtures. We show that this finding can be practically utilized to (a) predict V_s from V_p; (b) describe velocity-frequency dispersion between low-frequency and ultrasonic experiments; (c) predict the dry-frame elastic properties from ultrasonic data on liquid-saturated samples (where Gassmann's fluid substitution is not applicable); (d) predict the attenuation of *P*-wave velocity; and (e) establish tight constraints for the ranges of possible variation of V_s and V_p at a given porosity in some mineralogies. We also apply this approach to laboratory data (rather than empirical equations) and find that, in most of the cases, we can indeed match the velocity data with a narrow range of aspect ratios within wide ranges of porosity and mineralogy.

Although the actual rock may not be a physical realization of this mathematical model, we will show that there exist an elastic equivalency between DEM and the data. Our hypothesis is that if such elastic equivalency can be established with a

narrow range of AR and for a wide range of real samples, we can find an idealized physical analogue to real rock and then use this analogue to interrelate different properties of real samples.

When elastic equivalency is used to predict V_s from V_p in unconsolidated carbonate sediment, it is observed that the prediction is less accurate than for consolidated rocks and that it is necessary to multiply the DEM aspect ratios by an ad hoc factor in order to improve the V_s prediction. In order to solve this problem, we next develop an effective-medium model for estimating the elastic properties of high-porosity marine calcareous sediment and diatomite.

The porous grain model treats sediment as a pack of porous elastic grains. The effective elastic moduli of the porous grains are calculated using the differential effective-medium model (DEM), where the intragranular ellipsoidal inclusions have a fixed aspect ratio and are filled with seawater. Then the elastic moduli of a pack of these spherical grains are calculated using different granular medium models and a modified (scaled to the critical porosity) upper Hashin-Shtrikman bound above the critical porosity, and modified lower and upper Hashin-Shtrikman bounds below the critical porosity. In this study, the modified lower and upper bounds were found to be appropriate for carbonate marine sediment and diatomaceous sediment, respectively.

The porous-grain model is also applied to estimate the effective elastic properties of three basic porous grain-aggregate scenarios, depending on the effective fluid connectivity of the intragranular porosity and in the grains. Each scenario is a simplified representation of the natural rock's pore-space morphology and a closer representation of existing artificial composites. The realizations of each of these scenarios in composites or rocks are achieved either by creating or eliminating pore-to-pore connections, or by changing the period of the externally applied stresses to be faster or slower than the pore-to-pore diffusion times. To determine the effective elastic properties of the saturated porous-grain material in the three different porous-grain-aggregate scenarios, we use two models: the differential effective medium approximation (DEM) and the combination DEM-Gassmann, depending on whether

we wish to obtain the high frequency or the low frequency effective elastic moduli, respectively. In this approach, low and high frequency refer to fluid-related effects; but the wavelengths are still much longer than any scale of grains or intergranular pores.

We find that when comparing the V_p and V_s velocities predicted by our model with Ocean Drilling Program (ODP) data from three wells, the best match is achieved when the aspect ratio of intragranular pores is 0.5. This model assigns finite, non-zero values to the shear modulus of high-porosity marine sediment, unlike the suspension model commonly used in such depositional settings. This approach also allows us to obtain a satisfactory match with laboratory diatomite velocity data.

A similar staged approach is used to determine the elastic moduli of a cemented porous grain aggregate at low cement concentration. This is achieved by introducing the porous grain concept into the cementation theory. Then, the combination of the cementation theory (Dvorkin et al., 1994) for porous grain material with a self-consistent approximation, specifically, the coherent potential approximation (CPA) (Berryman, 1980), allows us to estimate the elastic properties of cemented porous grain aggregates at all cement concentrations (Dvorkin et al. 1999). Therefore, the porous grain model allows for a) varying the grain contact friction coefficient γ in the whole range from 0 to 1, for smooth to infinitely rough grains, respectively; b) combining the self-consistent approximation with the cementation theory to account for intergranular cement volume fractions from 0 to 1; and c) considering porous grain textures and the effect of frequency.

Our approach and models for non-cemented aggregates may be applied to sediment, such as calcareous and diatomaceous ooze, opal, and chalks. Our approach for cemented aggregates may be applied to carbonate rocks. The microstructural parameters of these models can be related to diagenesis and may be varied to mimic diagenetic processes of calcareous and diatomaceous ooze, and cemented and non-cemented carbonate rocks.

Acknowledgements

I would like to distinguish the enduring and insightful support of my adviser Jack Dvorkin, who has provided assistance and guidance without which I would have been unable to complete this dissertation. I would also like to thank Tapan Mukerji, Gary Mavko, Mark Zoback, and David Pollard, for their readiness to serve on my oral exam committee and for their thorough review and constructive comments on my dissertation. Thanks to Claude Reichard who provided valuable input throughout the process of writing this dissertation. Thanks to Tara Ilich and Fuad Nijim for helping me so much with all the paper works for this project. I thank Margaret Muir for her tremendous help all through my first quarter in Stanford.

I would like to thank my fellow coworkers in the rock physics group for their friendship and advice: Carmen Gomez, Piyapa Dejtrakulwong, Richa, Kaushik Bandyopadhyay, Tanima Dutta, Ratnanabha Sain, Kevin Wolf, Ramil Ahmadov, and Danica Dralus. A special thank to my friends Huyen Bui, Ezequiel Gonzalez, Stephanie Vialle, and Cinzia Scotellaro.

I deeply thank Pastors Glen and Dutchie Coulter and all my brothers and sisters from the Father's house, who always supported my family and me at all time during my time in Stanford University. A special thank to Douglas Alexander, Kathleen Alexander, David Dewey and Julie Dewey. Special thanks to Dwan's, Pizarro's, Contreras', Mulliken's, and Anderson's families, with whom we shared and learned so much.

I deeply thank my wife, Yasmary. She understands my nonattendance and has the endless patience. Without her love, support, and encouragement, I could not finish.

My daughters, Francis, Estefani, and Loana, are the main energy for me to endure the tough days and enjoy the good ones. I also thank my brothers and sisters for having faith in me and giving me cheers every time I talk to them. Finally, I would like to share this project with my mother, Berta Peña. To God be the glory of this work.

The Stanford Rock Physics and Borehole Geophysics Consortium have provided financial support for this research.

Contents

`

List of Tables

List of Figures

Chapter 1
Introduction

1.1 Rock Physics Models

This dissertation presents the results of using different inclusion and granular effective medium models and poroelasticity to predict the elastic properties of rocks with complex microstructures, such as carbonate rocks. Effective medium models account for the microstructure and texture of rocks, and can be used to predict the type of rock and microstructure from seismic velocities and densities.

Most rock physics models fall within three general classes: theoretical, empirical, and heuristic (Avseth et al., 2005).

1.1.1 Theoretical models

The theoretical models are continuum mechanics approximations of the elastic, viscoelastic, or poroelastic properties of rocks. Biot (1956) was one of the first to formulate the coupled mechanical behavior of a porous rock embedded with a linearly viscous fluid. At zero frequency, the Biot equations reduce to the Gassmann (1951)

relations. Biot (1962) generalized his formulation to include a viscoelastic frame, followed by Stoll and Bryan (1970). Stoll and Bryan's model used Biot's theory as a basis for the model, which account for losses due to inelasticity of the skeletal frame and to motion of the pore fluid relative to the frame.

Elastic models may be classified into five kind of models: (a) inclusion models, (b) contact models, (c) bounds, (d) transformation, and (e) computational models (Avseth et al. 2005). In this dissertation we use elastic bounds, effective medium models, and transformations in all chapters.

Inclusion models

Inclusion models approximate rock as a continuous elastic solid containing solid or fluid inclusions. The solid inclusions may represent solid grains, and the fluid inclusions represent the rock pore space. Mineral inclusions stiffer than the rock matrix stiffen the rock, while softer inclusions, such as fluid and soft minerals, soften the rock. Most of the inclusion models treat the pores as ellipsoids (Eshelby, 1957; Walsh, 1965; Eimer, 1967, 1968; Kuster and Toksoz, 1974; O'Connell and Budiansky, 1974, 1977; Cheng, 1978, 1993; Berryman, 1980; Norris, 1985a; Hudson, 1980, 1981, 1990; Hudson and Liu, 1999; Crampin, 1984; Johansen et al., 2002; Jakobsen et al. 2003). Berryman (1980) generalized the self-consistent formulation so that both the pores and the grains are considered ellipsoidal inclusions in the composite material. The differential effective medium (DEM) theory models two-phase composite by incrementally adding inclusions of one phase to the matrix phase (Cleary et al., 1980; Norris, 1985; Zimmerman, 1991). Schoenberg (1983) and Pyrak-Nolte et al. (1990a, b) have considered inclusions in the form of infinite planes of slip or compliance, to model fractures. Jakobsen et al. (2003) synthesized many of the existing effective medium models and placed them on a common footing using the T-matrix formalism (Mavko et al., 2009). They also modeled the elastic properties of shales using the T-matrix formalism. Some of these inclusion models are used and compared in Chapter 2.

Contact models

Contact models estimate the elastic properties of a random aggregate of spherical particles. They are often used to approximate unconsolidated rocks. The elastic properties of the random aggregate are determined by the deformability and normal and tangential stiffnesses of their grain-to-grain contacts. Most contact models (Brandt, 1955; Walton, 1987; Digby, 1981; Norris and Johnson, 1997; Makse et al., 1999; Jenskin, 2005) are based on the Hertz-Mindlin (Mindlin, 1949) solution for the elastic behavior of two elastic spheres in contact. The key parameters determining the stiffness of the rock are the elastic moduli of the spherical grains and the area of grain contact, which results from the deformability of the grains under pressure (Avseth et al, 2005). Dvorkin et al. (1994) described the effect of adding small amounts of mineral cement at the contacts of spherical grains.

Spherical contact models have been used as helpful analogs of soft sediments, but, as with the inclusion models, they are also based on idealized geometries. They are not easy to extend to irregular grain shapes, distributions of grain size (Brandt, 1955), or aggregate of grains of different minerals.

The porous grain model, introduced in Chapter 4 and 5, are based on granular medium models, and combination of several kind of models.

Bounds models

Bounds models calculate the elastic bounds of a composite material based on fundamental principles. The bounds are rigorous and are relatively free of assumptions about the material microstructure. The calculations of the bounds are based on the assumption that rock is a linear elastic composite material (Mavko et al., 2009; Avseth et al., 2009). The lower and upper bounds and their arithmetic average can be used as mixing laws and can be associated with sorting and cementing trends. Bounds rigorously describe suspensions (Voigt, 1928; Reuss, 1929; Hill, 1952; Hashin and Shtrikman, 1963; Walpole, 1966). Chapter 2 focuses on elastic bounds with effective medium models.

Transformation models

Transformation models, such as the Gassmann (1955) relations for fluid substitution, are relatively free of geometric assumptions. The Gassmann relations take measured V_p and V_s at one fluid state and predict the V_p and V_s at another fluid state. Berryman and Milton (1991) presented a geometry-independent scheme to predict fluid substitution in a composite of two porous media having separate mineral and dry-frame moduli (Avseth et al., 2009).

Computational models

In computational modeling, the rock morphology and properties are represented by a grid, and the elastic, poroelastic, or viscoleastic behavior is computed using finite-element (Garboczi and Bentz, 1991; Garboczi and Day, 1995; Arns et al., 2002; Grechka and Kachanov, 2006; Makarynska et al, 2008; Mahyar et al., 2009) and finite-difference modeling. These numerical estimations are independent of idealized rock microstructures, and they have the capability to estimate the effects of features observed in thin sections on the rock elasticity.

Computational modeling also uses discrete element models to simulate the simultaneous interactions of many discrete grains in a soft sediment (Garcia and Medina, 2006, 2007). Computational modeling also uses hybrid discrete and finite element models for simulation of rocks (Fakhimi, 2008).

1.1.2 Empirical models

Most empirical models are based on experimental observations at specific physical conditions and specific data sets. The typical approach of empirical modeling is to assume some functional form of the trend of the data and then determine the empirical coefficients by calibrating a regression to measured data. Examples of these regressions are the V_p - density relations of Gardner et al. (1974), the V_p - V_s relations of Greenberg and Castagna (1992), and the V_p -porosity-clay relation of Han (1986). In this dissertation, we use empirical models as proxies for data.

An empirical model can be also obtained from the results of numerical experiments.

An attractive empirical approach is to use a neural network as a way to determine nonlinear relations among various rock physics parameters (Avseth et al., 2009).

Usually, an empirical relation involves a two-step process: a modeling step to determine the functional form followed by a calibration step to determine the empirical coefficients (Avseth et al., 2009).

1.1.3 Heuristic models

A heuristic model is a non-mathematical rigorous way to relate parameters. In heuristic models, we present heuristic arguments to justify why rock physics parameters should be related in a certain form (Avseth et al., 2009). An example of these models is the Wyllie time-average, which relates velocity to porosity, $1/V = \phi/V_f + (1-\phi)/V_s$. The time-average equation is equivalent to a straight-ray, zero-wavelength approximation, which is not valid when modeling wavelengths that are very long relative to grains and pores. Another example is the Hashin-Shtrikman bound curves. Although these bounds are rigorous, when modifying and using them to describe, for instances, cementing (upper bound) and sorting (lower bound) trends, they are heuristic. We argue that sorting is the softest way to add mineral to a sand, thus we heuristically explain why a lower bound equation might be expected to describe sorting. We also argue that cementing is the stiffest way to add mineral to a sand, thus we present arguments to explain why an upper bound equation might be expected to describe cementing. However, even though these arguments are reasonable, we are not able to derive these models from the first principles. In this dissertation, we use heuristic models, e.g. soft-sand model (Dvorkin and Nur, 1996), as proxies for data. Hybrid models

Hybrid models combine experimental observations (empirical relations) with theoretical bounds and models. An example is the evolution of the rock physics interpretation of Han's (1986) experimental data set. Han (1986) measured V_p and V_s velocities of shaley sandstones with various porosity and clay content. Han observed that the velocity-porosity-clay follows trends of parallel contour of constant clay volume. Nur et al. (1998) observed that each of these contours had high- and low-porosity intercepts that had a clear physical interpretation: in the limit of zero porosity, which means that any

model should rigorously account for the properties of pure mineral, while in the limit of high porosity (the critical porosity), the rock should fall apart. When a rock is falling apart, it becomes a suspension. Thus, instead of using empirical relations, Han's data can be modeled using the upper Hashin-Shtrikman bound scaled to critical porosity, which better fits the data over a large range of porosities and can be extrapolated to porosity values out of the data set range.

Another example of hybrid model is Dvorkin's soft-sand model (Dvorkin and Nur, 1996). This model is a heuristic model, which uses a the Hertz-Mindlin model to describe clean, well-sorted sands, combined with a modified lower bound to interpolate these to lower porosity, poorly sorted sands. Such heuristic models attempt to mimic geological processes, but honoring physical principles that make the model universal (Avseth et al., 2009).

In this study, we use a hybrid of theoretical, bounds, transformations, empirical, and heuristic models to describe carbonate sediment.

1.2 Chapter Descriptions

All Chapters in this dissertation are self-contained. However, they are interrelated. Chapter 3, in part, is based on Chapter 2. Chapter 5 is an extension of Chapter 4 and uses results from Chapter 3. Chapter 2 focuses on using composites as analogs of rocks with different texture. We show that if enough information regarding the rock microstructure is available, effective-medium models produce better estimates of the elastic properties of the rock matrix than the average of Hashin-Shtrikman (1963). This Chapter will be submitted to *Geophysics*. In Chapter 3, we develop a methodology that consists of matching experimental with DEM and finding the range of AR required to achieve this match. We show that there exist an elastic equivalency between DEM and the data. Once the elastic equivalent model is found, it is used to predict the effective elastic moduli of rocks. This Chapter will be published in *Geophysics* this year. In Chapter 4, we introduce the porous grain concept (Ruiz and Dvorkin, 2009) and develop a rock physics model for sediment with microporosity contained within the mineral phase (e.g., carbonate sediment and rocks, chalks, and opalines). This Chapter has been published this year in

Geophysics. In Chapter 5, we exploit the porous grain model to describe a variety of arrangement of grains and consider different degrees of hydraulic connectivity in the pore space. This Chapter will be summated to *Geophysics* this year.

Chapter 2 focuses on using the elastic properties of composites as analogs of rocks with different textures and different elastic contrasts between their constituents. The effective elastic moduli of a composite depend mainly on the volume fraction of each grain and interphase (cement) constituents, grain shapes, degree of anisotropy of the individual crystals constituents, stiffness contrast among phases, and the bonding state on the interface between the phases (Tong et al., 2001; Hashin, 1991a and 1991b).

In this Chapter, to model the elastic moduli of artificial composites, we consider the coherent potential approximation (CPA) (Berryman, 1980; 1995), and a differential effective-medium (DEM) approximation (Norris, 1985a). These two approximations always satisfy the Hashin-Shtrikman bounds (Hashin and Shtrikman, 1963), which are rigorous bounds, and produce physically realizable results (Norris, 1985a; Berryman, 1995). We also test two models, which focus on the interaction of spherical inclusions at high concentrations, one developed by Devaney and Levine (1980) and the other by Mondescu and Muthukumar (1999).

We test the effective-medium models on a large composite data set in order to evaluate their predictions for a wide range of elastic moduli contrasts and inclusion shapes, with the goal of finding which model will most accurately determine the effective elastic moduli of sedimentary rocks with complex matrices.

We find that because the selected materials have microstructures are consistent with the DEM approximation, DEM provides consistently accurate predictions over a wide range of volumetric concentrations and with a fairly narrow range of aspect ratio.

Chapter 3 focuses on the prediction of the elastic properties of carbonates. We introduce the concept of *elastic equivalency* between rock physics models, using the inclusion aspect ratio as a single fitting parameter. We exploit this concept to make rock physics predictions. This chapter is self-contained but it is based on the results found in Chapter 2. In this chapter we limit ourselves to using only one inclusion theory, DEM, as formulated by Norris (1985a), with randomly oriented spheroidal inclusions. Therefore,

we deal with isotropic rock. Our approach consists of matching experimental data over wide ranges of porosity and mineralogy with DEM and finding the range of AR required to achieve this match. Although the actual rock may not be a physical realization of this mathematical model, we will show that there exist an elastic equivalency between DEM and the data. Our hypothesis is that if such elastic equivalency can be established with a narrow range of AR and for a wide range of real samples, we can find an idealized physical analogue to real rock and then use this analogue to interrelate different properties of real samples.

Chapter 4 introduces the *porous grain concept* and merges it with the existing rock physics models. This model is applied to marine carbonate sediment, diatomaceous rocks, and chalks (Ruiz and Dvorkin, 2009).

The porous grain model treats the high-porosity sediment as a pack of porous elastic grains, which represent minute calcareous or siliceous skeletons. This principle of theoretically replacing the actual mineral with a porous material can be applied, as appropriate, to various mineralogies and used with any of the existing rock physics models, including such traditional relations as by Wyllie et al. (1956), Raymer et al. (1980), and Krief et al. (1990).

Chapter 5 is an extension of the porous-grain model introduced in Chapter 4. In this Chapter, we develop a methodology to determine the effective elastic moduli of porous grain aggregates with various textures. The porous grain model is extended to allow: a) variations of the grain contact friction coefficient, b) combining the self-consistent approximation (Berryman, 1980) with the cementation theory (Dvorkin et al., 1994) to account for intergranular cement volume fractions from 0 to 1, and c) considering the effect of frequency. The porous-grains model can be applied to approximate three different porous grain-aggregate scenarios, depending on the effective fluid connectivity of the intragranular porosity in the grain. The model for non-cemented aggregates may be applied to sediment with porous grains. The model for cemented aggregates may be applied to carbonate rocks. The microstructural parameters of these models can be related to diagenesis and may be varied to mimic diagenetic processes of carbonate rocks.

1.3 References

Arns, C., Knackstedt, M., Pinczewski,W., and Garboczi, E., 2002, Computation of linear elastic properties from microtomographic images: Methodology and Match to Theory and Experiment, Journal of Geophysics Research, **67**, 1396-1405.

Avseth, P., Mukerji, T., and Mavko, G., 2005, Quantitative seismic interpretation: applying rock physics tools to reduce interpretation risk: Cambridge University Press.

Berryman, J. G., 1980, Long-wavelength propagation in composite elastic media, Journal of Acoustic Society of America, **68**, 1809-1831.

Biot, M. A., 1956, Theory of propagation of elastic waves in a fluid saturated porous solid: I. Low frequency range and II. Higher-frequency range: Journal of Acoustic Society of America, **28**, 168-191.

Biot, M. A., 1962, Mechanics of deformation and acoustic propagation in porous media: Journal of Applied Physics, **33**, 1482-1498.

Cheng, C.H., 1978, Seismic Velocities in porous rocks: Direct and inverse problems. Sc.D. thesis, MIT, Cambridge, Massachusetts.

Cheng, C.H., 1993, Crack models for a transversely anisotropic medium: Journal of Geophysical Research, **98**, 675–684.

Crampin, S., 1984, Effective anisotropic elastic constants for wave propagation through cracked solids: Journal of the Royal Astronomical Society, **76**, 135-145.

Dvorkin, J., and Nur, A., 1996, Elasticity of high-porosity sandstone: Theory for two North Sea Datasets: Geophysics, **61**, 1363-1370.

Eimer, C., 1967, Stresses in multi-phase media, Archiwum Mechaniki Stosowanej, **19**, 521.

Eimer, C., 1968, The boundary effect in elastic multiphase bodies, Archiwum Mechaniki Stosowanej, **20**, 87.

Eshelby, J.D., 1957, The determination of the elastic field of an ellipsoidal inclusion, and related problems: in Proceedings of the Royal Society of London, A241, 376–396.

Fakhimi, A., 2009, A hybrid discrete–finite element model for numerical simulation of geomaterials: Computers and Geotechnics, **36**, 386-395.

Garboczi, E., and Bentz, D., 1991, Fundamental Computer Simulation Models for Cement-Based Materials: Materials Science of Concrete, **2**, 249-277.

Garboczi, E., and Day, R., 1995, An algorithm for computing the effective linear elastic properties of heterogeneous materials: Three-dimensional results for compostes with equal phase porsson ratios: Journal of the Mechanics and Physics of Solids, **43**, 1349-1362.

Garcia, X. and Medina, E., 2006, Molecular dynamic modeling of the effects of cementation on the acoustical properties of granular sedimentary rocks, Condensed Matter Material Sciences, Condensed Matter e-prints

Garcia1, X., and E. Medina, 2007, Acoustic response of cemented granular sedimentary rocks: Molecular dynamics modeling: Physics Review, E-75.

Gassmann, F., 1951, Über die elastizität poröser medien: Veirteljahrsschrift der Naturforschenden Gesellschaft in Zürich, 96, 1-23.

Grechka, V. and Kachanov, M., 2006, Effective elasticity of fractured rocks: The Leading Edge, **25**, 152-155.

Hudson, J., 1980, Overall properties of a cracked solid. Mathematical Proceedings of the Cambridge Philosophical Society, **88**, 371-384.

Hudson, J., 1981, Wave speeds and attenuation of elastic waves in material containg cracks: Geophyscal Journal of the Royal Astronomical Society, **64**, 133-150.

Hudson, J., 1990, Overall elastic properties of isotropic materials with arbitrary distribution of circular cracks: Geophysics Journal International, **102**, 465-469.

Hudson, J., and Liu, E., 1990, Effective elastic properties of heavily faulted structures: Geophysics, **64**, 479-485.

Hill, R., 1952, The elastic behavior of crystalline aggregate, Proceedings of the Physics Society, London A, **65**, 349-354.

Jakobsen, M., J. Hudson, and T. Johansen, 2003, T-matrix approach to shale acoustics. Geophysics Journal International, **154**, 533-558.

Johansen, T. A., Jakobsen, M., and Ruud, B. O., 2002, Estimation of the internal structure and anisotropy of shales from borehole data: Journal of Seismic Exploration, **11**, 393-381.

Kroner, E., 1967, Elastic moduli of perfectly disordered composite materials: Journal of The Mechanical and Physics of Solids, **15**, 319-329.

Kuster, G. T., and M. N. Toksoz, 1974, Velocity and attenuation of seismic waves in two-phase media: part 1. Theoretical formulations: Geophysics, **39**, 587-606.

Mahyar M., Jones, A., Arns, C., Knackstedt, M., 2009, 3D imaging and simulation of elastic properties of porous materials: Computing in Science and Engineering, **11**, 65-73.

Makarynskaa, D., Gurevich, B., Cizc, R., Arnsd, C., Knackstedtd, M., 2008, Finite element modelling of the effective elastic properties of partially saturated rocks: Computers & Geosciences, **34**, 647–657.

Mavko, G., T. Mukerji, and J. Dvorkin, 2009, The rock physics handbook: Cambridge University Press.

O'Connell, R. J., and Budiansky, B., 1974, Seismic velocities in dry and saturated cracked solids, Journal of Geophysics Research, **79**, 4626-4627.

O'Connell, R. J., and Budiansky, B., 1977, Viscoelastic properties of fluid-saturated cracked solids, Journal of Geophysics Research, **82**, 5719-5735.

Ruiz, F., and Dvorkin, J., 2009, Sediment with porous grains: Rock-physics model and application to marine carbonate and opal: Geophysics, **74**, E1.

Stoll, R.D., and Bryan, G.M., 1970, Wave attenuation in saturated sediment: Journal of Acoustic Society of America: **47**, 1440-1447.

Voigt, W., 1928, Lehrbuch der Kristallphysik (Berlin: Teubner)

Walpole, L. J., 1966, On bounds for the overall elastic moduli of inhomogeneous systems. I. Journal of the Mechanichs and Physics of Solids: **14**, 151-162.

Walsh, J. B., 1965, The effect of cracks on the compressibility of rock: Journal of Geophysical Research: **70**, 381–389.

Chapter 2
Accuracy of DEM and SC estimations of elastic properties of complex rock matrix using composites as analogs

2.1 Abstract

At low porosity, the elastic moduli of the rock mineral matrix often dominates those of the whole rock. A sedimentary rock matrix may be considered as a composite and may include mineral constituents with very different moduli and shapes. To describe the fabric of these rocks, an unmanageable number of parameters may be needed. Understanding the elastic behavior of synthetic composites, which are easier to model, enables us to quantify the effect of each parameter on the elastic moduli of the rock matrix independently. We test whether the differential effective-medium (DEM) and self-consistent (SC) models can accurately estimate the elastic moduli of a complex rock matrix and compare the results with the average of upper and lower Hashin-Shtrikman bounds (HS). The testing was conducted using data from the literature on short-fiber-filled composites, particulate-filled composites, and crystalline aggregates, covering a wide range of inclusion concentrations, inclusion shapes, and elastic modulus contrasts. We find that when the material microstructure is consistent with the DEM approximation,

DEM is more accurate than both SC and the bound-average method for a variety of inclusion aspect ratios, concentrations, and modulus contrasts. DEM is found to be consistently accurate if a single effective inclusion aspect ratio is appropriately selected and held constant for the entire concentration range. If relatively little information is known about the rock microstructure, DEM can estimate the elastic properties of complex mixtures of minerals more accurately than heuristic estimates, such as the arithmetic average of the upper and lower elastic bounds. Finally, we propose a methodology for applying effective-medium models to estimate the elastic properties of sedimentary rocks with complex mineral matrices.

2.2 Introduction

The skeleton material of a sedimentary rock may be considered as a pack of glassy and/or imperfect crystalline grains and organic matter, completely or partially compacted. These grains may be entirely or partly welded by one or more cement minerals, and arranged in intricate ways. We call the composite rock skeleton material the matrix. In the matrix, different mineral grains may be randomly located in a continuous or discontinuous mode and may have random or preferred orientations. For instance, if in the rock matrix the grains are randomly spatially distributed and oriented, the matrix looks like a polycrystalline aggregate, where all crystallites (grains) are completely disordered. As another example, if the rock matrix contains one continuous and several discontinuous phases, we may treat the continuous phase as the host and the discontinuous phases as isolated host-embedded mineral inclusions. This is the case of hybrid composites. The mineral inclusions may be stiffer or softer than the mineral host, and of different shapes and sizes. In some rocks, this matrix may be composed of only two main minerals with simple microstructure. In other cases, this matrix may be complex, composed of several high-elastic-contrast minerals and having complex microstructure. To mathematically describe the structure of natural rock matrix, an unmanageable number of parameters is often needed, such as volume fractions of crystalline and amorphous material and their elastic moduli, nature of boding on the grain interface, type and volume fraction of cements. On the other hand, it is possible to

fabricate non-porous composites simple enough that they can be modeled with relatively few parameters. Therefore, by carefully selecting the parameters we are interested in, composites can be accurately mathematically modeled. Hereafter, we use the term composite to refer to artificial composites.

Composites can be fabricated with several constituent phases. The simplest are two-phase composites. Two-phase composites, including granular aggregates such as polycrystalline aggregates, can be classified in terms of the phase continuity and connectivity. Three main composite categories have been suggested (Ji and Xia, 2003; Gurland, 1979): a) composites with a stiff-phase-supported frame (SPSF), in which the stiff phase is continuous, while the compliant phase is discontinuous in the direction of the applied load; b) composites with a compliant phase-supported-frame (CPSF), in which the stiff phase is discontinuous while the compliant phase is continuous in the loading direction; and c) composites with a transitional frame (TF), in which both the stiff and the compliant phases are continuous (TFC) or discontinuous (TFD) in the loading direction. When all phases are discontinuous, there is no well-defined matrix phase, such as in completely random polycrystalline materials.

When fabricating composites, varying a specific host or inclusion feature, such as grain size, might create undesirable features. Examples of common undesirable experimental features are residual anisotropy, residual porosity or cracks, incompletely welded constituents, crystalline and/or glassy phases created by solid-solid reactions or during sintering, imperfect randomness, and inclusion agglomerations which increase the sizes of heterogeneities. Imperfections at the interface between the constituent phases and residual porosity are perhaps the two most common undesirable features. To mitigate these features, in some composites an adhesive ingredient is added to the mixture to bind the matrix and inclusions (Vollenberg and Heikens, 1990). By adding this ingredient, known as an interphase (cement), a three-phase composite is created.

Composites can be considered as analogs of rocks with predesigned composition and microstructure. The elastic properties of selected composite constituents can be designed to be the same as or comparable to those found in natural rocks. Combining these constituents, the composition and structural parameters of composites may be varied

independently, whereas in rocks the parameters can not be separately controlled.

The effective elastic moduli of a composite depend mainly on the volume fraction of each grain and interphase (cement) constituents, grain shapes, degree of anisotropy of the individual crystals constituents, stiffness contrast among phases, and the bonding state on the interface between the phases (Tong et al., 2001; Hashin, 1991a and 1991b). The bonding between phases (minerals) may be considered as perfect or imperfect. Various theoretical approaches for estimating the elastic moduli, such as micromechanics, variational principles, and multi-scattering theory, have been developed for perfectly bonded composite (e.g., Kuster and Toksoz, 1974, Hashin, 1963; Hashin, 1983; Torquato, 1991; Nemat-Nasser and Hori, 1993; Berryman, 1980; Norris, 1985a; Devaney and Levine, 1980; Mondescu and Muthukumar, 1999). It has been observed that imperfect bonding has a significant effect on the elasticity of composites (Achenback and Zhu, 1990; Vollenberg and Heikens, 1990; Gotz at al., 1991; Nan et al., 1997).

In this study, to model the elastic moduli of materials, we consider effective-medium models, which are based on wave scattering theory. In these models it is assumed that the wavelengths are much longer than the size of the inclusions. Specifically, we consider a self-consistent model (SC) known as the coherent potential approximation (CPA) (Berryman, 1980; 1995) and a differential effective-medium (DEM) approximation (Norris, 1985a). These two approximations always satisfy the Hashin-Shtrikman bounds (Hashin and Shtrikman, 1963), which are rigorous bounds, and, as a result, they produce physically realizable configurations (Norris, 1985a; Berryman, 1995). We also test two models which consider the interaction of spherical inclusions at high concentrations, one developed by Devaney and Levine (1980) and the other by Mondescu and Muthukumar (1999), hereafter referred to as DL and MM, respectively. DL and M are not necessary realizable, depending on the values of the selected material elastic properties, shapes, and concentrations, they can produce results out side the Hashin and Shtrikman bounds.

In order to formulate solvable equations, these theories are based on idealized assumptions about the material microstructures and mathematical approximations. The relationship between these mathematical approximations and the rock matrix microstructure is not always evident. However, each of these models still offers a useful

analog to the elastic behavior of a rock matrix with specific microstructure. For instance, a rock matrix where the host and inclusion parts can be identified may look more like a physical realization of DEM, whereas an aggregate of grains may look more like a physical realization of CPA.

In any model that estimates the elastic-wave velocity in porous rock, the elastic properties of the mineral matrix are required inputs. The correctness of this input is especially important in low-porosity rock, such as tight gas sandstone. The matrix of such rock can include elements of contrasting elastic properties, such as hematite and clay, pyrite and clay, siderite and quartz, etc. For example, in the tight gas sandstone shown in Figure 2.1, high-density and high-stiffness elements (white) are mixed with softer elements (gray).

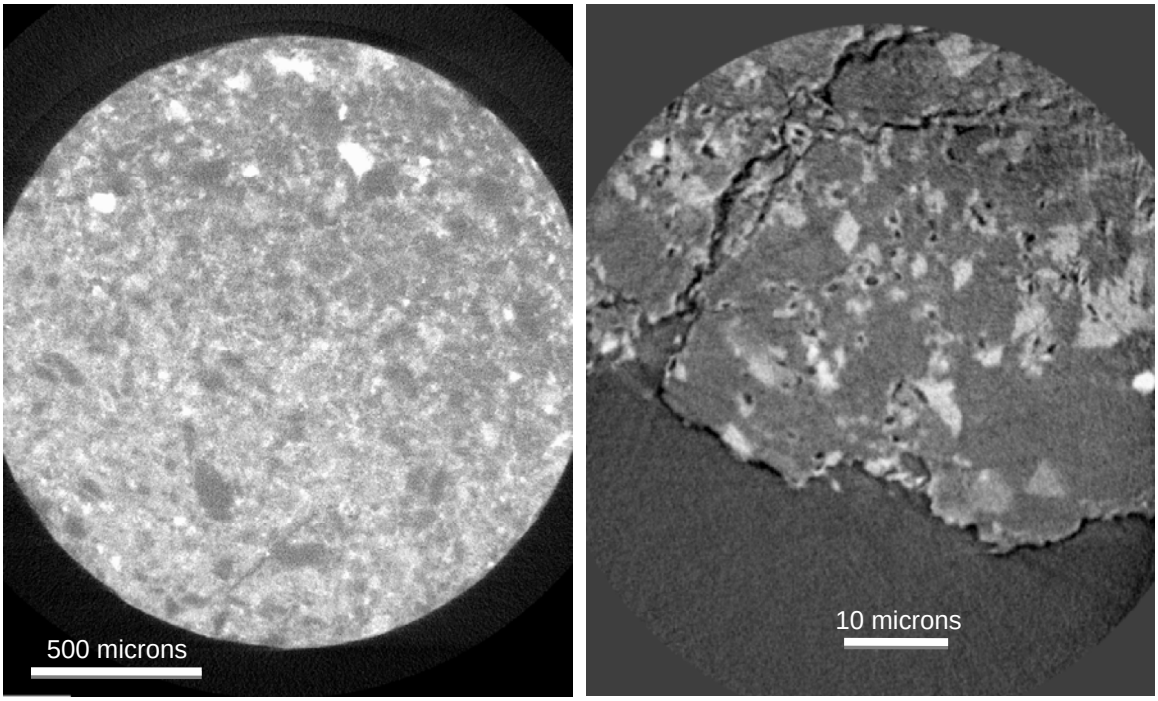

Figure 2.1: Tomographic slices of a 3D CT-scan image of tight gas sandstone. Left: micro-CT resolution. The pore space is not discernable. The elements of varying density, from high (white) to low (dark gray) are apparent. Right: nano-CT resolution. The micropores appear black and embedded into light-gray crystals. White crystals represent high-density and high-stiffness mineral. The dark-gray (lower-density) background is relatively soft. Courtesy Ingrain, Inc.

The intricacy of this matrix becomes especially clear in the nano-scale image, where

high-density and very stiff crystals (white), together with lower-density and less stiff crystals (light gray), are embedded into a low-density and soft matrix (dark gray).

If microstructure information is completely absent, the traditional method of estimating the effective elastic moduli of a matrix from the elastic moduli of its elements is Hill's (1952) average, which is the arithmetic average of the elastic upper (Voigt) and lower (Reuss) bounds. One can also use the arithmetic average of the upper and lower Hashin-Shtrikman (1963) bounds (HSA). Methods that set bounds on the effective composite elastic moduli are helpful for rock matrices and composites with low contrast in stiffnesses. However, in a situation where composites or rocks are made of contrasting elastic components, the difference between the upper and lower bounds can be large, which makes the Hill-average approach a poor estimate. If enough information regarding the rock microstructure is available, effective-medium models produce better estimates than the average of theoretical bounds. Consider, for example, a mixture of pyrite, whose bulk (K) and shear (G) moduli are 147 and 133 GPa, respectively, and clay with K = 21 GPa and G = 7 GPa (Mavko et al., 1998). At 30% pyrite concentration, the difference between the Voigt and Reuss bulk modulus bounds is about 30 GPa, and that between the upper and lower HS bounds is about 20 GPa. For the shear modulus, these differences are about 35 and 20 GPa, respectively. Because of the resulting large uncertainty of estimations by the bound method, we test whether the effective-medium models, which can give better predictions for specific phases' stiffness contrasts and microstructures, can better estimate the elastic properties of a sedimentary rock matrix. It is important to bear in mind that each theoretical model is applicable only to the specific material elastic contrasts and microstructures for which it was formulated.

We test the effective-medium models on a large data set of CPSF and SPSF composites in order to evaluate their predictions for a wide range of elastic moduli contrasts and inclusion shapes, with the goal of finding which model will most accurately determine the effective elastic moduli of sedimentary rocks with complex matrices.

The effective-medium approximations can be subdivided into two basic groups: a) asymmetric models, which are consistent with materials where host and inclusions can be identified, such as CPSF and SPSF composites, and b) symmetric models, which are

consistent with materials where no matrix can be identified, such as TF composites.

DEM models multiphase materials by incrementally adding inclusions of one phase to the phase identified as the matrix (Cleary et al., 1980; Norris, 1985a; Zimmerman, 1991; Mavko et al; 1998). DEM requires identifying any one of the mineral constituents as the matrix and all other minerals as isolated embedded inclusions. Therefore, DEM may generate more effective elastic-modulus estimates than the number of phases present in the rock. For a multiphase material, with specific volume concentrations of different phases, it is possible to obtain different estimates of the effective moduli, by altering the order of the differential addition. This is also true if the material has inclusions of a single phase, but of different shapes. If the stiffest mineral is identified as matrix, the rock matrix will behave as a SPSF composite. If the softest mineral is identified as matrix, the rock matrix will behave as a CPSF composite.

CPA, like DEM, also uses the solutions for the deformation of isolated inclusions, but the interaction of inclusions is approximated by replacing the background medium with an as-yet-unknown effective medium (Berryman, 1995). CPA produces only one estimate, regardless of the number of phases and inclusion shapes present in the rock. The rock is treated as an aggregate of all constituents, and none of mineral phases plays the role of matrix for the others (Berryman, 1995; Mavko et al., 1978). Berryman (1995) gives a specific form of the CPA approximation for multiphase composites.

DL approximation is also based on a self-consistent formulation of multiple-scattering theory. This approach assumes that the inclusions are spherical. In the particular case where the concentration of inclusions is low, this model reduces to the CPA. However, at high inclusion concentration, when the multiple-scattering effects are not negligible, DL estimates differ considerably from the CPA estimates (Devaney and Levine, 1980).

MM approximation is used for computing the effective elastic properties of a composite material containing rigid, mono-sized, spherical particles, which can either overlap or not, and are randomly dispersed in a host material. This model allows for an inclusion volume fraction that is high enough for a percolation transition to occur and clusters to form (Mondescu and Muthukumar, 1999; Sahimi, 2000).

DEM, DL and MM are consistent with materials where a matrix and inclusions can be identified, such as particulate composites, and yield formulas that are not symmetrical in the two phases. On the other hand, CPA is symmetric in all of the mineral constituents. DEM and CPA are realizable MM and DL methods are not

We find that because the selected materials have microstructures of the CPSF- and SPSF-type, which are consistent with the DEM approximation, DEM provides the most consistently accurate predictions over a wide range of volumetric concentrations and with minimum flexibility of input parameters (e.g., aspect ratio).

2.3 Composite Datasets

For testing the accuracy of the DEM and CPA models, compared with the HS bounds, we used twenty-three two-phase composite experimental data sets from the literature. These composites cover a wide range of inclusion concentrations and elastic-modulus contrasts (Tables 1 and 2). In most of these data sets, mixtures of different concentrations of constituents, such as resins, polymers, rubber, metals, and single crystal polycrystalline powders, were used to make non-porous composite samples.

The composite systems (matrix/inclusion) cover two main types: a) CPSF and SPSF, with an organic material (polymer) as host and glassy, organic, or metallic materials as inclusions, and b) composites with a polycrystalline material as host and polycrystalline materials as inclusions. In all the composites, the embedded inclusions are randomly located and oriented. An exception is the enstatite/forsterite composite system data set (Ji and Wang, 1999), which consists of mixtures of crystalline powders.

Table 1 shows the elastic moduli and densities of the composites materials used, and the sizes and shapes of the inclusions. Table 2 shows the density contrasts, the bulk and shear-modulus contrasts between host and inclusion materials, the type of test conducted to measure the elastic properties (ultrasound, resonant bar, or static measurements), and the composite type, based on the classification described in the introduction. In some of these isotropic composite data sets, the measured density and elastic moduli are available, and in others only the *P*-wave velocity (V_p), bulk (k) or Young's (E) modulus is available.

Most of these composite samples appeared to be free of residual porosity (ϕ_r); however, in some of the composite samples ϕ_r can be estimated, or it is reported, such as in the enstatite-forsterite system (Ji and Wang, 1999). The residual porosity, ϕ_r , is determined by computing the difference between the theoretical and measured density, ρ and ρ_m , respectively, as $\phi_r = (\rho - \rho_m)/\rho$.

Table 2.1: Data sets used in our study. Here, spheroids refer to oblate spheroids (close to spherical particles). In most data sets, the inclusion aspect ratio (AR) distribution or average (AR) is not reported. The inclusion size range or average and the constituent density are not reported in some data sets.

References	Host Properties				Inclusion Properties					
	Host	K_h (GPa)	G_h (GPa)	ρ_h (g/cm^{-3})	Inclusion	K_i (GPa)	G_i (GPa)	ρ_i (g/cm^{-3})	Size (μm)	Shape
Lees and Davidson (1977)	PMMA	5.80	1.25	1.17	Crystabolite	69.00	12.50	2.32		Spheroids
Zhang et al. (1996)	Resin	5.31	1.82	1.25	Aluminum	77.44	24.77	2.68	5-300	Spheroids
Bridge and Cheng (1987)	Polypropylene	4.29	1.44	0.91	CaCO3	67.00	33.10	2.70		Spheroids
Gomez et al. (2000)	Epoxy	5.52	1.38	1.14	PZ-Ceramic	163.52	52.05	7.70		
Piche and Hammel (1986)	Resin	5.70	2.00	1.18	Iron	166.24	82.86	7.84	50	Spheroids
Piche and Hammel (1987)	Resin	5.70	2.00	1.18	Iron	166.24	82.86	7.84		Flakes/Fibers
Nguyen et al. (1996)	Resin	8.00	1.60	1.26	Tungsten	306.00	162.00	19.30	0.5-5	Spheroids/short fibers
Sugawara et al. (2005)	Resin	5.34	1.69	1.15	Tungsten	306.00	162.00	19.30	1 - 3.	Spheroids
Lees (1973)	Vinyl	4.51	0.40	1.26	Tungsten	325.72	162.31	19.30		
Richard (1975)	Polyester	5.02	0.58		Glass	40.40	29.05			Spheroids
Smith (1976)	Epoxy-Polymer	4.73	1.08		Glass	46.91	30.89			Spheroids
Doi et al. (1970)	Cobalt	181.50	79.43		Carbide	382.08	298.10		1 - 23.	
Biwa (2001)	PMMA	5.91	2.25	1.19	Rubber	2.71	0.56	1.13	0.05 - 1	Spheroids
Ji and Wang (1999)	Enstatite	104.60	74.20	3.17	Forsterite	126.30	79.80	3.20	12	Spheroids (AR=0.67)
Pernot and Rogier (1993)	Glass-Ceramic	35.42	28.80	2.65	Stainless	160.80	74.20	7.95	< 50	Spheroids (AR~1)
Hasselman and Fulrath (1965a)	Glass	43.85	33.71		Tungsten	195.54	148.10		30	Spherical
Hasselman and Fulrath (1965b)	Glass	43.85	33.71		Alumina	281.92	163.50		50-100	Spheroids(AR=0.1-1.0)
Hasselman and Fulrath (1963)	Zirconium-Carbide	239.86	202.95	6.70	Graphite	4.79	4.54	1.90	100-200	Flat and Spheroids
Nishimatsu and Gurland (1960)	Cobalt	172.37	79.56		Carbide	418.61	288.22			
Quesenberry et al. (2003)	Epoxy	2.47	0.92	1.19	Glass	46.90	30.90	2.54		Spheres/short fibers
Dunn and Ledbetter (1995)	Aluminum	73.48	27.10	2.70	Mullite/Alumina	173.5/255	89.5/163	3.17/3.99	30/45/100	Short rods/Spheres
Vollenberg and Heikens (1990)	Polypropylene	3.25	0.55		Chalk	19.44	14.58		3.5/30/130	Irregular (AR ~1)
Gaudig et al. (2003)	Ferrite	163.49	79.85	7.84	Graphite	2.50	1.71	1.90		Vermicular/Spheroidal
Ledbetter and Dunn (1995)	Ferrite	163.49	79.85	7.84	Graphite	2.50	1.71	1.90		Spheroidal

Most of the selected composites are polymer based. During the tests conducted on polymer composite samples, multiple mechanisms, associated with the constituent's characteristics and test type (static or dynamic) may take place simultaneously contributing to different amounts of change in the elastic properties of the tested composite. To quantify the effect of a single mechanism, the composite samples need to be constructed and tested carefully. Interactions between the composite constituents may

cause changes in the microstructure of the composite and consequently produce changes in its effective elastic moduli and behavior. Different tests or different material combinations may induce different mechanisms. For instance, choosing large inclusion sizes reduces the formation of clusters of inclusions; applying small strains reduces breaking of the inclusions; and choosing spherical inclusions avoids preferred geometrical rearrangements and reduces residual anisotropy. When the inclusion volume fraction is large, interactions between inclusions may be large, and new mechanisms arise, such as friction at the inclusion contact area. In reinforced polymer composites, two main mechanisms may occur (Aksel and Hubner, 1996): a) the detachment of the host polymer from the inclusion surface (dewetting) and b) sliding of the polymer chains on the inclusion surface. Different combinations of material components may exhibit different degrees of adhesion between the host and the inclusion surface. The strength of the electrostatic bonds in the host polymer itself may be much higher than the strength of the bonds between the host and the inclusions surface. High-strain tests, such as those applied in stress-strain tests (static), may induce cracks in the host material. These cracks may have a large effect on the composite elastic moduli. Low-strain tests, such as those produced by ultrasonic tests, do not induce cracks, but may activate mechanisms in the interface between the host and the inclusions.

The embedding of an inclusion phase may cause spherulization, which changes the morphology and crystalinity of the host polymer. The magnitude of the changes may depend on the shapes and inclusion volume fraction (Vollenberg and Heikens, 1990). The first row of the polymer spherulites at the inclusion may act as an interphase. In this case, the two-phase composite becomes a three-phase composite. The elastic properties of this third phase are different from those of the host polymer and inclusion. The thickness of this interphase might depend on the inclusion characteristics, such as size and shape.

In practice, the connectivity among inclusions depends not only on the affinity between the inclusion and host materials, but also on the procedure used to construct the samples. If there is a strong affinity between the host polymer (or other material) and the inclusion material (e.g. ceramic, metal etc) a thin layer of a different polymer material surrounding each particle might appear even at high inclusion volume fraction. Usually,

if warm pressing or screen-printing is used on mixtures of inclusions with a fluid polymer, the constructed composites will usually have higher degree of connectivity than the composites where the inclusions are initially placed in contact, with a polymer then added using vacuum impregnation and backfilling (Gomez et al., 2000).

2.4 Comparison of theoretical and experimental data

2.4.1 Effect of stiffness contrasts

Figures 2.2 to 2.8 show the measured elastic properties and theoretical predictions for the two-phase composite data sets. The theoretical density of the mixtures, ρ, is given by, $\rho = (1 - C_1)\rho_2 + C_1\rho_1$, where ρ_1 and ρ_2 are the densities and C_1 and $C_2 = 1 - C_1$ are the volume fractions of the two-phase composite constituents. Since in all data sets the difference between calculated densities and measured densities is very small, we use the theoretical densities in our modeling. For the application of DEM described in this subsection, the aspect ratio of the inclusions was 1 (Figures 2.2 to 2.9), and for CPA the aspect ratio was 1, for both host and the inclusions.

In most of the composites, the experimental velocities fall inside the Hashin-Shtrikman bounds. At small inclusion concentrations, the lower Hashin-Shtrikman bound (HS^-) gives accurate results for the CPSF composites (Figures 2.2 to 2.5), and the upper Hashin-Shtrikman bound (HS^+) gives accurate results for the SPSF composites.

At low concentrations, the DEM, CPA and DL predictions for CPSF composites with aspect ratios close to unity approach the lower Hashin-Shtrikman bound (HS^-). For SPSF composites the model predictions approach the upper Hashin-Shtrikman bound (HS^+). At high concentrations, the difference between the model predictions and HS^- or HS^+ increases.

For the entire range of inclusion concentrations, the predictions of DEM and CPA lie between the HS bounds (Figure 2.2-2.9). The DL predictions also lie between the bounds, but only for moderate concentrations. MM produces results that may lie inside or outside the HS bounds (Figures 2.4, 2.5, 2.7, and 2.9).

Notice that as concentration increases, the prediction accuracy for all models deteriorates. The inclusions in most of the composites are spheroidal and have different

ranges of particle sizes (highly polydispersed). When small particles are present, they usually tend to agglomerate in clusters, such as in the cobalt/tungsten-carbide (Co/WC) system, even for low concentration values (Sahimi, 2003). As particle size increases, the tendency for clustering is reduced. At high concentration, the inclusion phase becomes more continuous because the degree of connectivity between particles increases. Theoretically, if the inclusion sizes are appropriately distributed, volume fractions close to unity could be achieved by nesting smaller inclusions within the interstices of the larger inclusions. However, the inclusion size spectrum in real composites has a restricted range, so the maximum inclusion volume fraction cannot approach unity (Phan-Thien and Pham, 1997). In powder metallurgy, a maximum concentration of 0.9 can be reached by compaction and plastic deformation of metal particles. In polymer-bonded explosives, the particles may occupy volume fractions greater than 0.9 (Banerjee and Adams, 2004).

As the inclusion volume fraction increases, more inclusions aggregate to form clusters. The volume fraction at which the first single cluster of inclusions spans the sample is called the percolation threshold volume. Depending on the contrast between the host and inclusion velocity, this single cluster may be the fastest (or slowest) way for a wave to propagate through the sample, for wavelengths that are smaller than the cluster size. At the percolation threshold, a transition occurs in the effective elastic properties of the material (Stauffer and Aharony, 1994; Gomez et al., 2000; Nur et al., 1998).

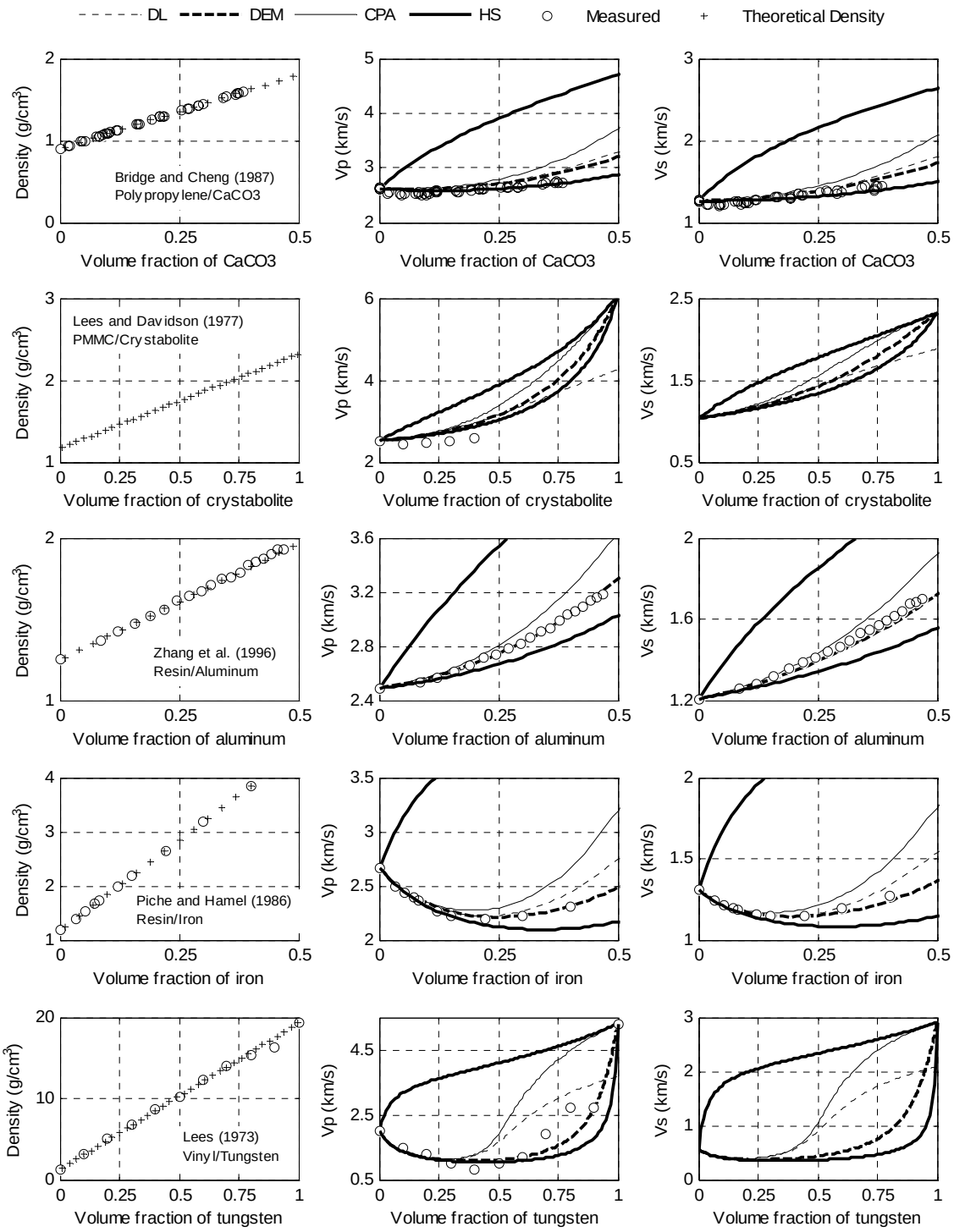

Figure 2.2. Left column: Measured and calculated effective density of the materials. Middle and right columns: comparison of ultrasonic experimental to calculated effective V_p and V_s velocities, respectively. The aspect ratio used in DEM and CPA was 1. All composites in this Figure are of the CPSF type.

Effective-medium models apply only to statistically homogeneous media. A moderately heterogeneous material may be assumed to be statistically homogeneous. Thus there exists a representative elementary volume (REV), and any part of the statistically homogeneous system with a volume considerably larger than the REV has identical physical properties (Gueguen et al., 1997; Gueguen et al., 2006). Beyond a certain degree of heterogeneity, effective-medium models are not valid; thus close to the percolation threshold, either below or above, these models should not be applied.

Decreasing the oblate inclusion aspect ratio is equivalent to increasing the connectivity between inclusions, such as in rocks with large number of fractures, or clustering of inclusions in composite materials. Thus, the percolation threshold will be reached earlier in materials with low-aspect-ratio inclusions than in those with high-aspect-ratio inclusions.

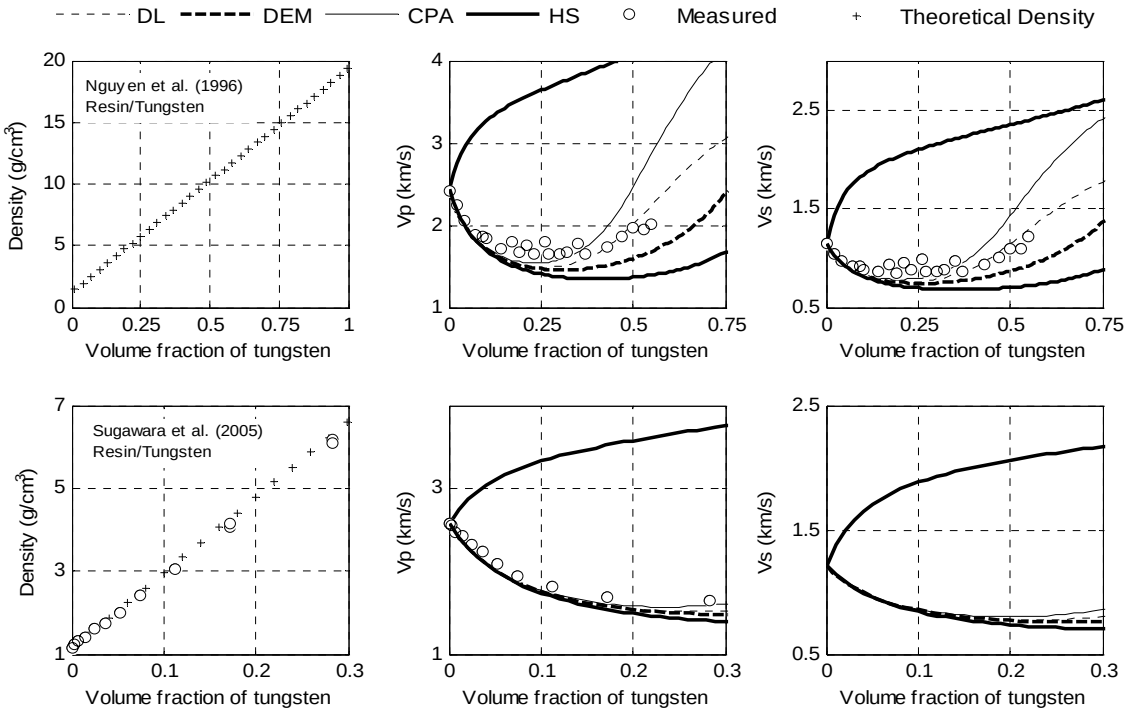

Figure 2.3. Left column: Measured and calculated density. Middle and right columns: comparison of ultrasonic experimental to calculated effective V_p and V_s velocities, respectively. The aspect ratio used in DEM and CPA was 1. These two composites are of the CPSF type.

The change in continuity or connectivity of the inclusion phase occurs gradually. The rate of this change, as more inclusions are added to the material, depends on the size and shape spectra of the inclusions. CPA gives a percolation transition of 0.59 for spherical inclusions. For irregularly-shaped and polydispersed particles, a percolation transition occurs at an inclusion volume fraction of about 0.59 (Sahimi, 2003). If the volume fraction is increased above the percolation transition, the continuous host material becomes discontinuous and the role of host and inclusion is switched. During this transition, the composite material goes from the CPSF (SPSF) to TF (TFD or TFC) type and ends as the SPSF (CPSF) type. During the transition, both phases, host and inclusion, may become continuous, forming a composite of the TFC type. As the concentration increases, more inclusions come into contact, but they cannot overlap, such as they do in the Co/WC system (Table 1). Thus, the final composite type is not exactly of the type CPSF or PSFS; rather it is a pack of particles welded by a cement phase (the host). The elastic properties of the pack depend on the area and forces at the contacts. However, from the Co/WC data set shown in Figure 2.7, it is not clear whether there is a percolation transition.

Another example where a percolation transition might occur is the sintered enstatite (En)/forsterite (Fo) set (Ji and Wang, 1999). In this particular data set, the particle sizes of the starting material before sintering are smaller than 15 μm. The grain sizes are distributed normally and have a mean value of 10-15 μm. Clusters of En or Fo are not observed at SEM scale. The measured V_p and V_s velocities of the mixtures fall below the HS^-; this may be due to the residual porosity of the specimens, which is about 0.5%-1.2%, as calculated from theoretical densities and volume fractions.

Numerical wave propagation modeling of epoxy-resin/tungsten and epoxy-resin/piezoceramic composite systems has shown that at low concentrations (<0.25) the formation of clusters of inclusions has negligible effects on the dynamic (low-frequency limit) elastic moduli of the composites (Gomez et al., 2000). However, at high inclusion volume fractions (> 0.30) the effect of connectivity due to clustering becomes significant, and the elastic moduli start increasing faster and depart from the lower HS bound (Gomez et al., 2000). In real composites, the percolation is not reached at the same inclusion

volume fraction for all materials. In the laboratory, images of the epoxy-resin/ceramic composites show that the degree of connectivity among inclusions is low, even at high volume fraction of ceramic inclusions (Gomez et al., 2000). Notice that the V_p versus volume fraction of ceramic is very close to the lower HS bound (Figure 2.9). Based on sectional micrographs of the tested epoxy/ceramic samples Gomez et al. (2000) concluded that this behavior was probably due to the low degree of connectivity among inclusions at high inclusion volume fraction and not due to residual anisotropy, residual porosity, microcracks or/and poor adhesion between host and inclusion. Figures 2.2-2.5 and 2.9 show that the departure from the lower HS bound starts at different concentrations, depending on the inclusion aspect ratio, type, and elastic moduli. For instance, for the polypropylene/CaCo3, polyester/glass, and hard-epoxy/glass systems, the departure from the HS- starts at an inclusion volume fraction of about 0.4, 0.35, and 0.30, respectively, whereas for resin/aluminum, resin/iron, and resin/tungsten, the departure starts at about 0.10, 0.15, and 0.10, respectively.

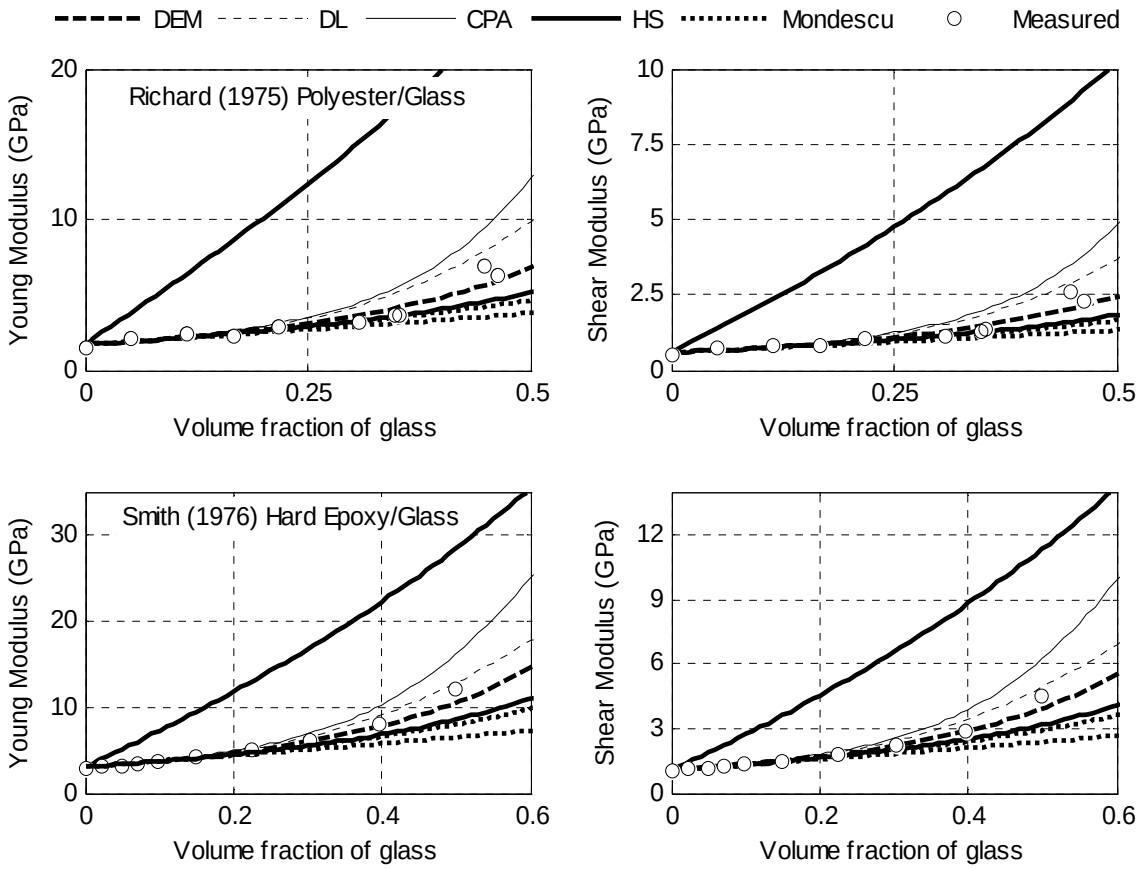

Figure 2.4. Comparison of static experimental to calculated shear and Young's moduli. The aspect ratio used in DEM and CPA was 1. These two composites are of the CPSF type.

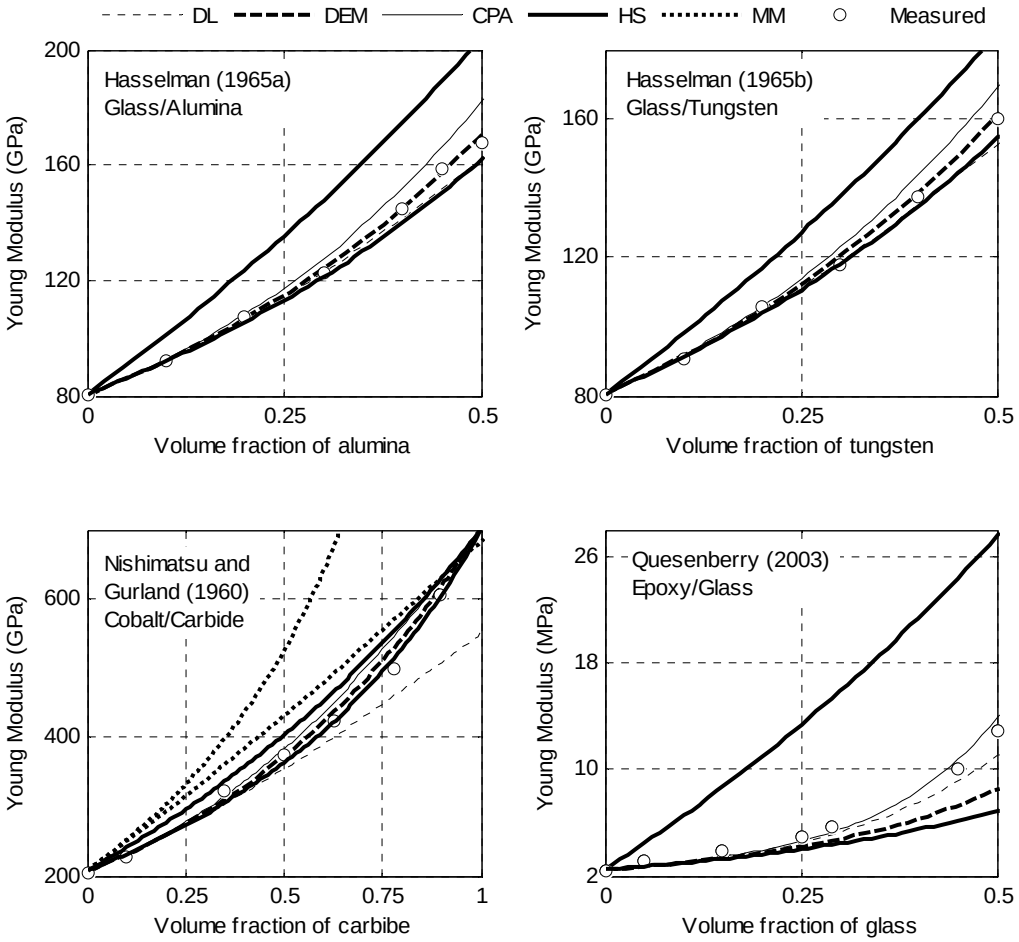

Figure 2.5. Comparison of experimental to calculated Young's modulus. The aspect ratio used in DEM and CPA was 1. All composites are of the CPSF type.

Figure 2.9 shows the Young's moduli for a glass-ceramic/316-L-stainless data set. This data set consists of mixtures of glass-ceramic and embedded 316-L-stainless particles (Pernet, 1993). These composites were prepared by the hot-pressing technique. The sizes of the stainless steel inclusions are <60 μm, with an inclusion size average of about 25 μm. The inclusions are approximately spherical. For these composites, the dynamic Young's moduli are considerably below the lower Hashin-Shtrikman bound at all inclusion volume fractions (Figures 2.6). Pernet (1993) concluded that this reduction in the Young's modulus was probably due to the incomplete adhesion between the host and inclusions. They estimated an unwelded surface fraction of about 20%. In this case, as in the previous example for the epoxy-resin/piezoceramic, the low degree of

connectivity among inclusions at all inclusion volume fractions may also contribute to this behavior.

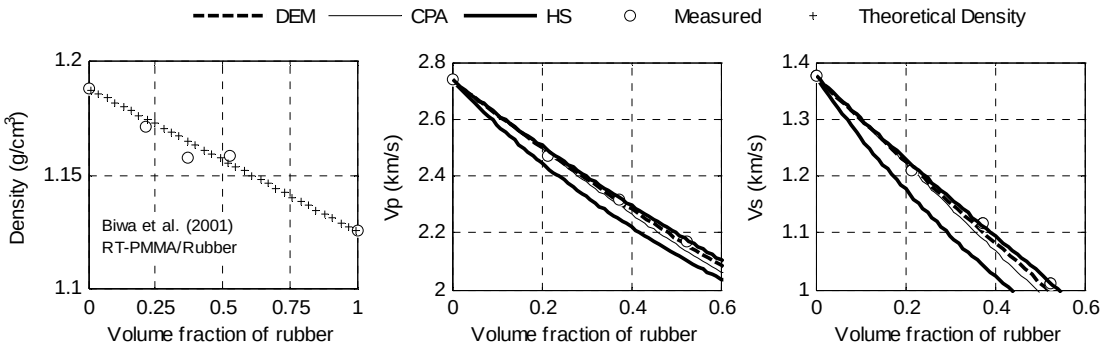

Figure 2.6. Left: Measured and calculated density. Middle and right columns: comparison of ultrasonic experimental to calculated effective V_p and V_s velocities, respectively. The aspect ratio used in DEM and CPA was 1. These composites are of the SPSF type.

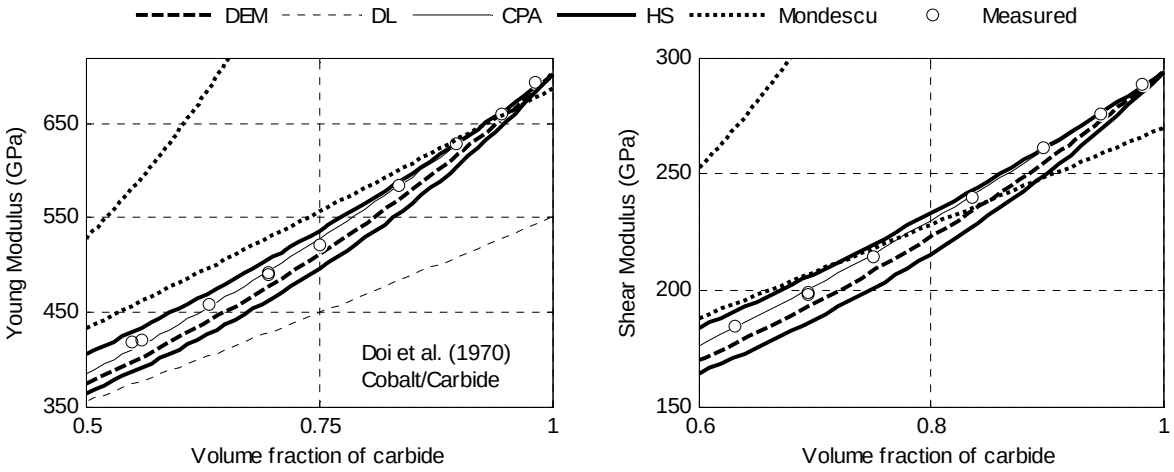

Figure 2.7. Comparison of dynamic experimental to calculated Young's modulus. The aspect ratio used in DEM and CPA was 1. These composites are of the SPSF type.

Table 2.2 shows the models that give the best visual overall agreement with the composite experimental data sets. DEM gives the best overall agreement with the experimental data, for most of the CPSF and SPSF composites. However, CPA produces more accurate results than DEM for the epoxy/glass (Quesenberry et al., 2003) and Co/WC systems (Doi et al., 1970). CPA and DEM produce similar results for the

resin/tungsten (Sugawara et al., 2005) and enstatite/fosterite systems (Ji and Wang, 1999), which are composites of the type CPSF and CPSF-TF-SPSF, respectively.

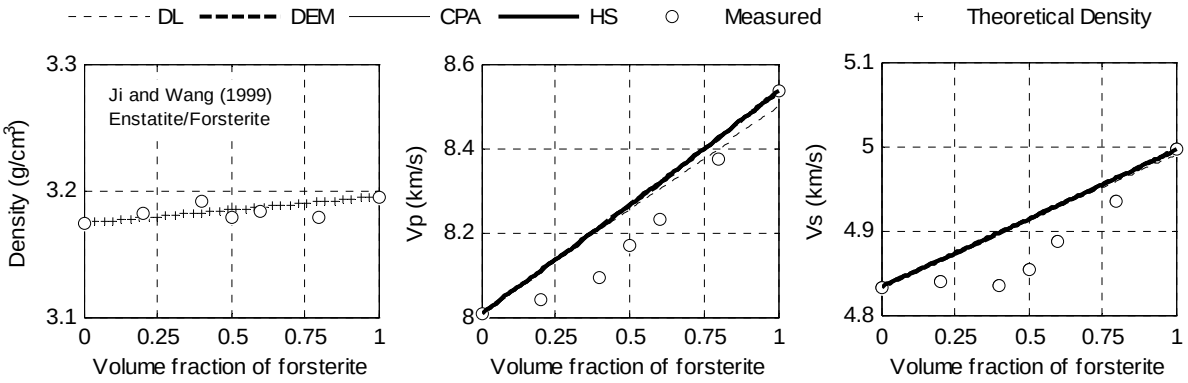

Figure 2.8. Comparison of ultrasonic experimental to calculated Young's modulus. The aspect ratio used in DEM and CPA was 1. These composites are of the TF type.

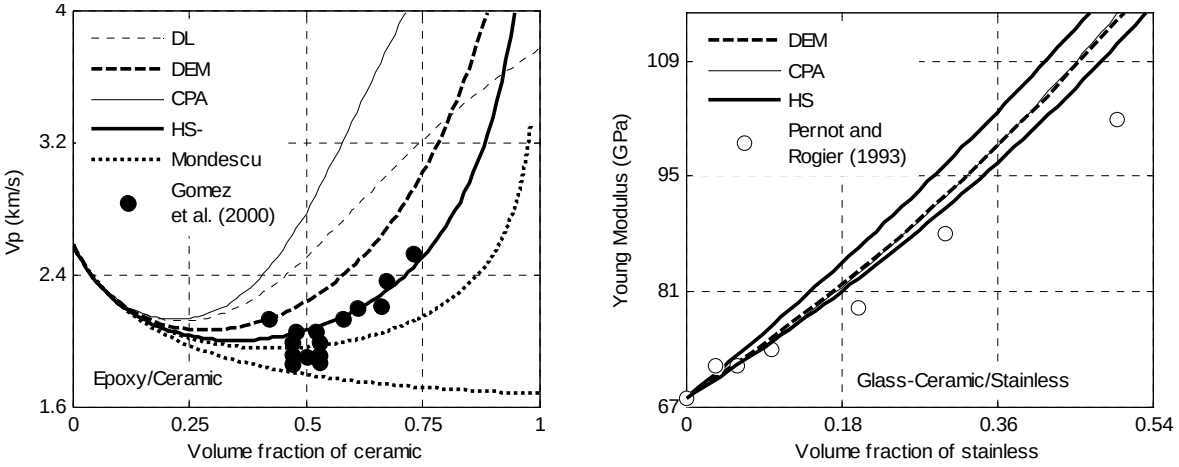

Figure 2.9. Comparison of ultrasonic experimental to calculated V_p velocity (left) and dynamic measured to calculated Young's modulus (right). The aspect ratio used in DEM and CPA was 1. These two composite systems are of the CPSF type.

Table 2.2: Models that give the best fit for each composite data set. For some composites two or more models may produce the same or approximately the same results, such as DL equal DEM (DL = DEM) or DL approximately equal to DEM (DL ~ DEM). In some cases both model predictions agree reasonably with the data, but their results are not the same, such as DEM/CPA.

References	Elastic Properties' Contrasts			Test Type	Composite Type	Best Fit Model
	κ_i/k_h	G_i/G_h	ρ_i/ρ_h			
Lees and Davidson (1977)	11.90	10.00	1.98	Ultrasonic	CPSF	HS-
Zhang et al. (1996)	14.58	13.60	2.14	Ultrasonic	CPSF	DEM = DL
Bridge and Cheng (1987)	15.60	23.00	2.98	Ultrasonic	CPSF	HS- / DEM ~ DL
Gomez et al. (2000)	29.62	37.72	6.75	Ultrasonic	CPSF	HS-
Piche and Hammel (1986)	29.17	41.35	6.67	Ultrasonic	CPSF	DEM
Piche and Hammel (1987)	29.17	41.35	6.67	Ultrasonic	CPSF	DEM
Nguyen et al. (1996)	38.25	101.25	15.32	Ultrasonic	CPSF	DL / DEM
Sugawara et al. (2005)	57.30	95.86	16.78	Ultrasonic	CPSF	CPA/DEM/DL
Lees (1973)	72.28	405.78	15.32	Ultrasonic	CPSF	DEM
Richard (1975)	8.05	49.73		Static	CPSF	HS-/DEM
Smith (1976)	9.91	28.62		Static	CPSF	DEM
Doi et al. (1970)	2.11	3.75		Res.Bar	CPSF/TF/SPSF	CPA
Biwa (2001)	0.46	0.25	0.95	Ultrasonic	SPSF	HS+
Ji and Wang (1999)	1.21	1.08	1.01	Ultrasonic	CPSF/TF/SPSF	All Good
Pernot and Rogier (1993)	4.54	2.58	3.00	Magnetorestrictive	CPSF	HS-
Hasselman and Fulrath (1965a)	4.46	4.39		Res.Bar	CPSF	DEM
Hasselman and Fulrath (1965b)	6.43	4.85		Res.Bar	CPSF	DEM
Hasselman and Fulrath (1963)	0.02	0.02	0.28	Res.Bar	SPSF	DEM
Nishimatsu and Gurland (1960)	2.43	3.62			CPSF/TF/SPSF	??
Quesenberry et al. (2003)	18.99	33.59	2.13	Static	CPSF	CPA
Dunn and Ledbetter (1995)	2.36	3.30	1.17	Static/Ultrasonic	CPSF	DEM
Vollenberg and Heikens (1990)	5.98	26.55	2.42	Static	CPSF	CPA
Gaudig et al. (2003)	0.02	0.02	0.24		SPSF	DEM/CPA
Ledbetter and Dunn (1995)	0.02	0.02	0.24		SPSF	DEM/CPA

Table 2.3: *P*- and *S*-wave impedances and reflection coefficients, I_p and I_s, and RCp and RCs, respectively. The last column (on the right) shows the normal wave incident elastic reflection coefficient (RCE).

References	Host Impedances			Inclusion Impedances			Reflection Coefficients		
	Host Material	Ip	Is	Inclusion Material	Ip	Is	RCp	RCs	RC_E
Lees and Davidson (1977)	PMMA	18.9	1.3	Crystabolite	199	29	0.827	0.915	0.809
Zhang et al. (1996)	Resin	19.3	2.2	Aluminum	296	66	0.878	0.936	0.845
Bridge and Cheng (1987)	Polypropylene	16.3	1.8	CaCO3	300	89	0.897	0.960	0.912
Gomez et al. (2000)	Epoxy	2.9	1.3	PZ-Ceramic	42	20	0.872	0.882	0.980
Piche and Hammel (1986)	Resin	22.3	2.6	Iron	2169	650	0.980	0.992	0.980
Piche and Hammel (1987)	Resin	22.3	2.6	Iron	2169	650	0.980	0.992	0.980
Nguyen et al. (1996)	Resin	28.7	1.8	Tungsten	10075	3127	0.994	0.999	0.995
Sugawara et al. (2005)	Resin	19.5	2.0	Tungsten	10075	3127	0.996	0.999	0.997
Lees (1973)	Vinyl	10.1	0.2	Tungsten	10463	3133	0.998	1.000	0.997
Richard (1975)	Polyester			Glass					
Smith (1976)	Epoxy-Polymer			Glass					
Doi et al. (1970)	Cobalt			Carbide					
Biwa (2001)	PMMA	24.4	3.1	Rubber	4	1	-0.725	-0.662	-0.269
Ji and Wang (1999)	Enstatite	1629.9	358.8	Forsterite	743	255	-0.373	-0.169	0.041
Pernot and Rogier (1993)	Glass-Ceramic	14.0	8.7	Stainless	45	24	0.529	0.471	0.814
Hasselman and Fulrath (1965a)	Glass			Tungsten					
Hasselman and Fulrath (1965b)	Glass			Alumina					
Hasselman and Fulrath (1963)	Zirconium/Carbide	4455.6	1117.0	Graphite	21	9	-0.991	-0.985	-0.957
Nishimatsu and Gurland (1960)	Cobalt			Carbide					
Quesenberry et al. (2003)	Epoxy	6.5	0.8	Glass	224	78	0.943	0.980	0.877
Dunn and Ledbetter (1995)	Aluminum	697.9	85.8	Mullite/Alumina	2814	284	0.603	0.536	
Vollenberg and Heikens (1990)	Polypropylene	~16.3	~1.82	Chalk	~86	~32.1	0.680	0.893	
Gaudig et al. (2003)	Ferrite	1584.0	254.8	Graphite	9	3	-0.989	-0.975	-0.969
Ledbetter and Dunn (1995)	Ferrite	1584.0	254.8	Graphite	9	3	-0.989	-0.975	-0.969

2.4.2 Effect of inclusion shape

In this subsection we investigate the effect of inclusion shape on the effective elastic moduli of composites. Figure 2.10 shows the HS bounds and DEM bulk modulus (k) predictions as a function of inclusion volume fraction (kaolinite or dolomite) and aspect ratio for hypothetical CPSF and SPSF rock matrix types.

The CPSF composites consist of mixtures of kaolinite and dolomite. In this case kaolinite plays the role of host, and dolomite the role of inclusions. The properties of the minerals are shown in Table 4. The volume fraction of kaolinite was varied from 0 to 1.

The SPSF composites consist of mixtures of kaolinite and dolomite as well, but in this case the dolomite and kaolinite play the role of host and inclusions, respectively. For

each composite type, two kinds of inclusion shapes were considered: a) oblate spheroidal, with aspect ratios varying between 0 and 1, to mimic flake or penny shaped inclusions; and b) prolate spheroidal, with aspect ratios varying between 1 and 30, to mimic fiber like inclusions.

At a fixed inclusion volume fraction, the bulk modulus varies over a wider range for oblate spheroids than for prolate spheroids (Figures 2.10). The same behavior is observed in both composite types, CPSF and SPSF. The range of bulk moduli variation for oblate spheroidal inclusions includes the range for prolate spheroids. This means that two materials with the same constituents and volume fractions, and with different inclusion aspect ratios, may have the same elastic bulk modulus. For oblate spheroids, the maximum bulk-modulus variation occurs for aspect ratios between 0 and 0.25; it varies smoothly from 0.25 to 0.5; and the variation between 0.5 and 1 is very small. On the other hand, for prolate spheroids, the maximum bulk-modulus variation occurs between 1 and 10, and it varies smoothly for aspect ratios greater than 10. The same behavior is observed for the shear moduli.

Figure 2.11 shows the DEM and CPA bulk modulus prediction as a function of volume fraction of dolomite and kaolinite for hypothetical CPSF and SPSF materials, respectively. The calculations were done for two aspect ratios: 0.01 and 1. Notice that DEM and CPA do not completely fill the space between the upper and lower HS bounds (Figures 2.10 and 2.11). Materials with elastic moduli between the HS bounds are physically realizable. This means that these effective-medium approximations cannot model all possible realizable material microstructures (Figure 2.11).

Table 2.4: Elastic properties of rock mineral constituents (Mavko et al., 2009).

Material	*K* (GPa)	*G* (GPa)	ρ (g/cm^3)
Hematite	100.20	95.2	5.24
Gulf Clay	21.00	7.0	2.60
Dolomite	94.90	45.0	2.87
Calcite	76.80	32.0	2.71
Quartz	37.00	44.0	2.65
Pyrite	147.40	132.5	4.93
Kaolinite	1.50	1.2	1.58
Water	2.25	0.0	1.00

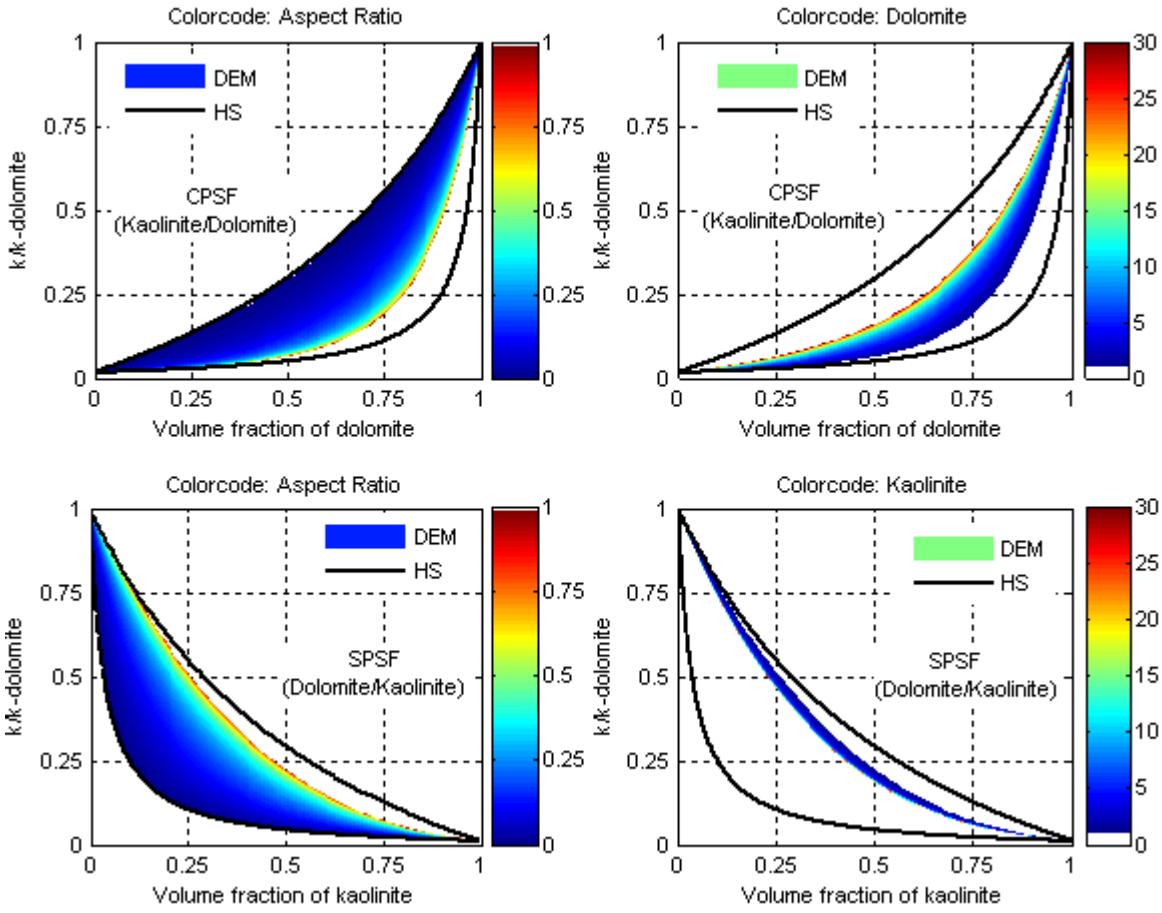

Figure 2.10. HS-bounds and DEM bulk modulus predictions as a function of concentration and aspect ratio for theoretical CPSF kaolinite/dolomite hypothetical rock matrix (upper frame) and for SPSF-dolomite/kaolinite hypothetical rock matrix (lower frame). Left column: CPSF (top) and SPSF (bottom) composites with oblate spheroidal inclusions. Right column: CPSF (top) and SPSF (bottom) composites with prolate spheroidal inclusions.

Figure 2.12 shows the bulk modulus predicted by DEM and CPA as a function of aspect ratio, for the same CPSF and SPSF composites shown in Figures 2.10 and 2.11. The aspect ratio of the inclusions is varied from 0.001 to 100. For the SPSF composite type, the bulk modulus was determined for four different volume fractions of kaolinite: 0.01, 0.05, 0.15 and 0.25. The same volume fractions of dolomite were used the CPSF composite type.

CPA produces smaller bulk modulus than DEM for a fixed aspect ratio. The

difference between the CPA and DEM estimates is small at low concentration and increases as concentration increases for both CPSF and SPSF materials.

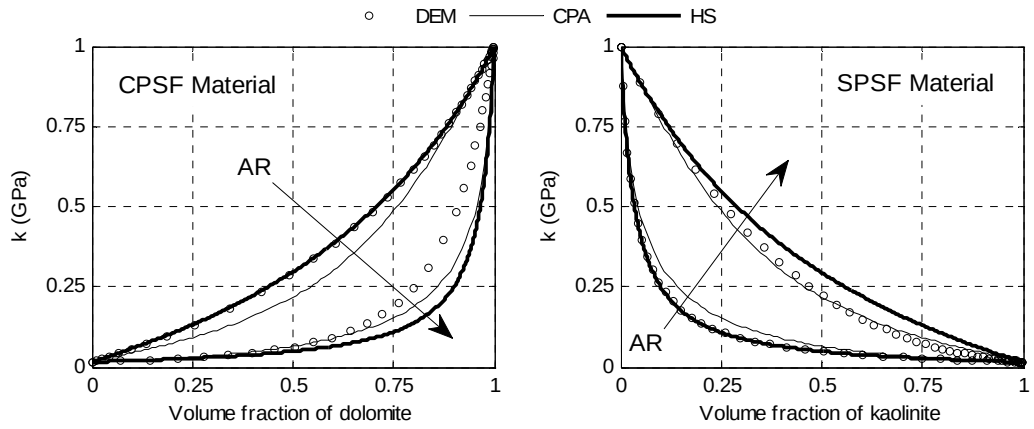

Figure 2.11. Left: Bulk modulus as a function of volume fraction of dolomite, for hypothetical composites of the type CPSF, where kaolinite is assumed to be the host and dolomite the inclusions. Right: Bulk modulus as a function of volume fraction of kaolinite, for hypothetical composites of the type SPSF, where dolomite is assumed to be the host and kaolinite the inclusions. In both composite types, the inclusions were assumed to be spheroidal, and the DEM and CPA predictions were done for two AR values: 0.01 and 1. The arrow indicates the direction of increasing aspect ratio. The upper and lower HS bounds are also shown.

The DEM and CPA predictions of elastic properties as a function of aspect ratio were compared with experimental data. The predictions were compared with six CPSF composite types (one resin/aluminum, two resin/tungsten and three resin/iron systems) and two SPSF types (zirconio-carbide/graphite and cast iron). The elastic properties of these composites are shown in Tables 1 and 2.

The resin/aluminum system consists of mixtures of aluminum powder randomly embedded in clear epoxy resin matrix with the aluminum concentration ranging from zero to 0.47 (Zhang et al., 1996). The aluminum powder particles had an aspect ratio between 0.1 and 1.0, while their size varied from 5 to 300 μm (polydispersed). The measured and predicted *P*- and *S*-wave velocities, as well as the bulk density are shown in Figure 2.13. At small concentrations of aluminum powder, below 0.12, the Hashin-Shtrikman lower bound gives accurate predictions of V_p and V_s of the mixture. CPA

accurately predicts V_p and V_s in the concentration range between zero and 0.25, but for concentrations greater than 0.25 it starts to overpredict the data. The mismatch between the CPA prediction and the data increases at high inclusion concentrations. The best V_p and V_s predictors in the entire inclusion concentration range are DEM and DL, which produce practically the same results. The aspect ratios versus porosity needed to match DEM velocities predictions to the data are essentially porosity-independent but slightly different for V_s and V_p.

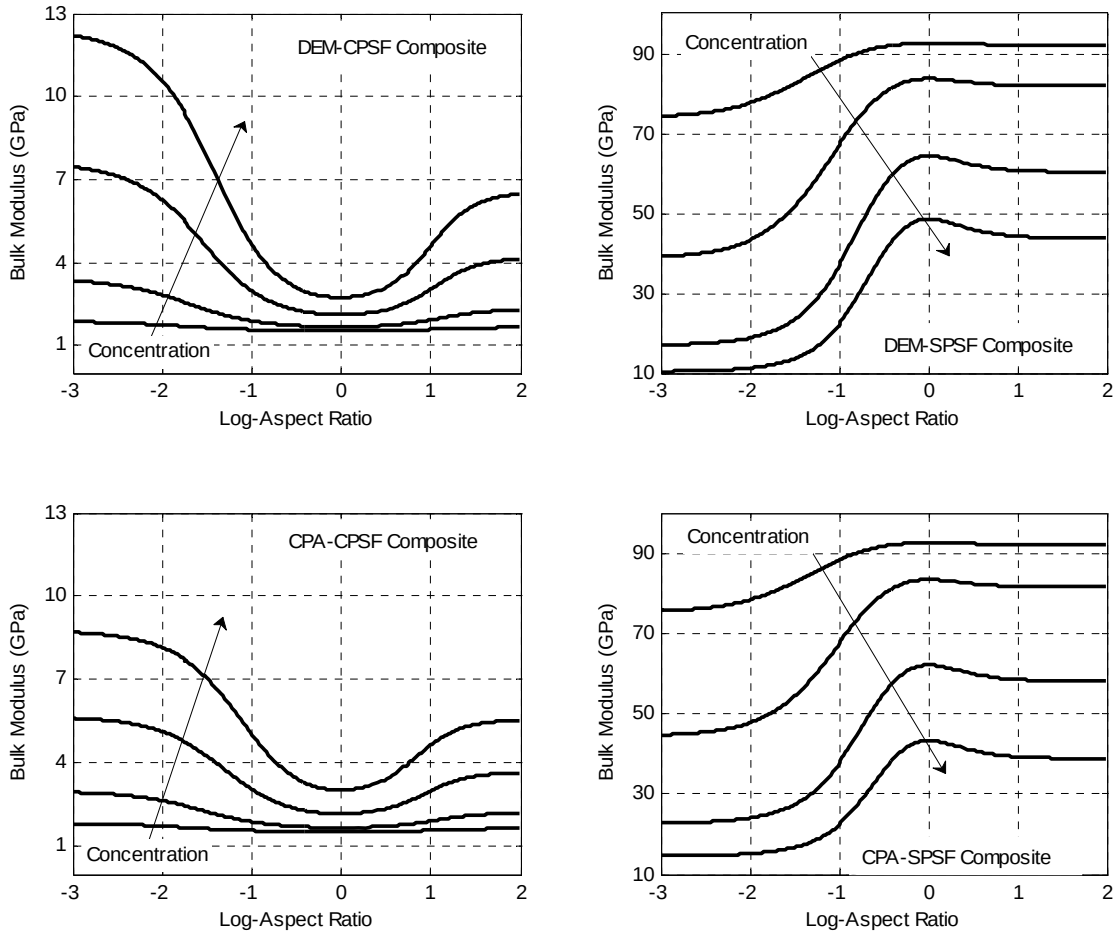

Figure 2.12. DEM and CPA bulk modulus prediction as a function of aspect ratio, for concentrations: 0.01, 0.05, 0.15 and 0.25. The arrows indicate the direction of increasing concentrations. The aspect ratios vary from 0.001 to 1 for oblate spheroids and from 1 to 100 for prolate spheroids. Upper frame: DEM predictions for CPSF kaolinite/dolomite hypothetic composites (left) and for SPSF dolomite/kaolinite composites (right). Lower frame: CPA predictions for CPSF kaolinite/dolomite hypothetic composites (left) and for SPSF dolomite/kaolinite composites (right).

An accurate overall visual agreement between the measured and the theoretical V_p and V_s velocities is found when a single aspect ratio equal to 0.37 is used in the entire concentration range. We deem this finding important because it illuminates the stability of predictions of two different measured properties with a single theory and single input parameter (the aspect ratio).

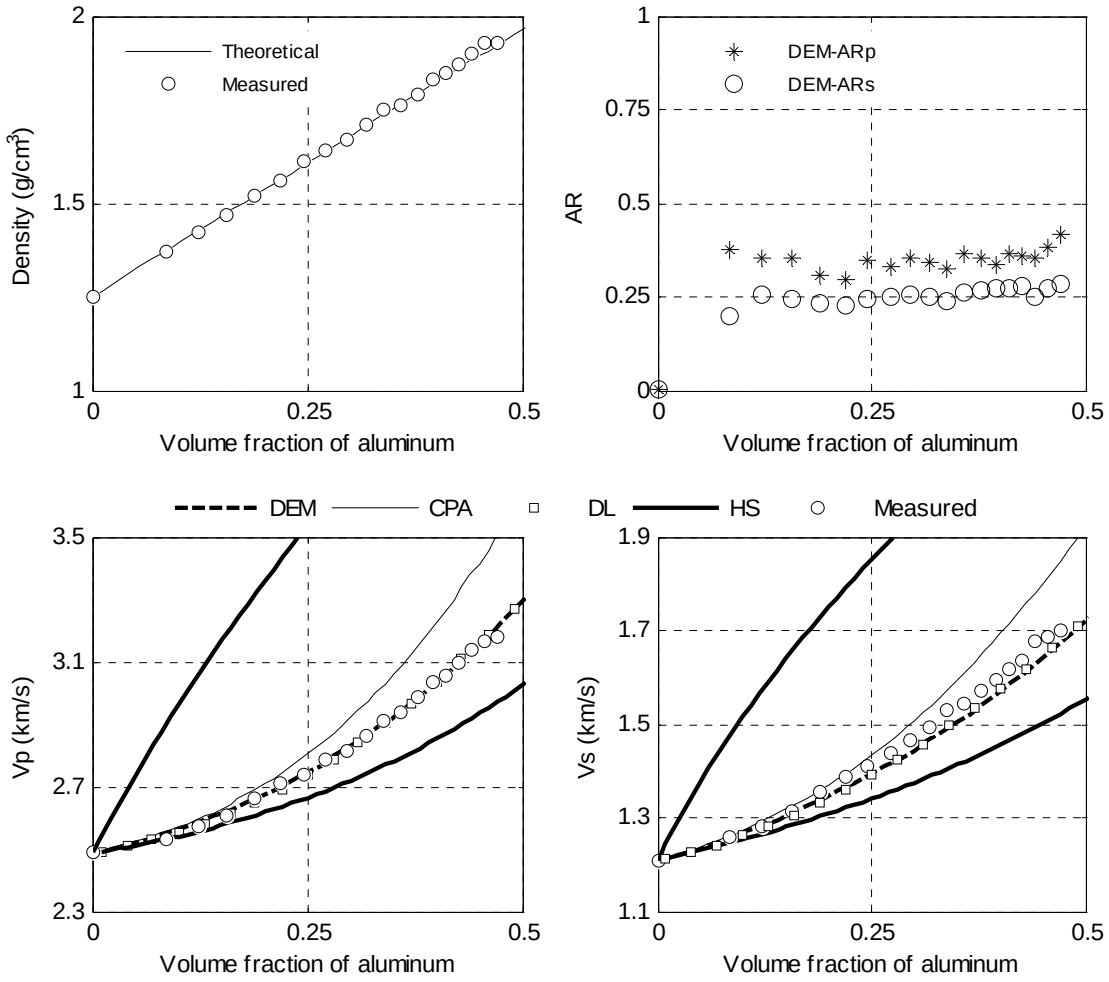

Figure 2.13. Upper frame: Left: Theoretical and measured density. Right: Aspect ratios needed to exactly match the DEM V_p -velocities (ARp) and V_s -velocities (ARs) with the measured ultrasonic velocities. Lower frame: V_p (left) and V_s (right) versus volume fraction of aluminum as measured and predicted by DL, and DEM and CPA for fixed inclusion aspect ratio 0.4 (Data from: Zhang et al., 1996).

The resin/tungsten system consists of mixtures of epoxy and tungsten particles (Nguyen et al., 1996). The particle size distributions were obtained using the diffraction pattern laser beam technique. The shape of the particles was obtained by scanning electron microscopy. Smaller particles (about 0.5μm) were essentially short fibers (AR ~ 8), while larger particles (about 5μm) had a spherical shape (AR ~ 1).

The measured and predicted *P*- and *S*-wave velocities as well as the bulk density are shown in Figure 2.14. The velocities were computed assuming spherical inclusions (AR = 1). At small concentrations of tungsten powder, below 0.05, the Hashin-Shtrikman lower bound gives accurate predictions of V_p and V_s of the mixture. CPA predicts V_p and V_s accurately in the concentration range between zero and 0.4, approximately, but for concentrations greater than 0.4, it starts overpredicting and becomes even less accurate at high concentrations. When assuming spherical inclusions (aspect ratio 1), DEM underpredicts the velocities for concentrations greater than about 0.05. The best V_p and V_s predictor for spherical inclusions in the whole inclusion concentration range is DL model (Figure 2.14). This model accounts for inclusion interaction at high concentration. However, this model assumes spherical particles, so when the particles are not spherical its predictions are not accurate. For the composite with average particle size 5μm, the DL predictions agree with the experimental values because the particles are approximately spherical. However, for the composites with average particle size 0.5μm, the experimental data deviate from the DL model predictions because these particles are not spherical, but rather short fibers.

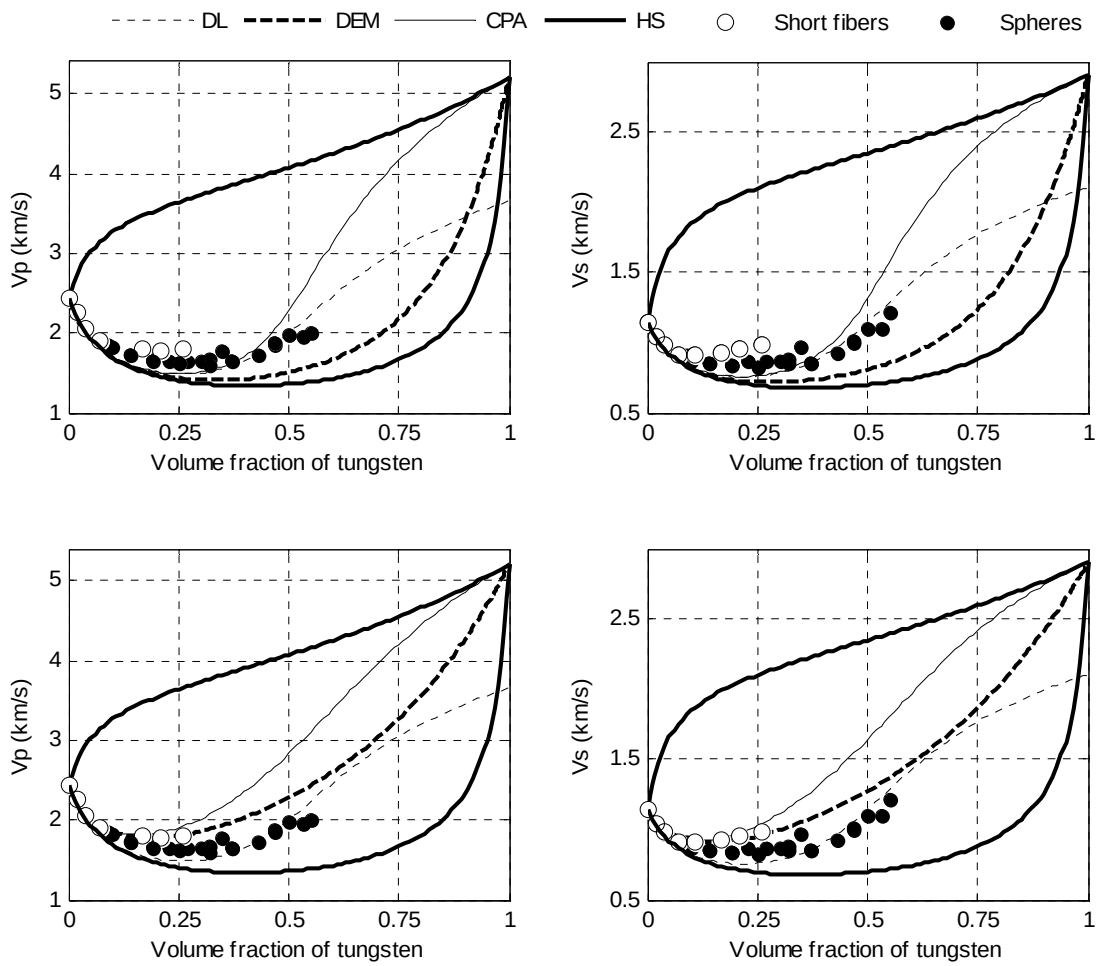

Figure 2.14. Comparison of theoretical and measured ultrasonic V_p and V_s velocities versus volume fraction of tungsten. Upper frame: The aspect ratio used in DEM was 1 and in CPA was 1 and 1 for matrix and inclusions respectively. Lower frame: The inclusion aspect ratio used in DEM and CPA was 9.5.

For the 0.5 μm average inclusion size, DEM produces the best estimates when the inclusions are modeled with a single aspect ratio, but considering the inclusions as short fibers and modeled with prolate spheroidal inclusions. The best agreement between predicted and measured velocities is found for an inclusion aspect ratio 9.5, which agrees with the SEM observations of tungsten powder inclusion (Nguyen et al., 1996). Figure 2.14 shows the predictions compared with the experimental data. DEM slightly overpredicts V_s at high concentrations. The V_p and V_s velocities of these composites with fiber particles can also be modeled using oblate spheroidal inclusions with AR =

0.13. CPA predictions also match the measured data if an inclusion aspect ratio 8.5 is used.

CPA estimates are also accurate, when the aspect ratio for the tungsten spherical particles and the resin (host), both are equal to 1. CPA overpredicts both V_p and V_s at high concentrations. However, for both oblate and prolate spheroid, it is possible to match the CPA results with the experimental data, using the aspect ratio as a fitting parameter. As shown in figures 2.10-2.12, the aspect ratios necessary to achieve an exact fit would be lower than those found with DEM. Figure 2.15 shows the aspect ratios versus volume fraction of tungsten needed to exactly match the DEM velocities with the measured velocities for samples with short-fiber and spherical inclusions. The aspect ratios needed to match the V_p velocities are very close to those needed to match the V_s velocities.

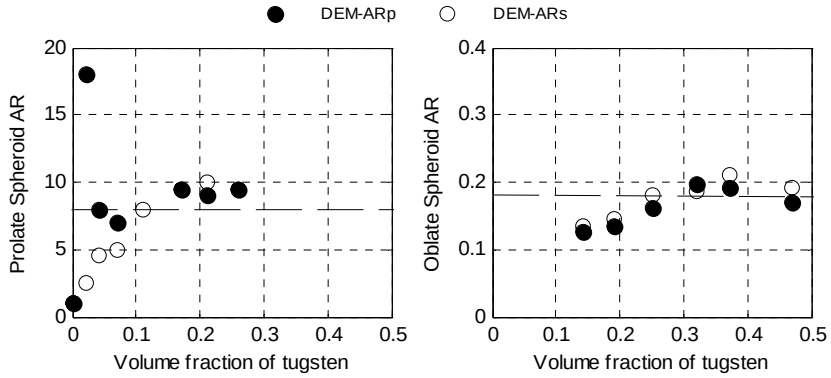

Figure 2.15. Left: aspect ratios needed to match DEM V_p and V_s velocity predictions with measured data for composites with 0.5 μm inclusions with aspect ratios about 8.5 (short fibers). Right: aspect ratios needed to match DEM V_p and V_s predictions with measured data for composites with 5 μm inclusions with oblate spheroidal inclusions.

The second resin/tungsten data set consists of mixtures of epoxy and embedded tungsten particles (Sugawara et al., 2005). The densities of the composites with tungsten powder of 1 μm particle size are no different from those of composites with tungsten powder of 3 μm particle size. The density of the composites did not depend on the particle size of the tungsten powder. However, as the concentration of tungsten powder increased, the difference between the measured values and the calculated values

increased. In this case, the measured values of the density may be as much as 10% smaller than the calculated values. This large residual porosity may cause reduction of the material elastic moduli.

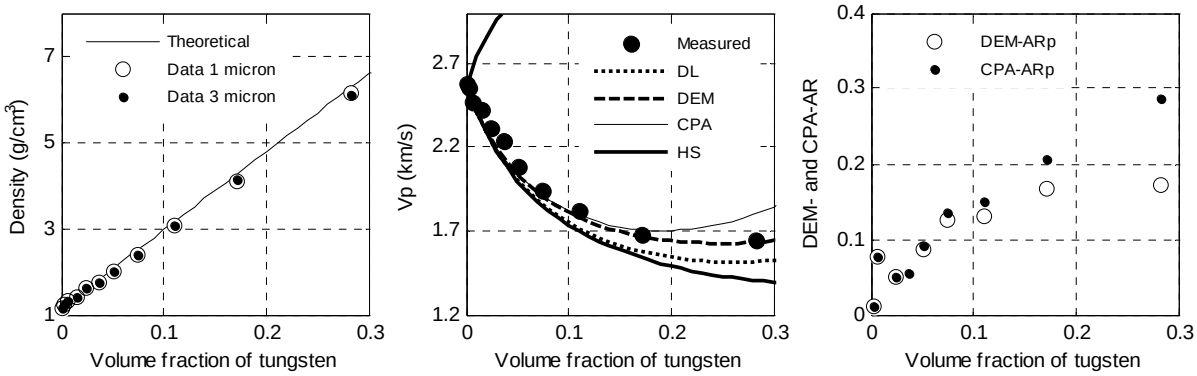

Figure 2.16. Left: bulk density for the 1μm and 3μm inclusion sizes. Middle: Predicted and measured V_p velocity. The aspect ratio used in DEM and CPA was 0.18. CPA would also match the data if an aspect ratio equal to 0.25 were used. DL underpredicts the data because the particle may be not spherical. Right: aspect ratios needed to match DEM and CPA V_p velocity with measured velocities. (Data from: Sugawara, 2005).

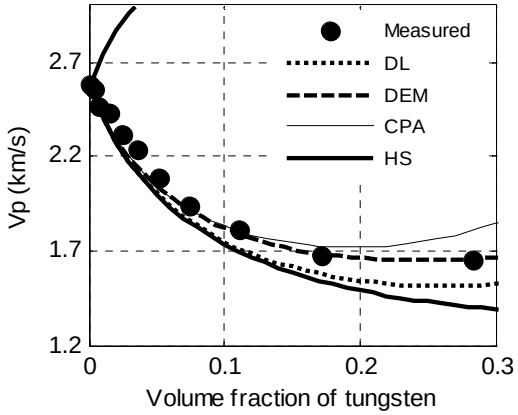

Figure 2.17. Predicted and measured V_p velocity. The aspect ratio used in DEM and CPA was 6. CPA also matches the data for an aspect ratio lower than 6. DL underpredicts the V_p velocities, because the particle may be not spherical.

The first resin/iron system consists of mixtures of epoxy resin and 50 μm-spherical iron inclusions (Piche and Hammel, 1986). The second and third resin/iron systems consist of iron flakes and short-fiber inclusions of different shapes (Piche and Hammel, 1987). The iron inclusions, in all three data sets are randomly oriented, having aspect ratios AR ~ 1 (spheroids), AR = 0.20 (flakes) and AR = 20 (short fibers). The powder of flake-like (oblate spheroid) particles has a long axis length of about 100 +/- 5 μm and short axis length of about 20 +/- 5 μm; the average AR is about 0.20 +/- 0.06. SEM images show that the bulk of the material appears to be compact and free of voids and that the inclusions are homogeneously distributed with random orientations. The particles were well separated for concentrations up to the 0.12 to 0.15 range, while the presence of contiguity became obvious at higher volume contents. The fiber inclusions have a broad distribution of lengths, ranging from 500 to 2000 μm with average diameter of about 70 +/- 20 μm. The average aspect ratio for the fibers (prolate spheroids) was estimated to be about 20 +/- 10. The samples appeared to be free of voids, and the fibers uniformly distributed in the matrix with random orientations. Velocities were measured at 0.5 MHz, which ensured that the measurements were free of dispersion, since wavelengths were much longer than most particle sizes. The measured and predicted *P*- and *S*-wave velocities for the three resin/iron systems with different inclusion shapes (oblate spheroids, short fibers and flakes) as well as the bulk density are shown in Figure 2.18.

The composites with spherical and flake shaped inclusions were modeled with DEM using aspect ratios 0.50 and 0.15, respectively (Figure 2.19, top and middle frames). The flake shaped inclusions were modeled as penny shaped inclusions. In order to match the measured V_p and V_s velocities for the composites with fiber inclusions, it was necessary to use two different aspect ratios, 7 and 22, respectively (Figure 2.19, bottom frame).

At small concentration of spherical iron inclusions, lower than approximately 15%, the HS^- gives accurate predictions of V_p and V_s of the mixture.

When assuming spherical inclusions (aspect ratio 1), DEM underpredicts the velocities for concentrations greater than about 0.25.

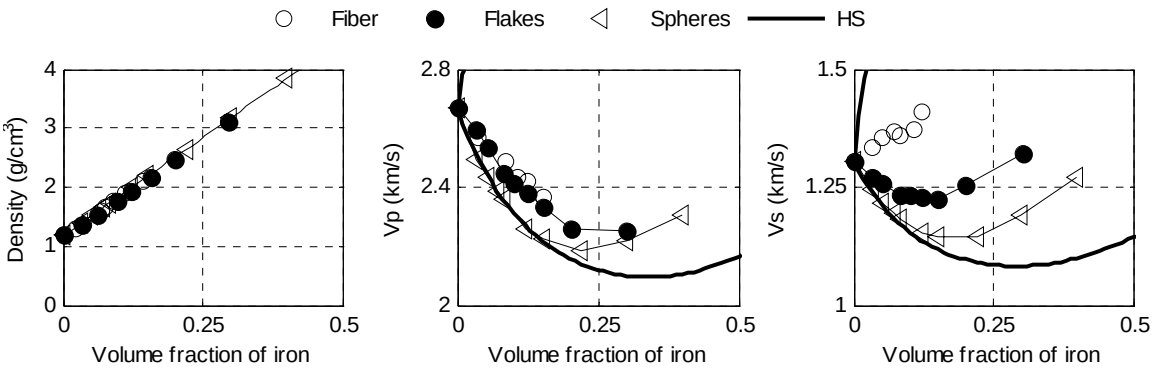

Figure 2.18. Left: Bulk density for iron fiber (open circles), iron flakes (filled circles) and iron spherical (open triangles) inclusions. Middle: *P*-wave velocity for iron fiber (open circles), iron flakes (filled circles connected with lines) and iron spheres inclusions. Right: *S*-wave velocity for iron fiber (open symbols) and iron flakes (filled circles) inclusions. (Data from: Piche et al., 1986 and 1987).

The fibrous and plate shaped inclusions increase the V_p and V_s velocities of the composites more than the spherical inclusions. The amount of increase depends on the aspect ratio of the inclusions. The specific surface area (*SA*) is one of the most important inclusion characteristics affecting the elastic properties (Babu et al., 2005). The amount of specific surface area (*SA*), which is a measure of the area of contact between the host and inclusions, depends on the inclusion size. A given volume of small particles has a higher specific surface area than the same volume of large particles. However, if the inclusions are too small, undesirable features might appear in the composite microstructure. The finer the particles are, the greater their tendency to agglomerate. Agglomeration increases material heterogeneity, and it can not be controlled, varying in a random manner, causing random variations of elastic properties.

The zirconium-carbide/graphite system consists of mixtures of graphite particles embedded in zirconium-carbide hosts. The size of the graphite particles ranged from approximately 20 to 30 μm. The graphite particles are polycrystalline and their shape ranged from relatively flat to nearly spherical, with the majority being approximately equidimensional. Residual porosity was not observed within the zirconium carbide host. The different values of Young's moduli, measured in two perpendicular directions,

indicate the presence of residual anisotropy.

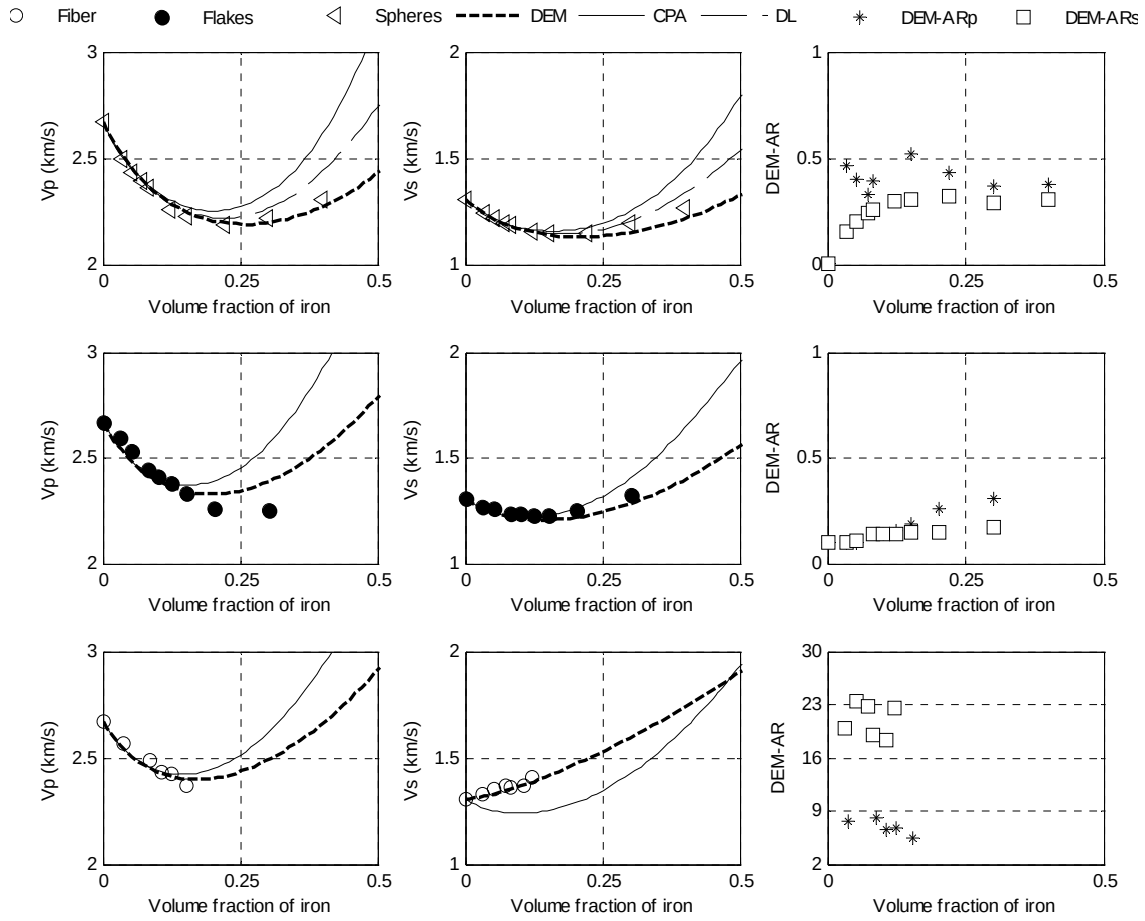

Figure 2.19. V_p (left) and V_s (middle) velocities versus volume fraction of iron as measured and predicted by DEM for fixed aspect ratios: 1 for spherical inclusions; 0.12 for plate like inclusions; and 7 and 22 for fiber like inclusions. Aspect ratios (right) needed to match the DEM V_p -velocities (ARp) and V_s -velocities (ARs) with measured velocities. (Data from: Piche and Hammel, 1986 and 1987).

This anisotropy is probably caused by preferred orientation of the graphite particles during hot-pressing (Hasselman and Fulrath, 1963). Figure 2.20 shows measured and predicted Young's modulus. The data can be modeled with DEM assuming spheroidal inclusions with a fixed effective aspect ratio equal to 0.3. DEM follows the trend of the data better than CPA, for the same inclusion aspect ratio. As shown in Figures 2.10-2.12,

in SPSF composites, the elastic moduli decrease as aspect ratio decreases. These composites can also be modeled assuming fiber-like inclusions with aspect ratio 7, which is an unrealistic shape for the graphite inclusions.

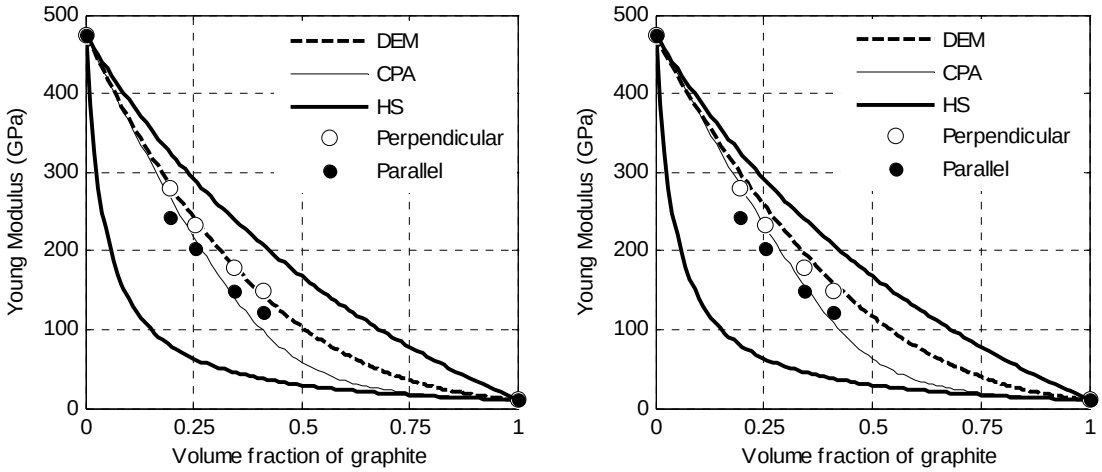

Figure 2.20. Young's modulus versus volume fraction of graphite as measured and predicted by DEM and CPA as a function of volume fraction of graphite. The symbols show the measured data in two perpendicular directions (open and filled circles). The HS bounds are also shown. Left: Young's modulus predicted by DEM and CPA for a fixed aspect ratio 0.3. Right: Young's modulus predicted by DEM and CPA for a fixed aspect ratio 7. (Data from: Hasselman, and Fulrath, 1963).

The iron/graphite system (ferritic cast-iron), which is not usually considered a composite material, is sometimes treated as a composite material consisting of graphite particles embedded in iron host (Ledbetter and Dunn, 1995; Gaudig, et al, 2003). The graphite phase, which is polycrystalline, was assumed to consist of randomly dispersed and oriented inclusions. Nodular iron contains nearly spherical graphite particles, whereas grey iron contains flakes, or disc-shape graphite particles.

Figure 2.21 shows the measured Young's modulus with the DEM and CPA predictions as a function of aspect ratio. Both DEM and CPA predictions are in good agreement with the experimental data. The DEM aspect ratios determined by matching the measured Young modulus exactly agree with the experimental aspect ratios measured

by Lohe et al. (1983) and corrected by Gaudig et al. (2003).

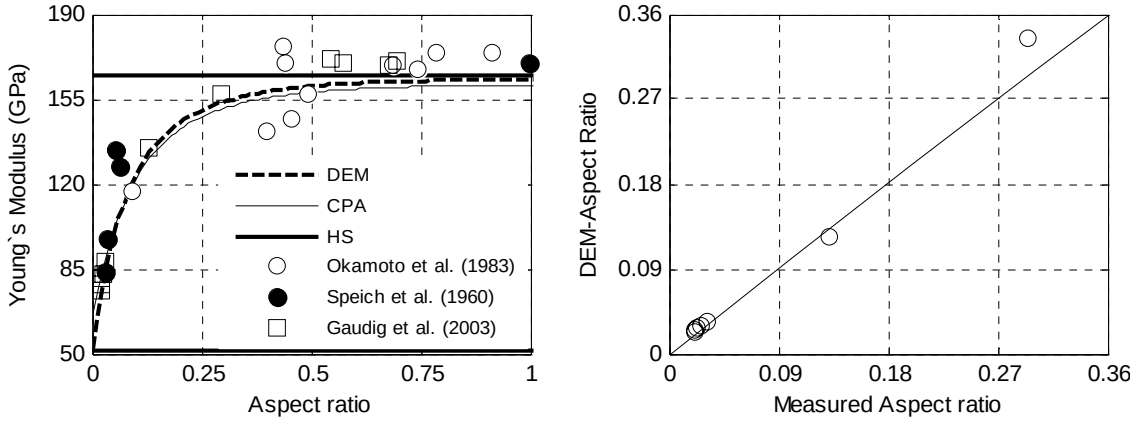

Figure 2.21. Left: Young's modulus versus aspect ratio of graphite inclusions as measured and predicted by DEM and CPA for fixed porosity 0.11. The horizontal curves represent the HS bounds. The symbols show the experimental data as measured by Okamoto et al., 1983 (open circles), Lohe et al., 1983 (open squares) and Speich et al., 1960 (filled circles). Right: DEM-predicted versus measured aspect ratios. (Data from: Ledbetter and Dunn, 1995; Gaudig et al., 2003).

2.4.3 Effect of order of incremental addition

As stated in the introduction, DEM may produce several estimates of the elastic properties of multiphase materials, depending on how the order of addition of each of the different phases is carried out (Bruggeman, D., 1935; Norris et al., 1985a; Nemat-Nasser and Hori, 1993; Phan-Thien and Pham, 1997; Endres, 2000; Markov, et al., 2005). This dependence is caused by the hierarchical microstructure imposed on the constructed composite by the addition process. An increasing inclusion size is implied by the order of addition. Previously added inclusions are considerably smaller than those added later. The order of addition sets the inclusion-size relationship among the different composite phases (Phan-Thien and Pham, 1997; Endres, 2000; Markov, et al., 2005). It is not obvious which of the possible DEM estimates is the most appropriate when modeling the elastic moduli of a given real multiphase material with different volume fractions of phases and wide distributions of inclusions sizes and shapes. For two different pore shapes Le Ravalet and Gueguen (1996) have proposed a method for achieving the

incremental addition. This method consists of constructing the material by adding the pore and crack component in a random order using Monte Carlo method. For two different pore scales, Markov et al. (2005) have used a two-step homogenization scheme, which consists of starting the adding with the smaller-scale inclusions. A similar method was used by Chinh (2000) for modeling the electrical properties of sedimentary rocks. A step-by-step homogenization approach using the DEM was proposed by Sheng (1991) and Hornby et al. (1994) for modeling the properties of rocks composed of phases at different scales.

In this subsection we compare the results produced by DEM with the CPA estimation and HS bounds. For three-phase hypothetical rock matrix, we compare the DEM estimates using the step-by-step homogenization approach with the CPA estimation and HS bounds.

Figure 2.22 shows the CPA and DEM theoretical estimates for mixtures of different volume fractions of resin and iron. For the DEM calculations, resin is first assumed as host (soft phase) and iron as inclusions (hard phase), and then iron is assumed as host (hard phase) and resin as inclusions (soft phase), simulating hypothetical CPSF and SPSF composites, respectively. DEM produces two different estimates, for the two possible arrangements of the two constituents, whereas CPA produces only one estimate. Since the real material microstructure is consistent with the lower DEM estimate, it predicts the measured data better than upper DEM and CPA, for both, spherical and flake like inclusions (Piche and Hammel, 1986 and 1987).

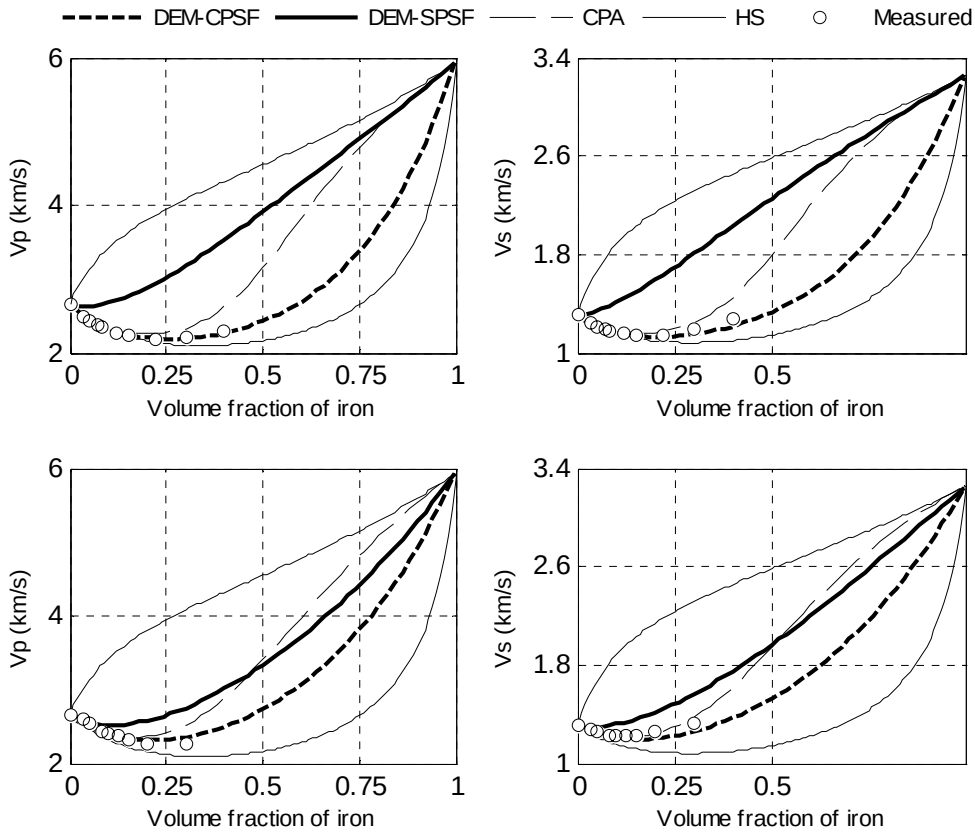

Figure 2.22. Comparison of theoretical and measured ultrasonic V_p and V_s velocities versus volume fraction of iron. The experimental data is for a resin/iron system with flaked iron inclusions. Upper frame: DEM and CPA V_p and V_s velocity predictions assuming oblate spheroidal inclusions with fixed aspect ratio 0.5. DEM is computed first by assuming resin as the host and iron as the inclusions (DEM-CPSF) and second iron as the host and resin as the inclusions (DEM-SPSF). Lower frame: the same as the upper frame, but the inclusions are assumed to be spheroids with lower aspect ratio with a fixed value 0.22 (Data from: Piche and Hammel, 1986 and 1987).

The iron-inclusion aspect ratio used in DEM and CPA for the resin/iron composite was 1 for spherical inclusions and 0.22 for the flake-like inclusions (Figure 2.22). The difference between the lower and upper DEM estimates, for the respective CPSF and SPSF materials, decreases with decreasing aspect ratio of the inclusions. When spherical inclusions are considered, the CPA predictions are between the upper and lower DEM estimates at all concentrations. When flake-like inclusions are considered, CPA estimates

are between the upper and lower DEM estimates, at low concentration, and greater than the upper DEM estimates at high concentration.

The numerical experiment described above (Figure 2.22) is repeated for mixtures of different concentrations of resin and aluminum (Figure 2.23). The theoretical velocity predictions are compared with experimental resin/aluminum data (Zhang et al., 1996). The aluminum-inclusions aspect ratio used in DEM and CPA was 0.4, which is very close to the measured value.

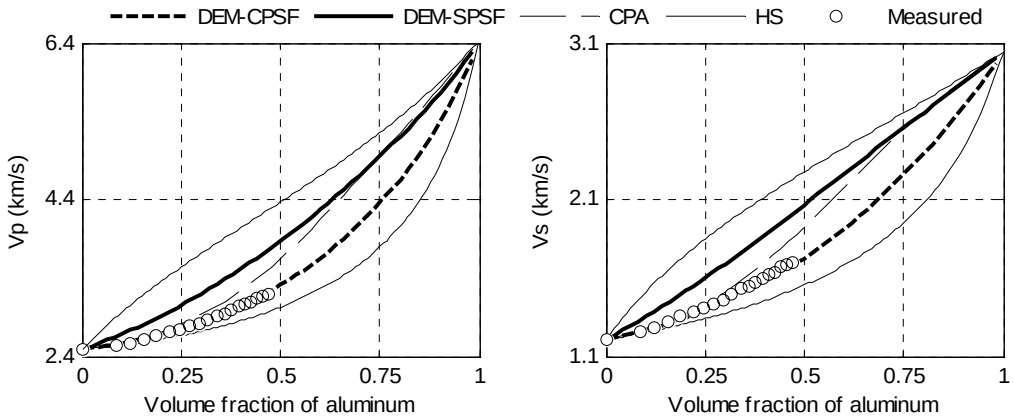

Figure 2.23. Comparison of theoretical and measured ultrasonic V_p and V_s velocities versus volume fraction of aluminum. The experimental data is for a resin/aluminum system. Left: V_p velocities according to DEM and CPA and HS bounds. The inclusions are assumed to be spheroidal with fixed aspect ratio of 0.40. DEM is computed assuming resin as the host and aluminum as the inclusions (DEM-CPSF) and then aluminum as the host and resin as the inclusions (DEM-SPSF). (Data from: Zhang et al., 1996).

Figures 2.24 shows the theoretical and measured Young's modulus for mixtures of different volume fractions of aluminum as host and mullite/Al_2O_3 composite as inclusions. The composite mullite/Al_2O_3 particles are approximately spherical and consist of mullite as host and short rods of alumina (Al2O3) as inclusions. The average aspect ratio of the Al_2O_3 rods is about 4. The volume fraction of Al_2O_3 is constant and equal to 20% of the volume fraction of the composite inclusion. The composite samples contain three average mullite/Al_2O_3 inclusion diameters, 30, 45 and 100 μm.

The CPA Young's modulus was computed specifying only the volume fractions and

aspect ratios for the aluminum, mullite and aluminum oxide (Al_2O_3) were 1, 1 and 4, respectively. The DEM estimates were computed in three different ways: a) assuming aluminum as host to which the spherical mullite inclusions are added first, followed by the short rod particles of alumina; b) assuming aluminum as host to which the short rod alumina particles are added first, followed by the spherical mullite inclusions; and c) the elastic properties of the composite mullite/Al_2O_3 inclusion was computed first, and then aluminum was kept as host and to which the composite particles were added as inclusions.

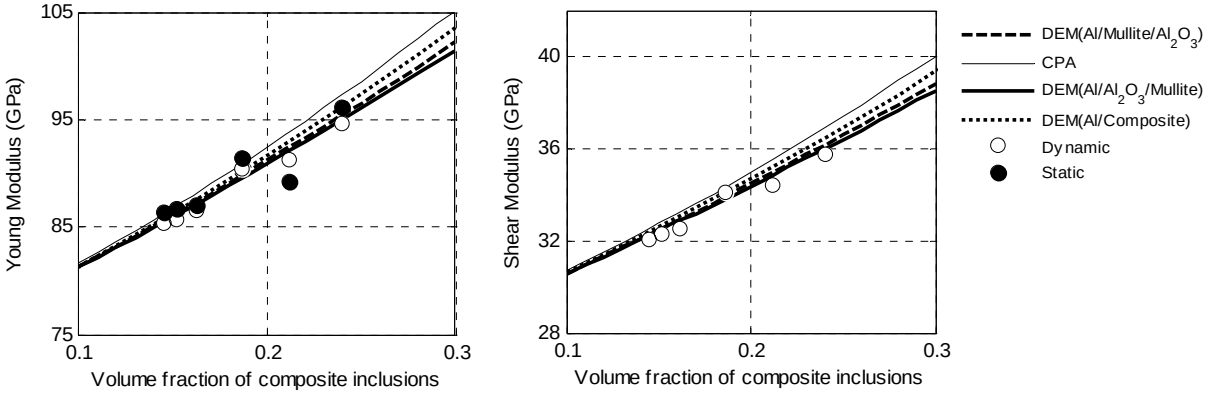

Figure 2.24. Static (filled circles) and dynamic (open circles) experimental elastic moduli compared with the DEM and CPA predictions, as function of volume fraction of mullite/Al_2O_3 composite inclusion (Data from: Dunn and Ledbetter, 1995).

Figure 2.25 shows the bulk and shear moduli of hypothetical rock matrices with high mineral moduli contrast. These rock matrices are composed of different volume fractions of hematite and kaolinite and constant volume fraction of quartz (0.6). The elastic properties of these minerals are shown in Table 4. The volume fraction of kaolinite is increased from 0.0 to 0.4, while the volume fraction of hematite is simultaneously decreased from 0.4 to 0, but the sum of these two volume fractions is kept constant and equal to 0.4. Thus, the total inclusion volume fraction is always 0.4. It is assumed that both mineral inclusions are spherical (AR = 1). Although the mineral phase of highest concentration is not always the host, in this hypothetical rock matrix, we identify quartz as the host, and hematite and clay as inclusions. If we do this, it is possible to compute two possible DEM estimates, depending on which mineral is added first: clay or hematite.

The same numerical experiment discussed above is repeated, but using dolomite and calcite as inclusions instead of hematite and kaolinite. In this case all methods, including the bound average method produce practically the same result.

The same behavior observed above for the bulk modulus was also observed for shear modulus.

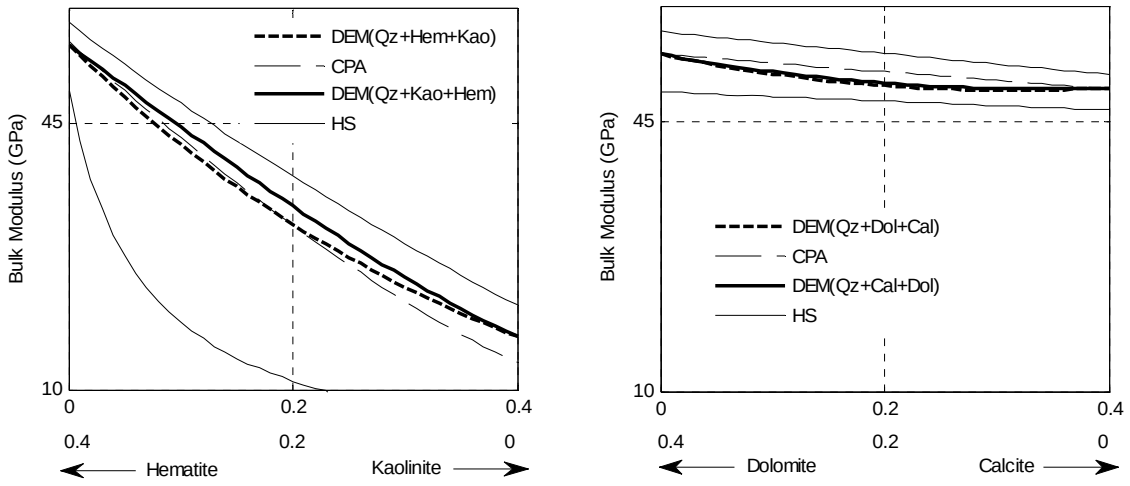

Figure 2.25. Bulk modulus versus volume fraction of kaolinite (left) and calcite as measured and predicted by DEM and CPA for a fixed aspect ratio 1.Left: hypothetical three-phase composite, assuming quartz (Qz) as host and hematite (Hem) and kaolinite (Kao) as spherical inclusions. The bulk and shear moduli are predicted by CPA, HSA and DEM. The DEM estimates are determined in two forms: a) adding the hematite first and then the kaolinite inclusions (Qz-Hem-Kao) and b) adding the kaolinite first and the hematite inclusions (Qz-kao-Hem). Right: the as upper frame but for a hypothetical rock matrix composed of Quartz (Qz), dolomite (Dol) and calcite (cal).

Figure 2.26 shows the bulk modulus of two hypothetical CPSF and SPSF rock matrices. The CPSF composite consists of 0.95 volume fraction of quartz (host) and 0.05 of kaolinite (inclusions). The volume fractions of both minerals are kept constant, but the kaolinite fraction may have inclusions with two different aspect ratios: 0.01 and 1. The volume fraction of kaolinite with one of the aspect ratios is increased from 0.0 to 0.05, while the volume fraction with the other aspect ratio is simultaneously decreased from 0.05 to 0, thus keeping the sum of these two volume fractions constant and equal to 0.05.

Two different DEM estimates were computed: one was obtained by adding first the smaller aspect ratio kaolinite inclusions (Qz + Kao(0.01) + Kao (1)) and then the inclusions with aspect ratio 1 ((Qz + Kao(1) + Kao (0.01))); and the other by adding first the inclusions with aspect ratio 1. The two DEM estimates produced significantly different results when the volume fraction of low aspect ratio kaolinite inclusions was high. CPA produced results lower than the DEM estimates for all volume fractions of kaolinite. The CPA and DEM bulk moduli decrease as the volume fraction of low-aspect-ratio kaolinite inclusions increases.

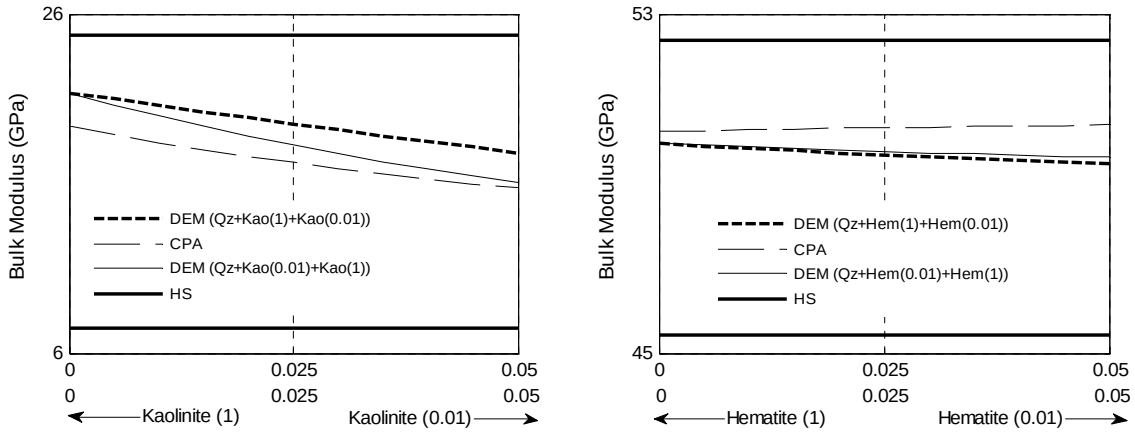

Figure 2.26. Bulk modulus of the three-phase hypothetical rock matrix, according to DEM and CPA and HS bounds. The inclusions aspect ratios used in DEM and CPA are 1 for quartz (Qz), 1 for the first kaolinite (Kao(1)), and 0.01 for the second kaolinite (Kao(0.01)). The rock matrix is composed of 0.95 quartz and 0.05 kaolinite. DEM(Qz + Kao + Hem) is the DEM estimation adding first the kaolinite with aspect ratio 1 and second the kaolinite with aspect ratio 0.01. DEM(Qz + Hem+ Kao) is the DEM estimation adding first the kaolinite with aspect ratio 0.01 and second the kaolinite with aspect ratio 1.

The same numerical experiment described above is repeated, but using hematite (stiff phase) as inclusions instead of kaolinite (soft phase). In this case, the two DEM estimates produce practically the same result, and CPA produces values higher than DEM. The DEM bulk modulus decreases as the volume fraction of low-aspect-ratio hematite inclusion increases, whereas the CPA bulk modulus slightly increases.

The same behavior observed above for the bulk modulus was also observed for shear modulus.

The numerical experiments discussed above (Figures 2.25 and 2.26) show that when the elastic-modulus contrasts of the composite constituents minerals are small, the resulting effective elastic moduli do not depend significantly on the manner in which the volume fractions of host and inclusions of different shapes are added (microstructure). On the other hand, when the modulus contrasts are high, the resulting elastic moduli indeed depend on the rock matrix microstructure.

2.4.4 Effect of interface adhesion

This subsection examines the effect of interface adhesion on the effective elastic moduli of composites. This effect on the elastic moduli may be very large. We will not model the effect of different degrees of adhesion. Adhesion is the propensity of different molecules to stick together due to attractive forces. The strength of the adhesion between the host and inclusion depends on the mechanism of interaction between them, and the surface area over which the host and inclusion contact. The area of contact depends on the inclusion surface asperities (Fuller and Tabor, 1975). The area of contact between materials that wet each other tends to be larger than those do not (Comyn, 1997; Kinloch, 1987).

Interfaces have a large effect on the elastic moduli of materials (Wang et al., 2009). Composites with incomplete or poor adhesion between the inclusions and host are common. In contrast to composites with completely welded inclusions, the elastic moduli of composites containing incompletely welded inclusions depend on the size of the inclusion (Wang et al., 2009; Vollenberg and Heikens, 1990).

In order to examine the effect of adhesion we use published data on polypropylene/chalk composites (Table 2.1) which consist of mixtures of polypropylene (pp) and chalk. The chalk particles are very irregularly shaped, but their average AR is close to unity. For the construction of these composites, three different sizes of chalk particles were used: 3.5 μm, 30 μm, and 130 μm. The adhesion between the chalk inclusions and the polymer host was observed to be poor. To achieve complete adhesion, the chalk particles were chemically treated to create a very thin adhesive interphase that couples the inclusion and matrix (Vollenberg and Heikens, 1990).

The composite samples were subjected to stress-strain tests by. The magnitude of the applied stress was between 0 and 20 MPa, producing strains of about 0-0.02. The tests conducted on the samples with different chalk inclusion sizes, show that for the three sample sizes, the deviation from linear elasticity takes place at about the same stress level for the completely welded chalk inclusions and at a different levels for the poorly adhered chalk inclusions (pure chalk).

Both the DEM and CPA predictions are in good agreement with the measured static Young's modulus of the samples with excellent adhesion, whereas the measured Young's modulus of the samples with poor adhesion is smaller or greater than the theoretical predictions depending on the inclusion size. The measured data that agree best with the CPA predictions are those for the 30 μm particles.

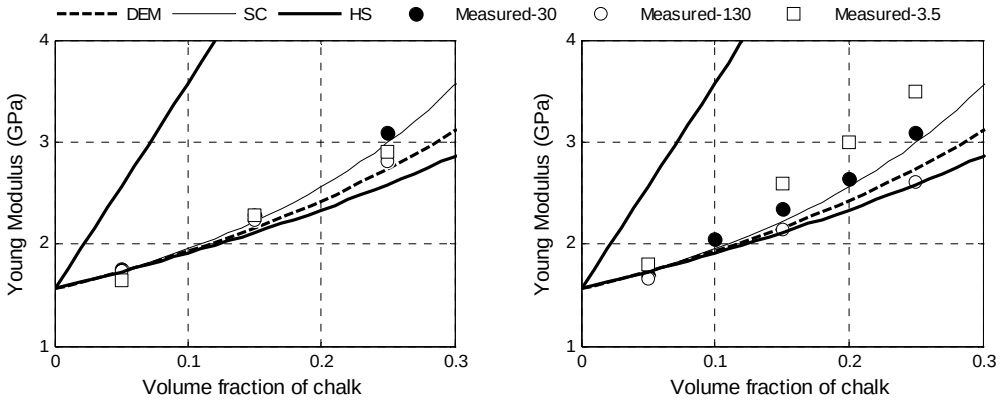

Figure 2.27. Comparison of DEM, CPA and HS-bounds predictions with measured Young's modulus as a function of volume fraction of chalk in completely (left) and incompletely (right) welded pp/chalk composite samples. Different symbols represent pp/chalk composites with different average chalk inclusion sizes : 3.5 μm (open squares), 30 μm (filled circles), and 130 μm (open circles). (Data from: Dunn and Ledbetter, 1995).

The variation of Young's modulus with inclusion size is not yet well explained (Vollenberg and Heikens, 1990). It has been observed that the morphology and the crystallinity of the pp-host are unaffected by the presence of the chalk particles with different shapes at all chalk volume fractions (Vollenberg and Heikens, 1990); and that the spherulite size is much larger than the inclusion size. Thus, the changes in the

Young's modulus with inclusion size are not due to interphase effects or changes in morphology or crystallinity of the host polymer.

2.4.5 Effect of multimineral matrices on the effective properties of liquid saturated rocks

In this subsection, we consider hypothetical porous rocks with three mineral constituents- quartz, kaolinite, and hematite-, and with fixed volume fractions- 0.50, 0.25 and 0.25, respectively. The porosity of the rock samples ranges from 0 to 0.5. We considered the dry and fluid-saturated cases. The effective elastic moduli of the dry and fluid-saturated rocks are estimated using DEM and CPA. These two models treat the fluid-saturated multimineral rock as a multiphase composite and assume that the fluid inclusions are isolated with respect to flow, thus simulating the high-frequency saturated rock behavior that may be appropriate at ultrasonic frequencies (Mavko, et al., 1996).

The effective properties of the bulk rock were computed using two different methodologies: a) the effective properties of the rock matrix were computed using the HS bound-average method and then effective-medium models (CPA and DEM) were used to compute the effective properties of the saturated rock, as a two-phase composite, and b) using only effective-medium models for the whole rock, treating the fluid inclusions as an additional phase in the rock.

For the dry-rock case, there is air in the pores. The elastic properties of the air are assumed to be very small, practically zero. For the saturated-rock case, water is used as saturator. The elastic properties of water are shown in Table 4.

As discussed in the introduction, DEM may produce different estimations depending on how the incremental addition is achieved. For this exercise, two different DEM estimations of the rock matrix moduli are computed: one by adding first the kaolinite inclusions and then the hematite inclusions, and the other by adding first the hematite inclusions. In both cases, the quartz phase is assumed the host material.

The effective bulk and shear moduli of these hypothetic rocks according to DEM, CPA, and HS bounds are shown in Figure 2.28. The aspect ratios used in DEM and CPA is 1 for all constituents. Different results are produced depending on the methodology

chosen. This implies that, if the minerals elastic contrast is high, the bound average method may introduce an important error into the calculation of the effective properties of the whole rock. However, using an inappropriate effective-medium model may be even worse. CPA alone produces considerably smaller elastic moduli than DEM.

Figure 2.29 shows the same numerical experiment described above, but the aspect ratio for the kaolinite was 0.1, instead of 1. In this case the kaolinite inclusions are flakes dispersed in a quartz host. Notice that this change in aspect ratio of the soft inclusions (kaolinite) causes significant changes in the elastic behavior as a function of porosity and reduction of the effective elastic moduli.

Figure 2.30 shows the same exercise described above but for quartz, calcite and dolomite, which are minerals with less contrasting elastic properties. For the DEM calculations, quartz continues to be the host, with dolomite and calcite being the inclusions. Notice that despite the elastic contrast among quartz, calcite and dolomite, the elastic bounds are very close to each other. This implies that the error possibly introduced into the calculation of the effective properties by using the bound average method may not be critical. In this case, DEM produces basically only one estimate, independently of the order of addition, under both dry and wet conditions.

In sedimentary rocks, except for the light and soft clay and coal minerals, and some heavy minerals, such as pyrite and hematite, the minerals typically found in greatest amounts are quartz, feldspar, mica, calcite, dolomite, anhydrite, and gypsum. Fortunately, the elastic contrasts among these minerals are not high enough to be critical in the calculation of the elastic properties of the matrix using the bound average methods. However, when clays or heavy minerals are present in considerable volume fractions in the rock matrix, the selection of the appropriate effective-medium model to determine the elastic moduli of the multimineralic rock matrix is important.

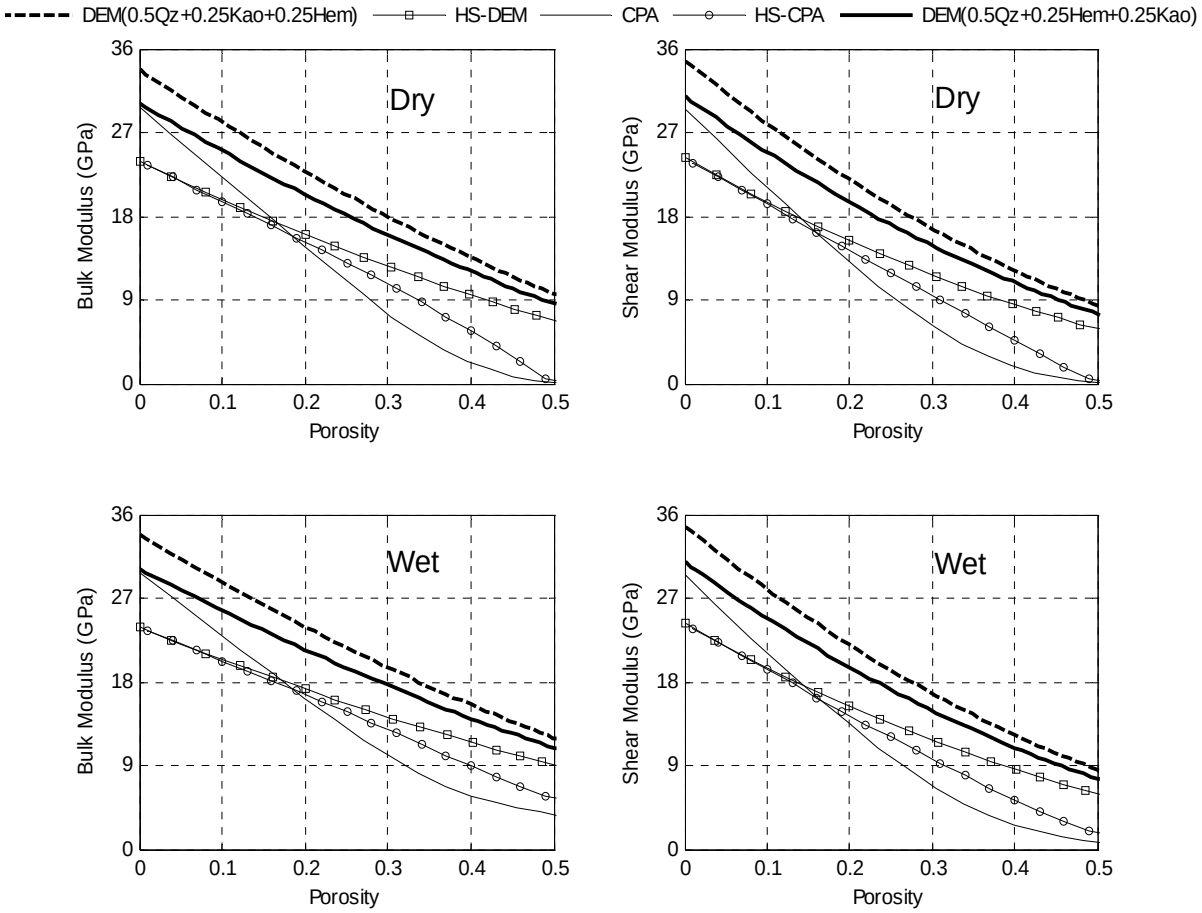

Figure 2.28. High frequency estimation of bulk and shear moduli of hypothetical porous rocks according to DEM and CPA. The aspect ratio used in both models for all constituents is 1. The rock matrix is composed of 0.50 quartz (Qz), 0.25 kaolinite (Kao) and 0.25 hematite (Hem). DEM1 is the DEM estimation adding first the kaolinite and second the hematite inclusions. DEM2 is the DEM estimations adding first the hematite and second the kaolinite inclusions. DEM3 is the DEM estimation using the HS bounds average method for the properties of the rock matrix. CPA1 and CPA2 are the estimations using only CPA and using the HS bound average for the matrix. Upper frame: bulk and shear moduli for the dry rock. Lower frame: bulk and shear moduli of the full water saturated rock.

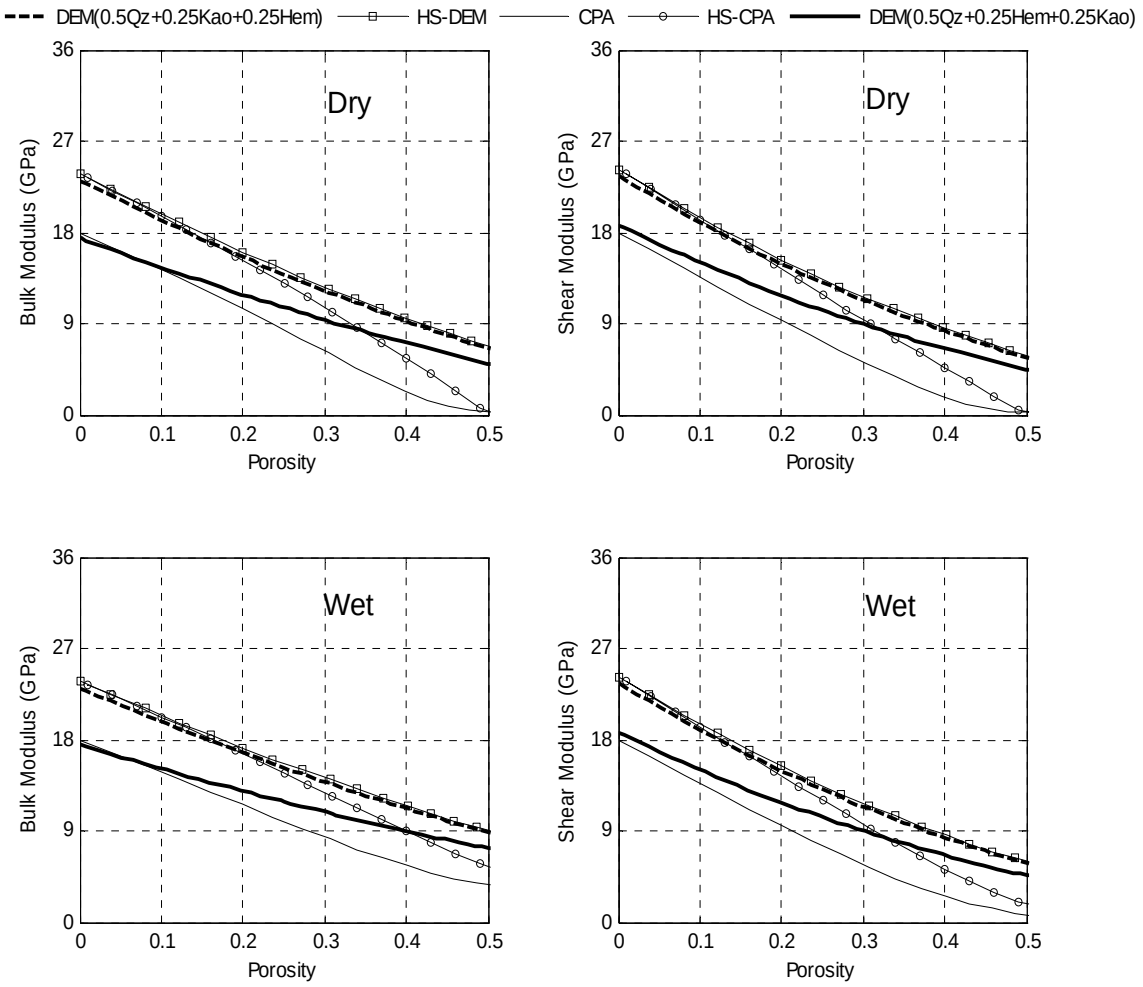

Figure 2.29. High frequency estimation of bulk and shear moduli of hypothetical porous rocks according to DEM and CPA. Here instead of having all aspect ratios 1 (Figure 2.28) we use aspect ratio 0.1 for kaolinite (Kao).

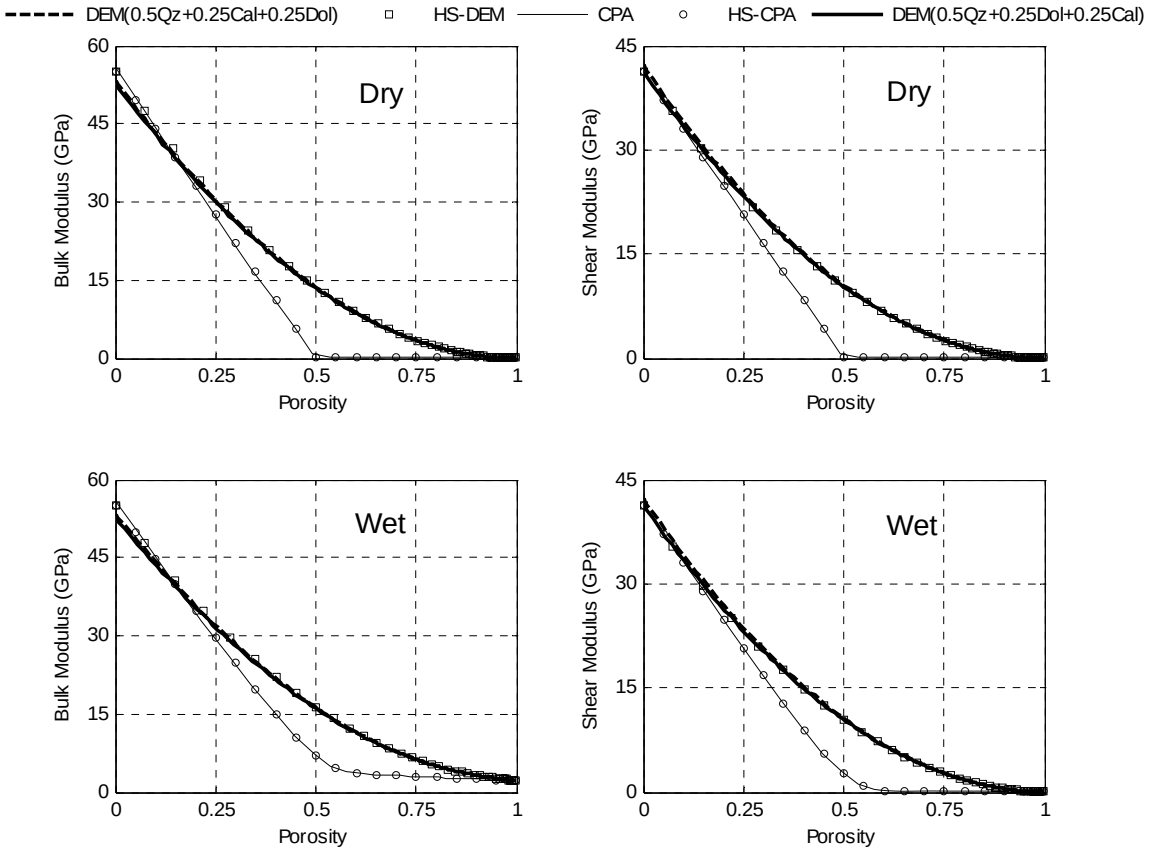

Figure 2.30. The same as Figure 2.28, but using dolomite (Dol) and calcite (Cal), instead of hematite (Hem) and kaolinite (Kao), respectively. High frequency estimation of bulk and shear moduli of hypothetical porous rocks according to DEM and CPA. Here instead of having all aspect ratios 1 (Figure 2.28) we use aspect ratio 0.1 for kaolinite (Kao).

2.5 Conclusions

We find DEM provides consistently accurate predictions for all analyzed composites in a wide range of volumetric concentration and with a narrow range of aspect ratios.

At low concentrations (~0.10), if the rock's microstructure is comparable with CPSF- or SPSF-materials, Hashin-Shtrikman bounds can be used as good predictors of elastic properties.

If a sedimentary rock's microstructure is comparable with CPSF- or SPSF-materials and some information about the grain (inclusion) spectrum is known, it is better to use effective-medium models to estimate the elastic properties of the rock matrix at all inclusion concentrations, instead of averaging the upper and lower Hashin-Shtrikman

bound. If grain aspect ratios are greater than 0.5, spherical inclusions are good approximations for the purpose of effective elastic properties.

DEM or CPA can be used as reliable model to invert for aspect ratios in rocks with known mineralogy.

For sedimentary rock with microstructure comparable to TF-materials, DEM gives good predictions, however, for polycrystalline rocks, a model that considers all the elements of the elastic tensor and the degree of anisotropy of each single crystal of the rock constituents would be a better approximation.

The results of calculating the effective elastic moduli of a composite appear to be remarkably stable for a wide range of inclusion concentrations and for predicting both *P*- and *S*-wave elastic constants. These results are intended to be used as a rigorous foundation for further effective-medium modeling of sedimentary rock matrices with complex mineralogy.

2.6 References

Achenbach, J., Zhu, H., 1990, Effect of interface on micro and macromechanical hexagonal-array fiber composites: Journal of Applied Mechanics, 57, 956-962.

Aksel, N., CE. Hubner, 1996, The influence of dewetting in filled elastomers on the changes of their mechanical properties: Archive of Applied Mechanics 66, 231-241, Springer-Verlag.

Anson, L. and R. Chivers, 1993, Ultrasonic velocity in suspensions of solids in solids, a comparison of theory and experiment: Journal of Physics D: Applied Physics, 26, 1566-1575.

Babu, P., Savithri, S., Pillai, U., Pai, B., 2005, Micromechanical modeling of hybrid composites: Polymer, 46, 7478-7484.

Banerjee, B., and Adams, 2004, On predicting the effective elastic properties of polymer bonded explosives using the recursive cell method: International Journal of Solids and Structures, 41, 481-509.

Berryman, J., 1980, Long-wavelength propagation in composite elastic media: Journal of Acoustic Society of America, 68, 1809-1831.

Berryman, J., 1992, Single-scattering approximations for coefficients in Biot's equations of poroelasticity: Journal of Acoustic Society of America, 91, 551-571.

Berryman, J., 1995, Mixtures theories for rock properties, in A Handbook of Physical Constants, T.J. Ahrens, ed. American Geophysical Union, Washington, D.C., 205-228.

Biwa, S., N. Ito, N. Ohno, 2001, Elastic properties of rubber particles in toughened PMMA ultrasonic and micromechanical evaluation: Mechanics of Materials, 33, 717-728.

Bridge, B., and K. Cheng, 1987, Non-destructive ultrasonic evaluation of CaCo3-filled polypropylene mouldings: Journal of Materials Science, 22, 3118-3128.

Bruggeman, D. A. G., 1935, Berechnung verschiedener physikalischer Konstanten von heterogenen Substanzen: Ann.Physik. (Leipzig) 24, 636-679.

Chinh, P., 2000, Hierarchical unsymmetrical effective medium approximation for the electrical conductivity of water-saturated porous rocks: Zeitschrift fur angewandte Mathematik and Physik (ZAMP), 51, 135-142.

Cleary, M. P, Chen, I.-W., & Lee, S.-M., 1980, Self-consistent techniques for heterogeneous media: ASCE Journal of Engineering Mechanics, 106, 861-887.

Comyn, J., 1997, Adhesion Science: Royal Society of Chemistry Paperbacks.

Connolly, P., 1999, Elastic impedance: The Leading Edge, 18(4), 438-452.

Dean, E., 1983, Elastic moduli of porous sintered materials as modeled by a variable-aspect ratio self-consistent oblade-spheroidal-inclusion theory: Journal of the American Ceramic Society, 66, 847-854.

Devaney, A., Levine, H., 1980, Effective Elastic Parameters of Random Composites: Applied Physics Letters, 37, 377.

Doi, H., Y. Fujiwara, K. Miyake, and Y. Oosawa, 1970, A systematic investigation of elastic moduli of WC-Co alloys: Metallurgical Transactions, 1, 1417-1425.

Dunn, M., and Ledbetter, 1995, Elastic moduli of composites reinforced by multiphase particles: Journal of Applied Mechanics, 62, 1023-1028.

Endres, A., 2000, Size scale considerations in modeling the electrical conductivity of porous rocks and soils: Exploration Geophysics, 31, 418-423.

Folk, R., 1965, Petrology of sedimentary rocks: Hemphill Publishing Company.

Gaudig, W., R. Mellert, U. Weber, and S. Schmauder, 2003, Self-consistent one-particle 3D unit cell model for simulation of the effect of graphite aspect ratio on Young's modulus of cast-iron: Computational Materials Science, 28, 654–662.

Gomez, T., G., A. Mulholland, G. Hayward, J. Gomatam, 2000, Wave propagation in 0-3/3-3 connectivity composites with complex microstructure: Ultrasonic, 38, 897-907.

Gosz, G., B. Moran, and J. Achenbach, J., 1991, Effect of a viscoelastic interface on the transverse behavior of fiber-reinforced composites: International Journal of Solids and Structures, 27, 1757-1765.

Gueguen, Y., M. Le Ravalec, and L. Ricard, 2006, Upscaling: effective medium theory, numerical methods and fractal dream: Pure and Applied Geophysics, 163, 1175-1192.

Gueguen, Y., T. Chelidze, and M. Le Ravalec, 1997, Microstructures, percolation thresholds and rock physical properties: Techtonophysics, 279, 23-35.

Gurland, J., 1979, A structural approach to the yield strength of two-phase alloys with coarse micromechanics: Material Science and Engineering, 40, 59-71.

Harvey, B. and R. Tracy, 1994, Petrology: Igneous, Sedimentary and Metamorphic: Freeman, 2nd Ed.

Hashin, Z., and Shtrikman, S., 1963, A variational approach to the elastic behavior of multiphase materials, Journal of the Mechanics and Physics of Solids, 11, 127-140.

Hashin, Z., 1991a, The spherical inclusion with imperfect interface: Journal of Applied Mechanics, 58, 444-449.

Hashin, Z., 1991b, Thermoelastic properties of particulate composite with imperfect interface: Journal of applied Mechanics and Physics of Solids, 39, 745-762.

Hashin, Z., 1992, Extremum principles for elastic heterogeneous media with imperfect interface and their application to bounding of effective moduli: Journal of applied Mechanics and Physics of Solids, 40, 767- 781.

Hashin, Z., 1983, Analysis of composite- a survey: Journal of Applied Mechanics, 50, 481-505.

Hasselman, D. and R. Fulrath, 1965a, Effect of spherical tungsten dispersions on Young's modulus of a glass: Journal of The American Ceramic Society-Discussions and Notes, 48, 548-549.

Hasselman, D. and R. Fulrath, 1965b, Effect of alumina dispersions on Young's modulus of a glass: Journal of The American Ceramic Society-Discussions and Notes, 48, 218-219.

Hasselman, D. and R. Fulrath, 1963, Experimental and calculated Young's moduli of zirconium carbide containg a disperse phase of graphite: Journal of The American Ceramic Society-Discussions and Notes, 46, 103-104.

Hill, R., 1952, The elastic behavior of crystalline aggregate: Proceedings of the Physical Society of London, A65, 349–354.

Hornby, B., L. Schwartz, and Hudson, J., 1994, Anisotropy effective-medium modling of the elastic properties of shales: Geophysics, 59, 1570-1583.

Ji, S., Z. Wang, 1999, Elastic properties of fosterite-enstatite composites up to 3.0 GPa: Journal of Geodynamics, 28, 147-174.

Ji, S., Q. Wang, B. Xia, and D. Marcotte, 2004, Mechanical properties of multiphase materials and rocks: a phenomenological approach using generalized means: Journal of structural Geology, 26, 1377–1390.

Ji, S., Q. Wang, and B. Xia, 2003, *P*-wave velocities of polymineralic rocks: comparison of theory and experiment and test of elastic mixture rules: Tectonophysics, 366, 165-185.

Kinloch, A., 1987, Adhesion and Adhesives: Science and Technology, Chapman and Hall.

Kroner, E., 1967, Elastic moduli of perfectly disordered composite materials: Journal of The Mechanical and Physics of Solids, 15, 319-329.

Kuster, G.T., and Toksoz, M.N., 1974. Velocity and attenuation of seismic waves in two-phase media. Geophysics, 39, 587-618.

Ledbetter, H. and M. Dunn, 1995, Microstructure and elastic-constant measurements of two-phase materials: in Proceedings, IEEE Ultrasonic Symposium, 625-633.

Lees, S., and C. Davidson, 1977, Ultrasonic measurement of some mineral filled plastic: IEEE Transactions on Sonics and Ultrasonics, 24, 222-225.

Lees, S., R. Gilmore and P. Kranz, 1973, Acoustic properties of tungten-vinyl composites: IEEE Transactions on Sonics and Ultrasonics, 20, 1-2.

Le Ravalec, M., and Y. Gueguen, 1996, High- and low-frequency elastic moduli for a saturated porous/cracked rock-differential self-consistent and poroelastic theories: Geophysics, 61, 1080-1094.

Lohe, D., O. Vohringer, E. Macherauch, 1983, Der Einfluß der graphitform auf den elastizitatsmodul von ferritischen Gusseisenwerkstoffen: Zeitschrift fur Metallkunde, 74, 265–273.

Mallick, S., 2001, AVO and elastic impedance, The Leading Edge, 20 (10), 1094-1104.

Mavko, G., Mukerji, T., and Dvorkin, J., 1998, The rock physics handbook, Cambridge University Press.

Markov, M., V. Levine, A. Mousatov and E. Kazatchenko, 2005, Elastic properties of double-porosity rocks using the differential effective medium model: Geophysical Prospecting, 53, 733-754.

Mondescu, R. and Muthukumar, M., 1999, Effective elastic moduli of a composite containing rigid spheres at nondilute concentrations: Journal of Chemical Physics, 110, 1123-1137.

Nan, C., R. Birringer, D. Clarke, H. Gleiter, 1997, Effective thermal conductivity of particulate composites with interracial thermal resistance, Journal of Applied Physics, 81, 6692- 6299.

Nemat-Nasser, S., M. Hori, 1993, Micromechanics: overall properties of heterogeneous materials: 2nd edition, Elsevier.

Nishimatsu, C., and J., Gurland, 1960, Experimental survey of the deformation of the hard-ductile two-phase alloy system WC-Co: in Transactions of the American Society for Metals, 52, 469–484.

Nguyen, T., Lethiecq, M., 1996, Experimental verification of the theory of elastic properties using scattering approximations in (0-3) connectivity composite materials: IEEE Transactions on Ultrasonics. Ferroelectrics, and Frequency control, 43, 640-645.

Norris, A., 1985a, A differential scheme for the effective moduli of composites. Mechanics of materials, 4, 1-16.

Norris, A., O., Sheng, and A. Callegari, 1985b, Effective-medium theories for two-phase dielectric media: Journal of Applied Physics, 57, 1990-1996.

Nur, A., G. Mavko, J. Dvorkin, and D. Galmudi, 1998, Critical porosity: a key to relating physical properties to porosity in rocks: The Leading Edge, 17, 357-362.

Pernot, F., R. Rogier, 1993, Mechanical properties of phosphate glass-ceramic-316 L stainless composites: Journal of Materials Sciences, 28, 6676-6682.

Phan-Thien, N., and D. Pham, 1997, Differential multiphase models for polydispersed suspensions and particulate solids: Journal of Non-Newtonian Fluid Mechanics: 72, 305-318.

Piché, L., and A. Hamel, 1986, Ultrasonic evaluation of filled polymers: I. Techniques and models for the elastic moduli of a resin filled with iron spherical inclusions: Polymer Composites, 7, 355-362.

Piché, L., and A. Hamel, 1987, Ultrasonic evaluation of filled polymers II. Elastic moduli of a resin filled with iron inclusions of different aspect ratios: Polymer Composites, 8, 22-28.

Quesenberry, M., P. Madison, and R. Jensen, 2003, Characterization of low density glass filled epoxies: Army Research Laboratory, ARL-TR-2938.

Richard, T., 1975, The mechanical behavior of a solid microsphere filled composite: Journal of Composite Materials, 9, 108.

Sahimi, M., 2003, Heterogeneous materials I: Liner transport and Optical Properties: Springer-Verlag Press.

Saito, K., M., Nishihira, and K. Imano, 2007, Experimental study on intermediate layer made of (0-3) composite materials for use in air-coupled ultrasonic transducers: Japanese Journal of Applied Physics, 46, 4479-4482.

Sheng, P., 1991, Consistent modeling of the electrical and elastic properties of sedimentary rocks: Geophysics, 8, 1236-1243.

Smith, J., 1976, The elastic constants of a particulate-filled glassy polymer: Comparison of experimental values with theoretical predictions: Polymer Engineering and Science, 16, 394-399.

Stauffer, D. and A. Aharony, 1994, Introduction to percolation theory: 2nd edition, Taylor & Francis, London, 1994.

Sugawara, K., M. Nishihira and K. Imano, 2005, Experimental study of acoustic properties of (0-3) composite materials for intermediate layer or backing of ultrasonic transducers: Japanese Journal of Applied Physics, 44, 4347–4349.

Thomsen, L., 1972, Elasticity of polycrystals and rocks: Journal of Geophysical Research, 77, 315-327.

Tong, J., Nan, C., 2001, Effect of inclusions shape on the effective elastic moduli for composites with imperfect interface: Acta Mechanica, 146, 127-134.

Torquato, S., 1991, Random heterogeneous media: microstructures and improved bounds on effective properties: Applied Mechanics Review, 44, 37-76.

Vollenberg, P., and Heikens, D., 1990, The mecanical properties of chalk-filled polypropylene: a preliminary investigation: Journal of Materials Sciences, 25, 3089-3095.

Walsh, J.B., 1965, The effect of Cracks on compressibility of rock: Journal of Geophysics Research., 70, 381-389.

Wang, J., Karihaloo B., and Duan, H., 2009, Scaling laws for properties of materials with imperfect interfaces: in IUTAM Symposium on Scaling in Solid Mechanics, 10, 157-163.

Watt, P., 1988, Elastic properties of polycristallie minerals: Comparison of theory and experiment: Physics and Chemistry of Minerals, 15, 579-587.

Watt, P. and R. J., O'Connell, 1980, An experimental investigation of the Hashin-Shtrikman bounds on two-phase aggregate elastic properties: Physics of the Earth and planetary interiors, 21, 359-370.

Watt, P., 1976, The elastic properties of composite materials: Reviews of Geophysics and Space Physics, 14, 541-563.

Widjajakusuma, J., 2004, Effective macroscopic elastic moduli of sedimentary rocks: in Proceedings, Komputer dan Sistem Intelijen, 636-644.

Wu, T.T., 1966. The effect of inclusion shape on the elastic moduli of a two-phase material. International Journal Solids Structures, 2, 1-8.

Zhang, M., Ebrom, D., McDonald, J., and Tatham, R., 1966, Comparison of experimental velocity measurements with theoretical results in a solid-solid composite material. Geophysics, 61, 1429–1435.

Zimmerman, R., 1991, Compressibility of sandstones, Elsevier, New York.

Chapter 3
Equivalent elastic approach: using DEM as a tool to make rock physics predictions

3.1 Abstract

We pose a question: can a theoretical inclusion model, specifically, the differential effective-medium model, be used to match experimental velocity data in rocks that are not necessarily made of inclusions such as clastics? It is indeed possible in some cases by using an almost constant inclusion aspect ratio within wide ranges of porosity and mineralogy. We first approach this question by using empirical velocity-porosity equations as proxies for data. By finding a DEM inclusion aspect ratio (AR) to match these equations, we find that the required range of AR is narrow. Moreover, a constant AR of about 0.13 can be used to accurately match empirical relations in competent sand, shale, and quartz/calcite mixtures. We show that this finding can be practically utilized to (a) predict V_s from V_p; (b) describe velocity-frequency dispersion between low-frequency and ultrasonic experiments; (c) predict the dry-frame elastic properties from ultrasonic data on liquid-saturated samples, where Gassmann's fluid substitution is not

applicable; (d) predict the attenuation of *P*-wave velocity; and (e) establish tight constraints for the ranges of possible variation of V_s and V_p at a given porosity in some mineralogies. We also apply this approach to laboratory data rather than empirical equations and confirm a positive answer to the main question with all applications of this result still valid.

3.2 Introduction

Inclusion theories often represent porosity, pore geometry and connectivity as distributions of ellipsoidal inclusions (Ament, 1953, Eshelby, 1957; Walsh, 1965; Wu, 1966; O'Connell and Budiansky, 1974; Kuster and Toksöz, 1974; Cheng, 1993; Berryman, 1980; Zimmerman, 1984, 1986, 1991a,b; Gurevich et al., 1998; Jakobsen et al. 2003b). These inclusion theories are based on extreme idealizations of the pore geometry and heuristic assumptions about the way in which high concentrations of pores elastically interact. These models offer useful analogs of the elastic behavior of some rocks, with specific microstructures, but their limitation to idealized inclusion shapes makes complex comparing the models to real rock microstructure. It is important to be aware that the shapes of rock pores are almost never ellipsoidal, and the methods for treating high concentration of pores (inclusions) are idealized and heuristic. It is not realistic to relate inclusions aspect ratios models to variations of rock texture resultant from different depositional or diagenetic processes.

Inclusion models, such as DEM (Norris, 1985) and the self-consistent approximation (Berryman, 1980), relate the elastic properties of rock to porosity (e.g., Xu and White, 1995), in spite of the fact that some rocks are composed of grains rather than inclusions (Figure 1). The mathematical flexibility of inclusion theories enables such exercises because by varying the inclusion aspect ratio (AR), it is possible to match almost any data point.

Therefore, we revisit this approach to use inclusion models, calibrated to measurements, as a single and flexible tool for implementing rock physics transforms. While many different formulations (O'Connell and Budiansky, 1974; Kuster and Toksöz, 1974; Berryman, 1980; Xu and White, 1995; Jakobsen et al. 2003a) can be used, we

focus on the DEM approach as formulated by Norris (1985), which assumes randomly oriented spheroidal inclusions (Appendix A). Therefore, we deal with isotropic rock. DEM can be used to model different rocks with few adjustable parameters. Our approach consists on matching experimental data in reasonably wide ranges of porosity and mineralogy with DEM and finding range of AR required to achieve this match. In other words, although the actual rock may not be like a physical realization of this mathematical model, we will find the elastic equivalency between DEM and data. The hypothesis is that if such elastic equivalency can be established with a narrow AR range for a wide range of real samples, we can find an idealized physical analogue to real rock and then use this analogue to interrelate different properties of real samples.

If we establish that a single AR can be used to estimate the elastic behavior of rock in a reasonably wide range of porosity and mineralogy, we can further exploit DEM to interrelate other properties of rock.

We proceed with this task and find that for pure quartz, quartz/clay, and quartz/calcite mineralogies, both V_p and V_s can be accurately matched by DEM with AR ≈ 0.13 in a porosity range from zero to 0.4. This finding enables us to predict V_s from V_p; quantify the effect of pore fluid on the velocity-frequency dispersion and assess attenuation; and derive constraints for the elastic properties narrower than the existing bounds.

We start by using the Raymer et al. (1980) empirical velocity-mineralogy-porosity model as a proxy for experimental data. We proceed with applying this concept to a number of laboratory data sets, which include ultrasonic velocity measurements from Coyner (1984), Rafavich et al. (1984), Han (1986), Kenter et al. (1997), Woodside et al. (1998), Asefa et al. (2003), Verwer et al. (2008) and Fabricius et al. (2008). The samples examined by these authors include siliciclastic, carbonate, and mixed carbonate-siliciclastic mineralogies. Finally, we demonstrate the utility of our findings on well logs from the Ocean Drilling Program (ODP) and a Venezuelan well (Graterol at al., 2004).

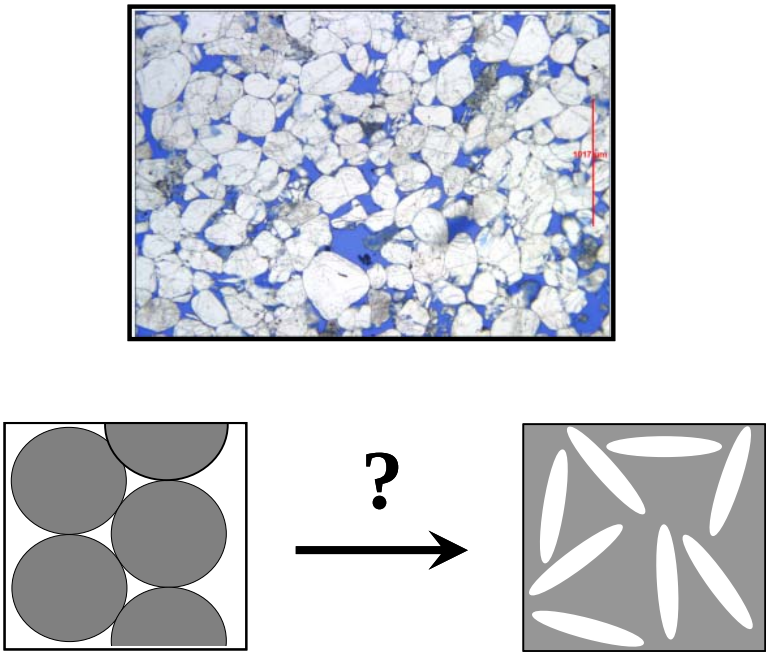

Figure 3.1. Top: Thin section of a sandstone with intergranular porosity. Bottom: granular rock and its equivalent elastic model, made of a continuous matrix and embedded elliptical inclusions with fixed aspect ratio.

3.3 DEM and empirical transforms

The Raymer et al. (1980) relation links V_p to porosity ϕ as $V_p = (1-\phi)^2 V_{ps} + \phi V_{pf}$, where V_{ps} is the velocity in the solid phase of the rock, and V_{pf} is the velocity in the fluid. In this equation, the mineralogy affects V_p through V_{ps}. For example, V_{ps} = 6.04 km/s in pure quartz, 4.51 km/s in a 50% quartz and 50% clay mixture, 6.22 km/s in a 50% quartz and 50% calcite mixture, and 6.64 in pure calcite. Raymer's equation was derived as an empirical fit to a large number of log data. Therefore, for our purposes, we can use it as experimental data. This equation was originally recommended for the porosity range between zero and 0.37. Here we slightly extend this range to 0.40.

To extend this experimental data set into the V_s domain, we apply the Krief et al. (1990) V_s predictor to V_p derived from Raymer et al. (1980): $(V_p^2 - V_{pf}^2)/V_s^2 = (V_{ps}^2 - V_{pf}^2)/V_{ss}^2$, where V_{ss} is the shear-wave velocity in the solid phase.

In this example, we assumed that rock was saturated with pure water with density of

1.00 g/cm3 density and velocity of 1.50 km/s. In Figure 2 we display the AR required to fit the data from the said relations by DEM. When applying DEM, we first assume that the rock is dry, find the dry-frame elastic moduli, and then use Gassmann's (1951) fluid substitution to arrive at the results for water-saturated rock (DEM/Gassmann). We observe that for pure quartz, 50% quartz and 50% clay, and 50% quartz and 50% calcite mineralogies, the AR required to match these data is stable versus porosity, almost the same whether we find AR by matching DEM results to V_p or V_s, and, moreover, is almost unchanged between these three mineralogies. For two other mineralogies (pure clay and pure calcite) examined in Figure 2, we find that AR varies versus porosity and also depends on whether it was determined from V_p or V_s. Still, even in these two cases, AR is confined within a narrow range between 0.1 and 0.2

Let us next select a single aspect ratio (e.g., AR = 0.13) and use it with DEM/Gassmann to predict V_p and V_s for all the five mineralogies. We find (Figure 3) that for the three mineralogies where the DEM-derived AR remain almost constant, these predictions are very accurate. Even for the two mineralogies where AR varied versus porosity, this single AR = 0.13 can still be used to predict the velocity with reasonable accuracy.

In order to use Gassmann's equations, we need to input the bulk moduli of the dry frame and pore fluid, K_{dry} and K_f, respectively. For a multimineral rock matrix whose minerals have small elastic contrasts, the accuracy of Gassmann fluid substitution is adequate if the bulk modulus of the solid phase (K_s) is computed using a mixing law, such as Hill's average (Hill, 1952). This stem from the fact that for many rocks, especially those with high porosity, $K_s >> K_{dry}$ and $K_s >> K_f$. Therefore, K_s may have a minor influence on the bulk modulus of the fluid saturated rock (K_{sat}), which allows application of Gassmann's equation to multimineral rocks. For the DEM modeling K_s is computed the same approach.

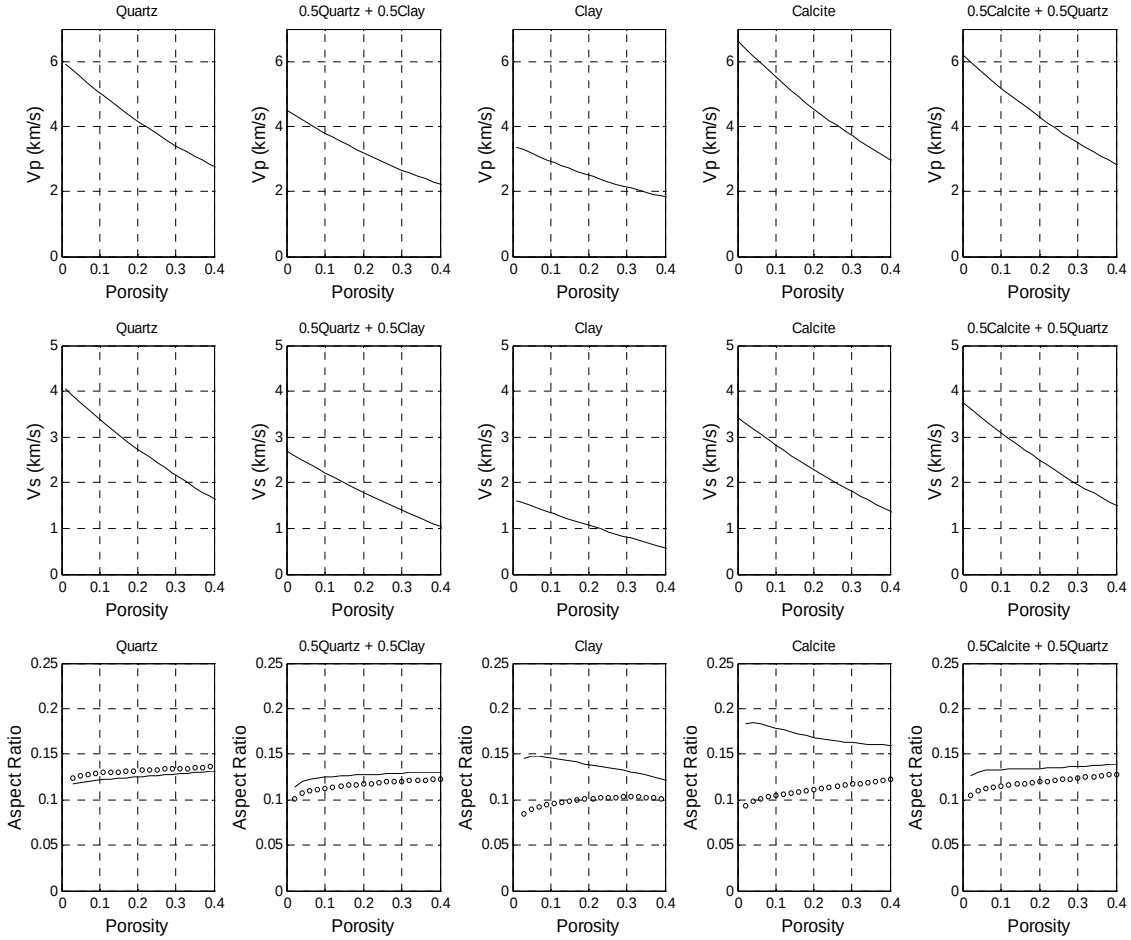

Figure 3.2. Top: the *P*-wave velocity versus porosity according to Raymer et al. (1980) for five mineralogies as marked on top of the frames. Middle: the *S*-wave velocity according to Krief et al. (1990) as derived from the *P*-wave velocity in the top row. Bottom: AR derived by matching DEM/Gassmann to the *P*-wave velocity (solid curve) and *S*-wave velocity (open circles).

Comparable results are obtained when using other empirical relations as proxies for experimental data. For instance, to extend the experimental data set into the V_s domain, we can apply Castagna et al. (1993), instead of Krief et al. (1990). Castagna et al. (1993), for wet limestone is $V_s = -0.05508V_p^2 + 1.01677V_p - 1.03049$, and for wet sandstone is $V_s = 0.80416V_p - 0.85588$, where the velocity is in km/s. We can also use the combination of the *P*-wave velocity (V_p) by Wyllie et al. (1956), which is $V_p^{-1} = \phi V_{pf}^{-1} + (1-\phi)V_{pm}^{-1}$, where V_{pf} and V_{pm} refer to the velocity in the pore fluid and mineral matrix, respectively, combined with the empirical *S*-wave velocity (V_s) by Krief

et al. (1990) or by Castagna et al. (1993).

In Appendix B, we discuss the prediction of V_s from V_p using a self consistent theory (Berryman, 1980) and compare the results to the DEM predictions. In Appendix C, we give another of the elastic equivalence approach, using the soft-sand model (Dvorkin and Nur, 1996) and DEM.

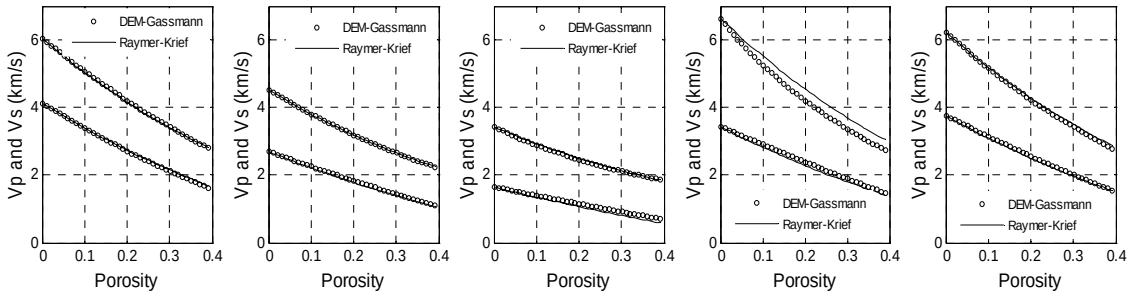

Figure 3.3. Velocity versus porosity for the five mineralogies examined in Figure 3.2. Solid curves are the same velocities as displayed in the first two rows of Figure 3.2. Symbols are the DEM/Gassmann predictions for a constant AR = 0.13. In the frames where the solid curves are not apparent, they are overshadowed by the symbols.

3.4 DEM and laboratory data

Consider next a laboratory dry-velocity data set that includes over 60 siliciclastic samples with a wide range of porosity and clay content (Han, 1986). By using the same technique as in the previous section for the Raymer/Krief velocity equations, we find the AR that makes DEM/Gassmann match the data. In this case, we use the room-dry data and then apply Gassmann's equation to obtain the velocity corresponding to water-saturated samples (low frequency velocities). Once again, we observe that the AR fall within a narrow range with an average value of 0.13 approximately (Figure 3.4).

Figure 3.4 shows data for chalk samples from Fabricius' et al. (2008) from four formations in the Danish central North Sea sector. As in the previous examples, we use data with subsequent water substitution. In this case, the DEM/Gassmann AR are approximately in the same interval as for Han's (1986) data, although the mineralogy and porosity ranges are different.

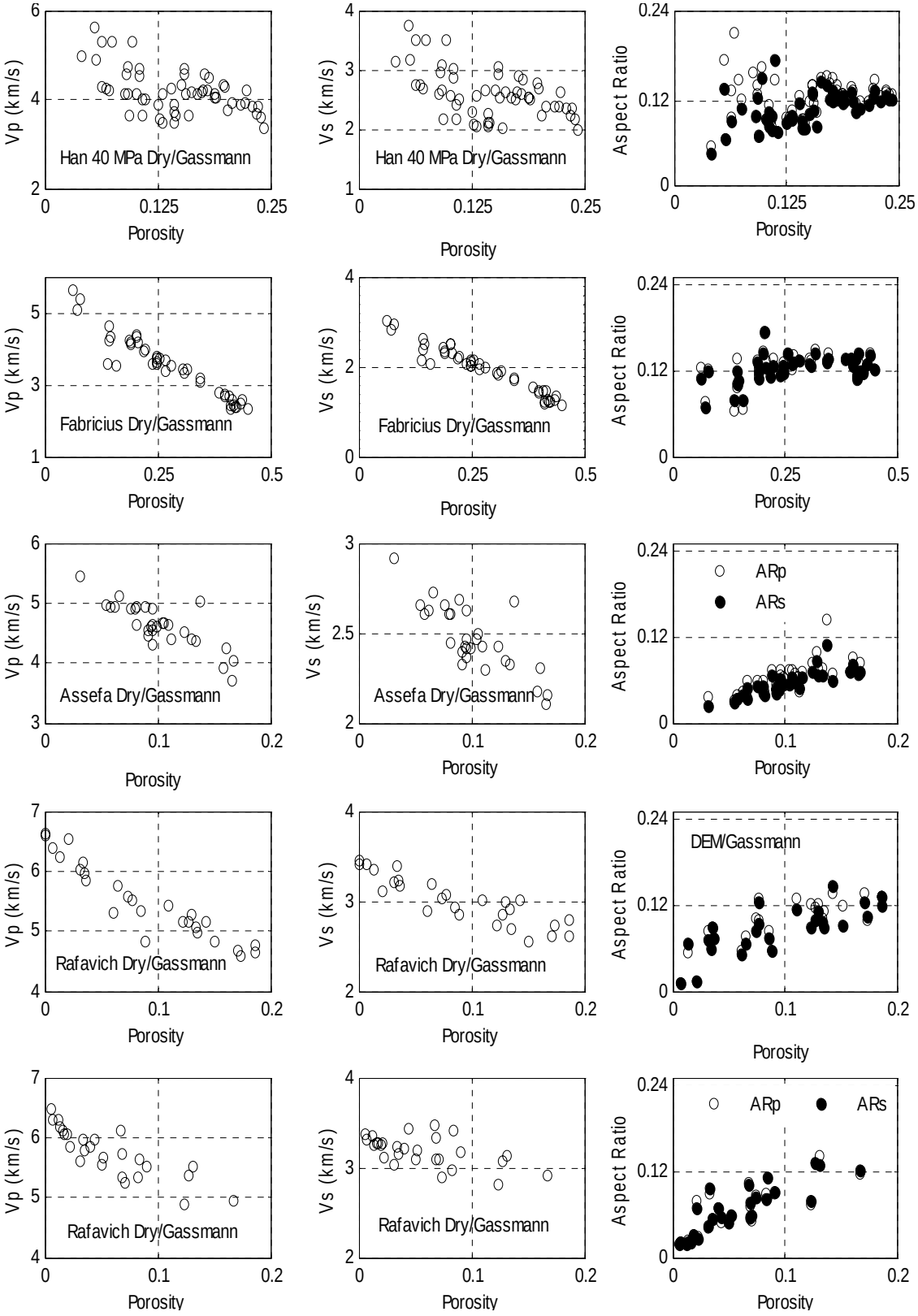
Vp (km/s)
Vs (km/s)
Aspect Ratio
Porosity
Han 40 MPa Dry/Gassmann
Fabricius Dry/Gassmann
Assefa Dry/Gassmann
Rafavich Dry/Gassmann
DEM/Gassmann
ARp
ARs

Figure 3.4. *P*- (left), *S*-wave (middle) velocity and AR (right) for both *P*- (open symbols) and *S*-wave (filled symbols) versus porosity. The AR are obtained by matching these data by DEM/Gassmann. From top to bottom. First row: velocities at 40 MPa confining pressure, after Han (1986). Second row: velocities at 7.5 MPa confining pressure, after Fabricius et al. (2008). Third row: velocities at 50 MPa confining pressure, after Assefa et al. (2003). Fourth and fifth rows: velocities at 40 MPa confining pressure, after Rafavich et al. (1984). These velocities are calculated from the room-dry experimental data using Gassmann's (1951) fluid substitution. The fluid is pure water with density 1.0 g/cm^3 and velocity 1.5 km/s.

This fact suggests an approximate AR universality of about 0.13 for varying mineralogy and porosity. This universality is likely to be related to the texture of the rocks under examination. However, because we have simply fit real data with an idealized mathematical model, we should not over-interpret the meaning of this universality. Rather, we concentrate on its practical use.

Figure 3.4 also displays data from Assefa et al. (2003) for pure carbonates. As in the previous examples, we use room-dry data with subsequent water substitution. In this case, the DEM/Gassmann AR are smaller than in the previous examples. Still, they are contained within a narrow interval.

Consider next two laboratory data sets from Rafavich et al. (1984). These data sets are based on cores extracted from two different wells. The room-dry measurements were conducted at in situ pressure conditions (about 40 MPa). The data displayed in Figure 3.5 are essentially carbonate (dolomite and calcite). We use these room-dry data with subsequent water substitution. Once again, we observe that the DEM/Gassmann AR fall within a narrow interval with 0.13 approximately in the middle (Figure 3.5).

As a second exercise, we use the same methodology but for experimental wet velocity data on full saturated rock samples. In this case, we find the AR that makes DEM match the velocity data at full saturation condition (high frequency velocities). In this case we consider two laboratory data sets. The first data set is from Kenter et al. (1997). These samples are of mixed carbonate/siliciclastic mineralogy. Because of the presence of carbonate (see Figure 3.2 for the pure calcite case), the DEM/Gassmann AR span a wider range than in the previous example (Figure 3.5).

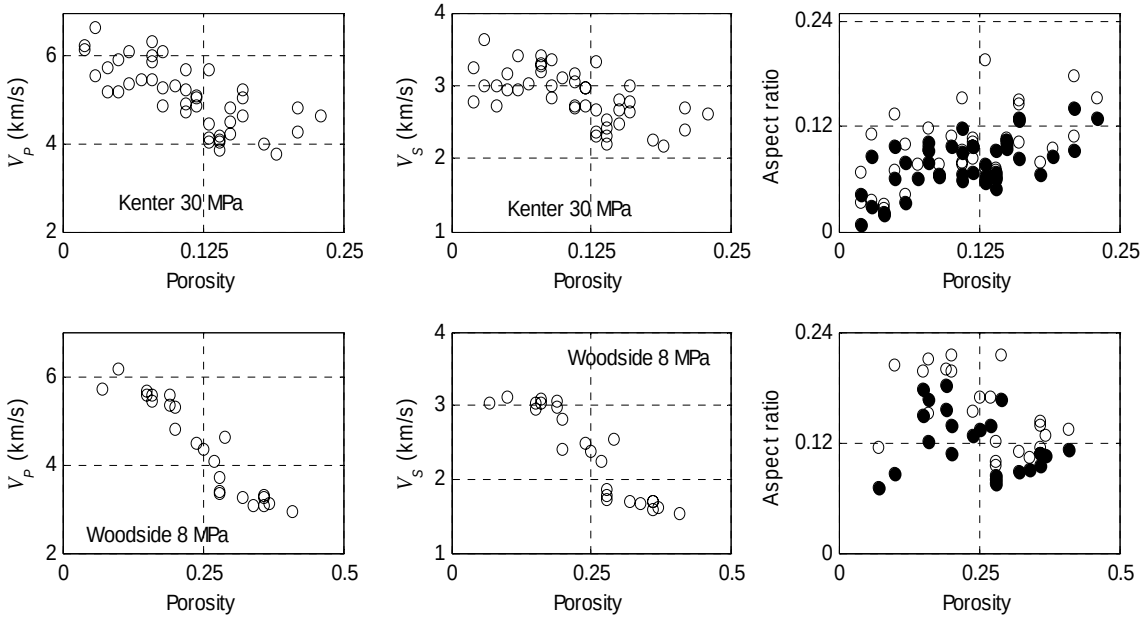

Figure 3.5. *P*- (left), *S*-wave (middle) wet-velocity and AR (right) for both *P*- (open symbols) and *S*-wave (filled symbols) versus porosity. The AR are obtained by matching these wet velocity data by DEM. Top: velocities at 40 MPa confining pressure, after Kenter et al. (1997). Bottom: velocities at 7.5 MPa confining pressure, after Woodside et al. (1998).

The second data set is for wet carbonates, according to Woodside et al. (1998). They measured ultrasonic velocities, densities, and porosities at in situ pressures in 68 plugs taken from the cores recovered at Ocean Drilling Project Sites 966 and 967. The AR results (Figure 3.5) are similar to those obtained for data from Kenter et al. (1997).

Both Rafavich (1984) and Assefa et al. (2003) visually measured the average pore size (longest and shortest pore diameter) on resin-impregnated polished thin sections. The aspect ratios were measured only on pores that were large enough (> 20μm) to be seen through an optical microscope. This analysis was performed mainly for the grainstone and packstone subsets of these data. The aspect ratios of the small pores, which constituted up to 10% of the total pore volume, were not measured (Assefa et al., 2003). The AR reported by Rafavich (1984) span an interval of 0.4-1.0. The aspect ratios reported by Assefa et al. (2003) are all about 0.25. These AR are much larger than those predicted by our DEM/Gassmann method.

This disparity emphasizes the fact that AR obtained from a mathematical model will

often differ from those in real rock (even if we assume that pores in real rock can be treated as ideal shapes). Indeed, no mathematical model can perfectly mimic real rock. Therefore, it can be erroneous to derive real pore-space geometry from idealized models. Nevertheless, a model can be useful and predictive, as we will show in the following sections.

3.5 Applications

In this section, we show the power of prediction of the approach presented in the above section. The methodology can be used to predict V_s from V_p, high and low frequency estimations of elastic moduli; wet elastic properties from dry properties; estimation of attenuation; and empirical constrains on elastic properties.

3.5.1 Vs Prediction

The methodology, when dry velocity data is available (Figure 3.4), is to (a) obtain the aspect ratio for each V_p data point by matching it with DEM/Gassmann and (b) use DEM/Gassmann with the same aspect ratio to calculate V_s for the same data point. These aspect ratios are then used to determine the dry bulk and shear moduli, K_{dry} and G, respectively. The methodology, when wet velocity data is available (Figure 3.5), is to (a) obtain the aspect ratio for each V_p data point by matching it with DEM alone and (b) use DEM with the same aspect ratio to calculate V_s for the same data point. These aspect ratios are then used to determine the wet-bulk and shear moduli, K_{sat} and G, respectively.

The results for Han's (1986) data are displayed in Figure 3.6. Here the dry elastic moduli and V_s are predicted with a high degree of accuracy. Similar accuracy is achieved for data from Fabricius et al. (2008) and Rafavich et al. (1984) (Figures 3.7). For the data from Assefa et al. (2003), we over-predict the measured V_s if we directly use the AR derived from the V_p (Figures 3.7). We have found an *ad hoc* correction for pure carbonate cases: when predicting V_s, use the AR derived from V_p and multiply it by 0.85.

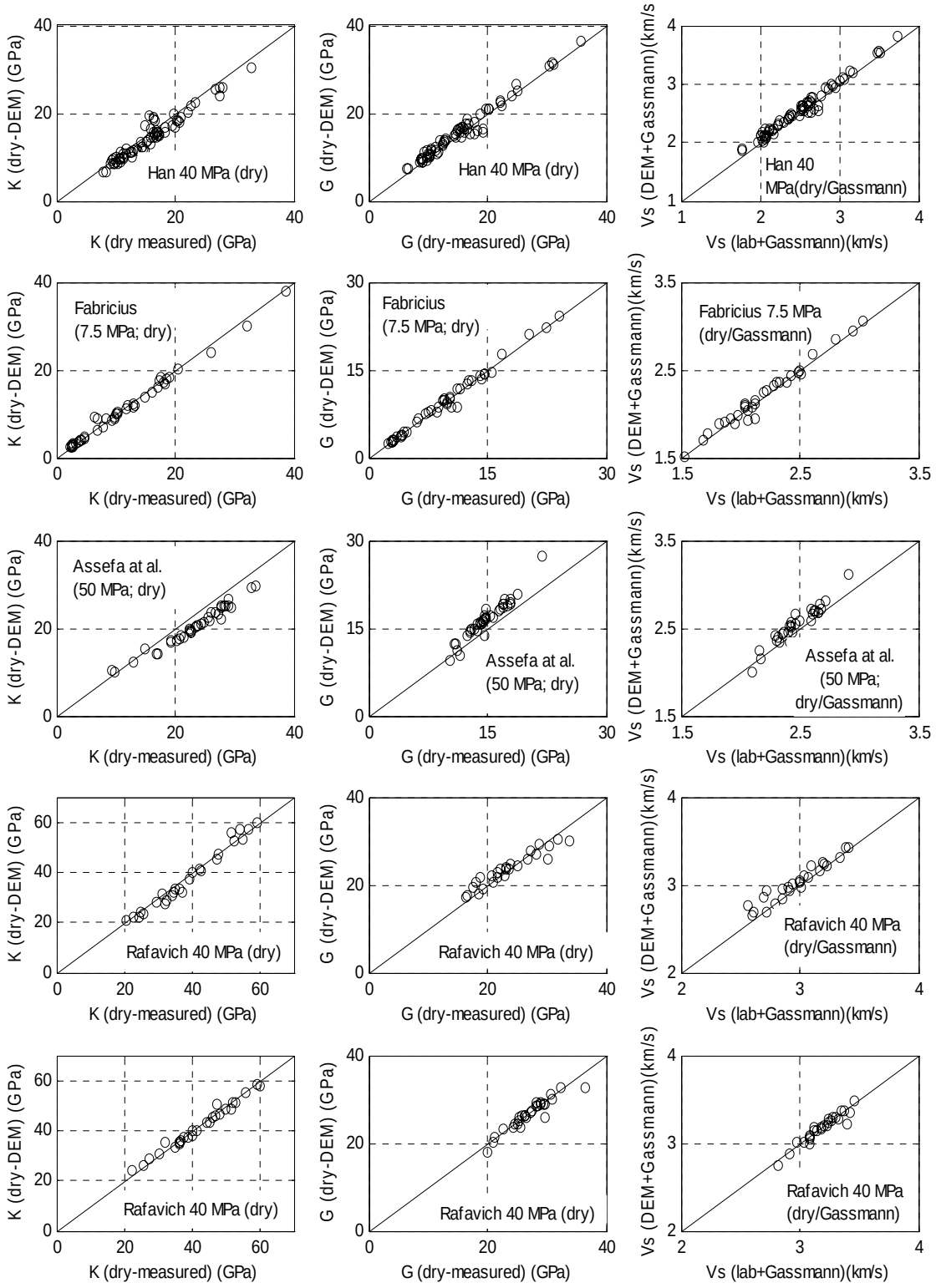
K (dry-DEM) (GPa)
K (dry measured) (GPa)
Han 40 MPa (dry)
G (dry-DEM) (GPa)
G (dry-measured) (GPa)
Han 40 MPa (dry)
Vs (DEM+Gassmann)(km/s
Vs (lab+Gassmann)(km/s)
Han 40
MPa(dry/Gassmann)
Fabricius
(7.5 MPa; dry)
Fabricius 7.5 MPa
(dry/Gassmann)
Assefa at al.
(50 MPa; dry)
Assefa at al.
(50 MPa;
dry/Gassmann)
Rafavich 40 MPa (dry)
Rafavich 40 MPa
(dry/Gassmann)

Figure 3.6. Dry bulk (left) and shear (middle) moduli and V_s prediction (right). From top to bottom. First row: for Han's (1986) data. Second row: for Fabricius' et al. (2008) data. Third row: for Assefa's et al. (2003) data. Fourth and fifth rows: for Rafavich's et al. (1984) data. These velocities are calculated from the room-dry experimental data using Gassmann's (1951) fluid substitution.

For the data from Kenter et al. (1997) the wet elastic moduli and the resulting V_s appears accurate (Figures 3.7).

Figure 3.8 shows the single aspect ratio distribution from all porosities for Han's (1986) data and for all carbonate data sets from Figures 3.4 and 3.5.

The next two examples are from well log data from a Venezuelan oil field and the ODP. Our V_s prediction methodology works well for the Venezuelan well, which is mostly siliciclastic (Figure 3.9-3.10). However, V_s is over-predicted in the ODP well (Figure 3.11-3.12) when we directly used the AR derived from V_p. Our ad hoc correction (the multiplication of the V_p-derived AR by 0.85) produces an accurate V_s prediction in this carbonate well.

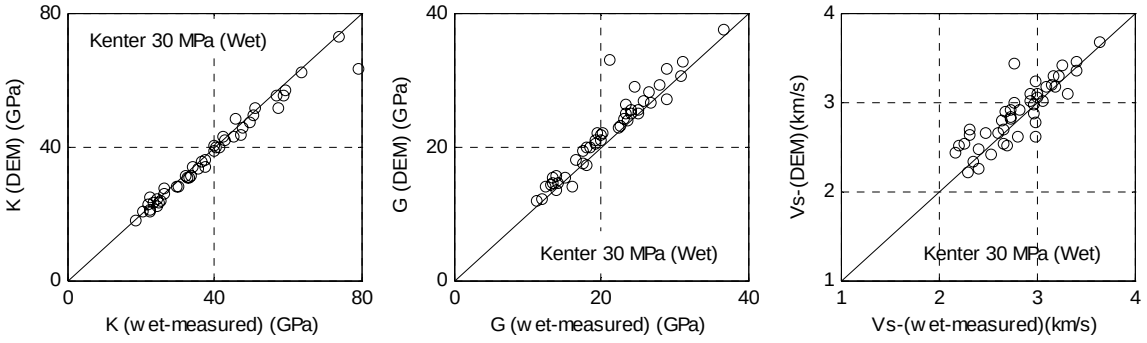

Figure 3.7. Wet bulk (left) and shear (middle) moduli and Vs prediction (right), for Kenter's et al. (1997) data.

Figure 3.10 shows the decimal logarithm of aspect ratios derived from V_p and the log-normal distribution of aspect ratios. The mean of the log-aspect ratio is -1.8742 and the standard deviation 0.6789. The mean and standard deviation of the original aspect ratio data are: 0.1925 and 0.1367, respectively. Figure 3.12 shows the distribution of aspect ratios for all porosities for the ODP well displayed in Figure 3.11. The mean of the aspect ratios is 0.1262 and the standard deviation is 0.0449.

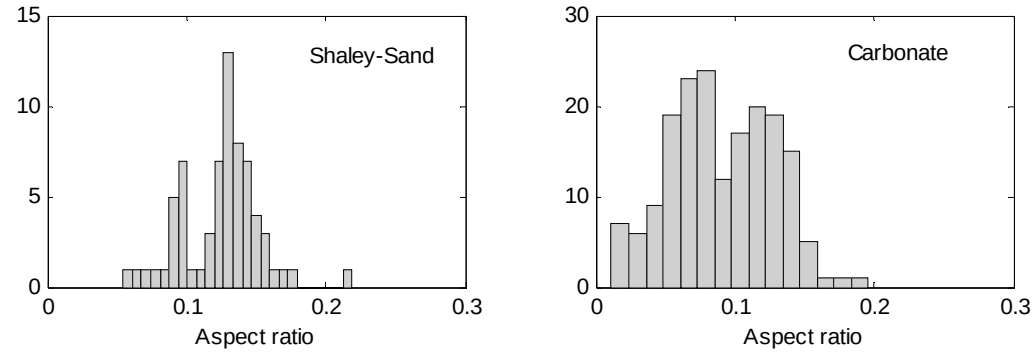

Figure 3.8. Aspect ratio distribution from all porosities for Han's (1986) data (left) and for all carbonate data sets from Figures 3.4 and 3.5 (right).

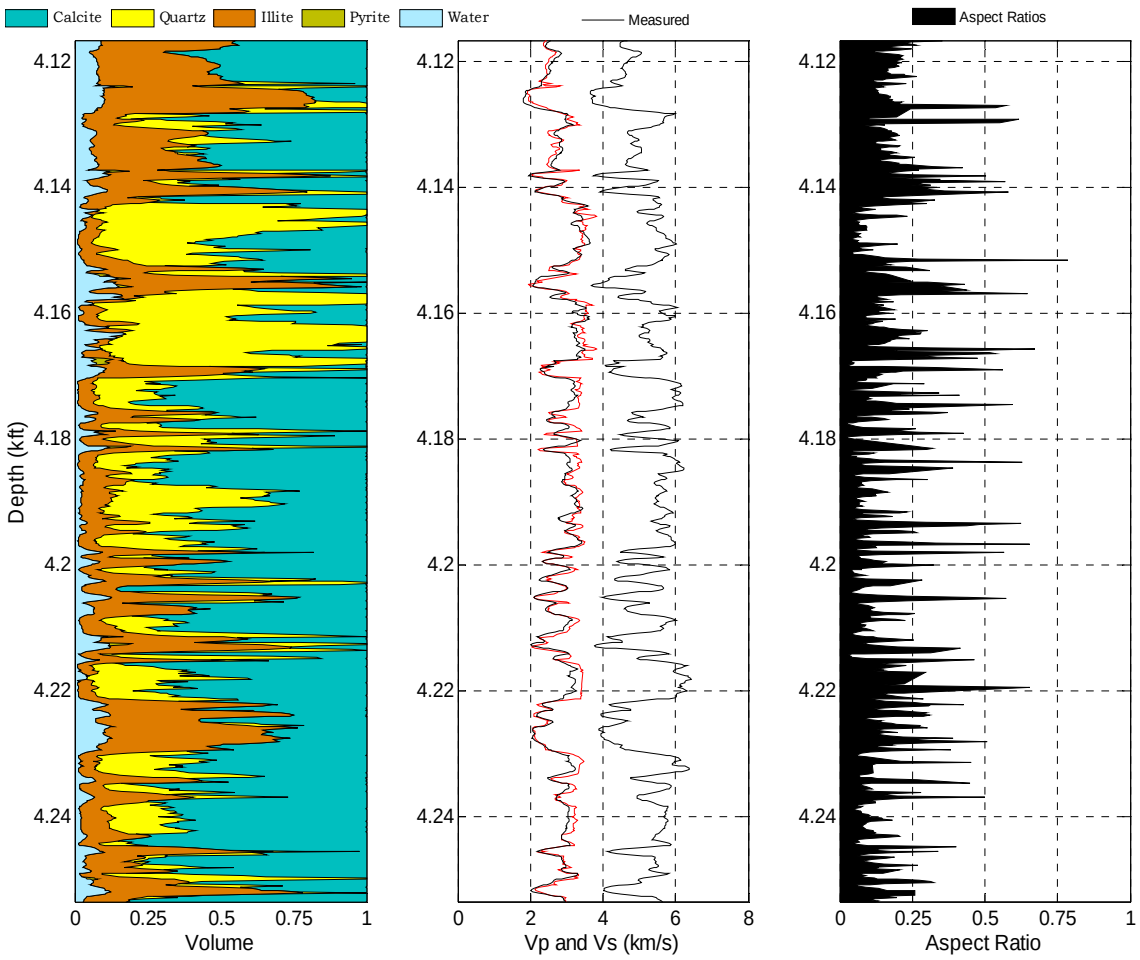

Figure 3.9. V_s prediction for the Venezuelan well. From left to right: mineralogy and porosity; measured (black) and predicted (red) V_s; AR derived from V_p using DEM/Gassmann.

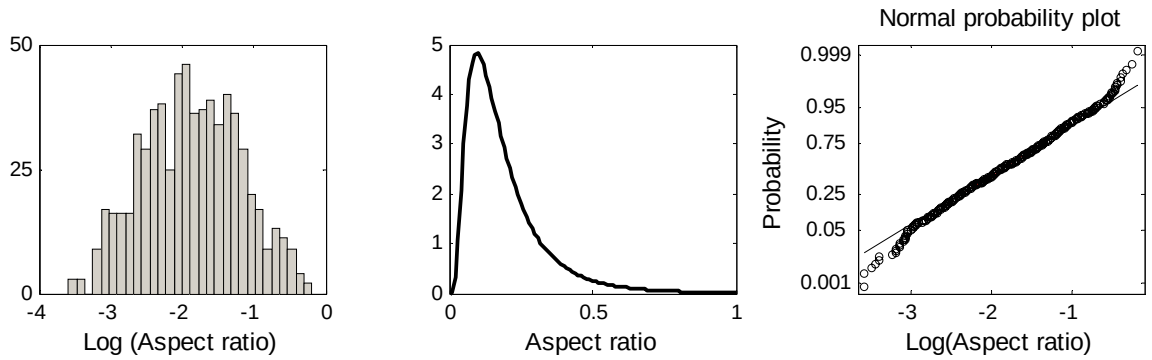

Figure 3.10. Left: Decimal logarithm of aspect ratios derived from V_p. Middle: Log-normal distribution of aspect ratios. Right: Normal probability plot of Log-aspect ratios.

3.5.2 Velocity-frequency dispersion and attenuation

Velocity-frequency dispersion was discovered decades ago when it manifested itself as a disparity between the velocity measured on wet samples at a very high frequency, f_H (on the order of 1 MHz) and at low frequency, f_L, calculated from dry-rock data using Gassmann's (1951) fluid substitution (e.g., Mavko and Jizba, 1991). The velocity measured at low frequency is usually smaller than that measured at high frequency because at high frequency (Winkler, 1986; O'Connell and Budiansky, 1977), the liquid in the pores is unrelaxed and resists the wave-induced deformation essentially as an elastic body.

DEM offers a simple recipe to calculate this difference in velocity. For example, to predict the velocity at high frequency from that measured at low frequency, we (a) obtain an AR for each V_p and V_s data point (separately for V_p and V_s) by matching it with DEM/Gassmann and (b) use DEM with these AR and with the liquid in the pores treated as an elastic body to calculate the high-frequency V_p and V_s for the same data point. Conversely, to predict the low-frequency velocity from high-frequency data, we (a) obtain the AR for each V_p and V_s data point (separately for V_p and V_s) by matching it with DEM which treats the liquid in the inclusions as an elastic body and (b) use DEM/Gassmann with the same AR to obtain the low-frequency V_p and V_s.

Here we show just one example of this transformation. In Figure 3.13 we display data from Coyner (1984), with the velocity measured on both room-dry and water-

saturated samples of Navajo sandstone. We predict the high-frequency velocity using the room-dry data.

In Figure 3.14 we show how low-frequency velocity can be obtained from ultrasonic wet velocity for the same data. In both cases (Figures 3.13 and 3.14) our predictions are close to the measurements.

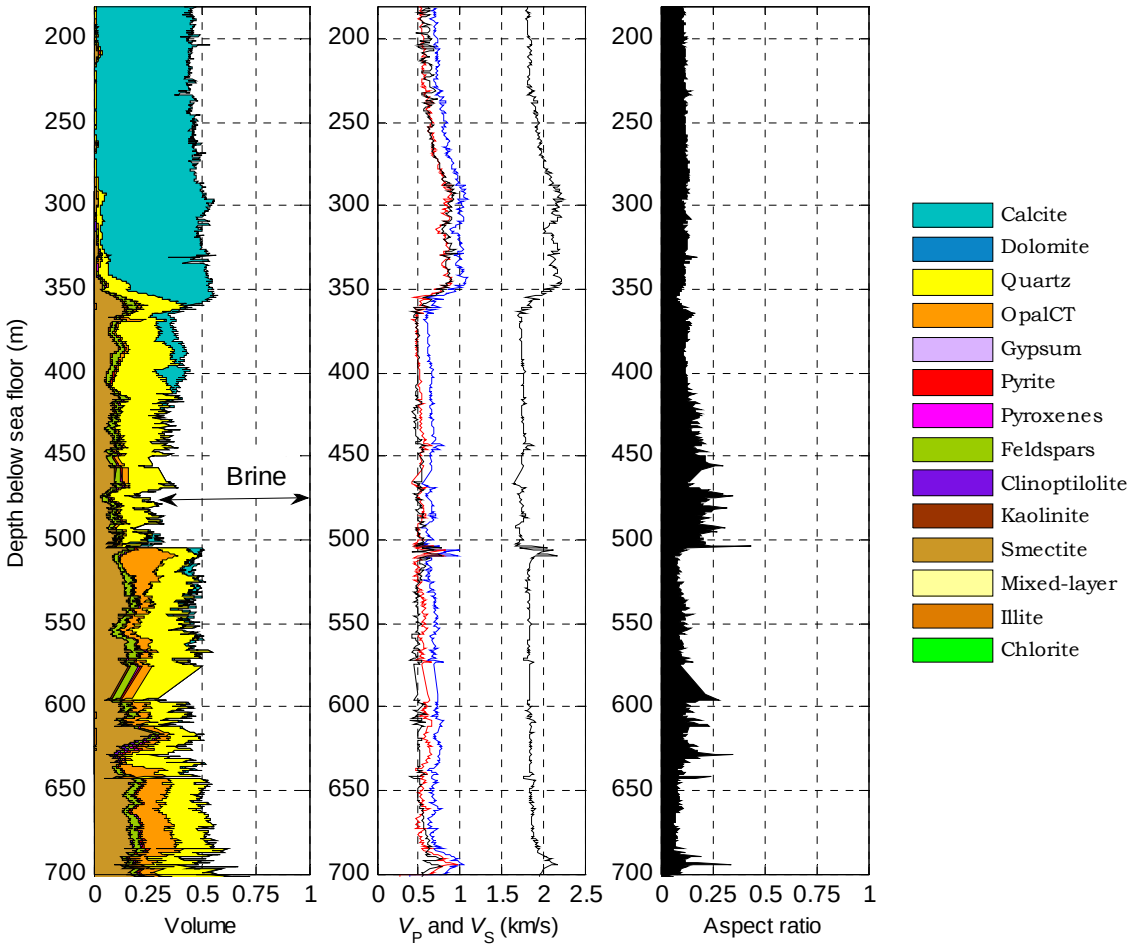

Figure 3.11. V_s prediction for the ODP (site 1172) well. The blue V_s curve is the prediction using directly the AR derived from V_p. The red V_s curve is prediction using the V_p-derived AR multiplied by 0.85.

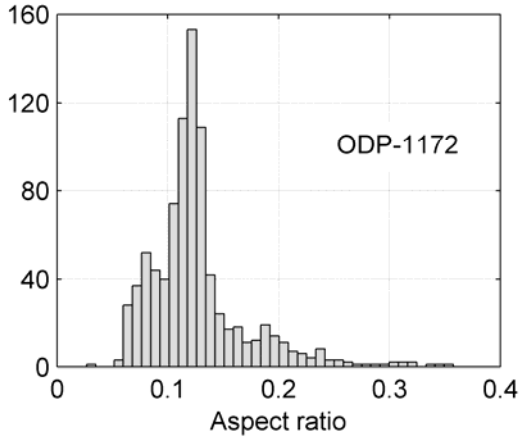

Figure 3.12. Distribution of aspect ratios for all porosities for the ODP well displayed in Figure 3.11.

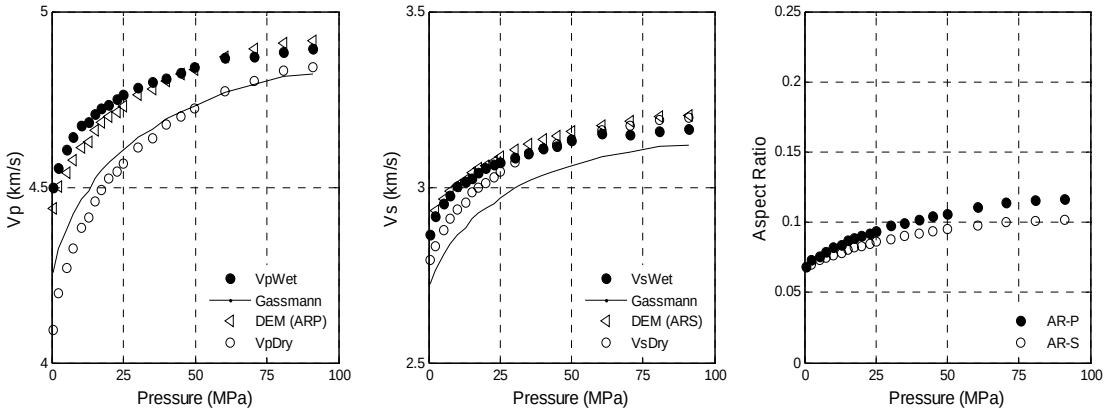

Figure 3.13. Left: V_p versus confining pressure; open circles are for room-dry ultrasonic data; filled circles are for wet ultrasonic data; the continuous curve is for low-frequency wet sample obtained by Gassmann's (1951) fluid substitution on the room-dry data; and triangles are for high-frequency velocity predicted from room-dry data using the DEM methodology as described in the text. Middle: same for Vs. Right: AR predicted using DEM on the room-dry data for V_p (filled circles) and V_s (open circles). The triangles displayed in the left frame are obtained using the V_p AR.

In Figure 3.15 we compare our predictions with the high-frequency predictions of Biot (1956a, b), the low frequency predictions of Gassmann (1951), and the high-frequency predictions of Mavko and Jizba (1991). Figure 3.15 also shows the porosity

and soft-porosity (the part of porosity with low aspect ratios) as a function of differential pressure. At low stress, Biot and Gassmann underestimate the data. Mavko-Jizba prediction is in mostly good agreement except for stresses lower than 20 MPa where it overestimates the saturated data by 3 percent (Mavko and Jizba, 1991). Similarly, our model predictions for V_s are in better agreement with the saturated data than the Biot and Gassmann predictions. Our methodology is complementary to the Mavko-Jizba method which is relatively independent of assumptions about idealized pore geometries and pore aspect ratios.

It is important to emphasize that our goal here is not to predict the pressure-dependency of V_p and V_s at low and high frequencies, but to predict velocities at fixed pressure. To achieve this goal, we adjust the AR so that the theory fits the velocity measurements at fixed pressure. The computed AR increase with the increasing pressure simply because the rock becomes stiffer (Figure 3.13).

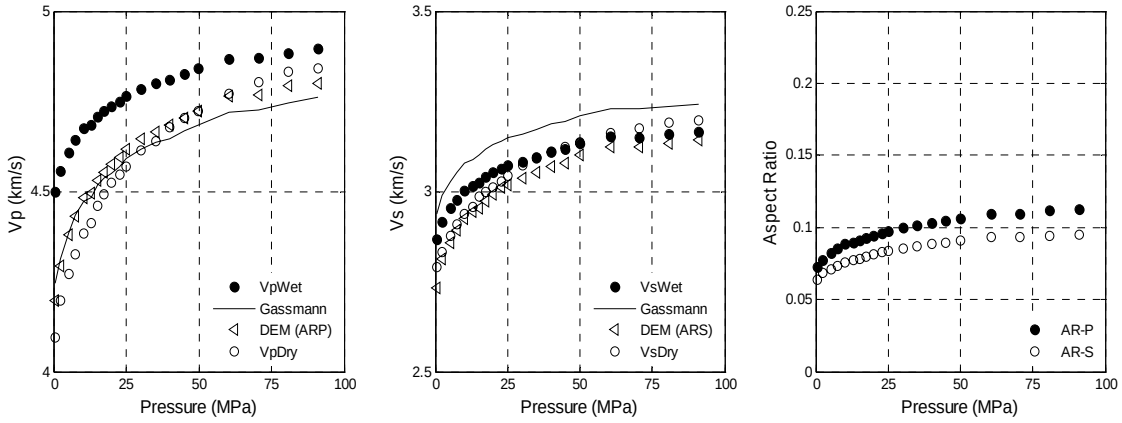

Figure 3.14. Left: V_p versus confining pressure; open circles are for room-dry ultrasonic data; filled circles are for wet ultrasonic data; the continuous line is for dry-rock velocity obtained from the ultrasonic data using Gassmann's (1951) fluid substitution from wet to dry (which is erroneous in this context because the wet-rock data come from ultrasonic measurements); and triangles are prediction for room-dry velocity using our methodology. Middle: same for V_s. Right: AR predicted using DEM on the ultrasonic data for V_p (filled circles) and Vs (open circles). The triangles and crosses displayed in the left frame are obtained using the V_p AR.

In a viscoelastic body, causality requires a very specific relation (e.g., Mavko et al., 2009; Dvorkin et al., 2003; Dvorkin and Uden, 2004) between attenuation (the inverse quality factor Q^{-1}) and velocity-frequency (and modulus-frequency) dispersion. It is the Kramers-Kronig equation, which, for a standard linear solid, gives the maximum Q_{Max}^{-1} as

$$Q_{Max}^{-1} = \frac{1}{2}\frac{V_{pH} - V_{pL}}{\sqrt{V_{pH}V_{pL}}}, \tag{3.1}$$

where V_{pH} is the *P*-wave velocity at very high frequency; and V_{pL} is the *P*-wave velocity at very low frequency.

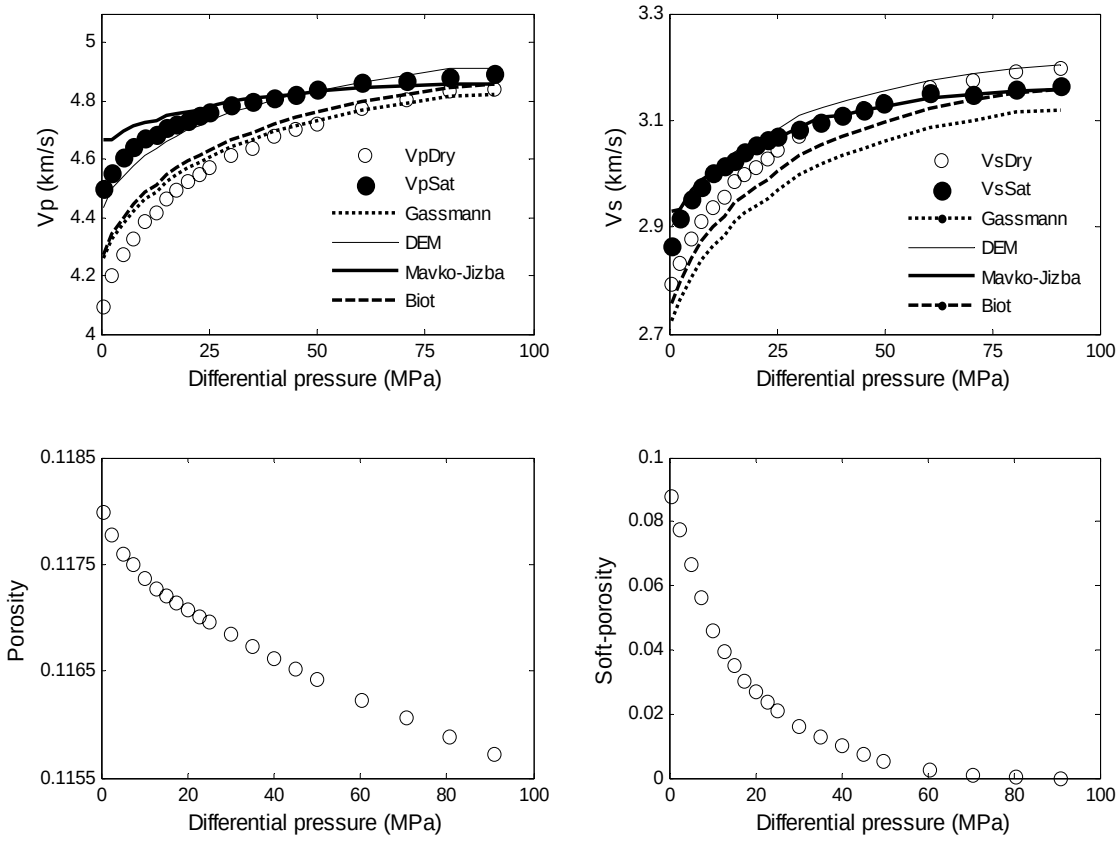

Figure 3.15. Comparison of our velocity predictions using DEM with the high-frequency predictions of Biot (1956a, b), the low frequency predictions of Gassmann (1951), and the high-frequency predictions of Mavko and Jizba (1991).

The technique discussed earlier in this section allows us to find V_{pH} from V_{pL}, the latter typically available from well data, if it is assumed to represent the low-frequency range of measurement. Dvorkin and Mavko (2006) show examples of this application. The measured V_{pL} and predicted V_{pH} and the resulting Q^{-1} according to equation 1 are shown in Figure 3.16. The estimated inverse quality factor is about 0.1, which appears to be reasonable for this soft wet formation (Bowles, 1997; Goldberg et al., 1991).

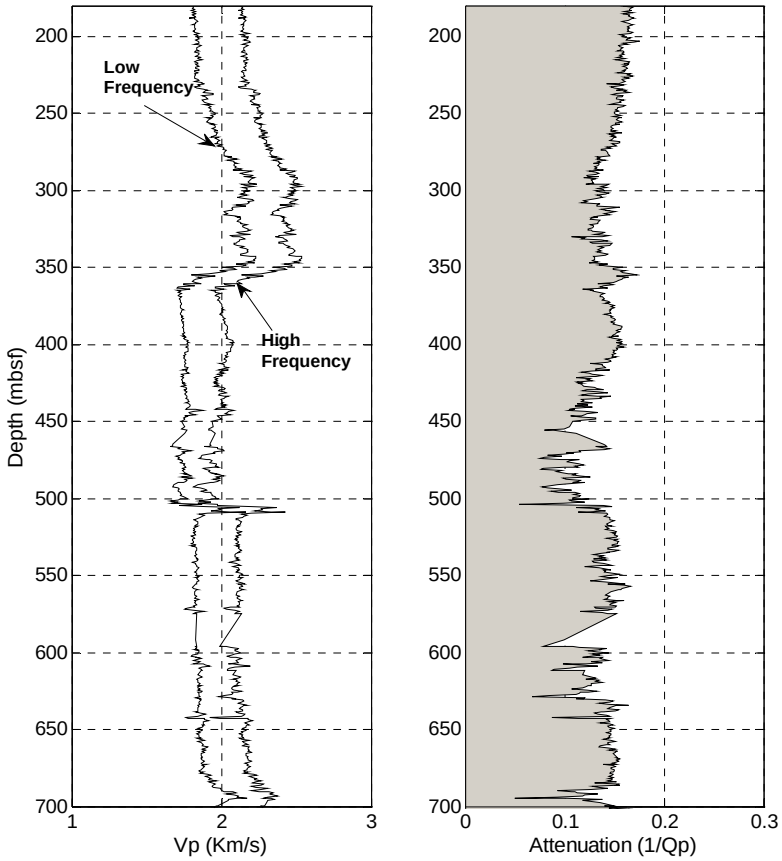

Figure 3.16. Left: measured V_p and predicted high-frequency V_p for the ODP Site 1172. Right: resulting inverse *P*-wave quality factor.

Notice that for the determination of Q_{Max}^{-1}, using the standard linear solid model (Equation 3.1), we do not need to predict velocities at all frequencies, only at high and low-frequency limits. DEM assumes that saturated inclusions are isolated with respect to flow; thus, it simulates high-frequency saturated-rock behavior that may be appropriate to

ultrasonic frequency ~1 MHz. Here, high-frequency refers to fluid-related effects, yet, because DEM is an effective-medium model, the wavelengths are still much longer than any scale of grains or pores (Budiansky, 1965; Wu, 1966; O'Connell and Budiansky, 1974; Berryman, 1980; Ruiz and Dvorkin, 2009). At low-frequency when there is time for wave-induced pore pressure increments to flow and equilibrate (Mavko et al., 2009; Boutéca and Guéguen, 1999), we find the effective moduli for rock with dry inclusions and then theoretically saturate the rock by using Gassmann's fluid substitution. In the application of this theory to well-log data, we assume that (arguably) these data fall into the low-frequency range.

Finally, for velocity and attenuation predictions at all frequencies (Dvorkin et al., 1995), a model with a spectrum of aspect ratios, instead of a single aspect ratio, is a better analog of rock porosity and pore shapes (Hudson et al., 1996; Chapman et al., 2002, Jakobsen et al., 2003b; Jakobsen and Johansen, 2005); however this calculation is beyond the scope of this study.

3.5.3 Empirical Constraints for Velocity

Rigorous elastic bounds for velocity, such as are provided by Hashin and Shtrikman (1963), are typically far apart for a porous rock. This fact limits the practical use of these bounds to estimate velocity from porosity and mineralogy.

Our recipe for constraining the velocity is as follows: (a) find the elastic moduli and density of the solid (mineral) phase by using, e.g., Hill's (1952) average; (b) compute the lower constraints for V_p and V_s from DEM/Gassmann using AR = 0.03; and (c) compute the upper constraints using AR = 0.30.

If we deal with ultrasonic data obtained on wet samples, DEM/Gassmann may be replaced by pure DEM where the pore fluid is treated as an elastic inclusion. Figure 3.17 shows an example of these constraints for the Kenter et al. (1997) ultrasonic wet-rock data. The DEM-derived constraints are much tighter than Hashin-Shtrikman (1963) bounds, especially for V_s. Of course, AR = 0.03 and AR = 0.30 have been selected ad-hoc. These values may be different for different data sets. Our recommendation is to establish the optimal range of AR on a typical test subset and then use it for the same type

of rock on a wider basis.

An example of such approach is given in Figure 3.18, where we used AR = 0.1 and 0.3 to constrain the velocity in a tight-sand well. As we see, the DEM-based constraints are much tighter than the Hashin-Shtrikman (1963) bounds.

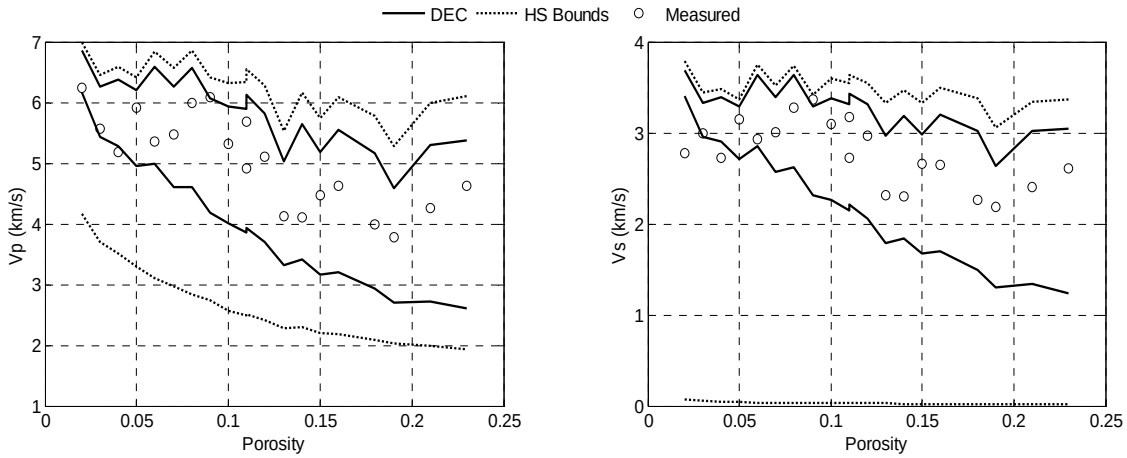

Figure 3.17. The Hashin-Shtrikman (1963) bounds (dotted curves) and DEM-based constraints (solid curves) for the Kenter et al. (1997) data (open symbols). Left: V_p; right: V_s.

3.6 Discussion

We show here that if treated and interpreted properly, an idealized elastic model, such as DEM, can be practically predictive in real rock, without over-generalizing its meaning and utility. The latter is critical in such applications. Indeed, we are attempting to match the overwhelming complexity of rock behavior with a single AR (or a single range of AR). When doing so, we need to stress that any generalization has to be based on meaningful examples, such as shown above. Overextending these results may be erroneous.

Consider, for example a data set by Verwer et al. (2008), consisting of dolomite/calcite samples. As we see, DEM, applied to ultrasonic wet-rock data, predicts AR as high as 0.4 and even approaching 1.0 in these samples (Figure 3.19). These values are much higher than 0.13 which is the value almost universally used in our analysis. This simply means that we always have to tread cautiously when applying mathematical models to real data. Such models may be relevant and useful for a certain type of rock

but completely invalid for another type of sediment. Figure 3.19 shows that although the AR range in the Verwer et al. (2008) data is quite different from that used in most examples here, it can still be successfully used to predict V_s from V_p.

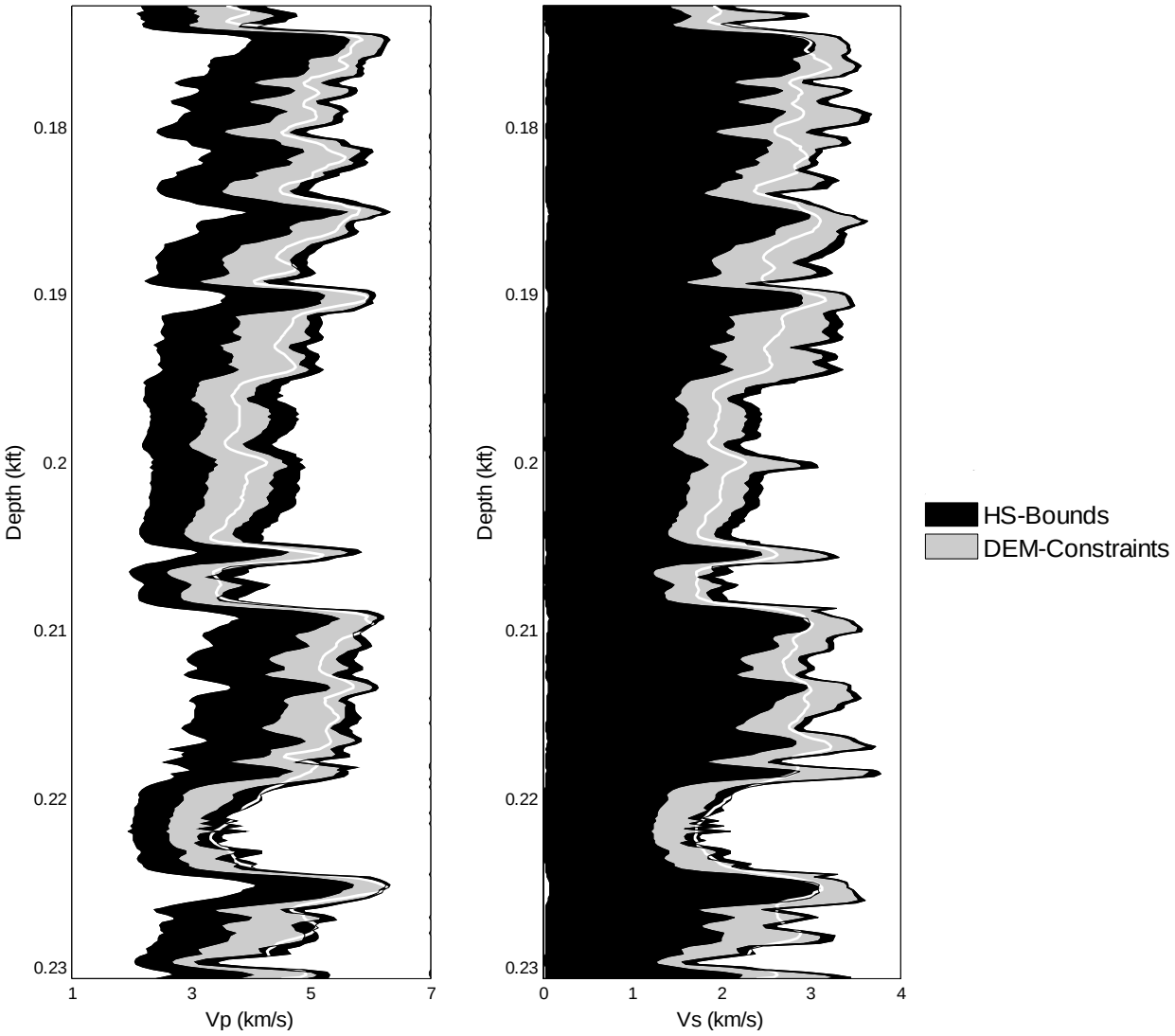

Figure 3.18. The Hashin-Shrikman (1963) and DEM-based constraints for V_p (left) and V_s (right) in a Venezuelan well (the same well as displayed in Figure 3.9). The AR range used in the DEM constraints was between 0.10 and 0.30. The white curve is the measured velocity.

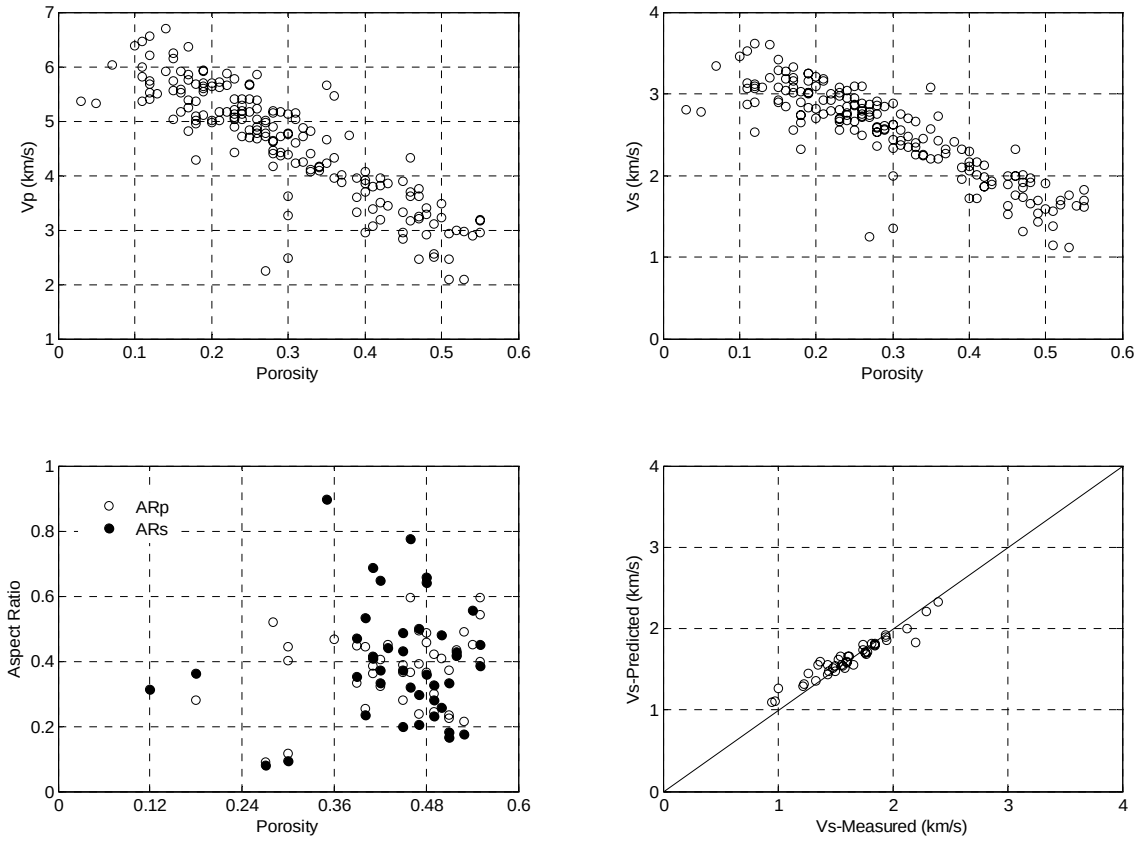

Figure 3.19. Top: V_p and V_s versus porosity (Data from: Verwer et al., 2008). Bottom-left: AR DEM-predicted from V_p and V_s. Bottom-right: V_s predicted from V_p using these AR.

Figure 3.20 shows that rock is not made of ideally shaped inclusions. The main point of this work is that certain effective-medium inclusion models can mimic the elastic properties of real rock if an appropriate aspect ratio is assigned to this model. Our goal is to make the use of a selected model reasonably general, rather than insist that the geometry of the model is the same as of real rock. Moreover, the aspect ratio is nothing more than a fitting parameter within the realm of a selected model.

For rocks with the same solid and fluid constituents, different effective medium models produce different results (Appendix B). Thus, the interpretation of rock pore aspect ratios may not be unique. The rock microstructure has a strong effect on its elastic properties. Thus, it is not appropriate to select which effective-medium model is the "best" for determining the elastic properties of all rock types. If our goal is to model a

specific rock type, it is preferable to pick the theory whose assumptions about microstructure match those of the rock modeled (Berge et al., 1995).

In general, rocks have cracks, cemented and non-cemented grains, cavities, different pore shapes, and different degrees of connectivity. In consequence, their effective elastic properties are the result of the combined effect of all these possible microstructural elements. The idea of the equivalent elastic model is not to choose a single model that best fits the microstructure; it is to use only one inclusion model with a single AR as a fitting parameter for all rock types. It can be argued that the principle advocated here can be used with any effective-medium model. The main point is that certain effective-medium inclusion models can mimic the elastic properties of real rock, if an appropriate aspect ratio is assigned to the model. Our goal is to make the use of a selected model reasonably general, rather than insist that the geometry of the model is the same as of real rock. Moreover, the aspect ratio is nothing more than a fitting parameter within the realm of a selected model.

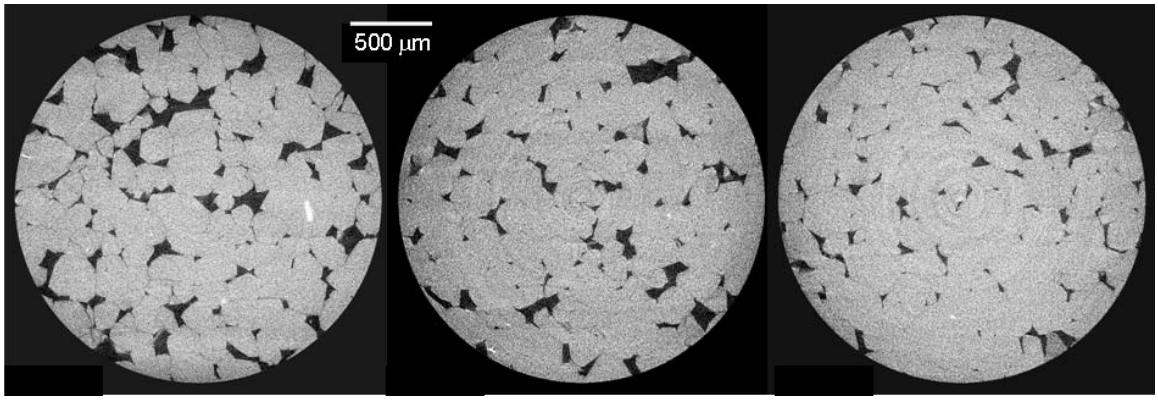

Figures 3.20. 2D slices of a 3D CT scan of Fontainebleau sandstone. As we can see, there are no ideal inclusions here. Speculating that we do see AR = 0.13 does not make sense. These pictures, once again, emphasize our main point: rock is not made of idealized inclusions; such inclusions can be assumed in a selected model to match elastic data. If a more-or-less constant AR can be used for a wide range of rock types, this model becomes predictive.

An additional comment is that our method does provide the maximum attenuation value rather than attenuation at all frequencies. This means that discretion has to be used when directly comparing our theoretical prediction with measured attenuation from well and/or seismic data. Nevertheless, given the very questionable accuracy of the latter, we

recommend using our theoretical estimate (as an estimate rather than definite answer).

3.7 Conclusions

We show that given a rock with known porosity and mineralogy and a complex microstructure, an idealized effective-medium model can represent the elastic properties with a narrow range of the aspect ratios. This inclusion aspect ratio range required for the differential effective-medium model to match measured velocity is narrow for many data sets, including laboratory and well data. We show a number of practical applications of this finding and caution against overextending the range of its applications without verifying and calibrating the model against a representative data set.

3.8 References

Ament, W. S., 1953, Sound propagation in gross mixtures: Journal of the Acoustical Society of America, 25, 638-641.

Assefa, S., C., C. McCann, and J. Southcott, 2003, Velocities of compressional and shear waves in limestones: Geophysical Prospecting, 51, 1-13.

Boutéca, M., and Y. Guéguen, 1999, Mechanical properties of rocks: Pore pressure and scale effects: Oil and Gas Science and Technology, 54, 703–714.

Bowles, F., 1997, Observations on attenuation and shear-wave velocity in fine-grained, marine sediments: Journal of Acoustic Society of America, 101, 3385-3397.

Cheng, C.H., 1993, Crack models for a transversely anisotropic medium: Journal of Geophysical Research, 98, 675–684.

Cleary, M.P., I.-W, Chen, and S.-M, Lee, 1980, Self-consistent techniques for heterogeneous media: American Society Civil Engineer, Journal of the Engineering Mechanics Division, 106, 861–887.

Coyner, K., 1984, Effects of stress, pore pressure, and pore fluids on bulk strain, velocity, and permeability in rocks: PhD. thesis, Massachusetts Institute of Technology.

Dvorkin, J., G. Mavko, and A. Nur, 1995, Squirt flow in fully saturated rocks: Geophysics, 60, 97-107.

Dvorkin, J., N. Amos, R. Uden, and T. Taner, 2003, Rock physics of a gas hydrate reservoir: The Leading Edge: 22, 842-847.

Dvorkin, J., and R. Uden, 2004, Seismic wave attenuation in a methane hydrate reservoir: The Leading Edge, 23, 730-732.

Dvorkin, J., Nur, 1996, Elasticity of high-porosity sandstone: Theory for two North Sea Datasets: Geophysics, 61, 1363-1370.

Dvorkin, J., Prasad, M., 1999, Elasticity of marine sediments: Rock Physics modeling: Geophysical Research Letters, 26, 194-197.

Dvorkin, J., G. Mavko, 2006, Modeling attenuation in reservoir and nonreservoir rock: The Leading Edge, 25, 1781-1784.

Eshelby, J.D., 1957, The determination of the elastic field of an ellipsoidal inclusion, and related problems: in Proceedings of the Royal Society of London, A241, 376–396.

Fabricius, I., L. Gommesen, A. Krogsboll, and D. Olsen, 2008, Chalk porosity and sonic velocity versus burial depth: Influence of fluid pressure hydrocarbons and mineralogy: The American Association of Petroleum Geologists Bulletin, 92, 201-223.

Gal, D., Dvorkin, J., and Nur, A., 1998, A Physical Model for Porosity Reduction in Sandstones: Geophysics, 63, 454-459.

Gassmann, F., 1951, Über die elastizität poröser medien: Veirteljahrsschrift der Naturforschenden Gesellschaft in Zürich, 96, 1-23.

Goldberg, D., M. Badri, and W. Wepfer, 1991, Ultrasonic attenuation measurements in Gabbros from hole 735B, in Proceedings of the Ocean Drilling Program: Scientific Results, 118, 253-259.

Gurevich, B., A. Sadovnichaja, S. Lopatnikov, and S. Shapiro, 1998, Scattering of a compressional wave in a poroelastic medium by an ellipsoidal inclusion: Geophysics Journal International, 133, 91–103.

Graterol, J., F. Ruíz, and M. Aldana, 2004, Estudio de la estabilidad de hoyo y cálculo de la ventana de lodo de perforación a partir de evaluación geomecánica y petrofísica con registros de pozo (parte 2): 12th Bianual International Meeting, Sociedad Venezolana de Ingenieros Geofísicos (SOVG), Paper 062.

Han, D., 1986, Effects of porosity and clay content on acoustic properties of sandstones and unconsolidated sediments: Ph.D. thesis, Stanford University.

Hashin, Z., and S. Shtrikman, 1963, A variational approach to the elastic behavior of multiphase materials: Journal of the Mechanics and Physics of Solids, 11, 127-140.

Hill, R., 1952, The elastic behavior of crystalline aggregate, Proceedings of the Physics Society, London A, 65, 349-354.

Hudson, J., E. Liu, S. Crampin, 1996, The mechanical properties of materials with interconnected cracks and pores: Geophysics Journal International, 124, 105-112.

Jakobsen, M., J. Hudson, and T. Johansen, 2003a, T-matrix approach to shale acoustics. Geophysics Journal International, 154, 533-558.

Jakobsen, M., T. A. Johansena and C. McCann, 2003b, The acoustic signature of fluid flow in complex porous media: Journal of Applied Geophysics, 54 , 219– 246.

Jakobsen, M., and T. Johansen, 2005, The effects of drained and undrained loading on visco-elastic waves in rock-like composites: International Journal of Solids and Structures, 42, 1597-1611.

Kenter, J, F. Podladchikov, M. Reinders, S. Van der Gaast, B. Fouke, and M. Sonnenfeld, 1997, Parameters controlling sonic velocities in a mixed carbonate–siliciclastic

Permian shelf-margin (upper San Andres Formation, Last Chance Canyon, New Mexico): Geophysics, 62, 505-520.

Klimentos, T., 1995, Attenuation of *P*- and *S*-waves as a method of distinguishing gas and condensate from oil and water: Geophysics, 60, 447-458.

Krief, M., J. Garat, J. Stellingwerff, and J. Ventre, 1990, A petrophysical interpretation using the velocities of P and S waves (full-waveform sonic): The Log Analyst, 31, 355-369.

Kuster, G. T., and M. N. Toksoz, 1974, Velocity and attenuation of seismic waves in two-phase media: part 1. Theoretical formulations: Geophysics, 39, 587-606.

Mavko, G., and D. Jizba, 1991, Estimation grain-scale fluid effects on velocity dispersion in rocks: Geophysics, 56, 1940-1949.

Mavko, G., T. Mukerji, and J. Dvorkin, 2009, The rock physics handbook: Cambridge University Press.

Mindlin, R.D., 1949, Compliance of elastic bodies in contact: Trans. Transaction of the American Society of Mechanical Engineers, 71, A-259.

Norris, A. N., 1985, A differential scheme for the effective moduli of composites: Mechanics of Materials, 4, 1-16.

O'Connell, R.J., and B. Budiansky, 1974. Seismic velocities in dry and saturated cracked solids: Journal of Geophysical Research, 79, 4626–4627.

Prasad, M., Dvorkin, J., 2001, Velocity to porosity transforms in marine sediments: Petrophysics, 42, 429 – 437.

Rafavich, F., C. Kendall, and T. Todd, 1984, The relationship between properties and the petrographic character of carbonate rocks: Geophysics, 49, 1622-1636.

Raymer, L. L., E. R. Hunt, and J. S. Gardner, 1980, An improved sonic transit time-to-porosity transform: 21st Annual Logging Symposium Transaction, Society of Professional Well Log Analysts, Paper P.

Ruiz, F., and J. Dvorkin, 2009, Sediment with porous grains: Rock-physics model and application to marine carbonate and opal: Geophysics, 74, E1–E15.

Verwer, K., H. Braaksma, and J. Kenter, 2008, Acoustic properties of carbonates: Effects of rock texture and implications for fluid substitution: Geophysics, 73, B51-B65.

Winkler, K., 1986, Estimates of velocity dispersion between seismic and ultrasonic frequencies, Geophysics, **51**, 183-189.

Woodside, J., J. Kenter, and A. Köhnen, 1998, Acoustic properties from logs and discrete measurements (sites 966 and 967) on Eratosthenes Seamount: controls and ground truth, in Proceedings of the Ocean Drilling Program: Scientific Results, 160, 535-543.

Walsh, J. B., 1965, The effect of cracks on the compressibility of rock: Journal of Geophysical Research, 70, 381–389.

Wu, T. T., 1966, The effect of inclusion shape on the elastic moduli of a two-phase material: International Journal of Solids and Structures, 2, 1–8.

Xu, S., and R. White, 1995, A new velocity model for clay-sand mixtures: Geophysical Prospecting, 43, 91–118.

Zimmerman, R. W., 1984, The elastic moduli of a solid with spherical pores: New self-consistent method: International Journal of Rock Mechanics and Mining Sciences, Geomechanics Abstract, 21, 339–343.

Zimmerman, R. W., 1986, Compressibility of two-dimensional cavities of various shapes: Journal of Applied Mechanics, Transaction, American Society of Mechanical Engineers., 53, 500–504.

Zimmerman, R. W., 1991a, Compressibility of Sandstones: Elsevier, New York.

Zimmerman, R. W., 1991b, Elastic moduli of a solid containing spherical inclusions. Mechanics of Materials, 12, 17-24.

Chapter 4
Sediment with porous grains: Rock physics model and application to marine carbonate and opal

4.1 Abstract

We offer an effective-medium model for estimating the elastic properties of high-porosity marine calcareous sediment and diatomite. This model treats sediment as a pack of porous elastic grains. The effective elastic moduli of the porous grains are calculated using the differential effective-medium model (DEM), where the intragranular ellipsoidal inclusions have a fixed aspect ratio and are filled with seawater. Then the elastic moduli of a pack of these spherical grains are calculated using different granular medium models and a modified (scaled to the critical porosity) upper Hashin-Shtrikman bound above the critical porosity and modified lower and upper (opal) Hashin-Shtrikman bounds below the critical porosity. In this study, the modified lower and upper bounds were found to be appropriate for carbonate marine sediment and diatomaceous sediment, respectively. We find that the best match between the model-predicted compressional- and shear-wave velocities and Ocean Drilling Program (ODP) data from three wells is achieved when the

aspect ratio of intragranular pores is 0.5. This model assigns finite, non-zero values to the shear modulus of high-porosity marine sediment, unlike the suspension model commonly used in such depositional settings. This approach also allows us to obtain a satisfactory match with laboratory diatomite velocity data.

4.2 Introduction

A host of empirical and theoretical rock physics relations and models deals with siliciclastic sediment composed of solid grains or carbonates with inclusions. However, such modles do not applied well to the large areas on earth covered with deposits of microscopic hollow fossil skeletons, either calcareous or siliceous. The motivation for this study is to concentrate on velocity-porosity-mineralogy relations for such sediment texture.

Calcareous sediments cover about 68% of the area in the Atlantic; 36% in the Pacific; and 54% in the Indian Ocean. The total coverage is about 48% of the world's seafloor (Sverdrup et al., 1942). In most cases, calcium carbonate is transferred to the sea floor by biological activities. Organisms utilize dissolved calcium carbonate to construct their skeletons (Figure 4.1). The remains of the microorganisms settle to the seafloor and form a bed of calcareous sediment (Mohamedelhassan and Shang, 2003). In deep water, shallow buried calcareous marine sediment is composed largely of minute skeletons (porous grains). When this sediment is deposited its porosity may be as high as 0.7 to 0.8 (Fabricius, 2003). Burial and the resulting compaction causes porosity reduction to approximately 0.5 to 0.6 within the first few hundred meters below the seafloor. The elastic properties of this overburden and their relation to porosity, mineralogy, and stress are important for proper seismic imaging of targets located underneath this calcareous sediment.

Another widely distributed deposit with porous grains is diatomite (Figure 4.2) which can be part of the overburden (e.g., in the North Sea) or hydrocarbon reservoirs (California, USA, Monterey formation). Diatomite is composed of the fossilized skeletal remains of microscopic plants called diatoms. Diatoms are made of siliceous skeleton and are found in almost every aquatic environment. Because their cell wall is composed of

hydrated silica ($Si(H_2O)_n$), they are well preserved in the sediments (Mohan, et al., 2006). Diatoms have the unique ability to absorb water-soluble silica present in their natural environment to form a rigid highly porous skeletal framework of amorphous silica. Atomic force microscopy (AFM) analysis of live diatoms has revealed the nanostructure of the valve silica to be composed of a conglomerate of packed silica spheres (Crawford et al., 2001; Losic et al., 2007). Hamm et al. (2003) performed real and virtual loading tests on diatom cells, using calibrated glass microneedles and finite element analysis. They show that the frustules are remarkably strong by virtue of their architecture and the material properties of the diatom silica.

Diatomite is structurally close to calcareous sediment because both have a biogenic origin and thus are composed of the skeletal parts of organisms. Both calcareous and diatomite materials have intergranular and intragranular porosity. Diatoms precipitate silica from seawater as amorphous opal (opal-A). After deposition, silica progresses from opal-A towards quartz, the stable phase, through an intermediate phase, opal-CT. Each transition occurs through dissolution and re-precipitation (Chaika, 1998; Chaika and Dvorkin, 2000).

Empirical relations combined with the theoretical Gassmann's (1951) approach between porosity, mineralogy, and the *P*- and *S*-wave velocity (V_p and V_s, respectively) have been developed for shallow buried marine calcareous sediment by, e.g., Hamilton (1971 and 1976); Hamilton, et al. (1982); and Richardson and Briggs (1993). A theoretical model by Wood (1955) simply assumes that shallow sediment is a suspension of solid particles in water and estimates the bulk modulus of this suspension as the harmonic average of the solid and fluid components.

However, Hamilton (1971), Hamilton et al. (1982), and Wilkens et al. (1992) have shown that shallow buried marine deposits do transmit shear waves. An implication of this is that there are contacts between the grains, which means that the suspension model is not adequate for such sediments. Hamilton (1971) points out that the suspension model is not valid for marine sediments, which have some rigidity, but still can be used to obtain a maximum estimate of the shear velocity, V_s. Wilkens et al. (1992) observe that Wood's estimation of the bulk modulus of the most porous sediments is close to the

dynamic bulk modulus.

To address this situation and estimate the shear modulus and, eventually, V_s, Hamilton (1971) and Wilkens et al. (1992) assume that the effective bulk modulus (K) is still given by the suspension model while the compressional modulus (M) is calculated from the measured V_p and bulk density (ρ_b) as $\rho_b V_p^2$. Then the shear modulus (G) is $(3/4)(M-K)$ and $V_s = \sqrt{G/\rho_b}$. A slightly different approach is proposed again in Hamilton (1971) and in Hamilton et al. (1982) where the decimal logarithm of the dry-frame bulk modulus (K_{Dry}) relates to porosity (ϕ) as $1.87355 - 3.41062\phi$, where the modulus is in GPa and porosity is in fractions of unity. Then, the saturated-rock bulk modulus K is computed from K_{Dry} using Gassmann's (1951) fluid substitution. Finally, the measured V_p is used to calculate M, and G is obtained from M and K as shown above.

The rock physics of diatomites has been addressed by Chaika (1998) who performed laboratory velocity measurements on samples from the Monterey formation (California). However, at that time no theoretical model was available to explain the observed relations between velocity and porosity (Chaika and Dvorkin, 2000).

Dvorkin and Prasad (1999) and Prasad and Dvorkin (2001) introduced a theoretical model for siliciclastic high-porosity marine sediment. This model extends the "soft-sand" model of Dvorkin and Nur (1996) into the high-porosity range between the critical porosity and 1. It connects the two end points, one given by the "soft-sand" model at the critical porosity and the other for pure pore fluid at porosity 1, by using the modified upper Hashin-Shtrikman bound (Hashin and Shtrikman, 1963). In this model, the critical porosity is used as an intermediate elastic endpoint so that the sediment frame can have non-zero elastic moduli above the critical porosity.

The principal modification to this model introduced here is to treat high-porosity sediment as a pack of porous elastic grains which represent minute calcareous or siliceous skeletons. The effective elastic moduli of the grains are calculated using the differential effective medium model (Appendix A), where the ellipsoidal inclusions have a fixed aspect ratio and are filled with seawater. The elastic moduli of a pack of these grains are calculated using a modified (scaled to the intergranular critical porosity) upper

Hashin-Shtrikman bound above the critical porosity and a modified lower Hashin-Shtrikman bound below the critical porosity. We apply this new model to three Ocean Drilling Program (ODP) well datasets and show that it matches the data, especially V_s, better than previous models.

This principle of theoretically replacing the actual mineral with a porous material can be applied, as appropriate, to various mineralogies and used with any of the existing rock physics models, including such traditional relations as by Wyllie et al. (1956), Raymer et al. (1980), and Krief et al. (1990). We use this approach to mimic Chaika's (1998) diatomite data by including porous solids into the modified upper Hashin-Shtrikman bound (Gal et al., 1998).

The main result of this work is the introduction of the porous-grain concept into the existing rock physics models. By using well log and laboratory data, we show that this approach helps match relevant data where other relations fail.

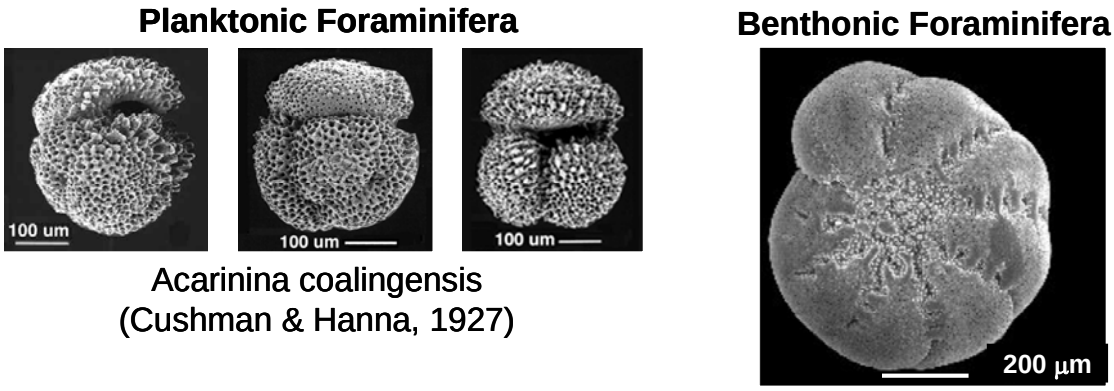

Figure 4.1. Left: Three planktonic foraminifera grains with different shapes. Right: Benthonic foraminifera grain.

4.3 Pack of porous grains

To model carbonate sediment, we propose a porous-grain-soft-sand (PGSO) model, which treats the sediment as a pack of porous elastic grains (Figure 4.3a). In this model, the intergranular porosity, ϕ_i, is defined as

$$\phi_i = (\phi_t - \phi_g)/(1-\phi_g), \tag{4.1}$$

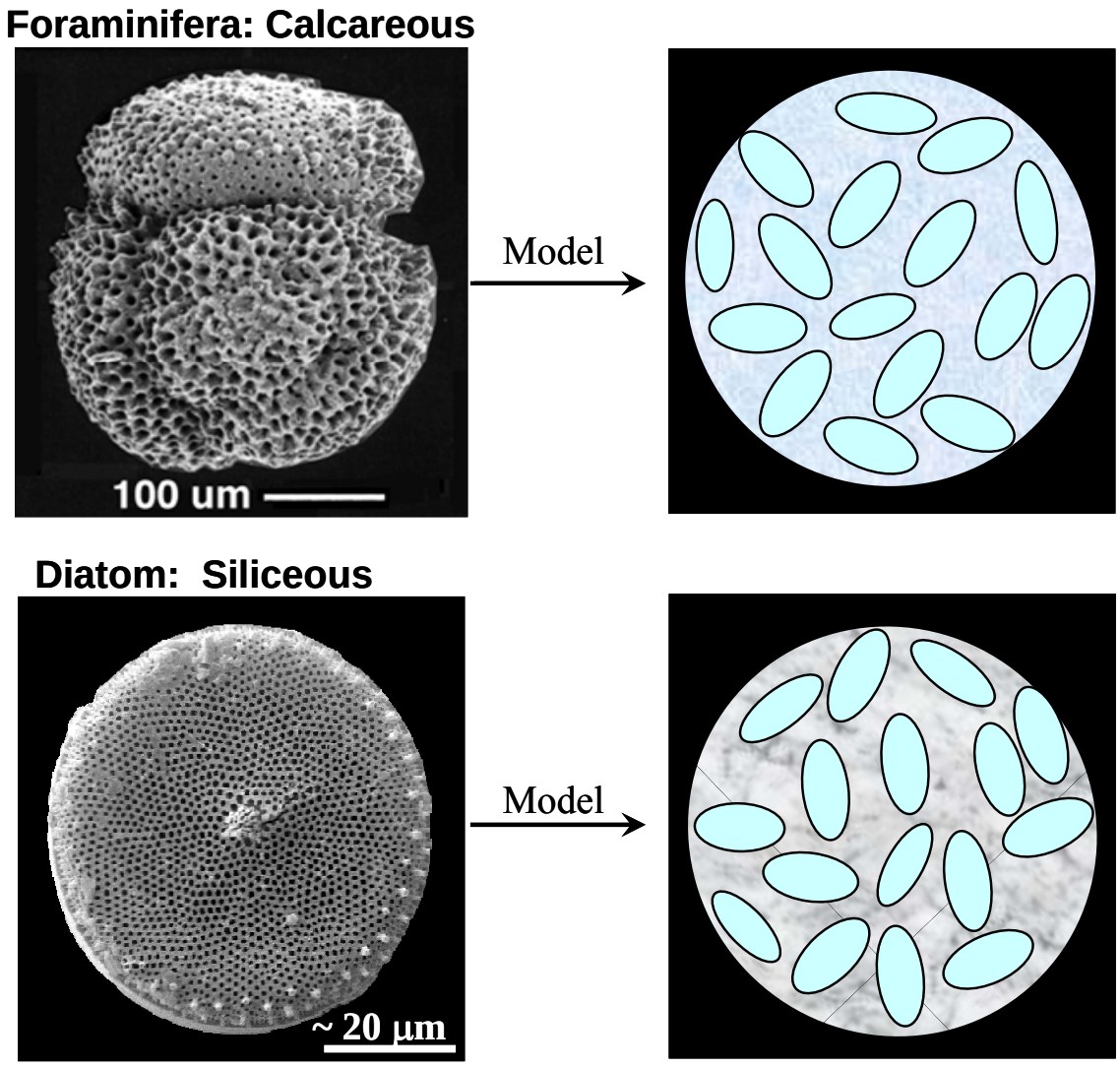

Figure 4.2. Upper frame: Calcareous foraminifera grain and its idealized mathematical model. Lower frame: Diatom with siliceous (spal) skeleton and and its idealized mathematical model.

where ϕ_g is the internal porosity of the grains defined as the ratio of the intragranular pore-volume to the total grain volume and ϕ_t is the total porosity. When $\phi_i = 0$, $\phi_t = \phi_g$ whereas when $\phi_g = 0$, $\phi_t = \phi_i$ (Figure 4.3c). ϕ_t can be calculated from the bulk density ρ_b as

$$\phi_t = (\rho_s - \rho_b)/(\rho_s - \rho_w), \tag{4.2}$$

where ρ_s is the density of the mineral and ρ_w is the density of water. In clean

calcareous sediment, the neutron porosity also provides an accurate estimate for ϕ_t.

The effective bulk (K_g) and shear (G_g) moduli of the grain material are calculated using DEM (Norris, 1985) where the ellipsoidal inclusions of the volumetric concentration ϕ_g (which is the intragranular porosity) have a fixed aspect ratio (AR) and are filled with seawater (Appendix A).

Once the elastic properties of a grain are determined, we assume that the granular sediment is a pack of such grains. The critical porosity ϕ_c of such packs is about 0.40 (Nur et al., 1998). Notice that at this critical porosity ϕ_c, the total porosity is $\phi_{tc} = \phi_g + \phi_c(1-\phi_g)$. To calculate the elastic moduli of the pack we examine two porosity domains: one where $\phi_i \le \phi_c$ and the other where $\phi_i > \phi_c$.

In the former domain, the elastic model connects two end-points in the elastic-modulus-porosity plane: the effective moduli at $\phi_i = 0$ (which are simply the moduli of the porous grain) and the moduli of a dense random pack of identical elastic porous spheres (with water-filled inclusions) at $\phi_i = \phi_c$. In order to interpolate between these two end points, we use the lower Hashin-Shtrikman bound, rescaled from the 0 to 1 porosity range to 0 to ϕ_c (as in the "soft-sand" model of Dvorkin and Nur, 1996). Specifically, the effective bulk (K_{Dry}) and shear (G_{Dry}) moduli of the dry granular frame comprised of water-saturated porous grains are

$$
\begin{aligned}
K_{Dry} &= \left(\frac{\phi_i/\phi_c}{K_{HM}+\frac{4}{3}G_{HM}} + \frac{1-\phi_i/\phi_c}{K_g+\frac{4}{3}G_{HM}}\right)^{-1} - \frac{4}{3}G_{HM}, \\
G_{Dry} &= \left(\frac{\phi_i/\phi_c}{G_{HM}+Z_1} + \frac{1-\phi_i/\phi_c}{G_g+Z_1}\right)^{-1} - Z_1, \quad Z_1 = \frac{G_{HM}}{6}\left(\frac{9K_{HM}+8G_{HM}}{K_{HM}+2G_{HM}}\right),
\end{aligned}
\tag{4.3}
$$

where K_{HM} and G_{HM} are the Hertz-Mindlin (Mindlin, 1949) moduli at the critical porosity.

K_{HM} and G_{HM} for a dense random pack of identical elastic spheres with the Hertz-Mindlin (Mindlin, 1949) contacts are (e.g., Mavko et al., 1998)

$$K_{HM} = \sqrt[3]{\frac{C^2(1-\phi_i)^2 G_g^2}{18\pi^2(1-\nu_g)^2}P}, \quad G_{HM} = \frac{5-4\nu_g}{5(2-\nu_g)}\sqrt[3]{\frac{3C^2(1-\phi_i)^2 G_g^2}{2\pi^2(1-\nu_g)^2}P},$$
$$\nu_g = \frac{1}{2}\frac{K_g/G_g - 2/3}{K_g/G_g + 1/3}, \tag{4.4}$$

where ν_g is the Poisson's ratio of the porous grains, P is the differential pressure acting upon the pack, and C is the average number of contacts that each grain has with its neighboring grains (the coordination number).

In the $\phi_i > \phi_c$ domain we also consider two end-points, one at $\phi_i = \phi_c$ and the other at $\phi_i = 1$. At the former, the effective elastic moduli K_{Dry} and G_{Dry} are given by equation 4.4 as K_{HM} and G_{HM}, while at the latter, they are simply zero. In-between these end-points we use (Dvorkin and Prasad, 1999)

$$K_{Dry} = \left[\frac{(1-\phi_i)/(1-\phi_c)}{K_{HM} + \frac{4}{3}G_{HM}} + \frac{(\phi_i - \phi_c)/(1-\phi_c)}{\frac{4}{3}G_{HM}}\right]^{-1} - \frac{4}{3}G_{HM},$$
$$G_{Dry} = \left[\frac{(1-\phi_i)/(1-\phi_c)}{G_{HM} + Z_1} + \frac{(\phi_i - \phi_c)/(1-\phi_c)}{Z_1}\right]^{-1} - Z_1. \tag{4.5}$$

Following Gassmann's (1951) fluid substitution equations, we assume that the shear modulus of the fully-water-saturated sediment is that of the dry frame ($G_{Sat} = G_{Dry}$), while its bulk modulus is

$$K_{Sat} = K_g \frac{\phi_i K_{Dry} - (1+\phi_i)K_f K_{Dry}/K_g + K_f}{(1-\phi_i)K_f + \phi_i K_g - K_f K_{Dry}/K_g}, \tag{4.6}$$

where K_f is the bulk modulus of seawater.

Finally, the elastic *P*- and *S*-wave velocities are

$$V_p = \sqrt{(K_{Sat} + \frac{4}{3}G_{Sat})/\rho_b}, V_s = \sqrt{G_{Sat}/\rho_b}. \tag{4.7}$$

A counterpart to PGSO is the porous-grain-stiff-sand (PGST) model. The only difference between the two is for $\phi_i < \phi_c$ (Figure 4.3b). In this porosity range, the same two end-points, one at zero porosity and the other at the critical porosity, are connected by the modified upper Hashin-Shtrikman bound (Gal, et al., 1998). As a result, we obtain

$$K_{Dry} = \left(\frac{\phi_i/\phi_c}{K_{HM}+\frac{4}{3}G_g} + \frac{1-\phi_i/\phi_c}{K_g+\frac{4}{3}G_g}\right)^{-1} - \frac{4}{3}G_g,$$
$$G_{Dry} = \left(\frac{\phi_i/\phi_c}{G_{HM}+Z_2} + \frac{1-\phi_i/\phi_c}{G_g+Z_2}\right)^{-1} - Z_2, \quad Z_2 = \frac{G_g}{6}\left(\frac{9K_g+8G_g}{K_g+2G_g}\right). \tag{4.8}$$

In the above models, the total porosity should be always larger or equal to the intragranular porosity. That is why the schematic velocity-porosity curves in Figure 4.3b are within the $\phi_g \le \phi_t \le 1$ interval.

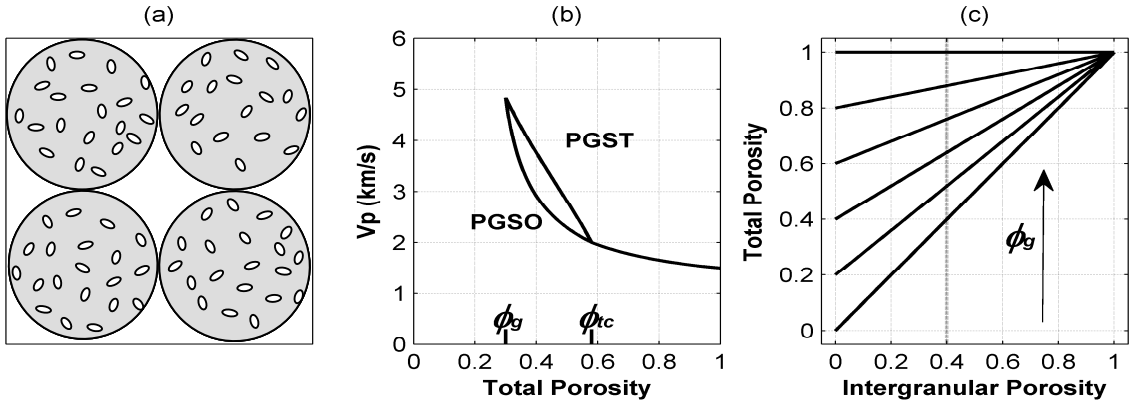

Figure 4.3. (a) Schematic representation of a rock with porous grains. (b) Velocity-porosity curves for PGSO and PGST (as labeled). These two models are the same in the porosity range between the critical porosity ϕ_{tc} and 1. (c) The total porosity versus intergranular porosity according to Equation 4.1. Each line is computed for a fixed intragranular porosity (ϕ_g), starting with zero (the lowest diagonal line) and ending at one (the upper horizontal line) with 0.2 step

The same approach, where we treat the solid phase as made of porous grains, is, in principle, applicable to any of the existing rock physics models. An example of this approach is the Wood-porous grain model (WPG), which is a modification of the Wood-Hamilton (Hamilton, 1971) method to obtain a maximum estimate of the shear velocity (Wilkens, et al., 1992), presented in Appendix D.

To apply the staged upscaling scheme explained above, where we first applied DEM to upscale porous grains and then the modified HS bounds to account for pores between the grains, we assumed that the intragranular ellipsoidal micropores are much smaller than those pores among grains.

4.3.1 Influence of aspect ratio and intragranular porosity on elastic properties

Figure 4.4 illustrates the effects of varying AR and ϕ_g on the *P*- and *S*-wave impedance (I_p and I_s, respectively) of pure-calcite material, as predicted by PGSO for dry and water-saturated sediment. The solid-phase bulk and shear moduli and density used in this example are K_s = 76.8 GPa, G_s = 32 GPa, and ρ_s = 2.71 g/cm3, respectively. The fluid's bulk modulus and density are 2.391 GPa and 1.034 g/cm3, respectively. The differential pressure is 1.61 MPa. Clearly, if $\phi_g = 0$, there is no effect of the aspect ratio of the intragranular inclusions on the impedance. However, as we increase ϕ_g, the effect of AR becomes more and more pronounced, so that for $\phi_g \geq 0.3$ and AR = 0.01, both I_p and I_s in the dry sediment are essentially zero. This is not so for I_p in water-saturated sediment. Here, the effect of the pore fluid on the *P*-wave propagation appears to be especially significant in low-AR, very compliant intragranular pores. Figure 4.5 displays similar plots for PGST and the same modeling parameters. The effects of ϕ_g and AR on the impedance are essentially the same as for PGSO. The difference between the two models is manifested in the abrupt change in the impedance-porosity behavior at ϕ_{tc}. Other input parameters, such as the differential pressure and pore-fluid-compressibility, may also significantly influence I_p and I_s (Dvorkin and Prasad, 1999). In water-saturated sediment, the latter exhibits larger sensitivity to pressure than the former. Also, large fluctuations in the salinity of the seawater, such as those that can occur due to proximity to a salt dome, may affect the compressibility of seawater and, as a result, the velocity and impedance in the soft sediment.

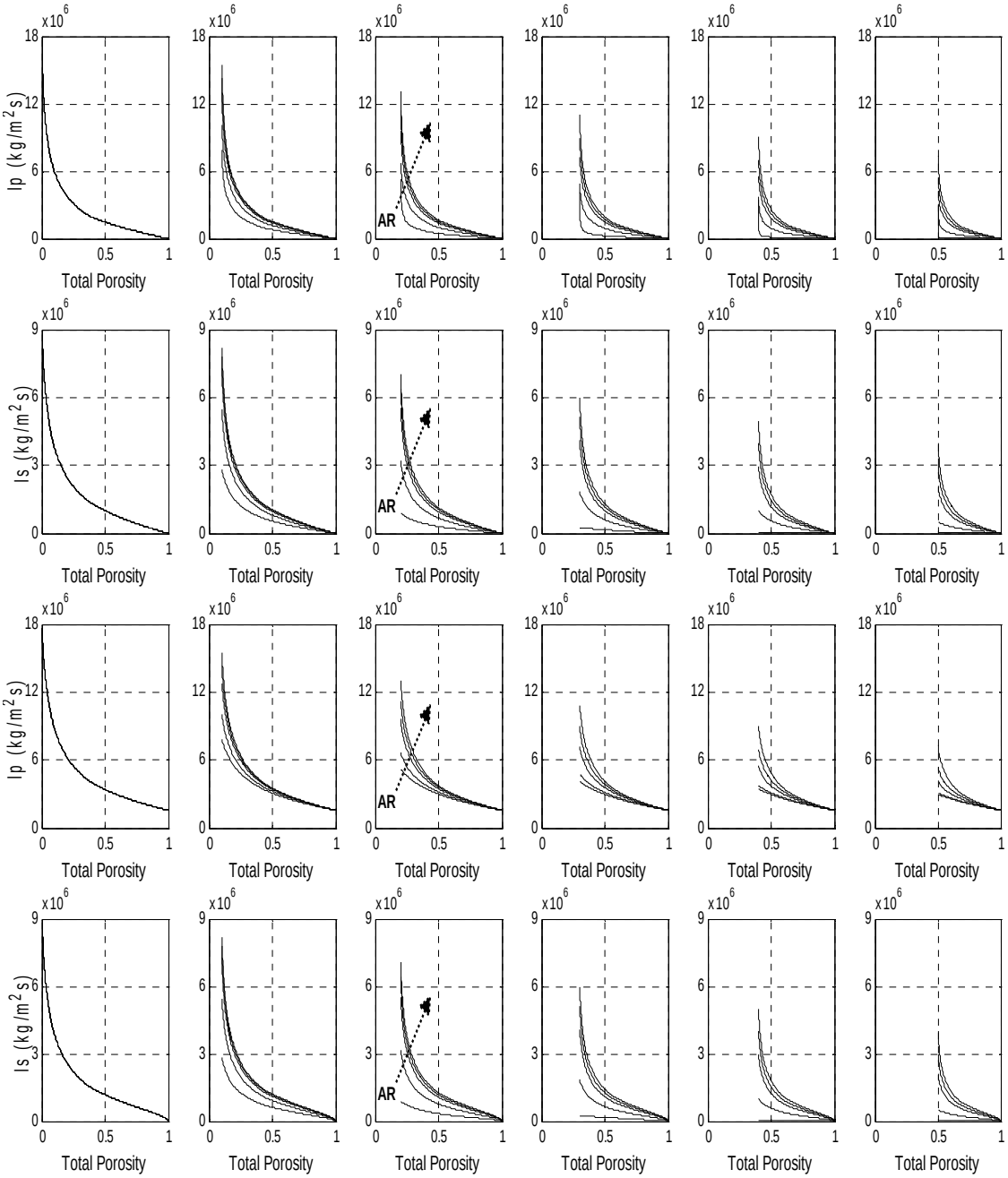

Figure 4.4. Sensitivity of the *P*- and *S*-wave impedance to intragranular AR and porosity at dry (upper two rows) and wet (lower two rows) conditions, using PGSO model. In this example, the intragranular porosity varies from 0.0 to 0.5, from left to right, with 0.1 step. The arrows in the third column frames indicate the direction of increasing AR. The AR used are 0.01, 0.03, 0.1, 0.2 and 1.0. The differential pressure, critical porosity, and coordination number are 1.61 MPa, 0.38, and 9, respectively.

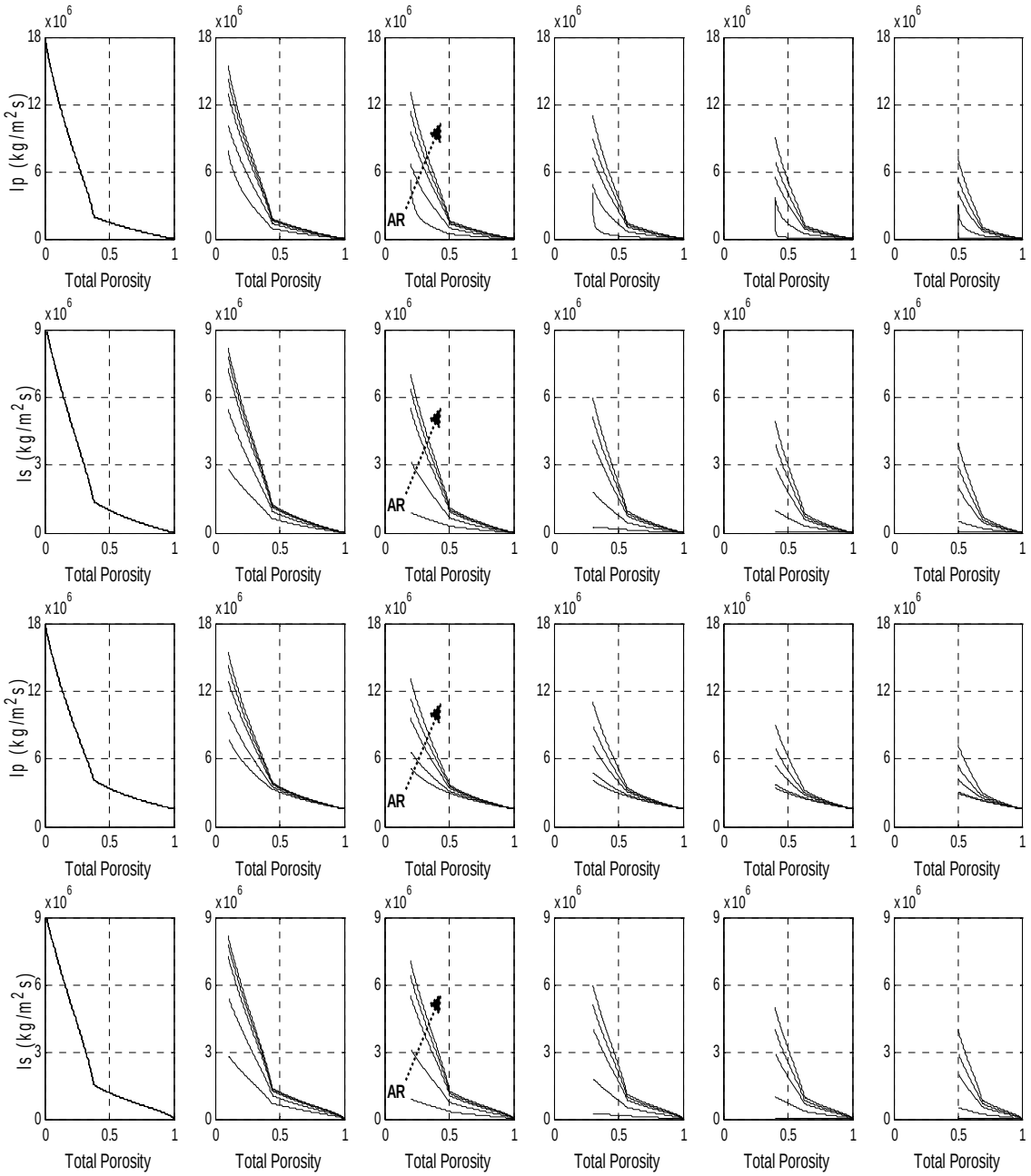

Figure 4.5. Same as Figure 4.4 but using the PGST model.

Figure 4.6 illustrates the effects of varying AR and ϕ_g on the *P*- and *S*-wave velocities (V_p and V_s, respectively) of pure-calcite material, as predicted by PGSO and PGST for water-saturated sediment. Different curves correspond to different intragranular porosity, ϕ_g. In this example, ϕ_g varies from 0.0 to 0.5 with 0.1 step.

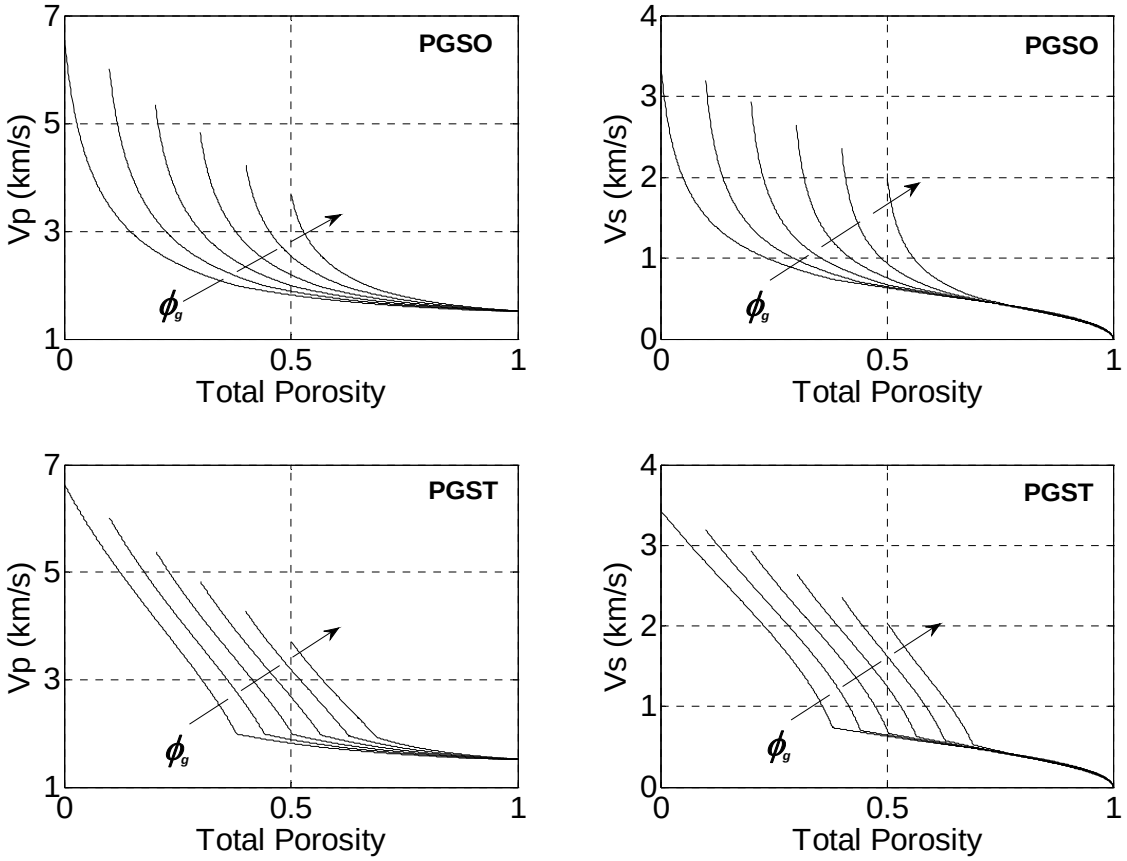

Figure 4.6. Sensitivity of the *P*- and *S*-wave velocities to intragranular porosity at wet condition, using PGSO (upper two rows) and PGST (lower two rows) models. In this example, the intragranular porosity varies from 0.0 to 0.5 with 0.1 step. The arrows indicate the direction of increasing ϕ_g. The differential pressure, critical porosity, intragranular aspect ratio and coordination number are 1.61 MPa, 0.38, 0.5, and 9, respectively.

4.4 ODP data sets

We studied deep marine carbonate sediment from three ODP well sites: 1172, 998 and 1007. The porosity of this sediment is between 0.25 and 0.80. For this study, we selected the depth intervals with essentially pure calcium carbonate content.

Site 998 (ODP, 1996) is located on the Cayman Rise (the Caribbean), between the Yucatan Basin to the north and Cayman Ridge and Cayman Trough to the south, at water depth 3190 m. We concentrated on the depth interval between 210 and 470 mbsf (meters below seafloor) which consists of nannofossil chalks.

Site 1172 (ODP, 2000a) is located at about 150 km southeast of Tasmania at water

depth 2622 m. The interval under examination (150 to 350 mbsf) consists of (a) white and light greenish gray nannofossil ooze and (b) pale yellow and light gray foraminifer-bearing nannofossil chalk with increased foraminifer content and minor components of clay and volcanic glass.

Site 1007 (ODP, 2000b) is located on the toe of the western Great Bahamas Bank slope in 669 m of water. In this site, the studied depth interval is divided into four units. Unit I, between zero and 203 mbsf, consists of a succession of nannofossil ooze and variable lithified wackestones that transit to packstones with increasing depth. Unit II, between 203 and 302 mbsf, is of early Pliocene age and consists entirely of bioturbated light gray to pale yellow foraminifer nannofossil chalk. Unit III, between 302 and 363 mbsf, displays variable degrees of lithification of foraminifer wackestone, nannofossil chalk, and nannofossil limestone. Unit IV, between 363 and 696 mbsf, is made of 5 to 10 cm thick layers of fine-grained packstone and also exhibits alternations between densely cemented and weakly cemented sediment (0.1 to 1.0 m thick) that shows evidence of compaction (ODP, 2000b). Petrographic studies and Scanning Electron Microscopy (SEM) images show different degrees of foraminifer cementation in this well (Kenter et al., 2002).

For all these sites measurements of V_p , ρ_b , neutron porosity, GR, as well as carbonate (CaCO3) and organic/inorganic carbon content are available. Site 1172 has, in addition, V_s data. Simple mineralogy (the CaCO3 content above 0.85) and absence of clay determined our choice of these data sources. Wireline logging was conducted with successful runs of the Schlumberger-GHMT-sonic tool string (ODP, 2000a).

4.5 Matching ODP data with models

In Figure 4.7, we compared the measured V_p and V_s with curves produced by DEM (not applied just to the grains but to the entire sediment treating it all as a solid with inclusions), Raymer et al. (1980), Wyllie (1956), and Castagna et al. (1993) models as well as PGSO and PGST, assuming pure calcite porous grains with isolated inclusions and fully brine saturated. The matrix in all models is pure calcite and the pore fluid is brine. The bulk modulus and density of the brine in each well were calculated according

to Batzle and Wang (1992) using salinity 36,000 ppm and site-specific temperature and pressure. In this study we assumed the same salinity for the calculation of the density and bulk modulus of the intragranular water, intergranular water and bottom sea floor water.

The total porosity (ϕ_t) in each well was calculated from the bulk density (ρ_b) by assuming that the density of the mineral (ρ_s) is that of calcite (2.71 g/cm3). The density of water (ρ_w) slightly varies with depth and location but remains very close to the value used above (1.034 g/cm3).

The model curves in Figure 4.7 were produced for fixed brine properties which are 2.391 GPa for the bulk modulus and 1.034 g/cm3 for density, averaged among the data sets. The differential pressure at sites 1007, 998 and 1172, ranges from approximately 1 to 8 MPa, from approximately 1 to 4.5 MPa, and from approximately 0.8 to 2.3 MPa respectively. For the purpose of Figure 4.7, the differential pressures at different sites were kept constant at 1.61 MPa for Site 1172, 4.18 MPa for Site 1007 and 2.68 MPa for Site 998, which are the averaged pressure values in each site depth interval. The DEM model employed here to calculate the elastic moduli of the porous grains used a single aspect ratio for all datasets. The best fit to the data is for AR = 0.1. The parameters used in PGSO and PGST in the entire interval are: intragranular porosity 0.26; critical porosity 0.38; coordination number 9; and aspect ratio of the intragranular inclusions 0.5. Among all these models, PGSO provides the best match to the velocity data; while DEM applied to the entire sediment with AR = 0.1 matches V_p, it overestimates V_s data for Site 1172.

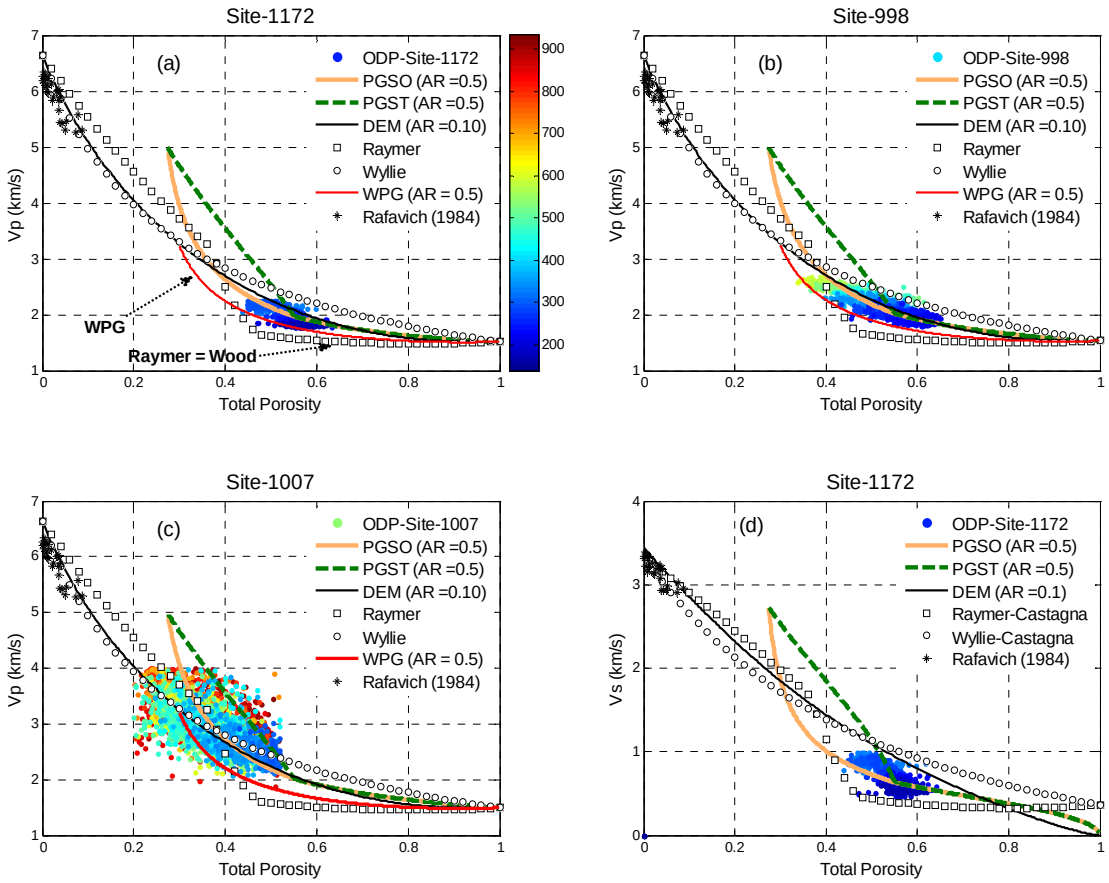

Figure 4.7. *P*-wave velocity versus total porosity for the three ODP data sets under examination: (a) Site-1172, (b) Site-998, (c) Site-1007, and (d) *S*-wave velocity Site-1172, all plots are color-coded by depth (in mbsf). Data from Rafavich (1984) that are essentially pure calcite low-porosity rock are displayed for reference (black crosses). The model curves displayed are: PGSO and PGST with the intragranular AR 0.5, coordination number 9, critical porosity 0.38, and intragranular porosity 0.26; DEM with aspect ratio 0.1 applied to the entire sediment by treating it as a solid with inclusions; Raymer et al. (1980) combined with Castagna et al. (1993), the latter to obtain the *S*-wave velocity; Wyllie et al. (1956) combined with Castagna et al. (1993); and the suspension model where the grains are modeled as a porous solid (WPG), with the same parameters as in PGSO and PGST

In Figures 4.8 to 4.10, we plot the predicted and measured V_p versus depth in each of the selected wells. In Figure 4.11, we plot the predicted and measured V_s versus depth in Site 1172. The input for the models used here are: (1) the bulk modulus and density of water which vary with depth according to the increasing pore pressure (hydrostatic) and temperature and (2) the differential pressure which is the integral of the bulk density

minus the density of water with respect to depth. The bulk density data were missing between the sea bottom and the shallowest depth datum. For the purpose of pressure estimation, these missing curves were approximated by a linear interpolation between the shallowest density data and the density at the sea bottom. The latter was 1.537 g/cm3, as calculated for a calcite sediment with (assumed) 0.70 porosity.

The original log curves contained many (apparently artificial) spikes. To remove them, we smoothed the curves by using the arithmetic average for porosity and density and the Backus (1962) average for the velocity. The running window contained between 10 and 15 original depth increments.

In all three wells, PGSO with intragranular inclusion aspect ratio 0.5 accurately matched the measured V_p, except for the lower-porosity intervals in Site 1007 (Figure 4.9). In these intervals, the soft-sand model is not suitable for the rock which is, apparently, more consolidated and harder than in the other parts of the wells. The Miocene section at Site 1007 has been affected by diagenesis; as a result, the sediments appear to be fully lithified below ~300 mbsf (ODP, 2000b). The DEM model used with a constant aspect ratio 0.1 also provides a good match to the data, except in the high-porosity intervals in Sites 1007 and 1172, where it is apparently not suitable. The suspension (Wood, 1955) model (not displayed here) strongly underestimates the data whereas both the Raymer et al. (1980) and Wyllie et al. (1956) equations (the former not displayed here) overestimate the velocity. Wood porous grain model (WPG), with intragranular inclusion aspect ratio 0.5, underestimates the V_p data in all three wells, however, the reduction decreases at shallow depth where the sediment is more in suspension condition.

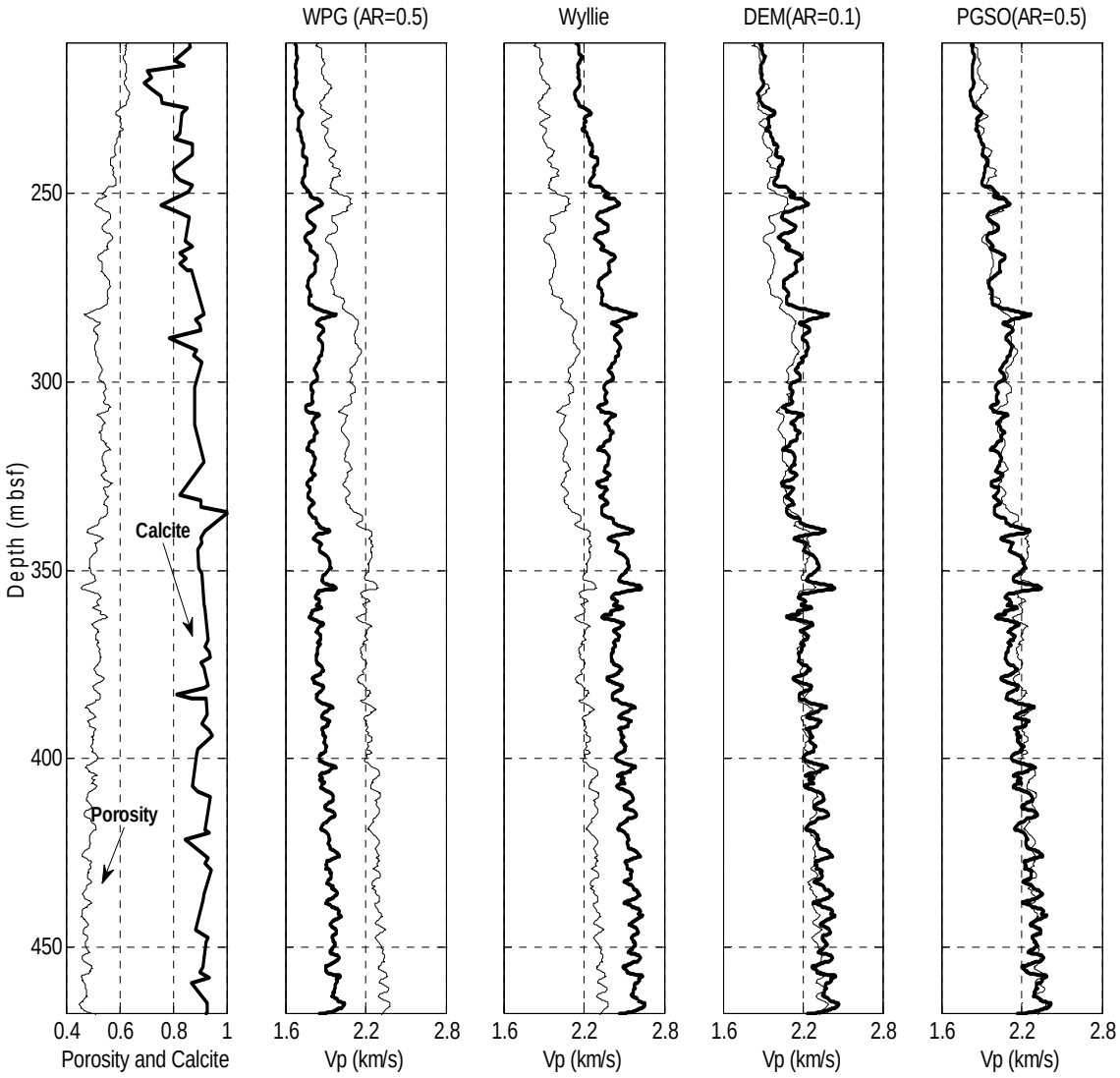

Figure 4.8. ODP-well site 998. From left to right: total porosity and $CaCO_3$ content; *P*-wave velocity as measured and predicted by Wood's suspension model with porous grains (WPG), Wyllie et al. (1956), DEM, and PGSO models. The aspect ratios used in this modeling are listed in the legend. The data are shown in thin solid line while the model predictions are shown in bold solid line.

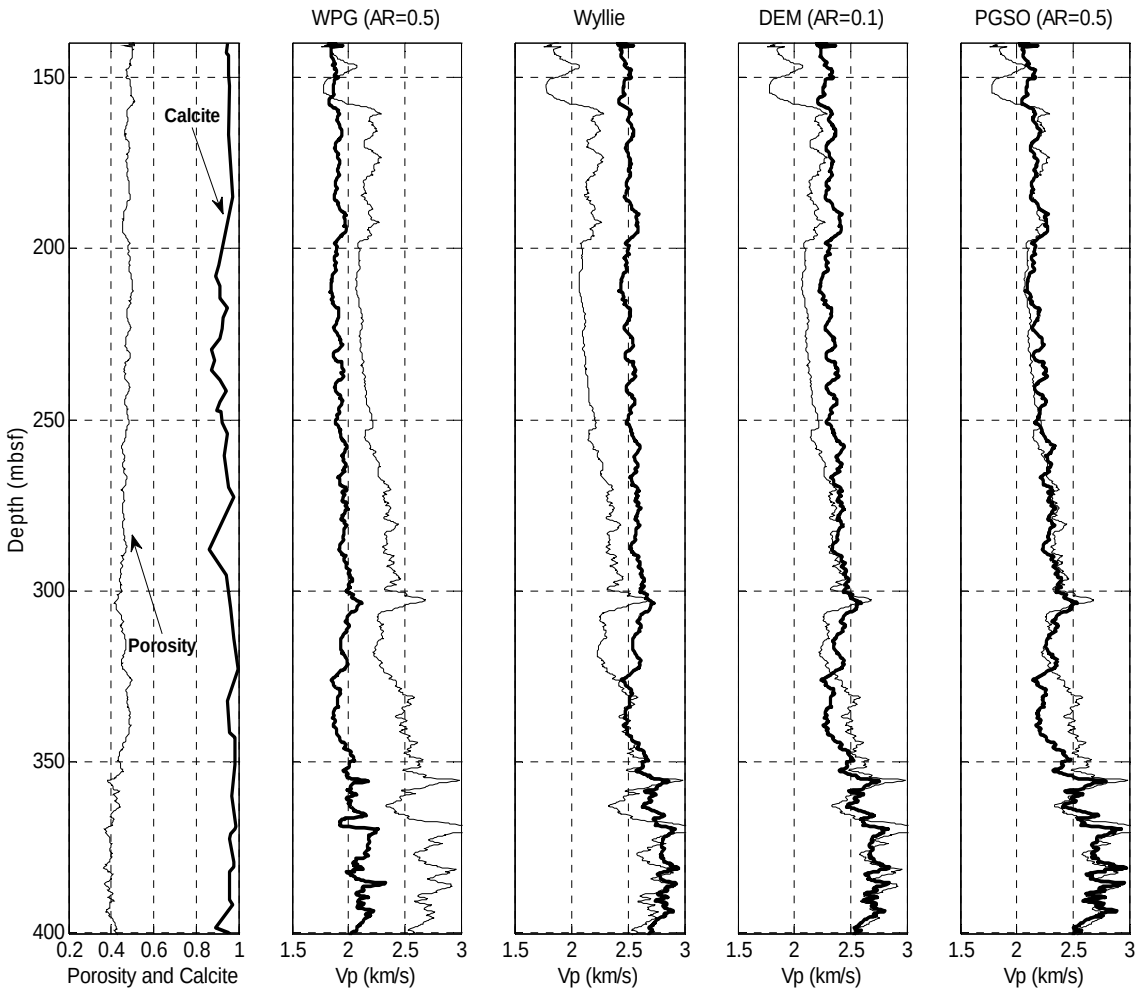

Figure 4.9. ODP-well site 1007. The display is the same as in Figure 4.5.

The Castagna et al. (1993) V_s predictor applied to the Wyllie et al. (1956) equation overestimates the measured V_s in the entire interval (Figure 4.11). So does the DEM model. The Hamilton-Gassmann (Hamilton, 1976) model provides a good V_s prediction only for very shallow depths where the porosity exceeds 0.45. The WPG (AR=0.5) model provides a good V_s prediction in the entire interval. However, PGSO was the only model that provided an accurate and consistent match to the measured V_s in Site 1172. PGSO used with the intragranular aspect ratio 0.5, coordination number 9, critical porosity 0.38, and intragranular porosity 0.26 accurately matched these data in the upper interval of the well, above 271 mbsf (Figure 4.11).

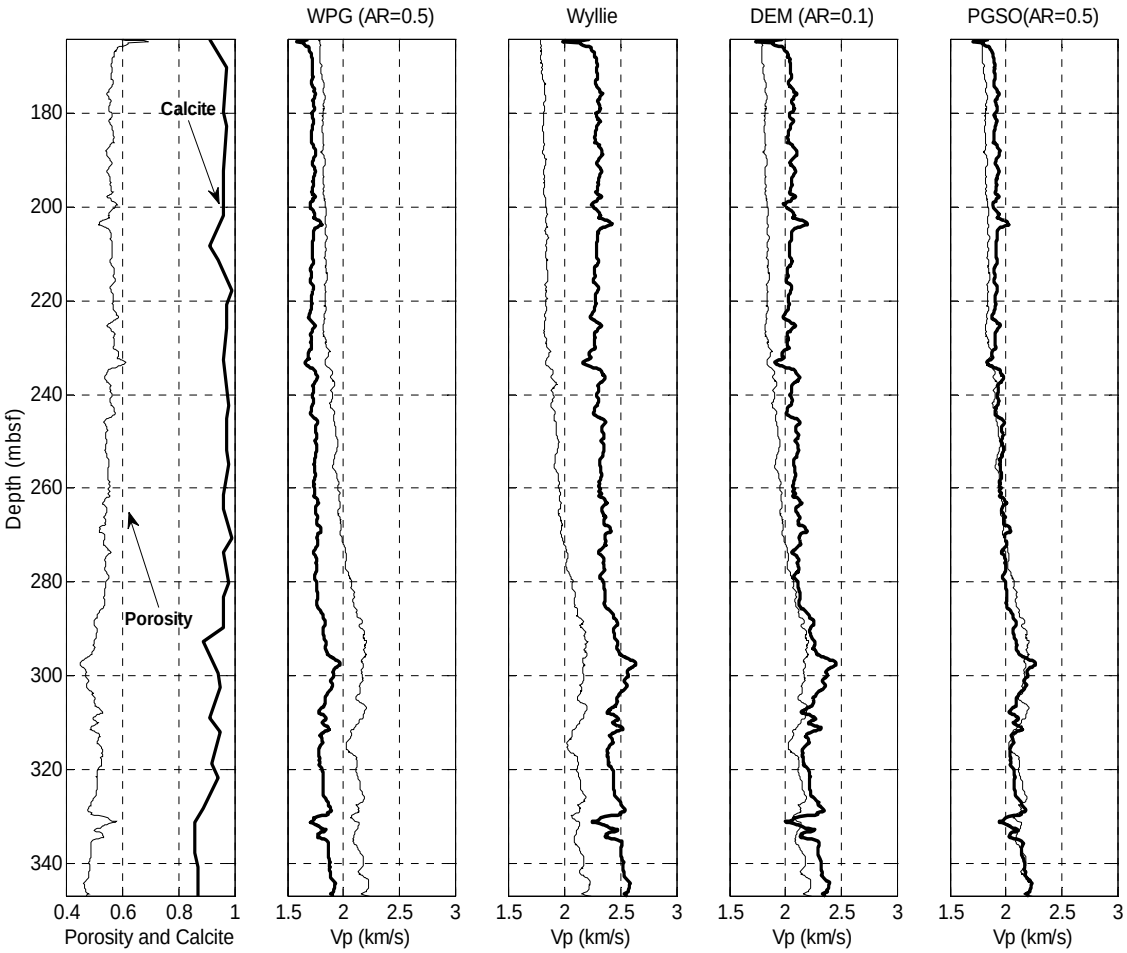

Figure 4.10. ODP-well site 1172. From left to right: total porosity and XRD-Calcite content; *P*-wave velocity as measured and predicted by Wood's suspension model with porous grains (WPG), Wyllie et al. (1956), DEM, and PGSO models. The aspect ratios used in this modeling are listed in the legend. PGSO model, for coordination number 15 and grain porosity 0.20, provides a satisfactory match to the data below 271 mbsf.

To achieve a good match in the lower part of the well, below 271 mbsf, where the sediment is more consolidated, we changed these parameters by increasing the coordination number C from 9 to 15 and simultaneously reducing the intragranular porosity from 0.26 to 0.20 which is consistent with the onset of compaction. These changes act to increase V_s but leave V_p essentially the same (Figures 4.10 and 4.11). The reason is that both the intragranular porosity ϕ_g and coordination number C affect the V_p/V_s ratio and, as a result, Poisson's ratio ν. However, these two ratios are more sensitive to changes in C than in ϕ_g (Figure 4.12): as C increases, the dry frame

becomes stiffer and, as a result, the wet-rock ν decreases. As a consequence, different variations of C and ϕ_g produce different effects on V_p and V_s, such as (a) simultaneously increasing or reducing V_p and V_s; (b) keeping both velocities constant; or (c) keeping V_p constant and increasing V_s, as in our case.

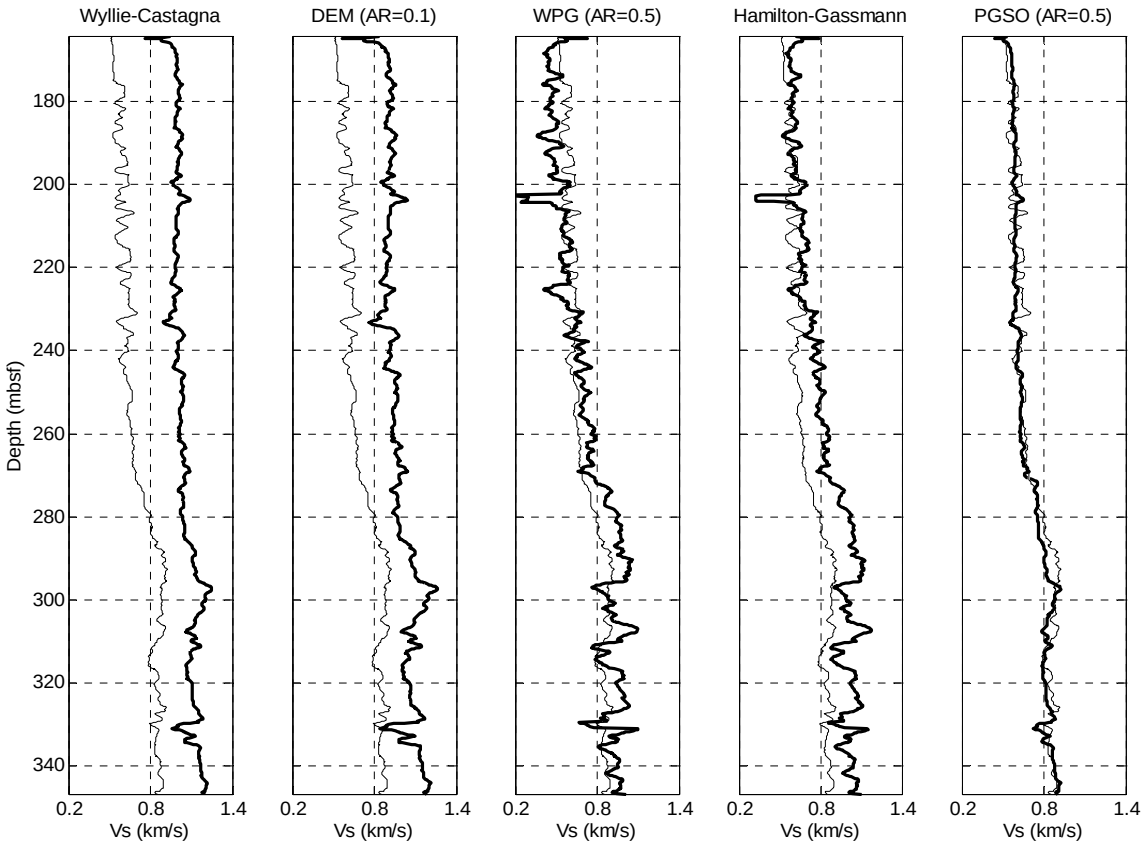

Figure 4.11. ODP-well site 1172. From left to right: *S*-wave velocity as measured and predicted by Wyllie et al. (1956)-Castagna et al. (1993), DEM, Wood's suspension model with porous grains (WPG), Hamilton (1971, 1982), and PGSO models. The parameters used in this modeling are the same as in Figure 4.7. PGSO provides a satisfactory match to the data below 271 mbsf.

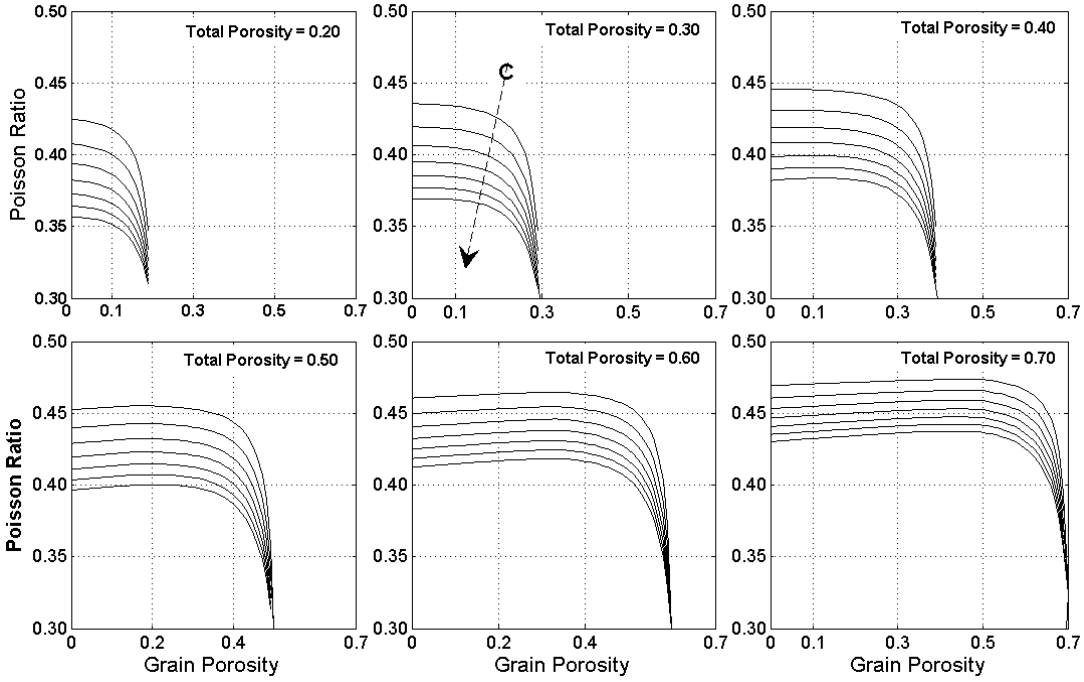

Figure 4.12. Wet-rock Poisson's ratio versus intragranular porosity according to PGSO. The coordination number is varied from 4 to 16 with a step of 2 and the total porosity varied from 0.20 to 0.70. All other PGSO model parameters are kept constant. The arrow in the top-middle frame indicates the direction of increasing coordination number C.

Figure 4.13 shows a cross-plot of V_p versus V_s as measured in Site 1172; the model predictions of Pickett (1963), DEM, Krief et al. (1990), Castagna et al. (1993) and PGSO are plotted. The first two predictors overestimate V_s at any given V_p. The Krief et al. (1990) method correctly predicts V_s in the high-porosity part of the interval while the Castagna et al. (1993) method overestimates it. Conversely, the latter provides a satisfactory V_s prediction in the lower-porosity part of the interval while the former underestimates V_s. PGSO, if used with consistently adjusted inputs, correctly predicts V_s in the entire interval.

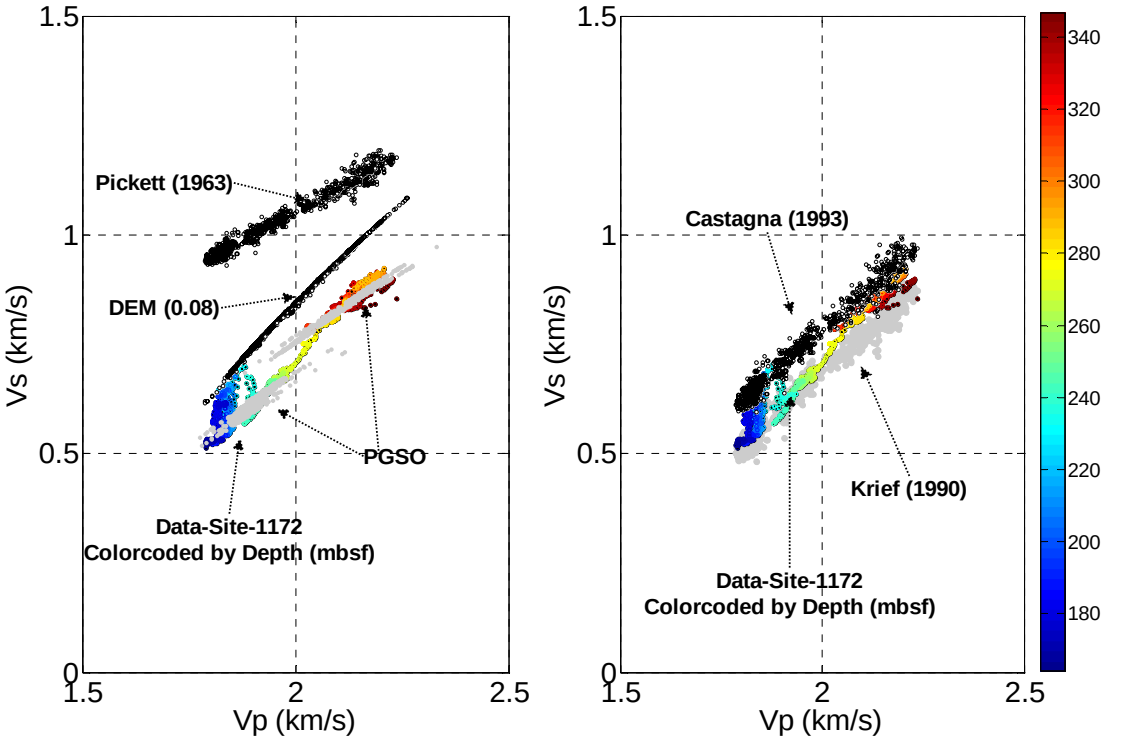

Figure 4.13. *S*- versus *P*-wave velocity. Comparison of Site-1172 data (color-coded by depth in mbsf) and predictions according to PGSO, DEM, and Pickett (1963) on the left, and Castagna (1993) and Krief et al. (1990). The two PGSO branches in the left- and right-hand frame correspond to the upper and lower depth intervals in this well.

Finally, in Figure 4.14, we compared the predicted to measured velocity according to selected models: DEM with AR = 0.1, Hamilton (1971), and PGSO. We observed that the latter model accurately mimics the data while the former two fail.

4.6 Diatomites

Consider the laboratory measurements by Chaika (1998) performed on room-dry diatomites from three Monterey formation reservoirs in California. The mineralogy of these samples includes opal-A, opal-CT, quartz, clay, analcima, and feldspar, as well as organic components (Figure 4.15). The elastic moduli and densities of these components are from Chaika (1998) and Mavko et al. (1998) and are shown in Table 4.1.

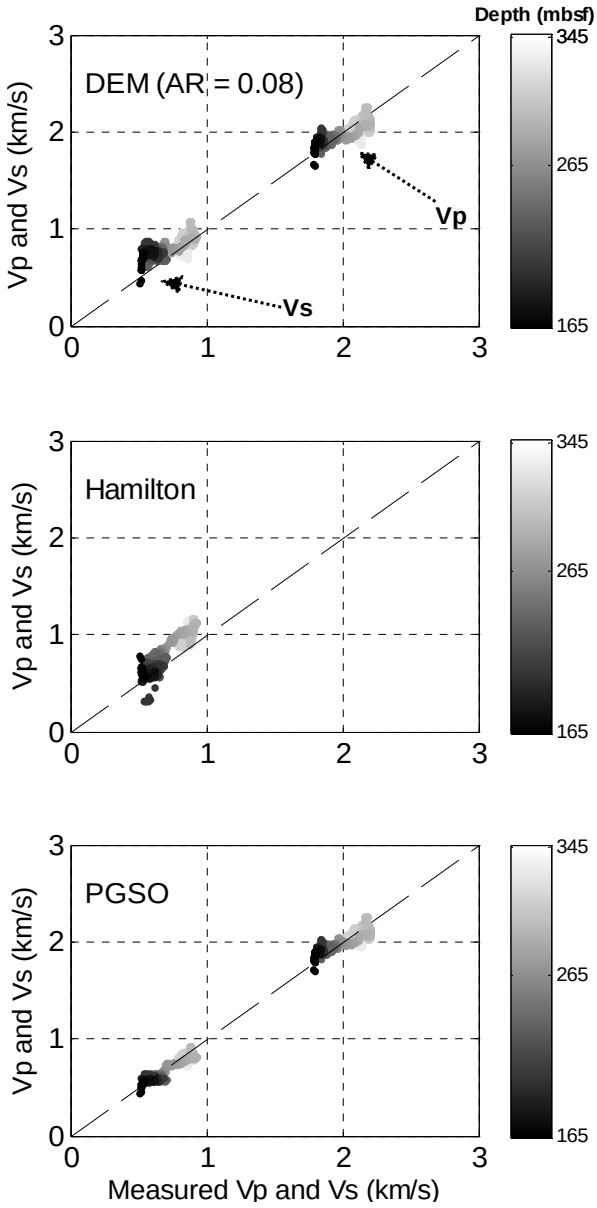

Figure 4.14. ODP well site 1172. Predicted versus measured *P*- and *S*-wave velocity, color-coded by depth in mbsf. In the upper two frames we use the DEM (AR = 0.1) and Hamilton-Gassmann (Hamilton, 1971) models while in the lower frame we use the PGSO model

Chaika (1998), identifies two distinct patterns of porosity reduction in reservoir rocks of the Monterey Formation as they undergo silica diagenesis from opal-A through opal-CT to quartz. In Pattern 1, the porosity reduction appears to be due to increased amounts

of non-silica minerals (and quartz, if present) and the grain density increases with decreasing porosity. In Pattern 2, the amount of opal-CT (and quartz, if present) increases while the fraction of non-silica minerals is relatively constant and the grain density decreases with decreasing porosity. Since the samples from Cymric are the only ones containing opal-A, they are the only rocks which could be called diatomite.

We modeled these data using PGSO and PGST models as described above, assuming siliceous porous grains with isolated inclusions. The model parameters, the same for all samples, are: intragranular AR = 0.6; coordination number 10; critical porosity 0.42; and intragranular porosity 0.15.

Table 4.1 Mineralogy of diatomite samples (Chaika, 1998, Mavko et al., 1998).

Mineral	Bulk Modulus (GPa)	Shear Modulus (GPa)	Density (g/cm^3)
Opal-A/CT	14.219	12.580	2.0
Quartz	37.88	44.31	2.649
Clay	21.83	7.0	2.56
Analcime	55.629	26.231	2.712
Pyrite	87.91	137.9	5.1
Calcite	76.8	32.0	2.71
Feldspar	53.36	27.04	2.56
Organic	2.937	2.733	1.3

We observed that PGSO only matches the high-porosity data (not displayed here) while PGST (Figure 4.15) provides a satisfactory match in the entire porosity range (because above the critical porosity both these models are the same). To further illustrate the quality of this match, we cross-plot the PGST-predicted velocity versus the measured data in Figure 4.15. In spite of a few outlying data points (mostly for V_s), we deem this match satisfactory and practically usable. This example illustrates the utility of the porous-grain approach not only with the soft-sand model but also with other existing models, the stiff-sand model in particular.

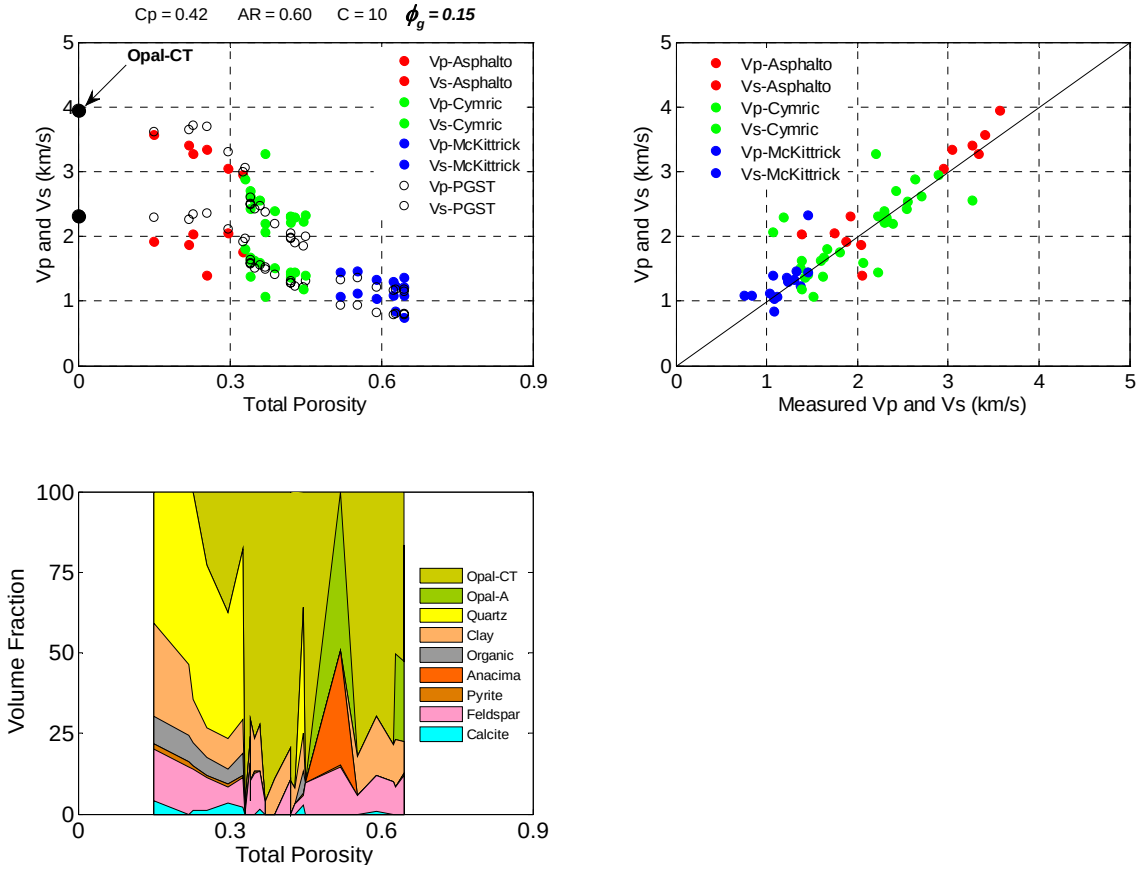

Figure 4.15. Top-left: *P*- and *S*-wave dry-rock velocity versus porosity as measured and predicted by PGST. The fill circles are measured *P*- and *S*-wave velocities on a zero porosity opal-CT sample. The measurements are room-dry at 10 MPa confining pressure. Top-right: Predicted (PGST) versus measured velocity. Bottom-left: X-ray mineralogical composition of opaline rock samples. The data are from Chaika (1998).

4.7 Discussion

The porous-grain concept appears to be generally applicable to medium-to-high porosity sediments. Consider for example Figure 4.16, which shows V_p versus ϕ_t for the marine chalk dataset used in Nur et al. (1998). The trend apparent in these data can be matched with a PGSO curve with a constant differential pressure 4 MPa; C = 9; ϕ_c = 0.42; and ϕ_g = 0.22. Fabricius (2003) uses a similar marine carbonate dataset. Figure 4.16 implies that the porous-grain model is appropriate for the Fabricius (2003) data as well. In the original paper, Fabricius (2003), in order to explain the velocity behavior of

chalk data with different degree of burial diagenesis, uses an additional (free) parameter (IF) to fill the space between the lower and upper modified Hashin-Shtrikman bounds with model curves. Here we can explain the data using a model with physics- and geology-driven parameters.

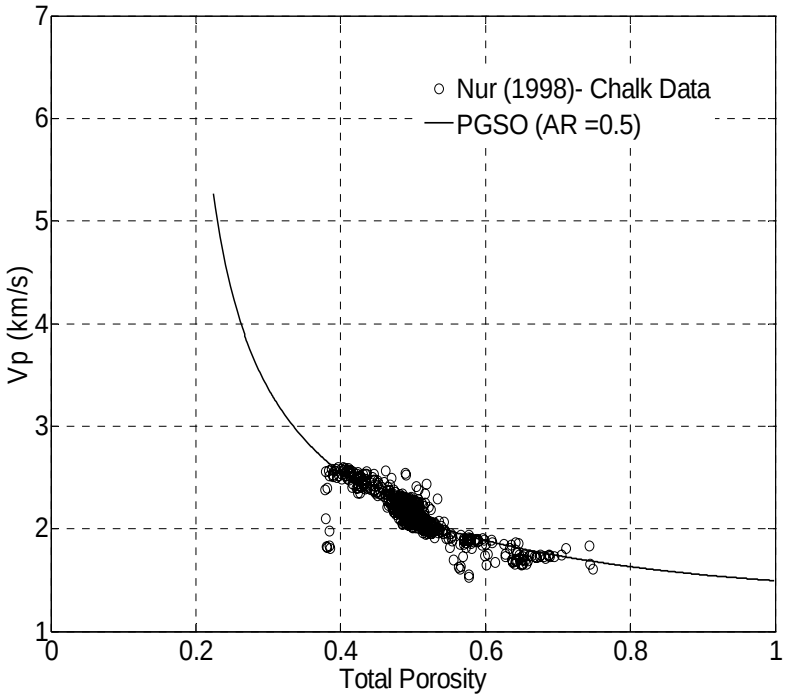

Figure 4.16. *P*-wave velocity versus total porosity cross-plots for the Nur et al. (1998) chalk data set. The model curve displayed is PGSO with the intragranular AR 0.5, coordination number 9, critical porosity 0.42, and intragranular porosity 0.22.

In the case of opal data sets, Chaika (1998) points out that the process of transiting from opal-A to opal-CT begins with grains in an unlithified rock of small hollow (porous) particles of opal-A where the particle contacts have small cross-sectional areas. Instead of forming overgrowth cements like clastic rocks, these opaline porous particles dissolve and reprecipitate as opal-CT (Williams et al., 1985); some new particles will form and some particles will grow. Both of these processes result in particle contacts with larger cross-sectional areas (equivalent to cementation), since both the "grains" and "cement" in this model are both composed of opal-CT. To predict the velocities of rocks coming from these three fields, Chaika (1998) uses two different rock physics models. The first model is the upper Hashin-Shtrikman bound scaled to the critical porosity, to describe the

samples from Asphalto and McKittrick. The second model is a combination of the Hertz-Mindlin theory with the upper Hashin-Shtrikman bound, for samples from Cymric. In both models, the total porosity was replaced with intergranular porosity. In this study, we observed that all three data sets (Asphalto, McKittrick and Cymric), can be modeled as a pack of porous cemented grains and that PGST provided a satisfactory match in the entire porosity range.

As with any rock-physics model, the PGSO and PGST models introduced here have advantages and disadvantages. Among the advantages are (1) the physically and texturally consistent treatment of calcareous sediment and opalines as comprised of porous grains, and (2) the consistency of the model predictions with selected offshore calcareous and on-shore opaline data. The disadvantages are intimately linked to the structure of the model which requires inputs, such as the intragranular porosity, intragranular inclusion aspect ratio, critical porosity, and coordination number, that (1) are somewhat idealized and (2) are not immediately available from experimental measurements.

However, this is a common feature of any micromechanical model. One way of resolving the resulting ambiguity is to (1) select inputs that are reasonable, such as the critical porosity varying within the 0.35 to 0.45 range and a coordination number varying between 5 and 15, and (2) calibrate these inputs to existing data and then link them to specific geographic locations and depth intervals. Once such a calibration is accomplished, the model can be used in a predictive mode away from well control.

The above-mentioned disadvantage of PGSO and PGST turns into an advantage if we utilize these models in an exploratory mode. By varying the inputs in reasonable and site-consistent ranges, we can explore the plausible ranges of the elastic properties as well as their interrelation.

The examples provided here emphasize that the existing V_s predictors may be accurate within certain depth ranges but do not provide correct predictions within the entire depth range. On the contrary, PGSO provides an accurate prediction in the entire depth interval at the expense of varying the model parameters within a reasonable and depositionally-consistent range.

4.8 Conclusions

The approach introduced here and the models following from this approach appear to be applicable to sediment with porous grains, such as calcareous and diatomatious ooze. The parameters of these models, specifically the intragranular porosity and coordination number, can be linked to compaction and diagenesis. To make such a link predictive, robust, and repeatable, one needs to systematically explore the applicability of this model to various high-quality data sets with established geologic records and mineralogies, an analysis that is beyond the scope of this paper. Finally, the approach introduced here, where we treat the solid phase as a porous material, can be used to modify any of the existing rock-physics models. These models can become part of the arsenal of rock-physics relations used in synthetic seismic generation as well as in real seismic data interpretation for rock properties.

4.9 References

Backus, G., 1962, Long-wave elastic anisotropic produced by horizontal layering: Journal of Geophysical Research, 67, 4427-4440.

Batzle, M., and Z. Wang., 1992, Seismic properties of pore fluids: Geophysics, 57, 1396-1408.

Boutéca, M., and Y. Guéguen, 1999, Mechanical properties of rocks: Pore pressure and scale effects: Oil and Gas Science and Technology, 54, 703-714.

Budiansky, B., 1965, On the elastic moduli of some heterogeneous materials: Journal of the Mechanics and Physics of Solids, 13, 223-227.

Berryman, J. G., 1980, Long-wavelength propagation in composite elastic media: Journal of Acoustic Society of America, 68, 1809-1831.

Castagna, J. P., M. L. Batzle, and T. K. Kan, 1993, Rock Physics -- The link between rock properties and AVO response, in J. P. Castagna, and M. Backus, eds., Offset-Dependent Reflectivity-Theory and Practice of AVO Analysis: Investigations in Geophysics, No. 8, Society of Exploration Geophysicists, 135-171.

Chaika, C., 1998, Physical Properties and Silica Diagenesis: Ph.D. thesis, Stanford University.

Chaika, C., and J. Dvorkin, 2000, Porosity reduction during Diagenesis of diatomaceous Rocks: The American Association of Petroleum Geologists Bulletin, 84, 1173–1184.

Crawford, S. A., M. J. Higgins, P. Mulvaney, and R. Wetherbee, 2001, Nanostructure of the diatom frustule as revealed by atomic force and scanning electron microscopy: Journal of Psychology, 37, 543-554.

Dvorkin, J., G. Mavko, and A. Nur, 1995, Squirt flow in fully saturated rocks: Geophysics, 60, 97-107.

Dvorkin, J., and A. Nur, 1996, Elasticity of high-porosity sandstone: Theory for two North Sea Datasets: Geophysics, 61, 1363-1370.

Dvorkin, J., and M. Prasad, 1999, Elasticity of marine sediments: Rock Physics modeling: Geophysical Research Letters, 26, 1781-1784.

Fabricius, I., 2003, How burial diagenesis of chalk sediments controls sonic velocity and porosity: The American Association of Petroleum Geologists Bulletin: 87, 1755-1778.

Gal, D., J. Dvorkin, and A. Nur, 1998, A physical model for porosity reduction in sandstones: Geophysics, 63, 454-459.

Gassmann, F., 1951, Über die elastizität poröser medien: Veirteljahrsschrift der Naturforschenden Gesellschaft in Zürich, 96, 1-23.

Grechka, V., 2008, Fluid substitution in porous and fractured solids: The non-interaction approximation and Gassmann theory: International Journal of Fracture, 148, 103-107.

Hamm, C., R. Merkel, O. Springer, P. Jurkojc, C. Maier, K. Prechtel, and V. Smetacek, 2003, Architecture and material properties of diatom shells provide effective mechanical protection: Nature, 421, 841-843.

Hamilton, E. L., 1971, Elastic properties of marine sediments: Journal of Geophysical Research, 76, 576-604.

Hamilton, E. L., 1976, Shear-wave velocity versus depth in marine sediments: A review: Geophysics, 41, 985-996.

Hamilton, E. L., R. T. Bachman, W. H. Berger, T. C. Johnson, and L. A. Mayer, 1982, Acoustic and related properties of Calcareous deep-sea sediments: Journal of Sedimentary Petrology, 52, 733-753.

Hashin, Z., and S. Shtrikman, 1963, A variational approach to the elastic behavior of multiphase materials: Journal of the Mechanics and Physics of Solids, 11, 127-140.

Kachanov, M., I. Tsukrov, and B. Shafiro, 1995, Materials with fluid-saturated cracks and cavities: Fluid pressure polarization and effective elastic response: International Journal of Fracture, 73, 61-66.

Kachanov, M., 2007, On the Effective elastic properties of cracked solids-Editor's comments: Letter in fracture and micromechanics: 146, 295-299.

Kenter, J., F. Ansemetti, F. Kramer, H. Westphal, and M. Vandamme, 2002, Acoustic properties of "Young" carbonate rocks, ODP Leg 166 and boreholes Clino, and Anda, Western Great Bahamas Bank: Journal of Sedimentary Research, 52, 129-137.

Krief, M., J. Garat, J. Stellingwerff, and J. Ventre, 1990, A petrophysical interpretation using the velocities of P and S waves (full-waveform sonic): The Log Analyst, 31, 355-369.

Le Ravalec, M., and Y. Guéguen, 1996, High and low frequency elastic moduli for a saturated porous/cracked rock-differential self-consistent and poroelastic theories: Geophysics, 61, 1080-1094.

Losic, D., R. Pillar, T. Dilger, J. Mitchell, and N. Voelcker, 2007, Atomic force microscopy (AFM) characterization of the porous silica nanostructure of two centric diatoms: Journal of Porous Materials, 14, 61-69.

Mavko, G., and D. Jizba, 1991, Estimation grain-scale fluid effects on velocity dispersion in rocks: Geophysics, 56, 1940-1949.

Mavko, G., T. Mukerji, and J. Dvorkin, 1998, The rock physics handbook: Cambridge University Press.

Mindlin, R. D., 1949, Compliance of elastic bodies in contact: Trans. Transaction of the American Society of Mechanical Engineers, 71, A-259.

Mohamedelhassan, E., and J. Shang, 2003, Electrokinetic-generated pore fluid ionic transport in an offshore calcareous soil: Canadian Geotechnical Journal, 40, 1185-1199.

Mohan, R., S. Shanvas, M. Thamban, and M. Sudhakar, 2006, Spatial distribution of diatoms in surface sediments from the Indian sector of Southern Ocean: Current Science, 91, 1495-1502.

Mukerji, T., and G. Mavko, 1994, Pore fluid effects on seismic velocity in anisotropic rocks: Geophysics, 59, 233-244.

Mukerji, T., G. Mavko, D. Mujica, and N. Lucet, 1995, Scale-dependent seismic velocity in heterogeneous media: Geophysics, 60, 1222-1233.

Norris, A. N., 1985, A differential scheme for the effective moduli of composites: Mechanics of Materials, 4, 1-16.

Nur, A., G. Mavko, J. Dvorkin, and D. Galmudi, 1998, Critical porosity: a key to relating physical properties to porosity in rocks: The Leading Edge, 17, 357-362.

O'Connell, R. J., and B. Budiansky, 1974, Seismic velocities in dry and saturated cracked solids: Journal of Geophysics Research, 79, 4626-4627.

O'Connell, R. J., and B. Budiansky, 1977, Viscoelastic properties of fluid-saturated cracked solids: Journal of Geophysics Research, 82, 5719-5735.

ODP, Proceedings of Ocean Drilling Program, 1996, Leg-165, Preliminary Report 65, NSF and Joint Oceanographic Institutions,

Carey, S., and H. Sigurdsson, 2000, Grain size of miocene volcanic ash layers from sites 998, 999, and 1000: Implications for source areas and dispersal: Proceedings of the Ocean Drilling Program, Scientific Results, 165, 101-113.

ODP, Proceedings of Ocean Drilling Program, 2000a, Leg-189, Preliminary Report 189: NSF and Joint Oceanographic Institutions.

Robert, C., 2004, Bulk and clay mineral assemblages of the Tasmanian area, Maastrichtian-Pleistocene: Proceedings of the Ocean Drilling Program, Scientific Results, 189, 1-34.

ODP, Proceedings of the Ocean Drilling Program, 2000b, Leg-166, Scientific Results, 137-143.

Pickett, G. R., 1963, Acoustic character logs and their application in formation evaluation: Journal of Petroleum Technology, 15, 650-667.

Prasad, M., and J. Dvorkin, 2001, Velocity to porosity transforms in marine sediments: Petrophysics, 42, 429-437.

Raymer, L. L., E. R. Hunt, and J. S. Gardner, 1980, An improved sonic transit time-to-porosity transform: 21st Annual Logging Symposium Transaction, Society of Professional Well Log Analysts, Paper P.

Richardson, M. D., and K. B. Briggs, 1993, On the use of acoustic impedance values to determine sediment properties: Proceedings of the Institute of Acoustic, 15, 15-23.

Shafiro, B., and M. Kachanov, 1997, Materials with fluid-filled pores of various shapes: effective elastic properties and fluid pressure polarization: International Journal of Solids and Structures: 34, 3517-3540.

Sverdrup, H., M. Johnson, and R. Fleming, 1942, The oceans: Their physics chemistry and general biology: (reprinted, 1970) Prentice-Hall Inc.

Thomsen, L., 1985, Biot-consistent elastic moduli of porous rocks: Low-frequency limit: Geophysics, 50, 2797-2807.

Wilkens, R. H., C. H. Cheng, and J. A. Meredith, 1992, Evaluation and prediction of shear-wave velocities in calcareous marine sediment and rocks: Journal of Geophysical Research, 97, 9297-9305.

Williams, L., G. Parks, and D. Crerar, 1985, Silica Diagenesis I. Solubility controls: Journal of sedimentary Petrology, 55, 301-311.

Wood, A. B., 1955, A textbook of sound: G. Bell and Sons, Ltd., London.

Wright, J., and D. Kroon, 2000, Planktonic foraminiferal biostratigraphy of Leg 166, Proceedings of the Ocean Drilling Program, Scientific Results, 166, 3-12.

Wu, T. T., 1966, The effect of inclusion shape on the elastic moduli of a two-phase material: International Journal Solids and Structures, 2, 1-8.

Wyllie, M. R., A. R. Gregory, and L. W. Gardner, 1956, Elastic wave velocities in heterogeneous and porous media: Geophysics, 21, 41-70.

Chapter 5
Aggregate of porous grains: Models and scenarios

5.1 Abstract

We propose an effective-medium model for estimating the elastic properties of a random aggregate of identical, spherical, poroelastic grains. These estimates are achieved using a two-stage approach where the elastic properties of the porous grains are calculated first, followed by the elastic properties of an aggregate of the homogenized spherical grains. In the first stage, the effective elastic moduli of the poroelastic grains are calculated using a differential effective-medium (DEM) model or the combination of DEM with Gassmann's equation, depending on the connectivity of the intragranular porosity. The intragranular pore space may be either air- or fluid-filled. In the second stage, we proceed to calculate the elastic properties of a dry aggregate of such grains using different grain-contact-stiffness theories. This calculation is done in two different porosity domains: below and above critical porosity. Below critical porosity, the elastic model connects two end points in the elastic-modulus porosity plane: the effective moduli at zero intergranular porosity (the effective moduli of the porous grains) and the moduli of a dense random aggregate of identical elastic porous spheres at the critical porosity. To interpolate between these two end points, we use the lower Hashin-Shtrikman bound

(HS–), rescaled from a porosity range of 0–1 to a range of 0 to critical porosity. Above critical porosity, we also consider two end points: one at the critical porosity (dense-aggregate moduli) and the other at porosity equal 1 (the moduli of air). At critical porosity, different grain-contact theories are used to determine the properties of the dry dense aggregate of porous grains. Below critical porosity, the upper Hashin-Shtrikman bound (HS+) is also used to produce a second estimate of the effective elastic properties, which may be consistent with a different aggregate texture. To apply this staged upscaling scheme, where we first upscale porous grains and then account for pores between the grains, we assume that the intragranular micropores are much smaller than the intergranular pores among grains. A similar staged approach is used to determine the elastic moduli of cemented porous grain aggregates at low cement concentration. The combination of the cementation theory for porous grain material with the self-consistent approximation allows us to estimate the elastic properties of a cemented porous grain aggregate at all cement concentrations.

Our approach and models for non-cemented aggregates may be applied to sediment, such as calcareous and diatomaceous ooze, opal, and chalks. Our approach for cemented aggregates may be applied to carbonates. The microstructural parameters of our models can be associated to diagenesis and may be varied to mimic diagenetic processes of carbonates.

5.2 Introduction

In this study we develop a methodology to determine the effective elastic moduli of porous grain aggregate with different textures. This work is an extension of the porous-grain model proposed by Ruiz and Dvorkin (2009). This extension enables us to: a) use Walton's model (Walton, 1985) in addition to the Hertz-Mindlin model (Mindlin, 1949), as it was formulated originally (Ruiz and Dvorkin, 2009); b) vary the grain contact friction coefficient γ in the whole range from 0 to 1, for smooth to infinitely rough grains, respectively; c) combine the self-consistent approximation (Berryman, 1980) with the cementation theory (Dvorkin et al., 1994) to account for intergranular cement volume fractions from 0 to 1; and d) considering the effect of frequency.

We treat a saturated porous-grain as an elastic solid with ellipsoidal inclusions filled with air or compressible fluid (Figure 5.1a). The porous-grains model can be applied to approximate three different porous grain-aggregate textural scenarios, depending on the effective fluid connectivity of the intragranular porosity in the grain (Figure 5.2). Each scenario is an idealized representation of the material's pore-space morphology and is less idealized for existing synthetic materials. The realizations of each of these scenarios in artificial composites or natural rocks are achieved either by creating or eliminating pore-to-pore connections, or by changing the period of the externally applied stresses to be faster or slower than the pore-to-pore diffusion times. To determine the effective elastic properties of the saturated porous-grain material in the three different porous-grain-aggregate scenarios, we use two models: DEM (Norris, 1985) and the combination DEM-Gassmann, depending on whether we want the high frequency or the low frequency effective elastic moduli, respectively. DEM assumes that saturated intragranular inclusions are isolated with respect to flow; thus, it simulates high-frequency (HF) saturated-grain behavior. At low frequency (LF < 100 Hz) when there is time for wave-induced pore-pressure increments to flow and equilibrate (Mavko, et al., 1998; Boutéca and Guéguen, 1999), it is better to find the effective moduli for dry intragranular inclusions and then saturate them with the Gassmann low-frequency relations (Mavko, et al., 1998). The combination DEM-Gassmann may be appropriate at well-log frequencies (~1 to 20 kHz). Any model which gives the low-frequency response or equalized pore pressure is called Gassmann-consistent (Thomsen, 1985).

In all three of these scenarios, to account for the effects of intergranular porosity on the undrained elastic properties, we use the combination of the modified Hashin-Shtrikman bounds, which are the bounds rescaled from a porosity range of 0–1 to a range of 0 to critical intergranular porosity (ϕ_{ic}), and Gassmann's equations if we want a low-frequency velocity approximation (well logs) or the combination of the modified Hashin-Shtrikman and DEM if we want a very high frequency (VHF) velocity approximation (ultrasonic measurements). In this case, DEM assumes that the intergranular pore space is made of fluid inclusions which are isolated with respect to flow; simulating the (VHF) saturated-aggregate behavior that may be appropriate to ultrasonic frequency (~1 MHz).

Here, HF and VHF refer to fluid-related effects; but the wavelengths are still much longer than any scale of grains or intergranular pores (Budiansky, 1965; Wu, 1966; O'Connell and Budiansky, 1974; Berryman, 1980).

A similar staged approach is used to determine the elastic moduli of a cemented porous grain aggregate at low cement concentration. This is achieved by introducing the porous grain concept into the cementation theory (Dvorkin et al., 1994). Then, by combining the cementation theory (Dvorkin et al., 1994) for porous grain material with a self-consistent approximation, specifically, the coherent potential approximation (CPA) (Berryman, 1980), we are allowed to estimate the elastic properties of cemented porous grain aggregates at all cement concentrations (Dvorkin et al. 1999).

Our approach and models for non-cemented aggregates may be applied to sediment, such as calcareous and diatomaceous ooze, opal, and chalks. Our approach for cemented aggregates may be applied to carbonate rocks. The microstructural parameters of these models can be related to diagenesis and may be varied to mimic diagenetic processes of calcareous and diatomaceous ooze, and cemented and non-cemented carbonate rocks.

5.3 Porous-grain scenarios

We treat a saturated porous grain as a linearly elastic solid with ellipsoidal inclusions filled with compressible fluid (Figure 5.1).

Three different porous-grain scenarios were considered, depending on the effective fluid connectivity of the intragranular porosity in the grain. Depending on the material's microstructure, one of the following different descriptions might be more appropriate than the others. Three porous-grain scenarios are considered (Ruiz and Dvorkin, 2009):

1) The intragranular pores are isolated, and the intragranular pores are not connected with the intergranular pores (Figure 5.2a).

2) The intragranular pores are connected, and the intragranular pores are not connected with the intergranular pores (Figure 5.2b).

3) The intragranular pores are connected, and the intragranular pores are connected with intergranular pores (Figure 5.2c).

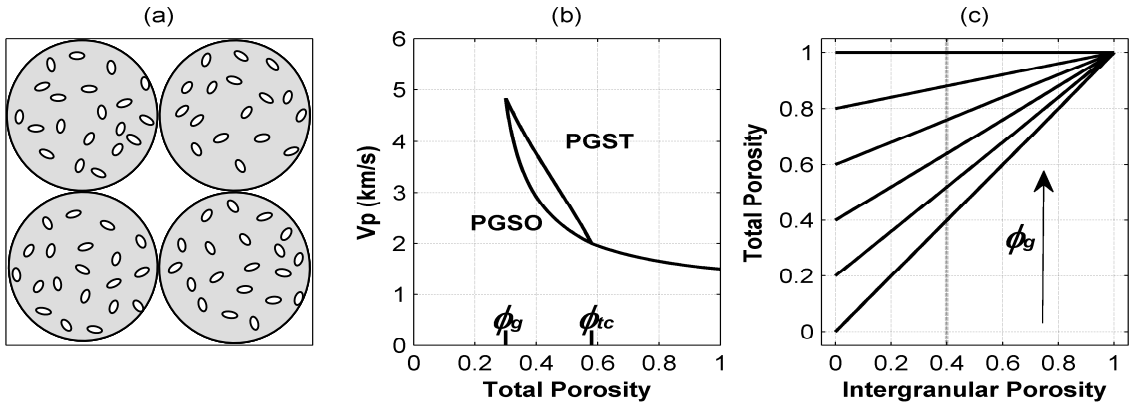

Figure 5.1. a) Schematic representation of a rock with porous grains. b) Velocity-porosity curves for PGSO and PGST (as labeled). These models are the same in the porosity range between the total critical porosity ϕ_{tc} and one. c) The total porosity versus intergranular porosity according to equation 1. Each line is computed for a fixed intragranular porosity ϕ_g, starting with zero (the lowest diagonal line) and ending at one (the upper horizontal line) in increments of 0.2. (figure from Ruiz and Dvorkin, 2009).

We suggest that realizations of each of these scenarios in artificial composites or natural rocks are through creating or eliminating pore-to-pore connections or changing the period of the externally applied stresses to be faster or slower than the pore-to-pore diffusion times. When we speak of high-frequency versus low-frequency response, the implication is that the connectivity is effectively controlled by the diffusion time versus frequency (Mavko and Jizba, 1991; Mukerji and Mavko, 1994; Dvorkin et al., 1995; Mukerji et al., 1995).

The elastic moduli of materials corresponding to each of these scenarios are different. These differences may be small or relatively large depending on the value of ϕ_g, ϕ_i, aspect ratios of the intragranular inclusions (α_g), orientation of the inclusions with respect to the direction of applied stress field (σ) and the magnitude and frequency of σ. All three of these scenarios are undrained states, in the sense that the total fluid mass in the porous grain aggregate is constant. No bulk flow takes place through the aggregate because it is considered jacketed, so fluid flows only inside the sample. We assume that materials corresponding to these porous grain scenarios have the same dry elastic properties. The dry elastic properties are computed in two steps: a) the elastic properties of the grains using DEM, and b) the elastic properties of the dry aggregate of

homogenized grains.

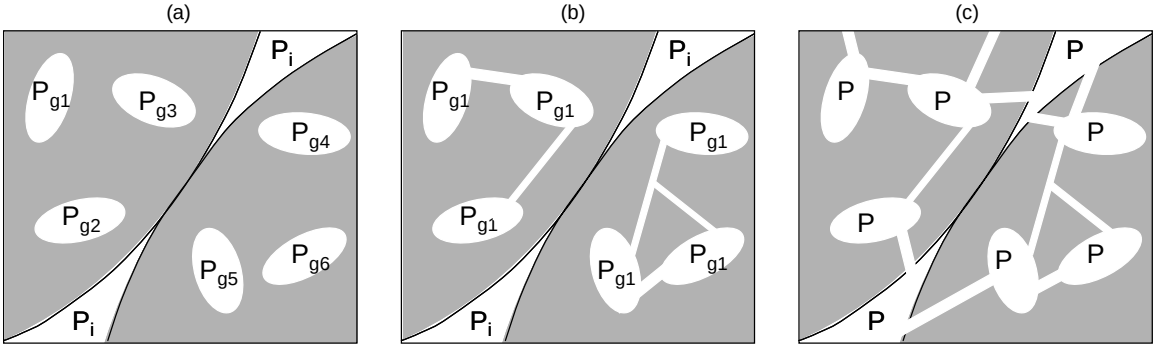

Figure 5.2. Three porous-grains scenarios. a) The intragranular inclusions are isolated. b) The intragranular inclusions are connected. c) The intragranular inclusions are connected and the intragranular porosity is connected with the intergranular porosity. (Figure from Ruiz and Dvorkin, 2009).

For the fluid saturated aggregate, we can define different degrees of fluid relaxation that depend on the degree of effective pore connectivity. Scenario 1 is the least relaxed because there is no pore-to-pore equilibration of pore pressure. Scenario 2 is slightly more relaxed, because intragranular pores are equilibrated with respect to pore pressures, but there is no effective fluid communication between the intragranular and the intergranular porosities. Scenario 3 is the most relaxed scenario. At low frequency, pressure can equilibrate in the material in scenario 3; in this relaxed scenario, all pores have the same pore pressure. The combination of poroelasticity and effective-medium theory allows us to derive high- and low-frequency moduli and to predict elastic-wave dispersion (Le Ravalec et al., 1996; Boutéca and Guéguen, 1999). The elastic moduli for materials of any of the scenario types are calculated in four steps: a) determination of the effective elastic moduli of the porous grain material, b) determination of the effective elastic moduli of the dry aggregate at critical porosity ($\phi_i = \phi_{ic}$), c) determination of the effective elastic moduli of the dry aggregate in the entire porosity domain, and d) determination of the effective elastic moduli of the saturated aggregate.

Combinations of these scenarios can also give rise to different scenarios with different degrees of fluid relaxation, for instance, some grains having isolated pores and some having connected intergranular porosity.

For a porous grain material of type (a), the fluid inside the pores will remain isolated at ultrasonic frequency, and the elastic properties of the porous grains can be estimated using DEM, which corresponds to a model with isolated pores or the high-frequency approximation.

5.4 Effective elastic moduli of the porous grain material

The effective bulk (K_g) and shear (G_g) moduli of the liquid saturated porous grain material, in the three porous grain scenarios, are calculated using DEM (Appendix A) and the combination DEM/Gassmann, for the low- and high-frequency estimations, respectively. For the low-frequency elastic moduli with DEM/Gassmann, we first assume that the porous grain is dry, use DEM to find the grain-dry-frame elastic moduli, K_{g-dry} and shear G_{g-dry}, and then use Gassmann's (1951) fluid substitution to determine the bulk, K_{g-sat}, and shear, G_{g-sat}, moduli of the fluid-saturated grain. The input parameters in DEM (Norris, 1985) are the intragranular porosity (ϕ_g) and aspect ratios (α_g) of the ellipsoidal intragranular inclusions.

For a saturated porous grain material of type mentioned in scenario 1, the fluid inside the pores will remain isolated at ultrasonic frequency, and the elastic moduli of the porous grains can be estimated using the DEM method. This corresponds to a model with isolated pores or the high-frequency range of acoustic waves (Mavko, at al., 1998). If an external hydrostatic pressure (isotropic) is applied in this jacketed aggregate of porous grains, generally the pore pressure P_g in each intragranular inclusion and the pressure in the intergranular pore space P_i will all be different.

For a scenario 2 porous-grain material, the elastic properties of the grains can be estimated using the DEM method for the high-frequency approximation (such as ultrasonic measurements). The DEM/Gassmann method can be used for the low-frequency approximation (e.g., well logs), because the fluid inside the pores can communicate, and fluid may flow from one pore to another, but no bulk flow takes place through the porous grain (O'Connell and Budiansky, 1977). If an external hydrostatic pressure is applied to the aggregate, the pressures in all intragranular inclusions are equal $P_g = P_{g1} = P_{g3} = ... = P_{gn}$, but will differ from P_i (Figure 5.2b). To compute the

effective elastic properties of the saturated porous grain using DEM/Gassmann, we first use DEM to find the dry-frame elastic moduli of a single grain with specific inclusion aspect ratios (Appendix A), and then use Gassmann's (1951) fluid substitution to arrive at the results for the water-saturated porous grain (DEM/Gassmann). Gassmann's fluid substitution assumes that the shear modulus of the fully fluid-saturated porous grain is that of the dry frame ($G_{sat} = G_{dry}$), while its bulk modulus is

$$K_{g-sat} = K_s \frac{\phi_g K_{g-dry} - (1+\phi_g) K_f K_{g-dry}/K_s + K_f}{(1-\phi_g) K_f + \phi_i K_s - K_f K_{g-dry}/K_s}, \tag{5.1}$$

where K_f is the bulk modulus of the intragranular fluid.

The difference between scenario 3 and scenario 2 is that if an external hydrostatic pressure is applied to the aggregate and the system is allowed to equilibrate, P_g will equal P_i. If a high-frequency external pressure is applied, depending on how high the frequency is with respect to flow, the material of scenario 3 either may or may not allow fluid diffusion inside each porous grain or between grains, and its elasic behaviour may be different or similar to materials for scenarios 1 and 2. For a porous-grain material of scenario 3, the elastic properties of the saturated grains can be estimated using the DEM method for the high-frequency approximation, and the DEM-Gassmann method for the low-frequency approximation, as in scenario 2.

We compute the elastic properties of the dry grain and then the dry aggregate using the DEM method and a granular medium model, respectively, and then to account for the intragranular and intergranular porosities for the saturated sample we use Gassman's equation. In this case the porosity to be input into Gassmann is the total porosity, instead of the intergranular porosity, and the properties of the solid phase are the properties of the grain skeleton material.

The elastic properties of fluid-saturated aggregates corresponding to each of these scenarios will depend on how fluids are distributed in the pore space. For instance, regardless of the saturation state of the intergranular pore space (dry, partially or fully fluid saturated), the intragranular pore space may be dry or partially or fully fluid saturated.

5.5 Effective elastic moduli of the dry porous grain aggregate close to critical porosity

Once the density (ρ_g), and bulk (K_g) and shear (G_g) moduli of the porous grain material are determined, we consider the properties of an aggregate of such homogenized grains in the high intergranular porosity range, close to and below the critical porosity (Figure 5.1b).

To determine the effective dry bulk (K_{dry}) and shear (G_{dry}) moduli for a dense random aggregate of identical elastic spheres at high intergranular porosities, several granular-medium approximations are available (Mindlin, 1949; Walton, 1985; Digby, 1981; Jenkins et al., 2005).

The dry bulk (K_{dry}) and shear (G_{dry}) moduli with the Walton's model (Walton, 1987; Digby, 1981) are (Jenkins, 2005)

$$K_{dry}^{(W)} = \frac{C(1-\phi_i)G_g}{3\pi(1-\nu_g)}\left[\frac{3\pi}{2}\frac{(1-\nu_g)}{(1-\phi_i)C}\frac{P_d}{G_g}\right]^{1/3}, \quad G_{dry}^{(W)} = \frac{3K_{dry}^{(W)}}{5}\frac{\left[2-\nu_g+3\gamma(1-\nu_g)\right]}{\left(2-\nu_g\right)} \quad (5.2)$$

where ν_g is the Poisson's ratio of the porous grains; P_d is the differential pressure (i.e., the difference between the overburden or confining pressure and the pore pressure) acting upon the aggregate; C is the average number of contacts per grain, or the coordination number; and γ is the coefficient of friction, a number which represents the friction between two grain contact and describes the strength of the transverse stiffness of the grain-to-grain contact. When $\gamma = 0$ the surface is considered smooth, which means that it does not exert any frictional force (perfect slip), whereas when $\gamma = 1$ the surface is considered infinitely rough, offering infinite frictional resistance (perfect stick). Walton's model (W) assumes that the relative displacement of the center of the contacting particles is given by the average strain. A consequence of this assumption is that $K_{dry}^{(W)}$ does not depend on $\gamma = 0$, because the transverse forces do not enter at all into this average strain approximation (Jenkins et al., 2005).

In rocks, the grain surface has asperities that make it rough, it is never infinitely smooth. The surfaces of two grain in contact are infinitely rough if they are welded. When the grain surfaces in contact are dry, motions of the two bodies in a direction

parallel to the touching surfaces is obstructed due to molecular adhesion and/or irregularities on the grain surfaces (Figure 5.3). When a thin film of fluid is present between the grains, the two grain surfaces are not in direct contact and friction will try to impede the motion between the two grain surfaces as well. The presence of the fluid on the grain surface reduces the friction coefficient (Persson et al., 2005). Mixed friction, which is in between these two extreme cases of perfect slip and perfect stick grain surfaces, occurs during the start-up of motion when the separating lubricant fluid film is not fully developed.

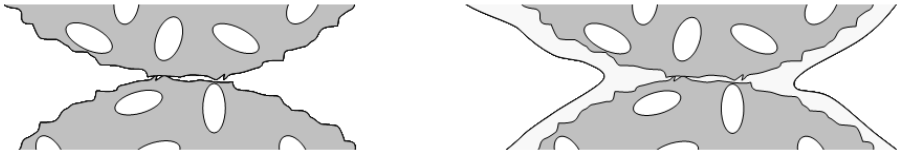

Figure 5.3. Left: dry grain surfaces in contact (dry friction). Right: wet grain surfaces in contact (lubricated friction).

5.6 Effective elastic moduli of the dry aggregate in the entire porosity domain

The assumptions made in Walton's model are appropriate only for high-porosity aggregates, close to and below the intergranular critical porosity (ϕ_{ic}), so they should not be used to estimate the effective moduli of the aggregate at low intergranular porosities. To estimate the elastic properties far from the critical porosity we will use a heuristic approach proposed by Dvorkin and Nur (1996) and Gal et al. (1998), which is basically an estimation of lower or upper bounds of the effective elastic moduli of the aggregate in the entire porosity domain.

To calculate the bulk and shear moduli of the aggregate two porosity domains are examined: one where $\phi_i \le \phi_{ic}$, and the other where $\phi_i > \phi_{ic}$, the consolidated-aggregate domain (grain-supported aggregate) and the suspension domain (fluid-supported suspension) (Nur et al., 1998), respectively. ϕ_{ic} is about 0.36 for a random aggregate of identical spherical (Nur et al., 1998). At this porosity a transition in the elastic property behavior occurs. When ϕ_{ic} = 0.36 and ϕ_{ic} = 0.30, the total critical porosity (ϕ_{tc}), using Equation 4.1, is $\phi_{tc} = \phi_g + \phi_{ic}(1-\phi_g) = 0.552$.

In the consolidated-aggregate domain where $\phi_i \le \phi_{ic}$, the elastic model connects two end-points in the elastic-modulus-porosity plane: the effective moduli at $\phi_i = 0$ (which are simply the moduli of the porous grain) and the moduli of a dense random aggregate of identical elastic porous spheres (with fluid-filled inclusions) at $\phi_i = \phi_{ic}$. In order to interpolate between these two end points, we use the lower Hashin-Shtrikman bound, rescaled from the 0 to 1 porosity range to 0 to ϕ_{ic}. Specifically, the effective bulk (K_{dry}) and shear (G_{dry}) moduli of the dry granular frame comprised of fluid-saturated porous grains are

$$K_{dry} = \left[\frac{\phi_i / \phi_{ic}}{K^{(W)}\Big|_{\phi i=\phi_{ic}} + \frac{4}{3} G^{(W)}\Big|_{\phi i=\phi_{ic}}} + \frac{1-\phi_i / \phi_{ic}}{K_g + \frac{4}{3} G^{(W)}\Big|_{\phi i=\phi_{ic}}} \right]^{-1} - \frac{4}{3} G^{(W)}\Big|_{\phi i=\phi_{ic}},$$

$$G_{dry} = \left[\frac{\phi_i / \phi_{ic}}{G^{(W)}\Big|_{\phi i=\phi_{ic}} + Z_1} + \frac{1-\phi_i / \phi_{ic}}{G_g + Z_1} \right]^{-1} - Z_1,\ Z_1 = \frac{G_C}{6} \left[\frac{9K^{(W)}\Big|_{\phi i=\phi_{ic}} + 8G^{(W)}_{dry}\Big|_{\phi i=\phi_{ic}}}{K^{(W)}\Big|_{\phi i=\phi_{ic}} + 2G^{(W)}\Big|_{\phi i=\phi_{ic}}} \right], \tag{5.3}$$

where $K^{(W)}\Big|_{\phi i=\phi_{ic}}$ and $G^{(W)}\Big|_{\phi i=\phi_{ic}}$ are the moduli of the dry aggregate at ϕ_{ic}, estimated using Equation 5.2.

In the fluid supported suspensions domain where $\phi_i > \phi_{ic}$, the two end-points are $\phi_i = \phi_{ic}$ and at $\phi_i = 1$. At $\phi_i = \phi_{ic}$ the effective elastic moduli K_{dry} and G_{dry} are equal to $K^{(W)}\Big|_{\phi i=\phi_{ic}}$ and $G^{(W)}\Big|_{\phi i=\phi_{ic}}$, while at $\phi_i = 1$ they are simply zero. To interpolate between these end-points we use (Dvorkin and Nur, 1996; Dvorkin and Prasad, 1999)

$$K_{dry} = \left[\frac{(1-\phi_i)/(1-\phi_{ic})}{K^{(W)}\Big|_{\phi i=\phi_{ic}} + \frac{4}{3} G^{(W)}\Big|_{\phi i=\phi_{ic}}} + \frac{(\phi_i - \phi_{ic})/(1-\phi_{ic})}{\frac{4}{3} G^{(W)}\Big|_{\phi i=\phi_{ic}}} \right]^{-1} - \frac{4}{3} G^{(W)}\Big|_{\phi i=\phi_{ic}},$$

$$G_{dry} = \left[\frac{(1-\phi_i)/(1-\phi_{ic})}{G^{(W)}\Big|_{\phi i=\phi_{ic}} + Z_1} + \frac{(\phi_i - \phi_{ic})/(1-\phi_{ic})}{Z_1} \right]^{-1} - Z_1. \tag{5.4}$$

We call this model, which is appropriate for soft sediment with porous grains, the dry-PGSO model. A counterpart to the dry-PGSO model is the dry-PGST model, which

is more appropriate for stiff sediment with porous grains. The only difference between the two is for $\phi_i < \phi_{ic}$ (Figure 5.1). In this porosity range, the same two end-points, one at zero porosity and the other at the critical porosity, are connected by the modified upper Hashin-Shtrikman bound (Gal, et al., 1998). As a result, we obtain

$$K_{dry} = \left(\frac{\phi_i / \phi_{ic}}{K^{(W)}\Big|_{\phi i=\phi_{ic}} + \frac{4}{3}G_g} + \frac{1-\phi_i / \phi_{ic}}{K_g + \frac{4}{3}G_g}\right)^{-1} - \frac{4}{3}G_g,$$
$$G_{dry} = \left(\frac{\phi_i / \phi_{ic}}{G^{(W)}\Big|_{\phi i=\phi_{ic}} + Z_2} + \frac{1-\phi_i / \phi_{ic}}{G_g + Z_2}\right)^{-1} - Z_2, \quad Z_2 = \frac{G_g}{6}\left(\frac{9K_g + 8G_g}{K_g + 2G_g}\right). \tag{5.5}$$

In the above models, the total porosity (ϕ_t) should always be greater than or equal to the intragranular porosity (ϕ_g). That is why the schematic velocity-porosity curves in Figure 5.1b are within the $\phi_g \le \phi_t \le 1$ interval.

Notice that K_g and G_g refer to the elastic moduli of the porous-grain material after homogenization. Thus, they may correspond to the effective elastic moduli of a dry or saturated grain. On the other hand, K_{dry} and G_{dry} refer to the properties of the aggregate in the entire porosity domain when there is no fluid in the intergranular pore space, but there can be fluid in the intragranular space.

5.7 Effective elastic moduli of the saturated aggregate

In all three of the above scenarios, once the elastic properties of the dry aggregate are determined by the dry-PGSO or dry-PGST models for $0 \le \phi_i \le \phi_{ic}$, we can account for the effects of the intergranular porosity on the undrained elastic properties. For the low-frequency approximation, we input the effective properties of the dry aggregate into Gassmann's equations; for the high-frequency velocity approximation, we use DEM.

Gassmann's fluid substitution assumes that the shear modulus of the fully fluid-saturated aggregate is that of the dry frame ($G_{sat} = G_{dry}$), while its bulk modulus

$$K_{sat} = K_g \frac{\phi_i K_{dry} - (1+\phi_i) K_f K_{dry} / K_g + K_f}{(1-\phi_i) K_f + \phi_i K_g - K_f K_{dry} / K_g}, \tag{5.8}$$

where K_f is the bulk modulus of the fluid. Notice that K_{sat} and G_{sat} refer to the elastic moduli of the aggregate, when the intergranular pore space is fully fluid saturated, but

there may or may not be fluid in the intragranular space. If the elastic properties of the fluid-saturated grains are computed using DEM/Gassmann or DEM alone, K_{sat} and G_{sat} correspond to the low-frequency (LF) and high-frequency (HF) effective bulk and shear elastic moduli, respectively. If both the elastic properties of the porous grains, K_g and G_g, and the properties of the aggregate, K_{sat} and G_{sat}, are computed using DEM instead of Gassmann, then K_{sat} and G_{sat} correspond to an even higher-frequency (VHF) approximation.

Finally, the *P*- and *S*-wave velocities and bulk density for the dry or saturated aggregate are given by,

$$\rho_{dry} = (1-\phi_i)\rho_g, \qquad V_{p-dry} = \sqrt{(K_{dry} + \frac{4}{3}G_{dry})/\rho_{dry}}, \qquad V_{s-dry} = \sqrt{G_{dry}/\rho_{dry}}, \tag{5.9}$$

and

$$\rho_{sat} = \rho_{dry} + \phi_i \rho_f, \qquad V_{p-sat} = \sqrt{(K_{sat} + \frac{4}{3}G_{sat})/\rho_{sat}}, \qquad V_{s-sat} = \sqrt{G_{sat}/\rho_{sat}}. \tag{5.10}$$

where ρ_s is the density of the grain skeleton mineral and $\rho_g = (1-\phi_g)\rho_s + \phi_g \rho_f$.

To compute the very-high-frequency elastic properties of the saturated aggregate using DEM, we first look for the hypothetical aspect ratios (α_i) required to fit the effective V_{p-dry} velocities of the dry aggregate by DEM. Then, the DEM method is applied again, assuming that the hypothetical inclusions with aspect ratio α_i are filled with fluid, to arrive at the results for water-saturated aggregate (Ruiz et al., 2009). We attempt to match the overwhelming complexity of the homogenized grain aggregate behavior with a single effective α_i (Figure 5.4). When doing so, we need to stress that this method is based on significant examples with real siliciclastic and carbonate rock data (Ruiz and Dvorkin, 2009), i.e. Chapter 3.

We need to highlight that here we simply use DEM to find the aspect ratio of an equivalent material that will provide exactly the same elastic properties at the same porosity as given by the granular-medium theories (Figure 5.4). Of course, there are not single-aspect-ratio cracks in granular aggregates. The analytical transform used here is purely analytical and does not refer to the true geometry of the pore space. The main

point is that DEM can mimic the elastic properties of the aggregate if an appropriate single aspect ratio is assigned to this model. Moreover, the hypothetical aspect ratio is nothing more than a fitting parameter.

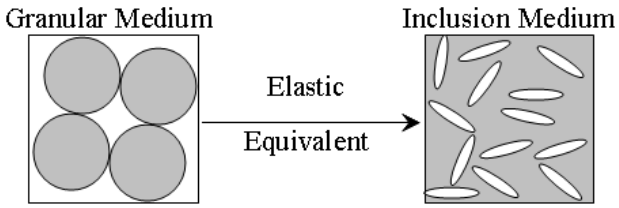

Figure 5.4. Two idealized equivalent physical models, analogues to real soft sands. One is a random dense aggregate of spherical grains and the other is a continuous matrix with isolated random distributed spheroidal pores of a specific aspect ratio, α_i. The elastic equivalency is achieved by finding the α_i needed to match the DEM predictions with those according to the porous-grain aggregate model.

5.8 Elastic moduli of the fluid

The porous grain models allow us to have a fluid type in the intragranular pore space different from that in the intergranular space. It also allows us to have mixtures of fluids. When there is more than one pore fluid type with different fluid bulk moduli (e.g., gas, oil and water), in one of the pore spaces, each fluid phase tends to have a different induced pore pressure (Mavko et al., 2009) and in consequence different bulk moduli. The effective bulk modulus of this fluid mixture, K_f, can be determined in several ways, depending on the assumption made about how fluids are spatially mixed. When the fluid phases are thoroughly mixed at the finest scales, these pore pressure variations can equilibrate with each other to a an average value. This is an isostress state, and as a result K_f is described well by the Reuss average as

$$\frac{1}{K_f} = \sum_{i=1}^{n} \frac{S_{fi}}{K_{fi}}, \tag{5.11}$$

This K_f is the bulk modulus that must be inserted into Gassmann's relation (Domenico, 1976; Murphy, 1984; Mavko and Nolen-Hoeksema, 1994, Cadoret, 1993; Mavko et al., 2009) when computing the wet moduli from the dry moduli.

If there are dissolved minerals in the fluids, e.g., salts, they need to be considered in the calculation of K_f, before inserting it into Gassmann's or DEM equations. At in situ

conditions, e.g., as burial depth increases, the properties of the fluid phases vary with the amount and type of dissolved salts, pressure and temperature, so they need to be determined for specific conditions (Batzle and Wang, 1992).

5.9 Numerical examples

Figure 5.5 shows the effects of friction, γ, intragranular aspect ratio and porosity, α_g and ϕ_g, respectively, on the V_p and V_s effective velocities of a hypothetical water saturated porous grain aggregate. This aggregate is assumed to be packed to a spatial-average coordination number $C = 9$. Figures 5.5 and 5.6 show the high frequency PGSO and PGST effective *P*- and *S*- wave velocities, V_p and V_s, respectively. The elastic properties of water are constant and equal to K_f = 2.25 GPa, G_f = 0 GPa and ρ_f =1 g/cm3. The solid phase is assumed to be pure calcite with elastic properties: K_s = 76.8 GPa, G_s = 32 GPa, and ρ_s =2.71 g/cm3. The differential pressure and coordination are constant and equal to 5 MPa and 9, respectively. The parameters γ, α_g and ϕ_g are varied from 0 to 1, from 0.05 to 1 and from 0.1 to 0.3, respectively (Figure 5.5). The V_p and V_s velocities were determined assuming a material described by scenario 2, where the intragranular pores are connected, and the intragranular pores are not connected with the intergranular pores (Figure 5.2b).

For all the selected values of intragranular aspect ratios (α_g) and intragranular porosities (ϕ_g), the effect of α_g and ϕ_g on V_p and V_s is greater than or comparable to the effect of friction coefficient (γ).

Figure 5.6 and 5.7 show the PGSO and PGST effective *P*- and *S*- wave velocities, V_p and V_s, respectively, for the three porous grain scenarios. Figure 5.5 shows the velocities for $\gamma = 0.5$, $\alpha_g = 0.5$ and $\phi_g = 0.2$. Figure 5.6 shows the velocity for the same parameters but using a smaller intragranular aspect ratio, $\alpha_g = 0.1$. The HF and LF velocities are basically the same for the two intragranular aspect rations. The VHF-velocities are significantly higher than the LF- and HF-velocities. We observed the same behavior for the PGST model.

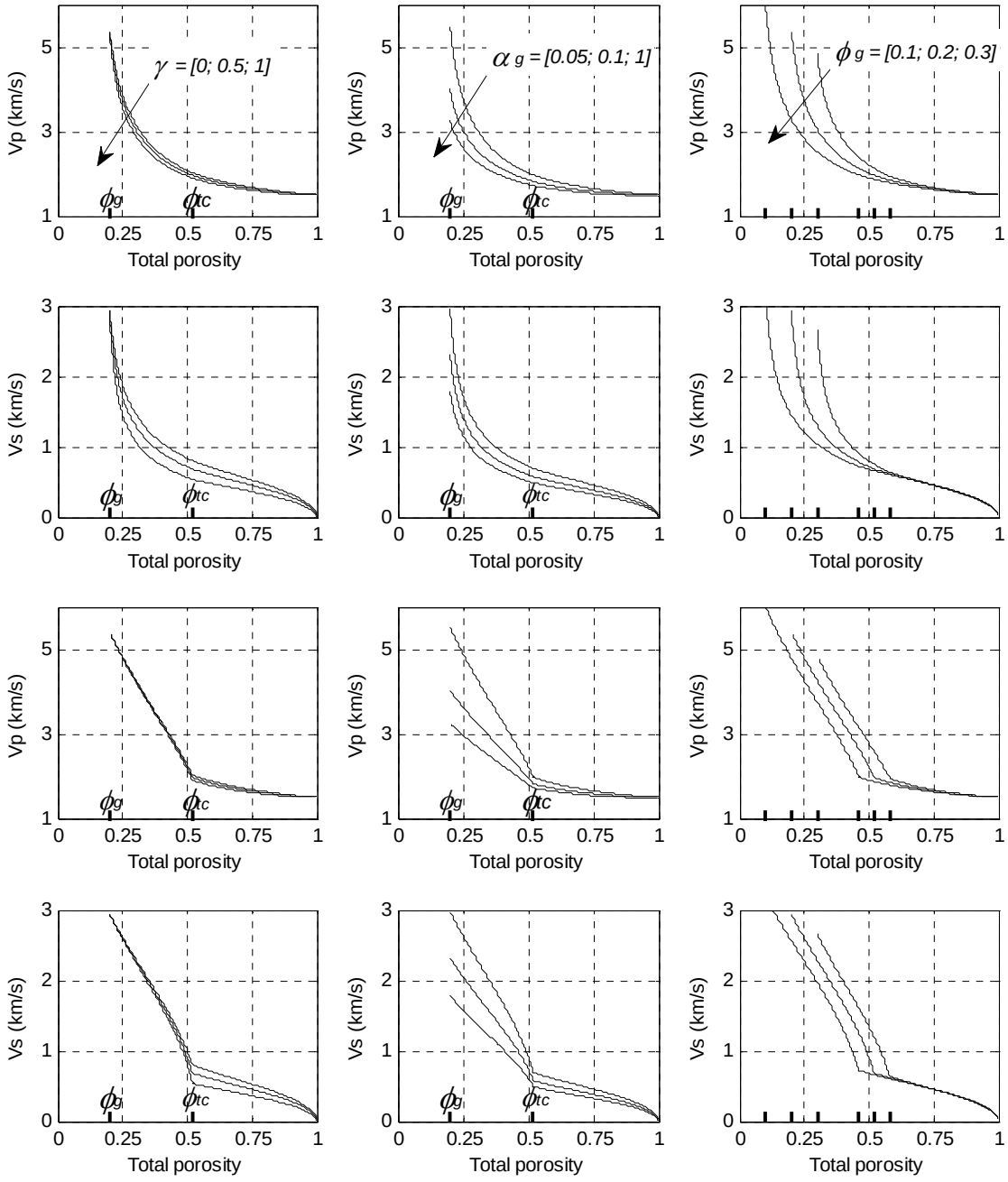

Figure 5.5. V_p and V_s velocities estimated using the PGSO (two upper frames) and PGST (two lower frames) models, assuming a material of scenario-2. Left column frame: effect of friction coefficient (γ). Middle column frame: effect of the intragranular aspect ratio (α_g). Right column frame: effect of the intragranular porosity (ϕ_g).

Figures 5.6 and 5.7 also display the aspect ratios required to fit the dry-aggregate velocity data by DEM. We find that the aspect ratio, α_p and α_s, required for DEM to match the PGSO and PGST V_p- and V_s-dry velocities are remarkably narrow, between 0.05 and 0.2. We find that it is not possible to match the velocities, using a single effective aspect ratio. We need an aspect ratio that increases nearly linear as porosity increases. The aspect ratios to match V_p and those to match V_s are almost the same for both, the PGSO and PGST models.

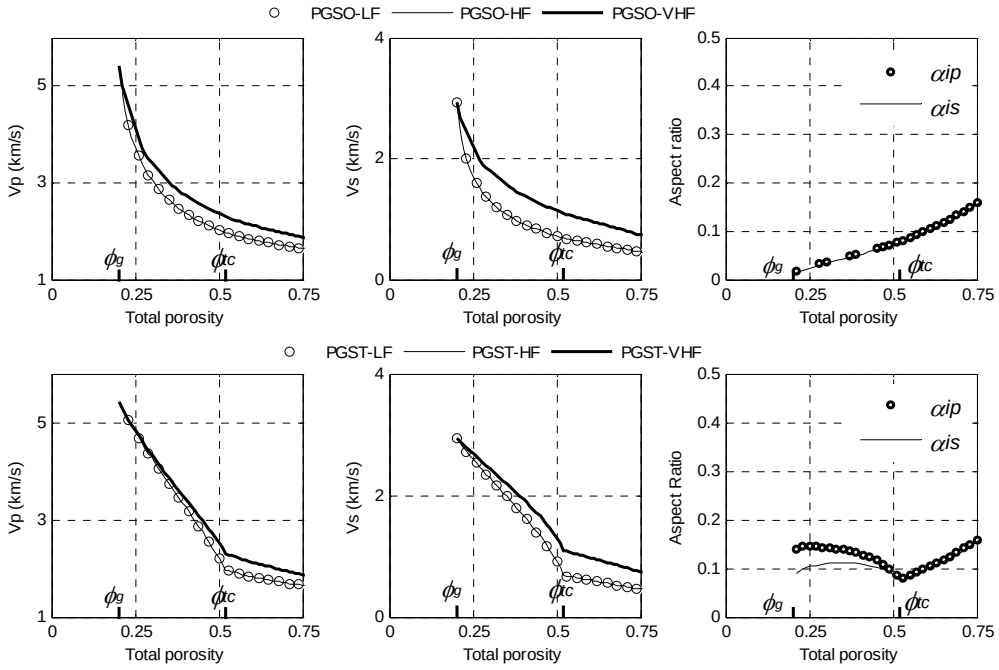

Figure 5.6. Top frames: Comparison of three possible scenarios for the porous grain model: The low frequency PGSO model (PGSO-LF), the high frequency PGSO model (PGSO-HF) and the very high frequency PGSO model PGSO-VHF. The parameters used are $\alpha_g = 0.5$, $\gamma = 0.5$ and $\phi_g = 0.2$. Bottom frames: Comparison of three possible scenarios for PGST model.

Figure 5.8 illustrates the effects of frequency on the V_p and V_s effective velocities. We show the PGSO and PGST effective velocities, computing the effective properties of the porous grains in three ways: using the DEM (PGSO-high frequency) method, using the combination DEM-Gassmann (PGSO-low frequency) method, and VHF. The

intragranular aspect ratios and porosity are 0.05 and 0.30, respectively. The difference between the low- and high-frequency velocities is greater at low porosities, so we can infer that the fluid flow in the intragranular pores has a significant influence only for small aspect ratios. Both PGSO and PGST show similar behavior.

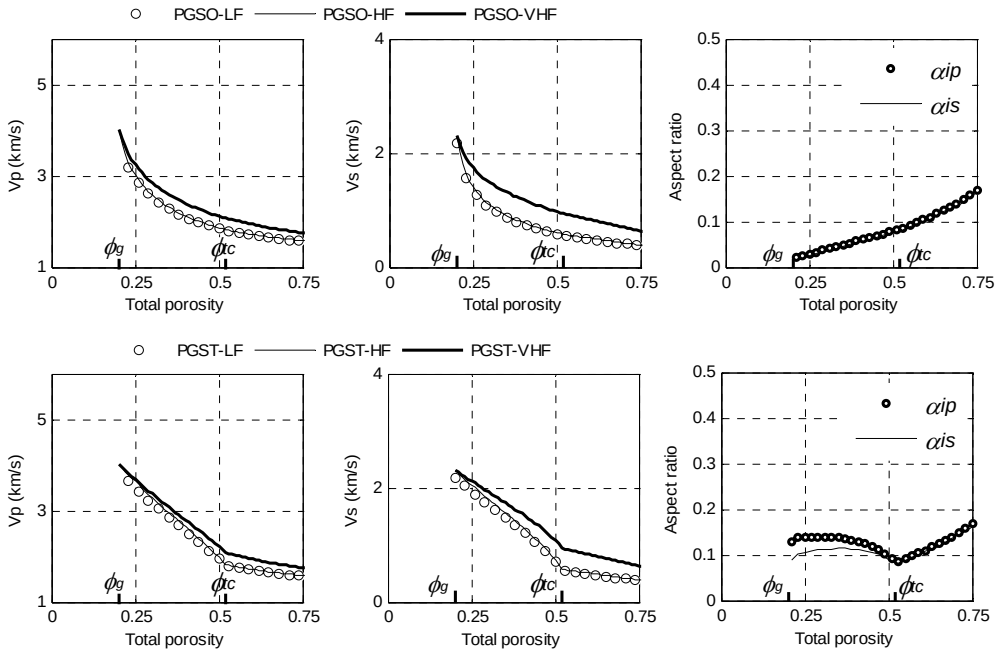

Figure 5.7. The same as Figure 5.4 but for intergranular aspect ratio $\alpha_g = 0.1$.

When $\phi_g = 0$, the grains are solid, and the low-frequency version (LF or HF) of PGSO gives the same results as the soft-sand model (Dvorkin and Nur, 1996), but with the flexibility of having γ as a variable. When $\phi_g = 0$ and $\gamma = 1$, PGSO gives exactly the same result as soft-sand model. The very high-frequency version (VHF) of PGSO gives a high-frequency version of the soft-sand model.

When $\phi_g = 0$, the grains are solid, and the low frequency version (LF or HF) of PGST gives the same results as the stiff-sand model (Gal et al., 1998), but with the flexibility of having a variable friction coefficient (γ). When $\phi_g = 0$ and $\gamma = 1$ PGST gives exactly the same results as stiff-sand model. The very high-frequency version (VHF) of PGST gives a high frequency version of the stiff-sand model, with a variable friction coefficient as well.

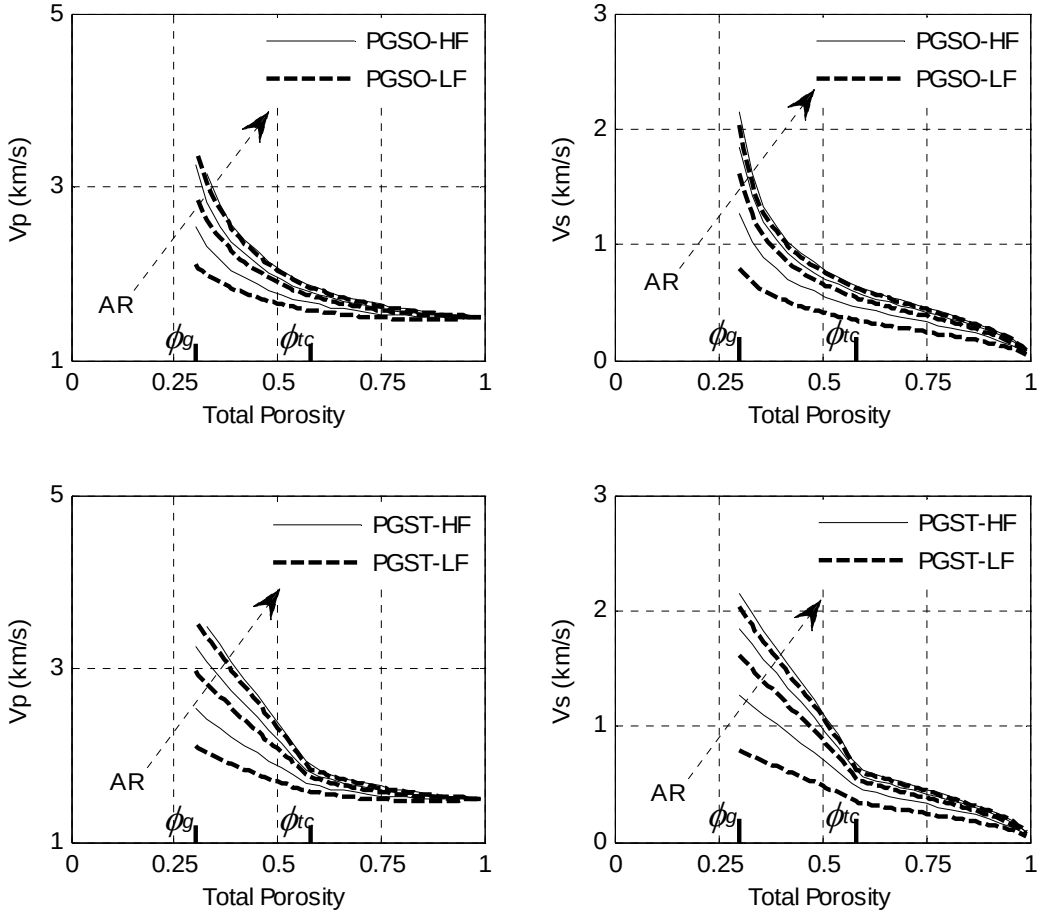

Figure 5.8. Top frames: V_p and V_s PGSO-velocities using DEM (high-frequency) and DEM-Gassmann (low-frequency) for the calculation of the effective properties of the porous grains. The calculation is done for three intragranular inclusions aspect ratios: 0.05, 0.1, and 0.25, and friction coefficient $\gamma = 1$. The arrow indicates the direction of increasing aspect ratios. Bottom frames: Same as top frames, but using the PGST model. We observed the same behavior for the PGST model. LF = low frequency; HF = high frequency.

The VHF-effective V_p and V_s velocities are considerably higher than the HF- and LF-V_p and V_s velocities (Figures 5.6 and 5.7). This is because DEM treats the intragranular and intergranular pore space as isolated inclusions, so all pores are stiff. Part of the intergranular pore space may be in a relaxed or unrelaxed state. However, this is not the situation for ultrasonic frequencies typically used in rock physics (~1MHz), where the propagating wave sees both soft and stiff pores (squirt and global flow). However, DEM is an effective-medium model, so we are also assuming that the dominant wavelength of

the traveling wave is still greater than the local heterogeneities (pores or grains). If the wavelength of the propagating wave were higher than pores and grains, we would have reflections among grains.

The input parameters ϕ_g, α_g, and C used in the porous grain aggregate models can be varied as a function of physical conditions, such as differential pressure (P_d) and temperature. Differential pressure can be estimated by integrating the bulk density log as a function of depth (z),

$$P_d(z) = g\int\left[\rho_b(z) - \rho_f(z)\right]dz\,, \tag{5.12}$$

where g is the gravity constant. As P_d increases with depth ϕ_i decreases and as a result C increases. C is not easily to be measured. C has been determined by counting the contacts in experimental samples (Wadsworth, 1960; Smith et al., 1929; Mavko et al., 2009). C is not directly measurable from a single planar digital image cross section, since it needs a 3-dimensional model. Zhang et al. (1994) investigated the properties of isostatically compacted aggregates calcite aggregates. The calcite specimens were isostatically compacted below to porosity 0.1. They found that at porosity 0.04, the permeability of the calcite aggregate vanished, implying a complete loss of connectivity in the pore space. These experiments provide insights into the evolution of pore-space topology of sedimentary rocks at depth in the Earth's crust. Several porosity-coordination number (ϕ-C) relations have been proposed (Dutta et al., 2009; Garcia and Medina, 2006; Makse et al., 2004; Zhang et al., 1994; Dullien, 1992; Smith and Olague, 1987; Murphy, 1982; Wade, 1964). Murphy (1982) gives an empirical ϕ - C relation, as follows, $C = 20 - 34\phi + 14\phi^2$. Garcia and Medina derived a ϕ - C power-law relation based on fitting data from numerical simulations of granular media, $C = C_o + 9.7(\phi_o - \phi)^{0.48}$, where $C_o = 4.46$ and $\phi_o =$ 0.384, for $\phi \le \phi_o$. Makse et al. (2004) derived a similar relation using numerical simulation of frictionless spheres: $C = 6 + 9.1(\phi_o - \phi)^{0.48}$, where $C_o = 6$ and $\phi_o = 0.37$, for $\phi \le \phi_o$.

The ϕ-C relationship of ordered aggregates (i.e., hexagonal, cubic, orthorhombic) is well-known (Mavko et al., 2009), but for random aggregates, C has to be determined experimentally (Zhang et al., 1994; Smith and Olague, 1987; Wade, 1964). Dutta et al.

(2009) investigated the variation of C with pressure and porosity using the elastic properties measured during the first confining pressure loading cycle of a sand sample from Pomponio Beach measured by Zimmer (2003). They obtain empirical ϕ - C relations by matching granular medium models with experimental data. The increase of pressure during the first loading cycle experiment is analogous to the increase of overburden pressure during burial. During burial, the rock is under an increasing mechanical compaction, and in consequence, the porosity is reduced (Dutta et al., 2009).

The application of one of the specific scenarios described above depends not only on the frequency we are interested in and the description of the medium, but also on physical conditions. If the applied stress field σ on the porous grains is not isotropic, the fluid pressure induced by σ depends on the shape and orientation of the inclusions (Kachanov et al., 1995; Shafiro and Kachanov, 1997) as well as on the frequency of σ. If we assume that the applied external stress field is isotropic and that all inclusions have identical aspect ratios, then P is the same in all intragranular inclusions. Thus, under these assumptions any fluid experiences the same pressure in all pores. This satisfies the Gassmann assumption of the pore-pressure equilibrium. The distributing of randomly oriented identical inclusions gives the correct Gassmann response for bulk modulus, but will not give the correct Gassmann shear modulus, which is the same as the dry-frame shear modulus.

If the intragranular inclusions are distributed randomly, but the applied external stress is not isotropic, then the pressures in individual ellipsoidal pores depend on the orientation of the applied stress, and the DEM method is inconsistent with the Gassmann theory.

If the intragranular inclusions have a preferred orientation, the elastic properties of the porous grain material can be computed applying the anisotropic version of DEM. In this case, the aggregate either may or may not become anisotropic, depending on the orientation of the axis of symmetry of each grain. Under uniaxial stress, σ_1, the aggregate of identical spherical grains is transversely isotropic, and if the grains are infinitely rough, the elastic properties are described by Walton's anisotropic model (Walton, 1987) (Appendix E).

The accuracy of inclusion-based models, e.g., DEM, is in question at high intragranular porosity (Kachanov, 2007; Grechka, 2007). Different inclusion models produce different estimations of elastic moduli (Appendix F). At low frequency, Gassmann predicts the change in the effective elastic moduli caused by a variation in the bulk modulus of fluid filling a fully interconnected pore space at any intragranular porosity, because porosity connectivity ensures pressure equilibrium in the pore fluid without any detailed information about the microstructure. Thus, in contrast to the inclusion models, Gassmann remains correct at arbitrary porosity (Mavko et al., 2009; Grechka, 2007).

To apply the two-staged upscaling scheme explained above, where we first applied DEM to upscaled porous grains and second the modified HS bounds to account for pores between the grains (intergranular pores), we assumed that the pores inside the grains (intragranular micropores) are much smaller than the intergranular pores.

5.10 Aggregate of cemented porous grains

5.10.1 Slightly cemented aggregate of porous grains

In Walton's model (Walton, 1987), it is assumed that the starting framework of uncemented grains is a dense random aggregate of identical spherical grains. Cementation theory (Dvorkin et al., 1994) predicts that even a small amount of contact cement reinforces the grains contact, causing a large increase of the elastic moduli of the aggregate. The initial volume of cement added in the opening between grains is the most important. The effect on the elastic properties of additional cement placed around this initial cement is relatively small. This theoretical prediction has been supported by several experiments (Ying, 1993; Tutuncu et al., 1997). Even by adding cement in the entire intergranular pore space, it is not possible to achieve the high relative stiffness increase produced by small volumes of cement at the grain contacts (Dvorkin et al., 1994; Dvorkin et al., 1999; Ying, 1993; Tutuncu et al., 1997).

If we now assume that the porosity reduction in the porous-grain aggregate is due to cementation exclusively, the porosity ϕ_{ic} of an uncemented sample is decreased to ϕ_i by the addition of a cement material gradually. Once a given volume of cement is added, the

effective bulk and shear elastic moduli of the aggregate of cemented porous grains are calculated as a function of the added cement. For the cemented porous grain model (CPG) the dry effective bulk ($K_{dry}^{(cpg)}$) and shear ($G_{dry}^{(cpg)}$) elastic moduli are given by

$$K_{dry}^{(cpg)} = \frac{1}{6} C(1-\phi_{ic})(K_{Cem} + (4/3)G_{Cem})\hat{S}_N, \qquad \text{and}$$

$$G_{dry}^{(cpg)} = \frac{3}{5} K_{dry}^{(cpg)} + \frac{3}{20} C(1-\phi_{ic}) G_{Cem} \hat{S}_\Gamma \tag{5.13}$$

The parameters $\hat{S}_N$ and $\hat{S}_\Gamma$ are proportional to the normal and shear stiffness, respectively, of a cemented two-grain combination (Mavko et al. 2009). They depend on the amount of contact cement and on the elastic moduli of the cement, K_{Cem} and G_{Cem}, and the homogenized porous-grain, K_g and G_g (Appendix G).

Part of the cement may be deposited at the grain contact and part away from it, so the radius "a" of the contact cement layer is not directly correlated to the amount of cement (Figure 5.9). The amount of contact cement, β, can be expressed as follows,

$$\beta = \frac{a}{R} = \begin{cases} 2\left[\dfrac{\phi_{ic}-\phi}{3C(1-\phi_{ic})}\right]^{0.25} & \text{if all cement is at the grain contact (Scheme - 1)} \\ \left[\dfrac{2(\phi_{ic}-\phi)}{3(1-\phi_{ic})}\right]^{0.5} & \text{if all cement is evenly on the grain surface (Scheme - 2)} \end{cases} \tag{5.14}$$

If by adding cement gradually ϕ_i is reduced to ϕ_{io}, $\phi_{ic} - \phi_{io}$ is the pore space of the uncemented aggregate occupied by cement in the cemented aggregate.

To account for the effects of intergranular porosity on the undrained elastic moduli, $K_{sat}^{(cpg)}$ and $G_{sat}^{(cpg)}$, we input the elastic moduli of the dry cemented porous-grains aggregate, $K_{dry}^{(cpg)}$ and $G_{dry}^{(cpg)}$, into Gassmann's equations or DEM, for the low- or high-frequency approximation, respectively.

In order to use Gassmann's equation we also need to input the elastic properties of the solid phase. The solid phase is a mixture of cement and homogenized grain materials. At $\phi_i = \phi_{ic}$, the solid phase has the elastic properties of the properties of the homogenized porous grain material. For porosities between ϕ_{io} and ϕ_{ic}, the elastic moduli of the porous-grain/cement mixture is determined using the coherent potential approximation

(Berryman, 1980) and density is given by

$$\rho_h = (1-\phi_{tc}+\phi_t)\rho_g + (\phi_{tc}-\phi_t)\rho_{cem}\,, \tag{5.15}$$

where ρ_{cem} is the density of the cement material .

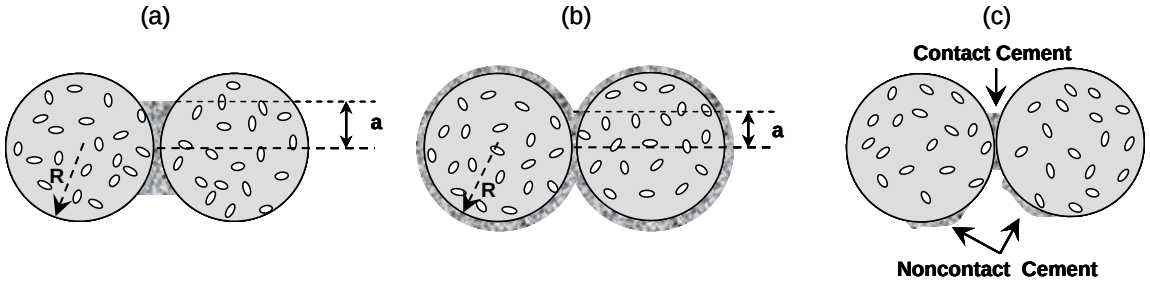

Figure 5.9. Cement schemes. a) cement at the gaps between grains (Scheme 1). b) Coat cement (Scheme 2). c) Contact and noncontact cement (Scheme 3).

For porosities between $\phi_{io} < \phi_i < \phi_{ic}$, the velocities and density of the dry porous grain aggregate are

$$\rho_{dry} = (1-\phi_t)\rho_h\,, \qquad V_{p-dry}^{(cpg)} = \sqrt{(K_{dry}^{(cpg)} + \frac{4}{3}G_{dry}^{(cpg)})/\rho_{dry}}\,, \qquad \text{and}$$

$$V_{s-dry}^{(cpg)} = \sqrt{G_{dry}^{(cpg)}/\rho_{dry}}\,. \tag{5.16}$$

The velocities and density of the saturated porous grain aggregate for porosities between ϕ_{io} and ϕ_{ic} are

$$V_{p-sat}^{(cpg)} = \sqrt{(K_{sat}^{(cpg)} + \frac{4}{3}G_{sat}^{(cpg)})/\rho_{sat}}\,, \qquad V_{s-sat}^{(cpg)} = \sqrt{G_{sat}^{(cpg)}/\rho_{sat}} \qquad \text{and} \tag{5.17}$$

$$\rho = (1-\phi_t)\left[(1-\phi_{tc}+\phi_t)\rho_g + (\phi_{tc}-\phi_t)\rho_{cem}\right] + \phi_t\rho_f\,. \tag{5.18}$$

If cement is present in enough abundance, it may be assumed that the intragranular pores are not hydraulically connected to the intergranular porosity.

The cement model is appropriate for a low volume fraction of cement. At high cement concentrations, an inclusion model may be more appropriate.

Figures 5.10 and 5.11 show the effect of frequency and cement scheme on the effective V_p and V_s of a hypothetical water saturated cemented porous grain aggregate. In

this example, the elastic properties of water are constant and equal to K_f = 2.25 GPa, G_f = 0 GPa, and ρ_f = 1 g/cm3. The solid phase is assumed to be pure calcite with elastic properties K_s = 76.8 GPa, G_s = 32 GPa, and ρ_s =2.71 g/cm3 and the cement is also calcite with the same elastic properties. C is constant and equal 9. The intergranular porosity ϕ_{io} = 0.18, which corresponds to a total porosity ϕ_{to} = 0.426. The critical intergranular porosity ϕ_{ic} = 0.4, which correspond to a total porosity ϕ_t = 0.58.

Figure 5.10 shows the velocities for cement scheme 2, when γ = 0.5 and ϕ_g = 0.3, and when α_g = 0.5 and α_g = 0.15. Figure 5.11 shows the HF velocities (scenario 2) for the same parameters as Figure 5.10, but for the two different cement schemes 1 and 2.

Figure 5.12 shows the V_p and V_s effective velocities predicted by CPG, PGSO, PGST, and Walton's model of a hypothetical water saturated aggregate. The cement and solid matrix materials are assumed to be pure calcite. The initial porosity for the PGSO, PGST, and Walton's models is ϕ_{ic} and for the CPG model is $\phi_o < \phi_{ic}$. The friction coefficient and intergranular critical porosity used in the PGSO and Walton's model are γ = 0 and ϕ_{ic} = 0.4, respectively. The friction coefficient for the PGST model is γ = 1. All other parameters are the same as those used in Figure 5.10. PGSO (γ = 0) and PGST (γ = 1) act as upper and lower elastic constraints. The predictions of Walton's and cement models are close to the lower and upper bound, respectively.

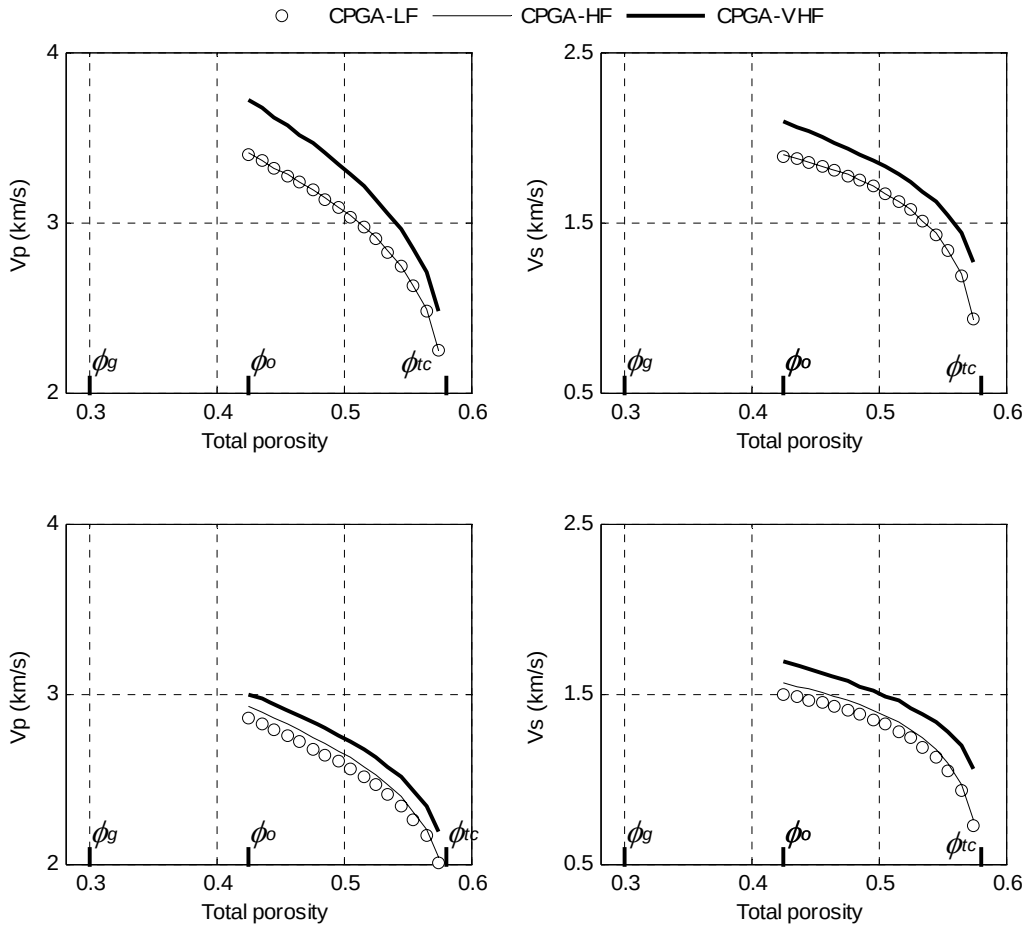

Figure 5.10. CPG V_p and V_s velocities for the cemented aggregate using cement scheme 2. Top frame: intragranular aspect ratio α_g = 0.50. Bottom frame: intragranular aspect ratio α_g = 0.15. The cement and solid matrix materials are assumed to be pure calcite.

5.10.2 Highly cemented aggregate of porous grains

The assumptions made in cementation theory (Dvorkin et al., 1994) are appropriate for high-porosity cemented aggregates, where only a small amount of cement is placed in the area close to the contact between grains. When the volume of cement in the intergranular pore space is high, the intergranular porosity and the connectivity among pores are reduced. For the determination of the elastic moduli of greatly cemented aggregate, an inclusion model is more appropriate because it is more consistent with the material microstructure than a granular-medium model. Thus, to determine the elastic properties of the aggregate in the entire porosity domain, it is necessary to combine

inclusion model with granular-medium model. None of these theories alone provide control over the detailed microstructure of the cemented aggregate at all cement concentrations (Dvorkin et al. 1999).

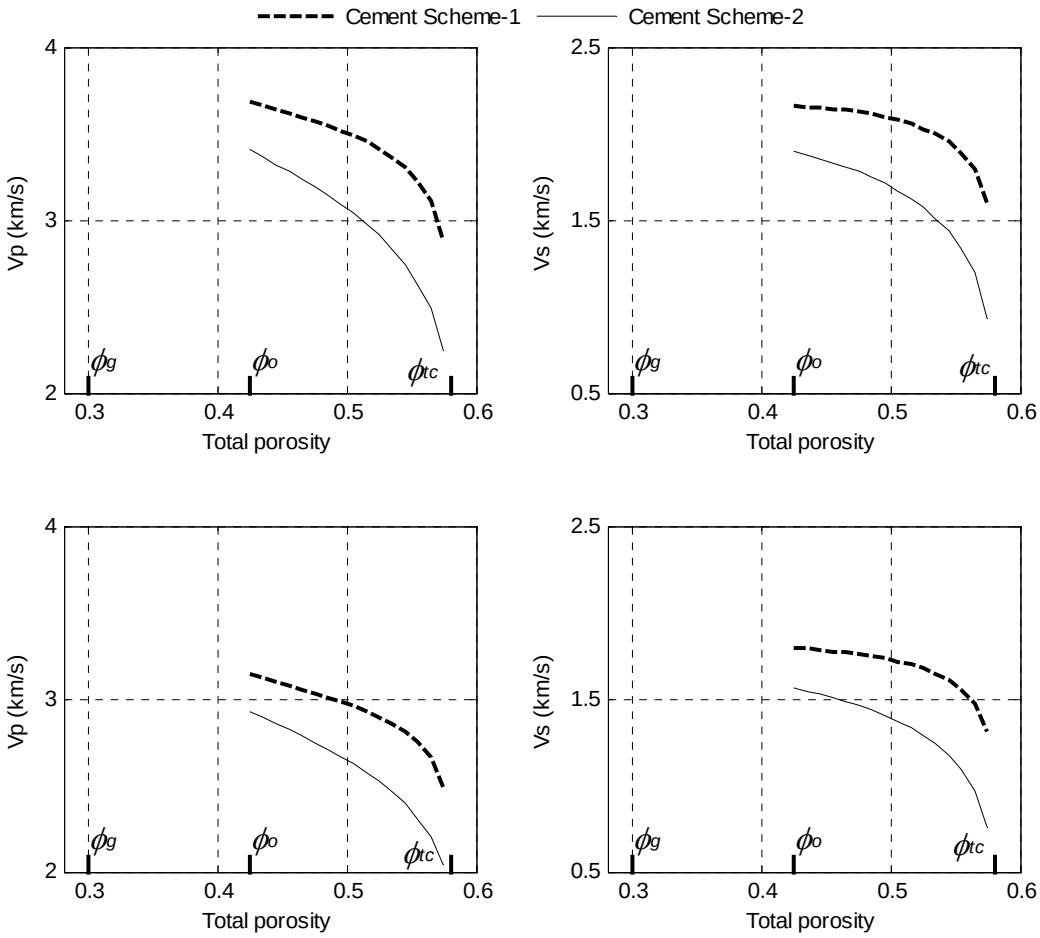

Figure 5.11. CPG V_p and V_s velocities for the cemented aggregate using cement squeme -1 and -2. Top frame: for intragranular aspect ratio α_g = 0.5. Botton frame: for intragranular aspect ratio α_g = 0.15. The cement and solid matrix materials are assumed to be pure calcite.

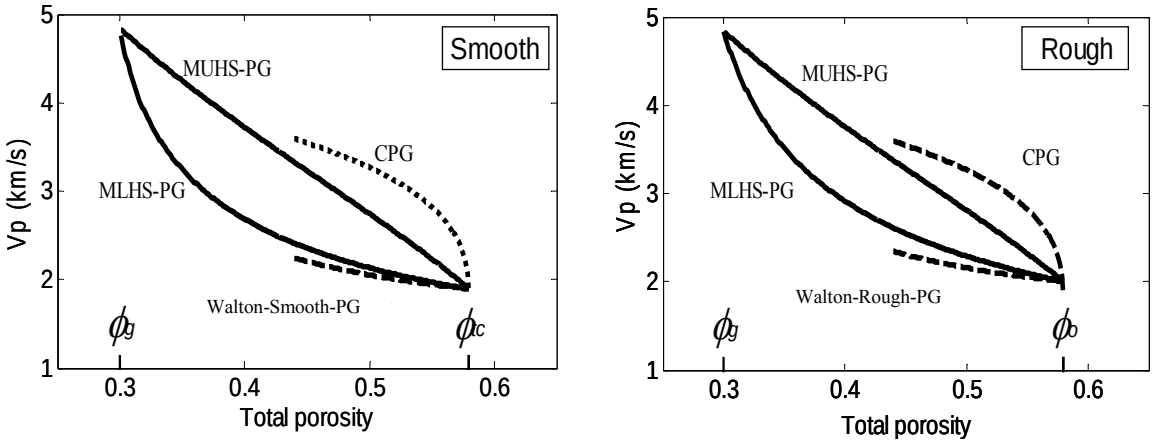

Figure 5.12. Comparison of V_p and V_s velocities for the cemented aggregate using CPG, PGSO, PGST, and Walton's model smooth (left) and rough (right)

The elastic properties of a well cemented aggregate can be determined following the same method proposed by Dvorkin et al. (1999). To calculate the bulk and shear moduli of the aggregate we examine two porosity domains: one where $\phi_{io} \le \phi_i \le \phi_{ic}$ and the other where $0 < \phi_i < \phi_{io}$; the granular medium domain, where the porous grain cementation theory (CPG) is applied; and the inclusion-porosity domain, where the CPA model is applied. The elastic moduli K_{ct} and G_{ct}, at $\phi_i = \phi_{io}$ are given by the CPG theory. In the inclusion porosity domain we use the coherent potential approximation (CPA) to connect the end points: the first at $\phi_i = \phi_{io}$ (Figure 5.13a), which corresponds to a small cement concentration $\phi_{ic} - \phi_{io}$, where the effective moduli of the aggregate are accurately given by the CPG model; and the second at 100% cement concentration (Figure 5.13c), where the intergranular porosity is zero and the effective moduli of the aggregate are given by the coherent potential approximation (CPA).

Case A

The cemented aggregate is a three-phase system composed of a hypothetical homogenized porous grain, cement, and pores. At $\phi_i = \phi_{io}$ the CPA model treats the cemented aggregate as an elastically equivalent two-phase system of pores in a homogeneous hypothetical matrix (Figure 5.13a). The shear and bulk moduli of this hypothetical matrix, K_h and G_h , are found by solving the coherent potential

approximation (CPA) equations for spherical inclusions, as follows,

$$(1-\phi_i)(K_h - K_{ct})P_h + \phi_i(K_f - K_{ct})P_f = 0\,, \tag{5.19}$$

$$(1-\phi_i)(G_h - G_{ct})Q_h + \phi_i(G_f - G_{ct})Q_f = 0\,, \tag{5.20}$$

where $P_{ho} = \dfrac{K_{ct} + (4/3)G_{ct}}{K_h + (4/3)K_{ct}}$, $P_{fo} = \dfrac{K_{ct} + (4/3)G_{ct}}{K_f + (4/3)G_{ct}}$, $Q_{ho} = \dfrac{G_{ct} + Z_{ct}}{G_{ho} + Z_{ct}}$,

$Q_{fo} = \dfrac{G_{ct} + Z_{ct}}{Z_{ct}}$, and $Z_o = \dfrac{G^{(ct)}(9K^{(ct)} + 8G^{(ct)})}{6(K^{(ct)} + 2G^{(ct)})}$

The density of the hypothetical matrix is $\rho_h = (1-\phi_{ic}+\phi_i)\rho_g + (\phi_{ic}-\phi_i)\rho_{cem}$. Since $G_f = 0$ and $K_f = 0$, for the dry case, $G_{dry}^{(h)}$ and $K_{dry}^{(h)}$ are found directly by

$$K_h = \frac{K_{dry}^{(ct)} - \phi K_f P_{fo}}{1 - P_{fo}\phi} = \frac{K_{dry}^{(ct)} G_{dry}^{(ct)}}{(1-\phi)G_{dry}^{(ct)} - (3/4)\phi K_{dry}^{(ct)}} \qquad \text{and}$$

$$G_{dry}^{(h)} = \frac{G_{dry}^{(ct)} Z_o}{Z_o - \phi(Z_o + G_{dry}^{(ct)})}$$

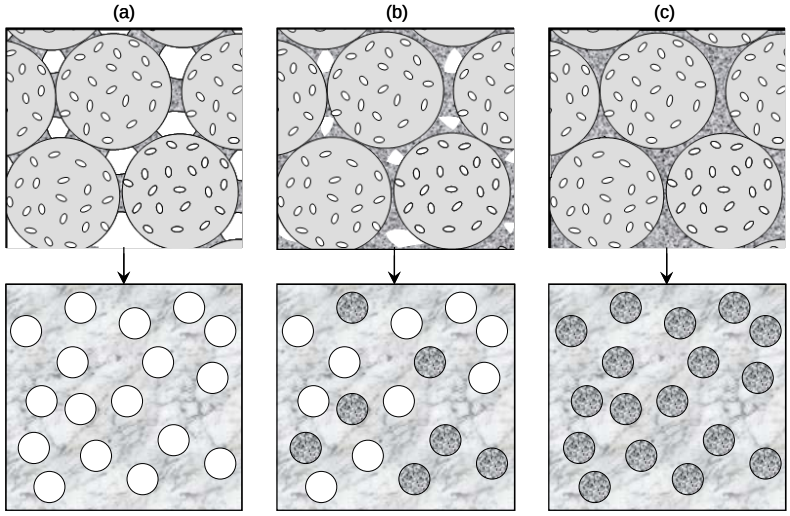

Figure 5.13. Cemented porous grain aggregate using cement scheme 1. Top frame: Cemented aggregate for different cement concentrations. Bottom frame: equivalent elastic media (of the granular media on the top frame) composed of a hypothetical homogeneous matrix with different concentrations of air- and cement-filled pores.

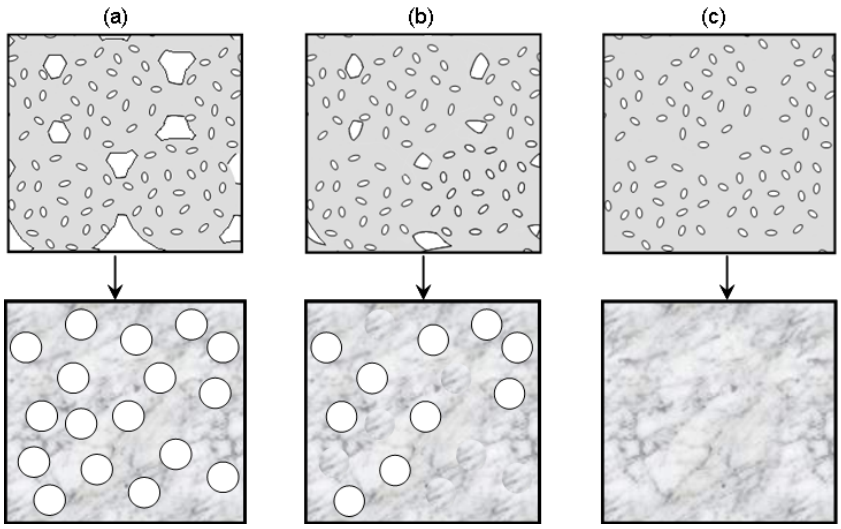

Figure 5.14. The same as Figure 5.13 but the cement and grain are the same minerals.

Case B

To find the moduli of the aggregate with 100% cement, K_{fc} and G_{fc}, we assume that they are identical to those of the homogeneous matrix (from previous step) whose voids are completely filled with cement (Figure 5.13c). The elastic moduli, K_{fc} and G_{fc}, of the matrix when all inclusions are filled with the cement are found by iteratively solving the CPA equations for spherical inclusions, as follows:

$$(1-\phi_{io})(K_h - K_{fc})P_{h1} + \phi_{io}(K_{Cem} - K_{fc})P_{Cem1} = 0 \tag{5.21}$$

$$(1-\phi_{io})(G_h - G_{fc})Q_{h1} + \phi_{io}(G_{Cem} - G_{fc})Q_{Cem1} = 0 \tag{5.22}$$

where $P_{h1} = \dfrac{K_{fc} + (4/3)G_{fc}}{K_h + (4/3)G_{fc}}$, $P_{Cem1} = \dfrac{K_{fc} + (4/3)G_{fc}}{K_{Cem} + (4/3)G_{fc}}$, $Q_{h1} = \dfrac{G_{fc} + Z_{fc}}{K_h + Z_{fc}}$,

$Q_{Cem1} = \dfrac{G_{fc} + Z_{fc}}{G_{Cem} + Z_{fc}}$, and $Z_1 = \dfrac{G_{fc}(9K_{fc} + 8G_{fc})}{6(K_{fc} + 2G_{fc})}$

Case C

If the concentration of the fluid filled inclusion is ϕ_f, the concentration of the cemented inclusions is $\phi_{io} - \phi_f$, and the volumetric fraction of the matrix with respect to

the whole rock is 1-ϕ_{io} (Figure 5.13b). The elastic moduli of the cemented porous grain aggregate, K_{cpa} and G_{cpa}, when only some of the intergranular inclusions are filled with cement and some are air or liquid filled are found by solving iteratively the CPA equations for spherical inclusions, as follows:

$$(1-\phi_{io})(K_h - K_{cpa})P_{h2} + (\phi_{io} - \phi_f)(K_{Cem} - K_{cpa})P_{Cem2} - \phi_f K_f P_{f2} = 0 \tag{5.23}$$

$$(1-\phi_{io})(G_h - G_{cpa})Q_{h2} + (\phi_{io} - \phi_e)(G_{Cem} - G_{cpa})Q_{Cem2} - \phi_e G_f Q_{f2} = 0 \tag{5.24}$$

where

$$P_{h2} = \frac{K_{cpa} + (4/3)G_{cpa}}{K_h + (4/3)K_{cpa}}, P_{Cem2} = \frac{K_{cpa} + (4/3)G_{cpa}}{K_{Cem} + (4/3)G_{cpa}}, P_{f2} = \frac{K_{cpa} + (4/3)G_{cpa}}{K_f + (4/3)G_{cpa}}$$

$$Q_{h2} = \frac{G_{cpa} + Z_2}{K_h + Z_2},\ Q_{Cem2} = \frac{G_{cpa} + Z_2}{G_{Cem} + Z_2},\quad Q_f = \frac{G_{cpa} + Z_2}{Z_2},\quad Z = \frac{G_{sc}(9K_{cpa} + 8G_{cpa})}{6(K_{cpa} + 2G_{cpa})}$$

Finally, the *P*- and *S*-wave velocities and density of the dry or saturated aggregate at any cement concentration greater than $(\phi_{ic} - \phi_{io})$ or for porosities in the interval $0 \le \phi_f \le \phi_{io}$ are given by

$$V_p = \sqrt{(K_{cpa} + \frac{4}{3}G_{cpa})/\rho},\ V_s = \sqrt{G_{cpa}/\rho}, \text{and } \rho = (1-\phi_{io})\rho_g + (\phi_{io} - \phi_f)\rho_{cem} + \phi_f \rho_f$$

Figure 5.15 shows the effective V_p and V_s velocities predictions for a dry aggregate of cemented porous grains. The velocities are predicted by the combined CPG and CPA models in the entire porosity range. The matrix material is assumed to be pure calcite and the cement material is assumed to be pure calcite and pure clay. The elastic properties used for the clay are K_{fc} = 21 GPa and G_{fc} = 7 GPa, and ρ_{fc} = 2.55 g/cm3.

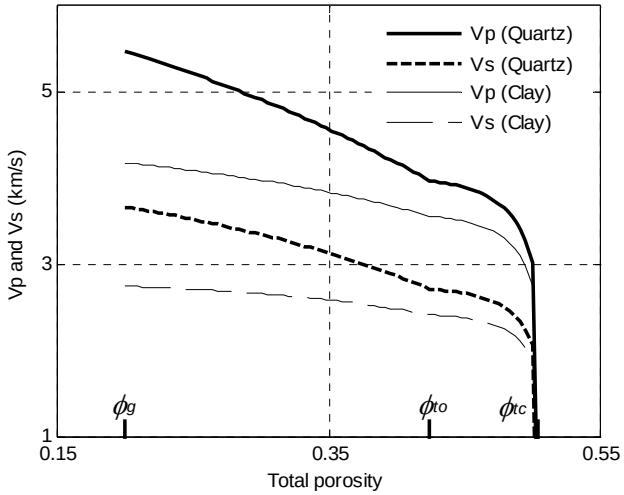

Figure 5.15. Comparison of V_p and V_s for a dry, cemented, porous-grain aggregate for two cement materials: calcite and clay. The velocities were predicted by using the combination of CPG and CPA models.

Figure 5.15 shows the effective V_p and V_s velocities predictions for a dry aggregate of cemented porous grains. The velocities are predicted by the combined CPG and CPA models in the entire porosity range. The matrix and cement materials are assumed to be pure calcite.

5.11 Conclusions

Our approach and models may be applied to sediment and rocks made of porous grains, such as calcareous and diatomaceous ooze, opal, and chalk and carbonate rocks. The microstructural parameters of these models can be associated with diagenesis. For instance, different degrees of compaction and cementation can be modeled by varying the coordination number, differential pressure, friction coefficient between grains, intragranular aspect ratios, intergranular and intragranular porosity, intergranular and intragranular fluid type, and the elastic properties of the cement and grains. The combination of the porous grain cementation (CPG) theory with the coherent potential approximation (CPA) allows us to estimate the elastic properties of siliciclastic and carbonate rocks at all cement concentrations.

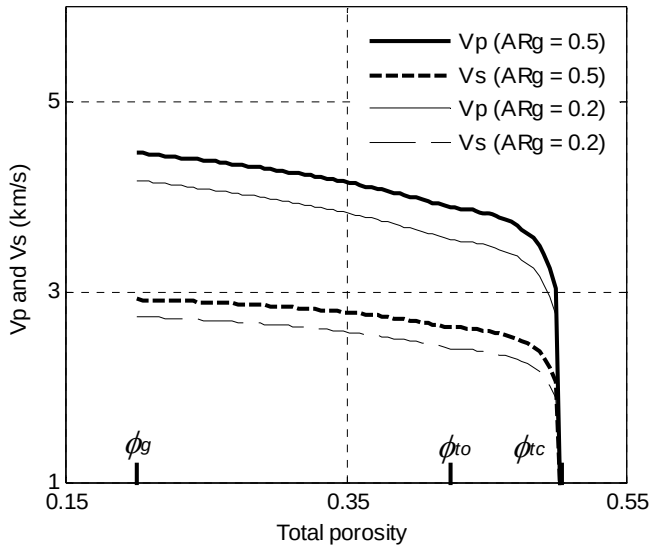

Figure 5.16. Comparison of V_p and V_s for a dry, cemented, porous-grain aggregate for two intragranular aspect ratios: α_g = 0.5 and α_g = 0.2. The matrix and cement materials are assumed to be pure calcite. The intergranular porosity (ϕ_g) was fixed and equal to 0.20.

These porous grain models are heuristic and based on several assumptions about the rock or material microstructure, so they are just approximations and simplifications of the reality. The purpose of this approach is to capture the trend of the material elastic moduli as a function of different microstructural parameters.

5.12 References

Batzle, M., and Wang., Z., 1992, Seismic properties of pore fluids: Geophysics, 57, 1396-1408.

Boutéca M., and Guéguen Y., 1999, Mechanical properties of rocks: Pore pressure and scale effects, Oil & Gas Science and Technology – Rev. IFP, 54, 703-714.

Budiansky, B., 1965, On the elastic moduli of some heterogeneous materials, Journal of the Mechanics and Physics of Solids, 13, 223-227.

Berryman, J. G., 1980, Long-wavelength propagation in composite elastic media, Journal of Acoustic Society of America, 68, 1809-1831.

Chaika, C., 1998, Physical Properties and Silica Diagenesis: Ph.D. thesis, Stanford University.

Christensen, R., 1982, Introduction to the mechanics of composites, Moscow.

Chaika, C., and Dvorkin, J., 2000, Porosity reduction during Diagenesis of diatomaceous Rocks, The American Association of Petroleum Geologists Bulletin, 84, 1173–1184.

Chang, C. S., Misra, A., and Sundaram, S. S., 1990, Micromechanical modeling of cemented sands under low amplitude oscillations: Géotechnique, 40, 251–263.

Dutta, T., Mukerji, T., Mavko, G., Lane, T., 2009, Compaction trends for shale and clean sandstone in shallow sediments, Gulf of Mexico: The Leading Edge, 28, 260-266.

Digby, P., 1981, The effective elastic moduli of porous granular rocks: Journal of Applied Mechanics, 48, 803-808.

Dvorkin, J., Mavko, G., and Nur, A., 1995, Squirt flow in fully saturated rocks: Geophysics, 60, 97-107.

Dvorkin, J., and Nur, A., 1996, Elasticity of high-porosity sandstone: Theory for two North Sea Datasets: Geophysics, 61, 1363-1370.

Dvorkin, J., and Prasad, M., 1999, Elasticity of marine sediments: Rock Physics modeling: Geophysical Research Letters, 26, 1781-1784.

Dvorkin, J., 1996, Large strains in cemented granular aggregates: Elastic-plastic cement: Mechanics of Materials, 23, 29-44.

Dvorkin, J., A. Nur, and H. Yin, 1994, Effective properties of cemented granular materials, Mechanics of Materials, 18, 351-366.

Dvorkin, J., G. Mavko, and A. Nur, 1991, The effect of cementation on the elastic properties of granular material, Mechanics of Materials, 12, 207-217.

Dvorkin, J., J. Berryman, and A. Nur, 1999, Effective moduli of cemented sphere packs: Mechanics of Materials, 31, 461-469.

Fernandez, A. L., and Santamarina, J. C., 2001, Effect of cementation on the small-strain parameters of sands: Canadian Geotechnical Journal, 38, 191–199.

Gal, D., Dvorkin, J., and Nur, A., 1998, A physical model for porosity reduction in sandstones: Geophysics, 63, 454-459.

Garcia, X., M. Araujo, and E. Medina, 2004, *P*-wave velocity-porosity relations and homogeneity lengths in a realistic deposition model of sedimentary rock: Waves in Random Media, 14, 129–142.

Garcia, X. and Medina, E., 2006, Molecular dynamic modeling of the effects of cementation on the acoustical properties of granular sedimentary rocks, Condensed Matter Material Sciences, Condensed Matter e-prints

Garcia1, X., and E. Medina, 2007, Acoustic response of cemented granular sedimentary rocks: Molecular dynamics modeling: Physics Review, E-75.

Garcia, X., and Medina, E.A., 2006, Hysteresis effects studied by numerical simulations: Cyclic loading-unloading of a realistic sand model: Geophysics, 71, F13-F20.

Gassmann, F., 1951, Über die elastizität poröser medien: Veirteljahrsschrift der Naturforschenden Gesellschaft in Zürich, 96, 1-23.

Grechka, V., 2007, Fluid substitution in porous and fractured solids: The non-interaction approximation and Gassmann theory: International Journal of Fracture, 148, 103-107.

Hashin, Z., and Shtrikman, S., 1963, A variational approach to the elastic behavior of multiphase materials: Journal of the Mechanics and Physics of Solids, 11, 127-140.

Jenkins, J., Johnson, D., Ragione, L. La., and Makse, H, 2005, Fluctuations and the effective moduli of an isotropic, random aggregate of identical, frictionless spheres: Journal of the Mechanics and Physics of Solids, 53, 197-225.

Kachanov, M., Tsukrov, I., and Shafiro, B., 1995, Materials with fluid-saturated cracks and cavities: Fluid pressure polarization and effective elastic response, International Journal of Fracture 73, 61-66.

Kachanov, M., 2007, On the Effective elastic properties of cracked solids-Editor's comments,

Le Ravalec, M., and Guéguen, Y., 1996, High and low frequency elastic moduli for a saturated porous/cracked rock-differential self-consistent and poroelastic theories. Geophysics, 61, 1080-1094.

Makse, H., N. Gland, D. Johnson, and L. Schwartz, 2004, Granular Packings: Nonlinear elasticity, sound propagation and collective relaxation dynamics: Physics Review, 70,

Mavko, G., and Jizba, D., 1991, Estimation grain-scale fluid effects on velocity dispersion in rocks, Geophysics, 56, 1940-1949.

Mavko, G., Mukerji, T., and Dvorkin, J., 1998, The rock physics handbook: Cambridge University Press.

Mindlin, R. D., 1949, Compliance of elastic bodies in contact: Trans. Transaction of the American Society of Mechanical Engineers, 71, A-259.

Mukerji, T., and Mavko, G., 1994, Pore fluid effects on seismic velocity in anisotropic rocks, Geophysics, 59, 233-244.

Mukerji, T., Mavko, G., Mujica, D., and Lucet, N., 1995, Scale-dependent seismic velocity in heterogeneous media, Geophysics, 60, 1222-1233.

Murphy, W., 1982, Effects of microstructure and pore fluids on the acoustic properties of granular sedimentary materials: PhD Thesis, Stanford University.

Norris, A. N., 1985, A differential scheme for the effective moduli of composites. Mechanics of Materials, 4, 1-16.

Nur, A., Mavko, G., Dvorkin, J., and Galmudi, D., 1998, Critical porosity: a key to relating physical properties to porosity in rocks: The Leading Edge, 17, 357-362.

O'Connell, R. J., and Budiansky, B., 1974, Seismic velocities in dry and saturated cracked solids, Journal of Geophysics Research, 79, 4626-4627.

O'Connell, R. J., and Budiansky, B., 1977, Viscoelastic properties of fluid-saturated cracked solids, Journal of Geophysics Research, 82, 5719-5735.

Persson, B., Tartaglino, U., Albohr, O., and Tosatti, E., 2005, Rubber friction on wet and dry road surfaces: The sealing effect. Physics Review B 71.

Prasad, M., and Dvorkin, J., 2001, Velocity to porosity transforms in marine sediments: Petrophysics, 42, 429-437.

Raymer, L., E. Hunt, and J. Gardner, 1980, An improved sonic transit time-to-porosity transform: 21st Annual Logging Symposium Transactions, Society of Professional Well Log Analysts, Paper P.

Ruiz, F., and Dvorkin, J., 2009, Sediment with porous grains: Rock-physics model and application to marine carbonate and opal: Geophysics, 74, E1.

Shafiro, B., and Kachanov, M., 1997, Materials with fluid-filled pores of various shapes: effective elastic properties and fluid pressure polarization

Smith, W., Foote, P., and Busand, P., 1929, Packing of homogeneous spheres, Physics Review, 34, 1271-1274.

Thomsen L., 1985, Biot-consistent elastic moduli of porous rocks: Low-frequency limit, Geophysics, 50, 2797-2807.

Tutuncu, A., Dvorkin, J., Nur, A., 1997, Influence of cementation and permeabilikty on wave velocities in poorly consolidated sands: International Journal of Rock Mechanics and Mining Sciences, 34, 3-4.

Wadsworth, J., 1960, Experimental examination of local processes in packed beds of homogenous spheres, Natural Resources Council of Canada, Mechanical Engineering Report MT-41 February.

Wilkens, R. H., Cheng, C. H., and Meredith, J. A., 1992, Evaluation and prediction of shear-wave velocities in calcareous marine sediment and rocks: Journal of Geophysical Research, 97, 9297-9305.

Wood, A. B., 1955, A textbook of sound: G. Bell and Sons, Ltd., London.

Wu, T. T., 1966, The effect of inclusion shape on the elastic moduli of a two-phase material: International Journal Solids and Structures, 2, 1-8.

Wyllie, M. R., Gregory, A. R., and Gardner, L. W., 1956: Elastic wave velocities in heterogeneous and porous media, Geophysics, 21, 41-70.

Yin, H. and J. Dvorkin, 1994, Strength of cemented grains: Geophysical Research Letters, 21, 903-906.

Yin, H., 1993, Acoustic velocity and attenuation of rocks: isotropic, intrinsic anisotropy and stress induced anisotropy: PhD. Thesis, Stanford University.

Appendix A:

Differential effective medium model (DEM)

Differential effective medium theory assumes that a composite material may be constructed by making infinitesimal changes in an already existing composite. If the effective bulk and shear constants of the composite are $K^*(y)$ and $G^*(y)$ where the volume fraction of the inclusion phase is y, the equations governing the changes in these constants are (Mavko et al., 2009)

$$\begin{aligned}(1-y)\frac{d}{dy}[K^*(y)] &= (K_2 - K^*)P^{(*2)}(y) \\ (1-y)\frac{d}{dy}[G^*(y)] &= (G_2 - G^*)Q^{(*2)}(y)\end{aligned} \tag{A-1}$$

with initial conditions $K^*(0) = K_1$ and $G^*(0) = G_1$, where K_1 and G_1 are the bulk and shear moduli of the initial host material, respectively, and K_2 and G_2 are the bulk and shear moduli of the incrementally added inclusions, respectively.

In porous rock, y is simply the total porosity ϕ. The coefficients P and Q are geometric factors dependent upon the shape of the inclusion (Mavko et al., 2009). Here we used the ellipsoidal inclusions.

The superscript "*2" for P and Q indicates that the factors are for the inclusions while the subscript "*" is for the background medium whose bulk modulus is K^* and the shear modulus is G^*. Fluid-saturated cavities are simulated by setting the inclusion

shear modulus to zero.

The coefficients P and Q for ellipsoidal inclusions of arbitrary aspect ratio are given by

$$P = \frac{1}{2}T_{iijj}, Q = \frac{1}{2}(T_{ijij} - \frac{1}{3}T_{iijj}), \tag{A-2}$$

where the tensor $\mathbf{T}$ relates the uniform far-field strain to the strain within the ellipsoidal inclusion (Wu, 1966). In this study the elastic properties of the inclusions are set as those of seawater at in situ conditions while the matrix properties are for pure calcite.

Appendix B

Elastic equivalency using a self consistent model

In this appendix we compare the prediction of V_s based on V_p using a self-consistent theory (SC), known as the coherent potential approximation (Berryman, 1980), with a differential effective-medium (DEM) theory prediction (Norris, 1985) discussed in the main paper. These models represent porosity and pore shape as ellipsoidal inclusions with different aspect ratios (AR). DEM assumes isolated pores embedded in a host material that remains continuous at all porosities, while SC treats grains and pores symmetrically, an approach which instead of requiring a single background material, allows grains and pores to be connected or disconnected depending on the porosity range. Both models are physically realizable and offer useful analogs of the elastic behavior of some rocks with specific microstructures. For instance, rocks composed of grains look more like a physical realization of SC than DEM (Berge et al., 1995) and rocks with vugs, such as some carbonates, look more like a physical realization of the DEM. For rocks with the same solid and fluid constituents, these two models produce different results; i.e. it is necessary to use self-consistent aspect ratios (SC-AR) significantly greater than the DEM aspect ratios (DEM-AR) to match the same velocity. In consequence, the interpretation of rock pore aspect ratios may not be unique. The rock microstructure has a strong effect on its elastic properties. Thus, it is not appropriate to select which effective-

medium model is the "best" for determining the elastic properties of all rock types. If our goal is to model a specific rock type, it is preferable to pick the theory whose assumptions about microstructure match those of the rock modeled (Berge et al., 1995). In general, rocks have cracks, cemented and non-cemented grains, cavities, different pore shapes, and different degrees of connectivity. In consequence, their effective elastic properties are the result of the combined effect of all these possible microstructural elements. The idea of the equivalent elastic model is not to choose a single model that best fits the microstructure; it is to use only one inclusion model with a single AR as a fitting parameter for all rock types. It can be argued that the principle advocated here can be used with any effective-medium model. The main point is that certain effective-medium inclusion models can mimic the elastic properties of real rock, if an appropriate aspect ratio is assigned to the model. Our goal is to make the use of a selected model reasonably general, rather than insist that the geometry of the model is the same as of real rock. Moreover, the aspect ratio is nothing more than a fitting parameter within the realm of a selected model.

Figure B-1 shows the V_p and V_s velocities versus porosity according to SC model for wet calcite. The SC-velocities were modeled using aspect ratios (SC-AR) equal to 1.0 and 0.25, for the mineral and the pores, respectively, and were kept constant in the entire porosity range. We computed the DEM aspect ratios (DEM-AR) by matching DEM to the SC-V_p and -V_s. The computed DEM-AR are lower than the SC-AR in the entire porosity range, and the differences increase with porosity. The aspect ratios to match V_p (DEM-ARp) and those to match Vs (DEM-ARs) are almost equal. Similar results are obtained when: a) modeling self-consistent velocities using lower aspect ratios for the solid constituents and b) modeling self-consistent velocities using different minerals.

As a second exercise, we repeat the same example shown in Figure 3.1, but using the self-consistent model instead of DEM. Figure B-2 shows the AR required to fit the velocity data from SC by DEM. The velocities from SC are computed assuming a constant AR = 1.0 for the solid mineral and a constant AR = 0.25 for the pores.

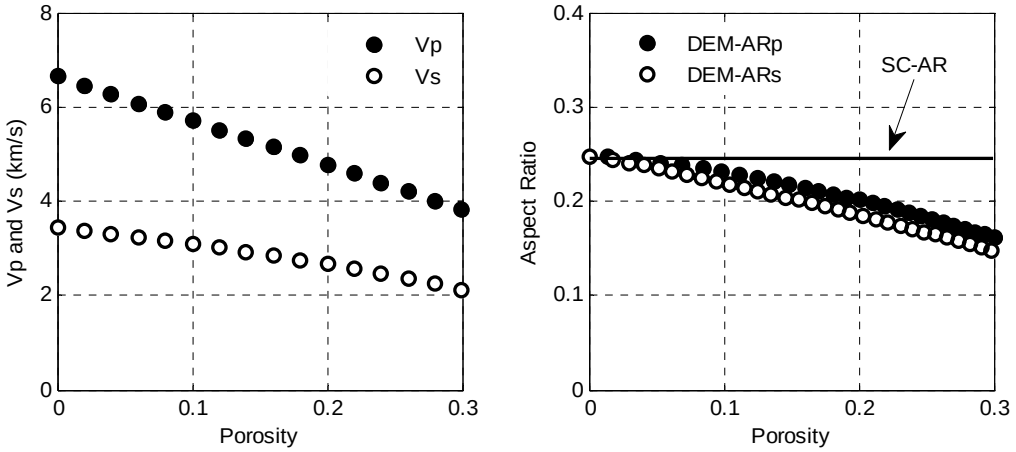

Figure B-1. Left: *P*- and *S*-wave velocity versus porosity according to SC for five wet calcite. The aspect ratios used to model the self consistent velocities are constant and equal to 1.0 and 0.25, for the mineral and the pores, respectively. Right: AR derived by matching DEM to the SC-P-wave velocity (filled circles) and *S*-wave velocity (filled circles). The same is observed for different minerals.

We observe that for all mineralogies, the self-consistent AR required to match Raymer's data show a greater variation with porosity compared to those ones computed using DEM (Figure B-2). For pure quartz, 50% quartz and 50% clay, and 50% quartz and 50% calcite, the calculated SC-AR depends only slightly on whether it was determined from V_p or V_s. For pure clay and calcite, the SC-AR depends more strongly on whether it was determined from V_p or V_s.

Figure B-3 shows the *P*- and *S*-wave velocity versus porosity for the five mineralogies examined in Figure B-2. Symbols are the SC/Gassmann *S*-wave velocities prediction for the AR derived from SC by matching SC/Gassmann to the *P*-wave velocity according to Raymer et al. (1980).

If the SC-AR required to match the Raymer's et al. (1980) V_p data are used to predict V_s using SC/Gassmann again, we observe that the V_s prediction is also accurate and computationaly faster than DEM, however the SC-AR vary considerably with porosity (Figure B-3).

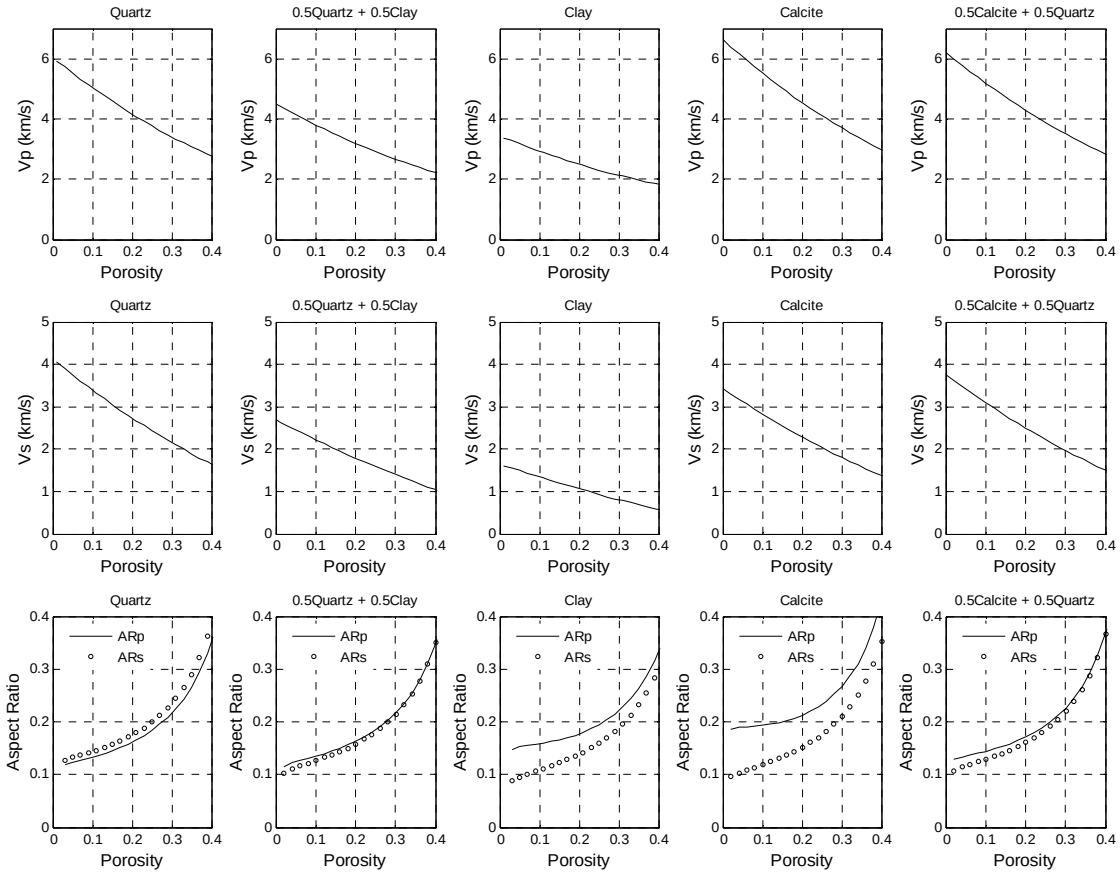

Figure B-2. Top: the *P*-wave velocity versus porosity according to Raymer et al. (1980) for five mineralogies as indicated at the top of the frames. Middle: the *S*-wave velocity according to Krief et al. (1990) as derived from the *P*-wave velocity in the top raw. Bottom: AR derived by matching SC/Gassmann to the *P*-wave velocity (solid curve) and *S*-wave velocity (symbols).

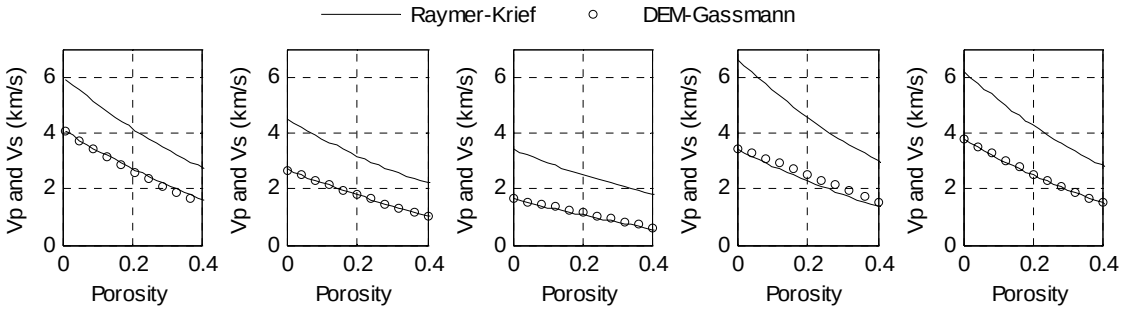

Figure B-3. Velocity versus porosity for the five mineralogies examined in Figure B-2. Solid curves are the same velocities as displayed in the first two rows of Figure B-2. Symbols are the SC/Gassmann *S*-wave velocities prediction for the AR derived from SC by matching SC/Gassmann to the *P*-wave velocity according to Raymer et al. (1980).

The next example is from well log data from the Venezuelan oil field. Our V_s prediction methodology using self-consistent approximation works well for the Venezuelan well (Figure B-4). Notice that the SC-aspect ratios are different than those shown in Figure 3.7.

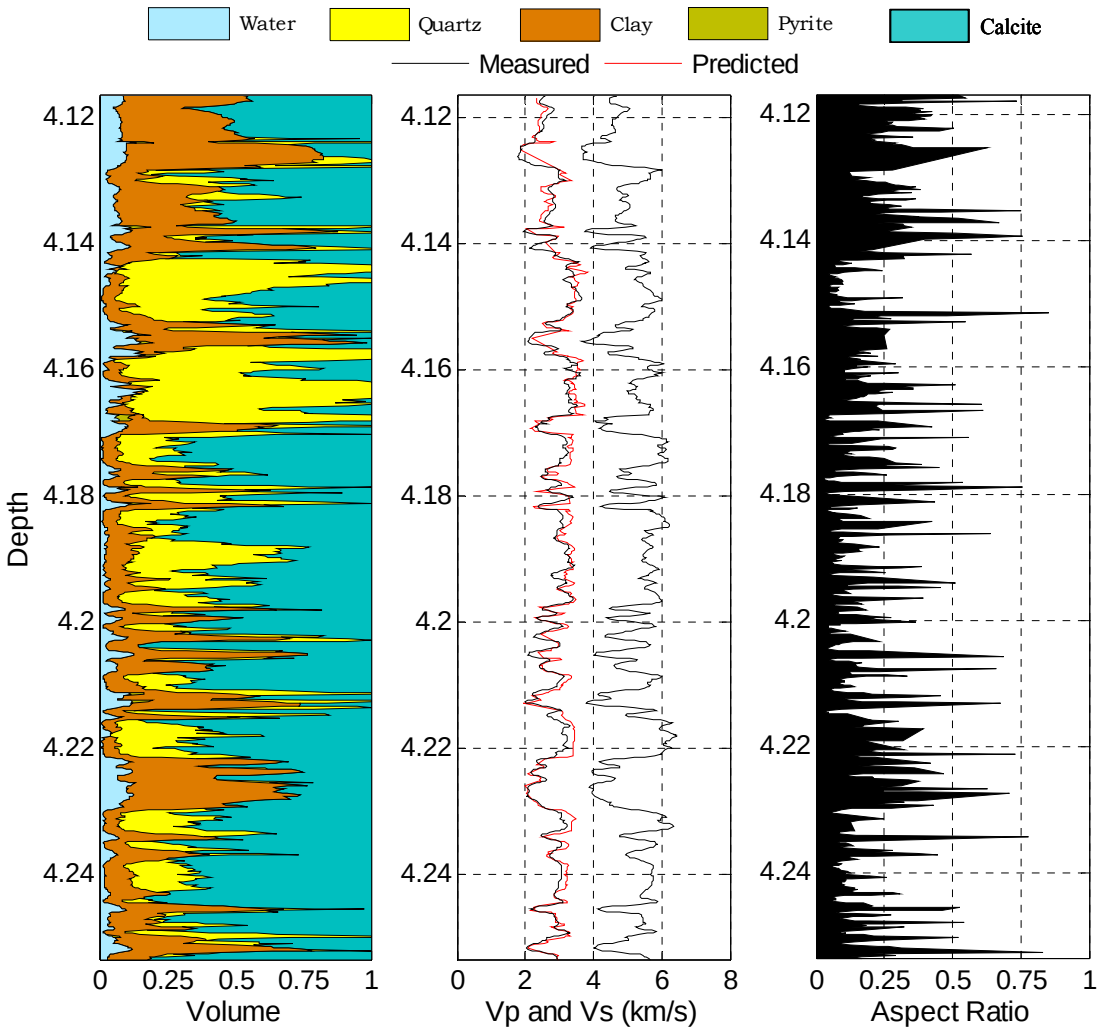

Figure B-4. V_s prediction for the Venezuelan well. From left to right: mineralogy and porosity; measured (black) and predicted (red) V_s; AR derived from V_p using Self consistent approximation/Gassmann. Compare this figure with Figure 3.7 in the main Chapter 3.

Appendix C

Elastic equivalency using granular medium models

In this appendix, the equivalent elastic model concept is applied to granular-medium, models. The velocities determined using-granular medium models are matched with the velocities determined directly using DEM in wet rock, treating the fluid in the pores as an elastic inclusion (high-frequency estimate) as well as a combination of DEM for dry rock with subsequent Gassmann's fluid substitution (low frequency estimate). For this exercise, two heuristic, granular-medium models were used, the soft-sand model (Dvorkin and Nur, 1996) and the stiff-sand model (Gal et al., 1998). We explore the elastic equivalency between DEM and these models, even though the actual rocks may not be like a physical realization of the soft- and stiff-sand model.

The soft-sand model has been used successfully to model deep-ocean shallow-buried sediments (Dvorkin and Prasad, 1999; Prasad and Dvorkin, 2001). This model is based on the Hertz-Mindlin theory (Mindlin, 1949) and the modified Hashin-Strikman lower bound. The contact Hertz-Mindlin theory (Mindlin, 1949) gives expressions for the effective bulk (K_{HM}) and shear (G_{HM}) moduli of a dry, dense, random pack of identical spherical grains subject to a hydrostatic pressure P. To find the effective bulk (K_{Dry}) and shear (G_{Dry}) moduli at a different porosity, Dvorkin and Nur (1996) proposed a heuristic modified Hashin-Strikman lower bound based on the original Hashin-Strikman lower

bound (1963). The modified bounds are

$$K_{Dry} = \left(\frac{\phi/\phi_c}{K_{HM} + \frac{4}{3}G_{HM}} + \frac{1-\phi/\phi_c}{K + \frac{4}{3}G_{HM}}\right)^{-1} - \frac{4}{3}G_{HM},$$
$$G_{Dry} = \left(\frac{\phi/\phi_c}{G_{HM} + Z_1} + \frac{1-\phi/\phi_c}{G + Z_1}\right)^{-1} - Z_1, \quad Z_1 = \frac{G_{HM}}{6}\left(\frac{9K_{HM} + 8G_{HM}}{K_{HM} + 2G_{HM}}\right), \tag{C-1}$$

where ϕ_c is the critical porosity and K and G are the elastic moduli of the solid phase.

This model connects two end members, one with zero porosity and the moduli of the solid phase, and the other with critical porosity and pressure-dependent moduli as given by the Hertz-Mindlin theory

$$K_{HM} = \sqrt[3]{\frac{C^2(1-\phi_c)^2 G^2}{18\pi^2(1-\nu)^2}P}, \quad G_{HM} = \frac{5-4\nu}{5(2-\nu)}\sqrt[3]{\frac{3C^2(1-\phi_c)^2 G^2}{2\pi^2(1-\nu)^2}P}, \tag{C-2}$$

where ν is the Poisson's ratio of the porous grains, P is the differential pressure acting upon the pack, and C is the average number of contacts that each grain has with its neighboring grains (the coordination number).

To determine the effective velocities for low frequency water-saturated rock, Gassmann's (1951) formula is used. Following Gassmann's (1951) fluid substitution equations, K_{Dry} and shear G_{Dry} are given by:

$$K_{Sat} = K\frac{\phi K_{Dry} - (1+\phi)K_f K_{Dry}/K + K_f}{(1-\phi)K_f + \phi K - K_f K_{Dry}/K}, \quad \text{and} \quad G_{Sat} = G_{Dry}, \tag{C-3}$$

where K_f is the bulk modulus of water.

Finally, the elastic *P*- and *S*-wave velocities and the bulk density, ρ_b, are

$$V_p = \sqrt{(K_{Sat} + \frac{4}{3}G_{Sat})/\rho_b}, \quad V_s = \sqrt{G_{Sat}/\rho_b}, \text{ and } \rho_b = (1-\phi)\rho_s + \phi\rho_f. \tag{C-4}$$

The elastic equivalency between the soft-sand and DEM models is achieved by finding the AR required to match the dry or wet soft-sand elastic moduli with those provided by DEM, where the pore fluid is treated as an elastic inclusion (high-frequency

estimate) and the combination DEM-Gassmann (low-frequency estimate), respectively (Figure C-1).

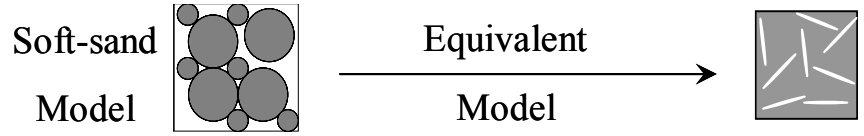

Figure C-1. Two idealized equivalent physical models, analogues to real soft sands. One is a random dense pack of spherical grains and the other is a continuous matrix with isolated random distributed pores of a single aspect ratio, AR. The elastic equivalency is achieved by finding the AR needed to match the DEM predictions with those according to the soft-sand model.

Figure C-2 shows the AR required for fitting the velocities from the soft-sand model by the DEM/Gassmann combination. We assume that the rock is saturated with pure water with 1.00 g/cm3 density and 1.50 km/s velocity. The input parameters for the soft-sand model are K = 37 GPa, G = 44 GPa, K_f = 2.25 GPa, P = 10 MPa, C = 9, and ϕ_c = 0.44 (same as used in Prasad and Dvorkin, 1999). In the DEM modeling we use the same values for K, G, K_f and vary AR to fit the soft-sand model results.

When modeling with DEM/Gassmann and the soft-sand model, we first assume that the rock is dry, find the dry-frame elastic moduli, and then use Gassmann's (1951) fluid substitution to arrive at the results for water-saturated rock. Notice that for all mineralogies, the AR required to match these data increases linearly with increasing porosity (Figure C-2). For all mineralogies, the AR required are small and confined within a range approximately between 0.02 and 0.1, in the entire porosity range; the most important result is that the AR at all porosities are independent of whether they were determined from V_p or V_s.

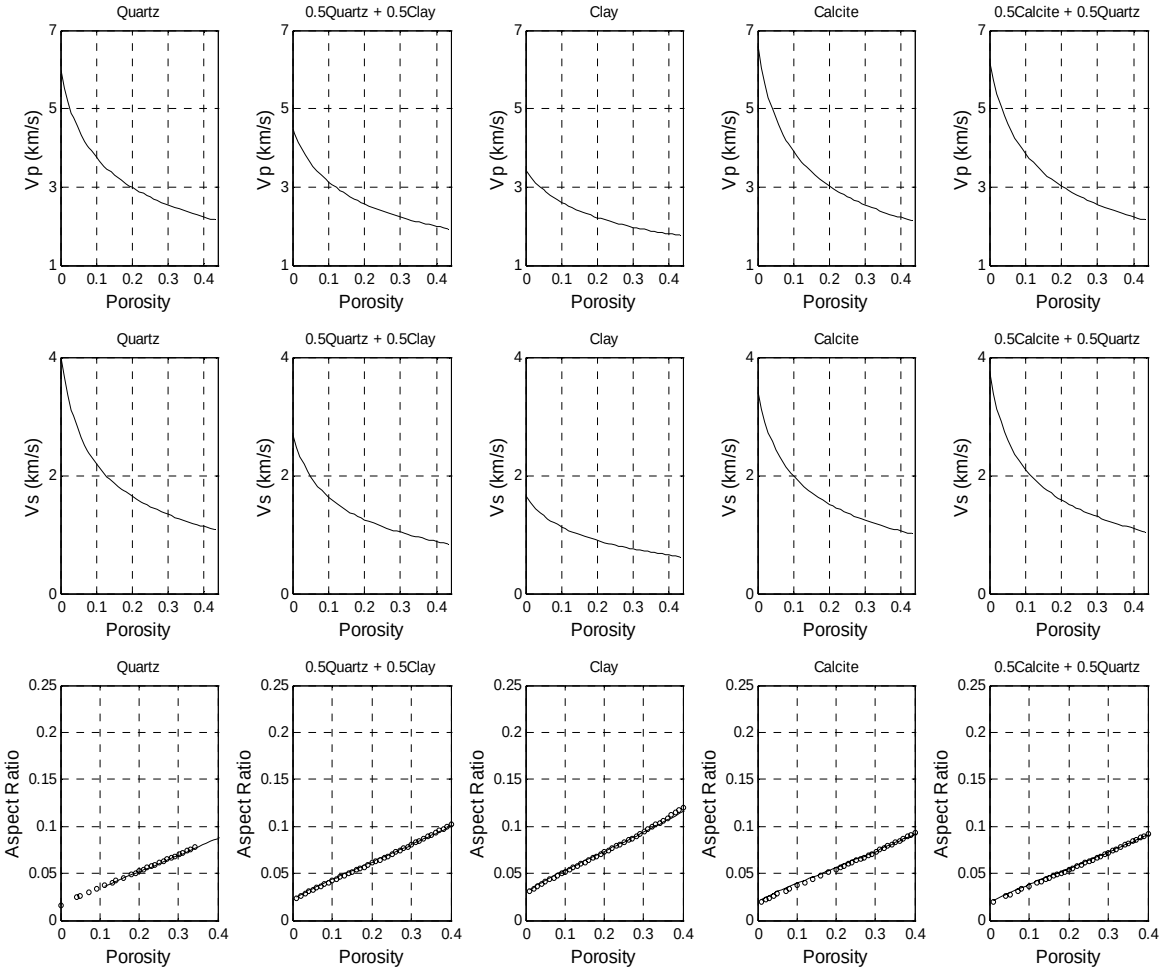

Figure C-2. Top and middle: the *P*- and *S*-wave velocities versus porosity according to soft-sand model (Dvorkin and Nur, 1996) for five mineralogies as indicated at the top of the frames. Bottom: AR derived by matching DEM/soft-sand model to the *P*-wave velocity (solid curve) and *S*-wave velocity (symbols).

In the soft-sand model, C and P were kept constant. If any of these parameters increases, the AR needed to match the soft-sand model velocities will increase as well, simply because an increase in C and/or P will make rock stiffer.

The technique discussed in the main text of this chapter allows us to find the velocities at high frequency from those at low frequency velocities. To achieve this, we use the aspect ratios obtained in the low-frequency range (as discussed earlier) and then compute the elastic moduli for these inclusions using DEM alone, rather than the DEM/Gassmann combination. The results are displayed in Figure C-3.

Let us reiterate that the AR obtained using this fitting technique are not sensitive to

whether determined from V_p or V_s. Based only on V_p, these results allow as, based only on V_p, to estimate: (a) V_s, (b) high-frequency wet-rock velocity from dry-rock data (and vice-versa), and (c) maximum *P*- and *S*-wave attenuation.

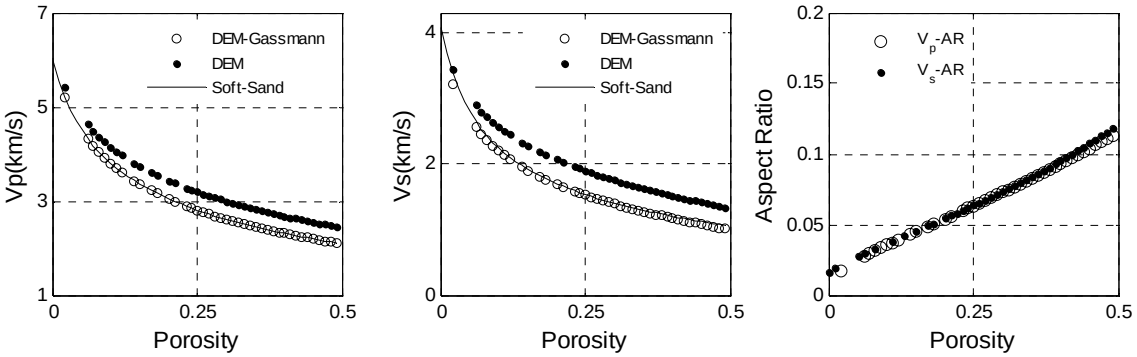

Figure C-3. Upper frame: high and low frequency wet-rock DEM V_p and V_s obtained from the AR required to match the dry-rock DEM elastic moduli with those provided by the soft-sand model. Left: V_p versus porosity; open circles are for wet DEM-Gassmann velocities (low frequency); filled circles are for wet-DEM velocities (high frequency); the continuous curve is for soft-sand wet velocities (low frequency). Middle: same for V_s. Right: Fitting AR for V_p (open circles) and V_s (filled circles).

Figure C-4 shows the estimated *P*- and *S*-wave maximum quality factors, Q_p and Q_s, respectively. These were estimated from the predicted low and high frequency velocities.

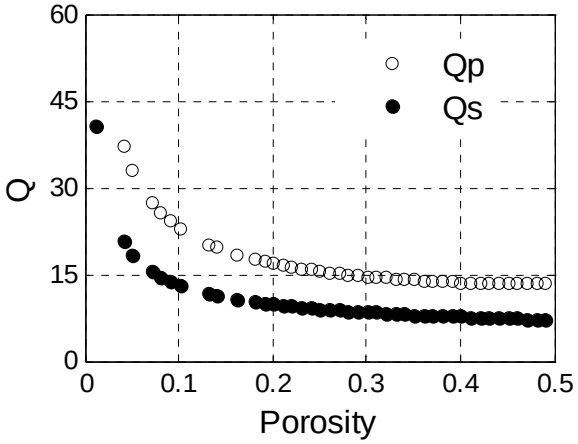

Figure C-4. Estimated maximum Q_p and Q_s as a function of porosity.

A counterpart to the soft-sand model is the stiff-sand model. In this model, the two end-points, one at zero porosity and the other at the critical porosity, are connected by the modified upper Hashin-Shtrikman bound (Gal, et al., 1998). This model gives

$$K_{Dry} = \left(\frac{\phi/\phi_c}{K_{HM} + \frac{4}{3}G} + \frac{1-\phi/\phi_c}{K + \frac{4}{3}G}\right)^{-1} - \frac{4}{3}G,$$
$$G_{Dry} = \left(\frac{\phi/\phi_c}{G_{HM} + Z} + \frac{1-\phi/\phi_c}{G + Z_2}\right)^{-1} - Z_2, \quad Z_2 = \frac{G}{6}\left(\frac{9K + 8G}{K + 2G}\right). \tag{C-5}$$

Figure C-5 shows the AR needed to match the stiff-sand wet-rock elastic moduli with those provided by the DEM-Gassmann combination. All input parameters are the same as used for the soft-sand model earlier in the text.

As expected, the AR here differ from these obtained for the soft-sand model. However, the implications for predicting various rock properties are essentially the same.

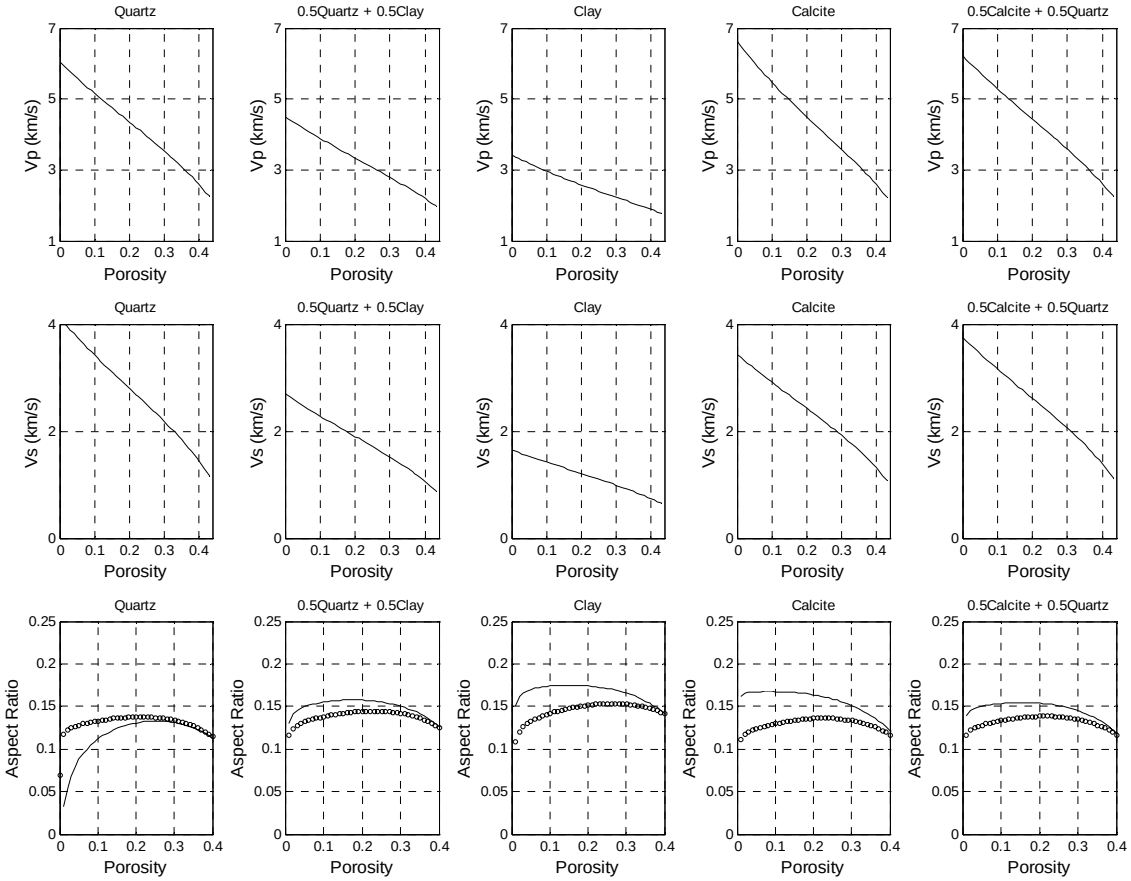

Figure C-5. Top and middle: the *P*- and *S*-wave velocities versus porosity according to the stiff-sand model (Gal et al., 1998) for five mineralogies as marked in the frames. Bottom: AR derived by matching DEM-Gassmann model to the stiff-sand model using the *P*- (solid curve) and *S*-wave velocities (symbols).

Appendix D

Application of the porous grain concept to Wood's model

The Wood (1955) model assumes that in high-porosity unconsolidated sediment, the *P*-wave velocity can be estimated as in a suspension of solid particles in the load-bearing fluid:

$$V_p = \sqrt{\frac{K_R}{\rho_b}}, \tag{D-1}$$

where K_R and ρ_b are the Reuss average of the bulk moduli of the solid and fluid phases, and the bulk density of the suspension, respectively:

$$\begin{aligned} K_R^{-1} &= \phi_i K_f^{-1} + (1-\phi_i) K_g^{-1}, \\ \rho_b &= \phi_i \rho_f + (1-\phi_i)\rho_g, \end{aligned} \tag{D-2}$$

In the original model the subscript "g" refers to the properties of the pure non-porous mineral. Here we modify this approach by assuming that the grains are porous and, therefore, $\rho_g = \rho_s(1-\phi_g) + \rho_f \phi_g$ and K_g is determined from DEM. ϕ_i is the intergranular porosity according to equation 4.1.

Hamilton (1971) and Wilkens et al. (1992), acknowledges the fact that such unconsolidated sediment still supports shear-wave propagation and, therefore, its shear modulus is not zero (as assumed by the suspension model). They point out that the

suspension model is not valid for marine sediments, which have some rigidity, but still can be used to obtain a maximum estimate of the shear velocity, V_s. To estimate V_s, they calculate the effective shear modulus of sediment as $G = (3/4)(M - K_R)$, where the compressional modulus M is calculated from the measured *P*-wave velocity V_p and bulk density ρ_b as $\rho_b V_p^2$. Then $V_s = \sqrt{G/\rho_b}$. Here we follow the same ad-hoc approach but using porous grains instead of a pure solid. The corresponding model V_s curve is displayed in Figure 4.11.

An example of calculating V_p in a suspension of porous calcite grains in seawater for varying intragranular porosity with fixed aspect ratio as well as for varying aspect ratios with fixed intragranular porosity is displayed in Figure D-1.

Our results suggest that Wood's estimation of the bulk modulus of the most porous sediments is fairly closet o the dynamic bulk modulus, an observation which can be used to estimate shear wave velocity.

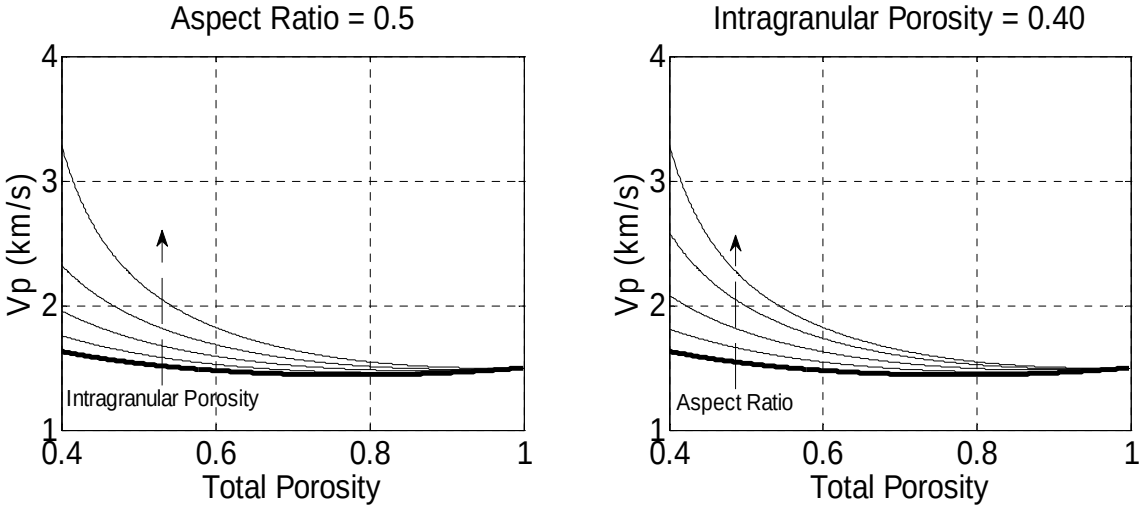

Figure D-1. The *P*-wave velocity versus porosity in a suspension of porous grains. Left – the intragranular AR is fixed at 0.5. The intragranular porosity is changing from zero (the bold baseline) to 0.4 with increment 0.1. The velocity increases with increasing intragranular porosity. Right – the intragranular porosity is fixed at 0.4. The intragranular AR is decreasing from 0.5 (the upper curve) to 0.0 (the curve above the bold baseline). The baseline curves in both frames are for suspension with non-porous mineral grains.

Appendix E

Anisotropic porous-grain aggregate model

Under uniaxial stress σ_1, a dry aggregate of identical porous spheres is transversely isotropic (Walton, 1987). We assume that the intragranular inclusions are distributed randomly and that they are not affected by the applied stress, σ_1. If the porous spherical grains are infinitely rough, the elastic properties of the aggregate can be described by the following five constants:

$$C_{11}^{(1)} = 3(\alpha + 2\beta),\ C_{12}^{(1)} = \alpha - 2\beta,\ C_{13}^{(1)} = 2C_{12}^{(1)},\ C_{33}^{(1)} = 8(\alpha + \beta) \text{ and } C_{44}^{(1)} = \alpha + 7\beta \quad \text{(E-1)}$$

If the porous spherical grains are smooth, the elastic properties of the aggregate can be described by the following five constants:

$$C_{11}^{(0)} = 3\alpha,\ C_{12}^{(0)} = C_{44}^{(0)} = \alpha,\ C_{13}^{(0)} = 2C_{12}^{(0)},\ \text{ and } \ C_{33}^{(0)} = 8\alpha \quad \text{(E-2)}$$

where

$$\alpha = \frac{(1-\phi_i)C}{32\pi^2 B}\sqrt[3]{\frac{24\pi^2 B(2B+A)}{A(1-\phi_i)C}\sigma_1},$$

$$\beta = \frac{(1-\phi_i)C}{32\pi^2 (2B+A)}\sqrt[3]{\frac{24\pi^2 B(2B+A)}{A(1-\phi_i)C}\sigma_1},$$

$$A = \frac{1}{4\pi}\left(\frac{1}{G_g} - \frac{1}{K_g + G_g/3}\right), \quad \text{and} \quad B = \frac{1}{4\pi}\left(\frac{1}{G_g} + \frac{1}{K_g + G_g/3}\right)$$

Measurements of shear modulus in unconsolidated sands have been often observed to be lower than those predicted by the Hertz-Mindlin effective medium models (Winkler, 1983; Goddard; 1990; Zimmer et al. 2007). To overcome this situation, Bachrach and Avseth (2008) suggest that the effective media approximation based on contact mechanics can be calibrated by incorporating nonuniform contact models, which treat the contact stiffness as a spatial variable. This is achieved by expanding the effective medium theory of Norris and Johnson (1997) to account for variable contact models. The effective stiffness matrix for nonuniform contacts is given, as follows (Bachrach and Avseth, 2008),

$$C_{ij} = xC_{ij}^{(1)} + (1-x)C_{ij}^{(0)} \tag{E-3}$$

where x is the fraction of rough sphere contacts in the aggregate.

Equation E-3 suggests the Voigt average, which implies isostrain, is the one appropriate isostrain condition to the binary contact problem (Bachrach and Avseth, 2008).

To account for the effects of intergranular porosity on the undrained elastic properties, the anisotropic version of Gassmann's relations needs to be used (Mavko et al., 2009). Brown and Korringa (1975) derived a theoretical formulas relating the effective elastic moduli of an anisotropic dry rock to the effective moduli of the same rock containing fluid:

$$S_{ijkl}^{(dry)} - S_{ijkl}^{(sat)} = \frac{(S_{ij\alpha\alpha}^{(dry)} - S_{ij\alpha\alpha}^{o})(S_{kl\alpha\alpha}^{(dry)} + S_{kl\alpha\alpha}^{o})}{(S_{\alpha\alpha\beta\beta}^{(dry)} - S_{\alpha\alpha\beta\beta}^{o}) + (\beta_f - \beta_o)\phi} \tag{E-4}$$

where the elements of the dry compliance tensor $S_{ijkl}^{(dry)}$ are given by Walton's equations.

Once the $C_{ijkl}^{(sat)}$ tensor is determined, the shear and Young's moduli, G and E, respectively, are computed for all directions. $G(\theta)$ in an arbitrary plane depends on the direction in which shear is applied. For a hexagonal system it is given by,

$$G(\theta)^{-1} = S_{44} + \left[S_{11} - S_{12} - \frac{S_{44}}{2} \right] \sin^2(\theta) + 2\left[S_{11} + S_{33} - 2S_{13} - S_{44} \right] \cos^2(\theta) \sin^2(\theta) \qquad \text{(E-5)}$$

The Young's modulus for an arbitrary direction of tension is given by (Nye, 1957)

$$E(\theta)^{-1} = S_{11} \sin^4 \theta + S_{33} \cos^4 \theta + (S_{44} + 2S_{13}) \sin^2 \theta \cos^2 \theta \qquad \text{(E-6)}$$

where θ is the angle between the arbitrary direction and the material axes. The quasi-compressional wave phase velocity V_{qp}, vertically polarized shear wave velocity V_{qsv}, and horizontally polarized shear wave velocity V_{sh}, in a transversely isotropic medium, are given by (Musgrave, 1970)

$$\rho V_{pp}^2 = C_{44} + \frac{1}{2}(h\cos^2\theta + a\sin^2\theta) + \frac{1}{2}\left[(h\cos^2\theta + a\sin^2\theta)^2 - 4(ah - d^2)\cos^2\theta\sin^2\theta \right]^{\frac{1}{2}},$$

$$\rho V_{qsv}^2 = C_{44} + \frac{1}{2}(h\cos^2\theta + a\sin^2\theta) - \frac{1}{2}\left[(h\cos^2\theta + a\sin^2\theta)^2 - 4(ah - d^2)\cos^2\theta\sin^2\theta \right]^{\frac{1}{2}}$$

$$\rho V_{sh}^2 = C_{44}\cos^2\theta + C_{66}\sin^2\theta \qquad \text{(E-7)}$$

where $a = C_{11} - C_{44}$, $h = C_{33} - C_{44}$, *and* $d = C_{13} + C_{44}$. The parameter θ is the angle measured from the symmetry axis.

Figure E-1 shows the low- and high-frequency shear ($G(\theta)$) and Young's ($E(\theta)$) moduli for a water-saturated porous-grain aggregate for two different intragranular aspect ratios: α_g = 0.5 and α_g =0.1. The matrix was assumed to be pure calcite.

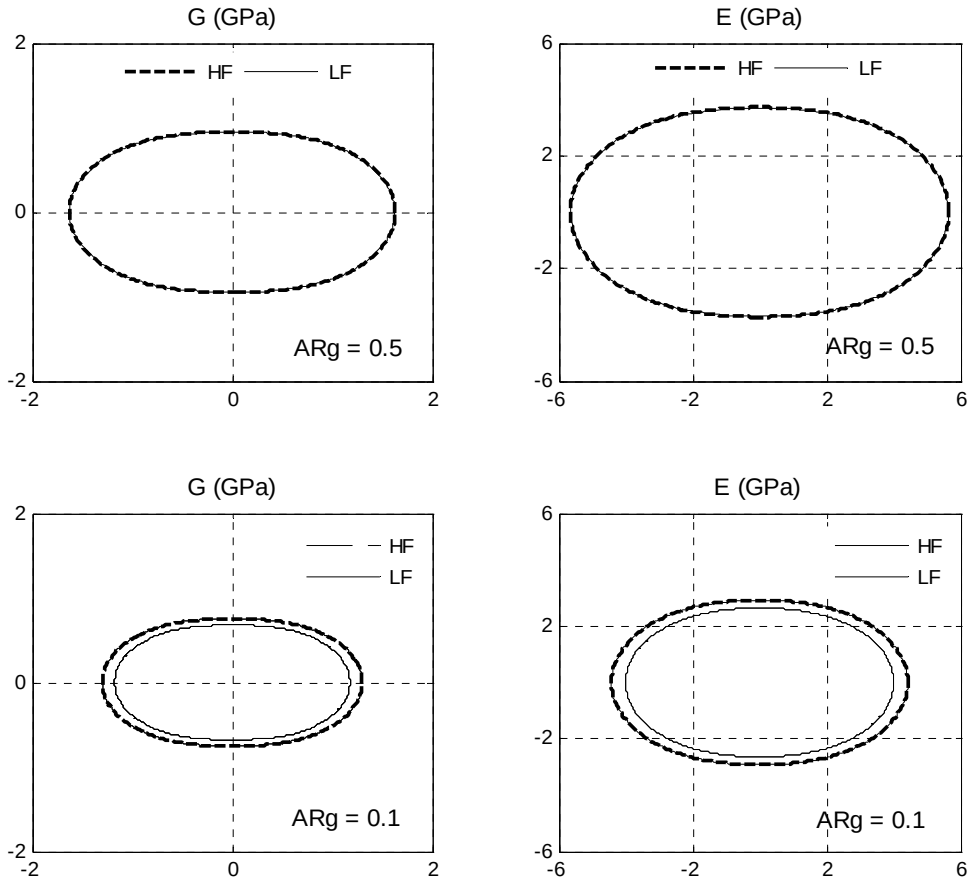

Figure E-1. Low- and high-frequency shear and Young's moduli predicted by Walton's anisotropic model for two different aspect ratios. The porosity was fixed at 0.2. The vertical and horizontal scales in all plots is in GPa.

Appendix F

VHF effective elastic properties using DEM and CPA

Figure F-1 shows a comparison of the VHF effective elastic properties of the aggregate estimated using DEM and SC. The friction coefficient and the intragranular porosity used are: $\gamma = 0.5$ and $\alpha_g = 0.5$, respectively.

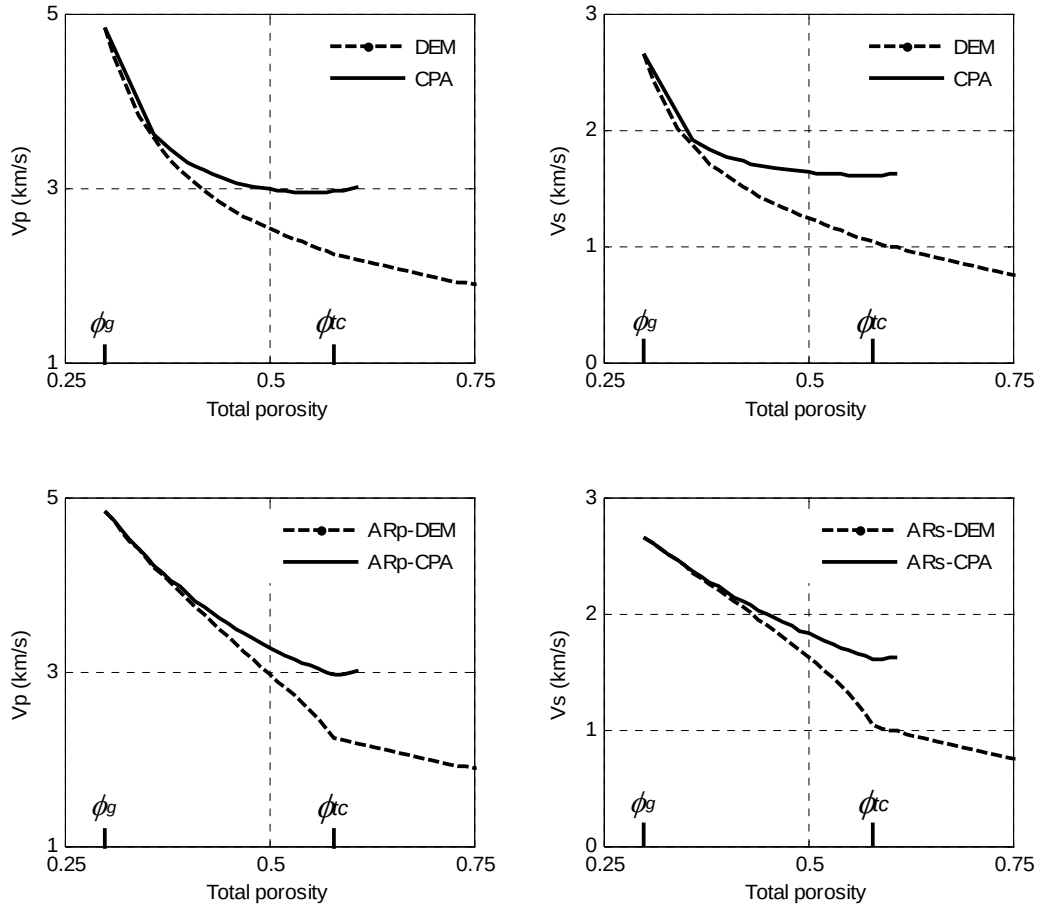

Figure F-1. Comparison of the very high frequency (VHF) *Vp* and *Vs* predicted by DEM and CPA. Top Frame: PGSO model. Bottom frame: PGST model.

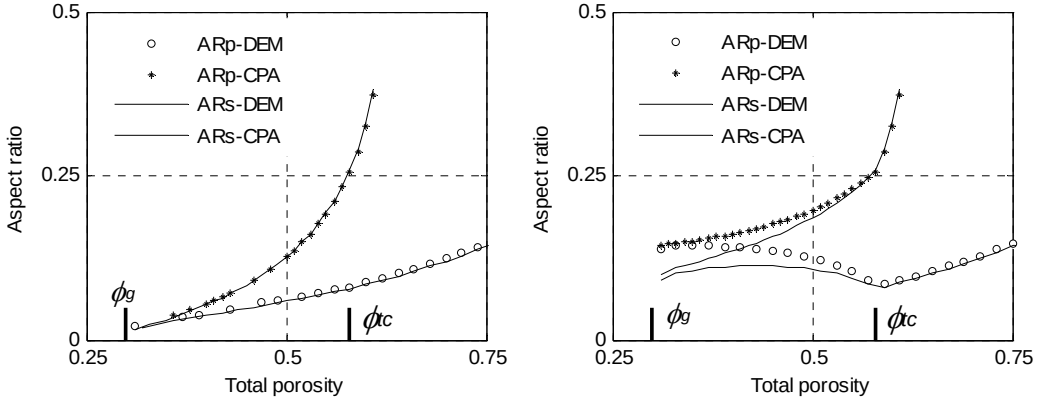

Figure F-2. DEM and CPA aspect ratios needed to match the PGSO (left) and PGST (right) *Vp* and *Vs* velocities.

Appendix G

Cemented sand model

The cemented-sand model allows one to calculate the bulk and shear moduli of dry sand in which cement is deposited at the grain contacts. The cement is elastic, and its properties may differ from those of the sand grains. The effective dry-rock bulk and shear moduli according to this model (Dvorkin and Nur, 1996) are,

$$K_{dry} = \frac{1}{6} C(1-\phi_o)(K_{Cem} + 4G_{Cem}/3)\hat{S}_N, \qquad G_{dry} = \frac{3}{5} K_{dry} + \frac{3}{20} C(1-\phi_o) G_{Cem} \hat{S}_\Gamma \qquad \text{(G-1)}$$

where the parameters $\hat{S}_N$ and $\hat{S}_\Gamma$ are proportional to the normal and shear stiffness, respectively, of a cemented two grain combination. They depend on the amount of the contact cement and on the properties of the cement and the grains as defined in the following relations:

$\hat{S}_N = A_N \beta^2 + B_N \beta + C_N$,

where

$A_N = -0.024153 \Lambda_N^{-1.3646}$,

$B_N = 0.20405 \Lambda_N^{-0.89008}$,

$C_N = 0.00024649 \Lambda_N^{-1.9864}$ and

$\hat{S}_\Gamma = A_\Gamma \beta^2 + B_\Gamma \beta + C_\Gamma$

$$A_\Gamma = -10^{-2}(2.26\nu^2 + 2.07\nu + 2.3)\Lambda_\tau^{0.079\nu^2+0.1754\nu-1.342}$$
$$B_\Gamma = (0.0573\nu^2 + 0.0937\nu + 0.202)\Lambda_\tau^{0.0274\nu^2+0.0529\nu-0.8765}$$
$$C_\Gamma = -10^{-4}(9.654\nu^2 + 4.945\nu + 3.1)\Lambda_\tau^{0.01867\nu^2+0.4011\nu-1.8186}$$
$$\Lambda_N = \frac{2G_C}{\pi G}\frac{(1-\nu)(1-\nu_C)}{(1-2\nu_C)}, \qquad \Lambda_\tau = \frac{G_C}{\pi G},$$

This model considers three certain schemes of cement deposition (Figure 5.9, main paper). The three cases in which cement is located at the grains are a) the cement is deposited away from the grain contact (noncontact cement), b) the cement is deposited at grain contacts, and c) all cement is deposited at grain surfaces (Dvorkin et al., 1994; Dvorkin et al., 1999; Yin and Dvorkin, 1994).

The parameter "a" in the model is the radius of the contact cement layer, and R is the grain radius. The amount of cement can be expressed through the ratio β of the radius of the cement layer "a" to the grain radius R:

$$\beta = \frac{a}{R} = \begin{cases} 2\left[\dfrac{S\phi_o}{3C(1-\phi_o)}\right]^{0.25} & \text{Scheme 1} \\ \left[\dfrac{2S\phi_o}{3(1-\phi_o)}\right]^{0.5} & \text{Scheme 2} \end{cases} \tag{G-2}$$

where S is the volume fraction of the pore space of the uncemented sand occupied by cement in the cemented sand.

Appendix H

Composite data sets

This appendix contains the composite data sets used in Chapter 2. All data sets were collected from the literature.

Symbols used in the Tables:

Vol = Volume fraction of inclusion
Vp = P-wave velocity
Vs = S-wave velocity
Rhob = Bulk density
K = Bulk modulus
G = Shear modulus
PR = Poisson ratio
PZ = Particle size
WF = Weight fraction of inclusion concentration

Table H-1: All artificial composite data sets.

Measured properties

References	Vol	Vp (km/s)	Vs (km/s)	k (Gpa)	G (Gpa)	E (Gpa)	PR	Rhob (g/cc)	PZ	WF
Lees and Davidson (1977)	0.0001	2.5177								
	0.2119	2.4851								
	0.3192	2.6457								
	0.3405	2.7003								
	0.5403	2.7385								
Lees and Davidson (1977)	0.0000	2.5225								
	0.0978	2.4498								
	0.1973	2.4844								
	0.2960	2.5156								
	0.3982	2.5848								
Zhang et al. (1996)	0.0000	2.4880	1.2070					1.250		
	0.0850	2.5310	1.2590					1.370		
	0.1230	2.5700	1.2820					1.420		
	0.1570	2.6090	1.3160					1.470		
	0.1890	2.6620	1.3530					1.520		
	0.2190	2.7110	1.3870					1.560		
	0.2460	2.7350	1.4090					1.610		
	0.2720	2.7830	1.4390					1.640		
	0.2960	2.8170	1.4640					1.670		
	0.3180	2.8630	1.4950					1.710		
	0.3390	2.9120	1.5310					1.750		
	0.3590	2.9350	1.5450					1.760		
	0.3780	2.9830	1.5700					1.790		
	0.3950	3.0320	1.5920					1.830		
	0.4120	3.0550	1.6170					1.850		
	0.4270	3.0960	1.6360					1.870		
	0.4420	3.1370	1.6750					1.900		
	0.4570	3.1640	1.6870					1.930		
	0.4700	3.1820	1.6980					1.930		

Continuation: Table H-1: All artificial composite data sets.

Bridge and	0.0000	2.6230	1.2700					0.905		
Cheng (1987)	0.0000	2.6180	1.2550					0.905		
	0.0000	2.6110	1.2540					0.905		
	0.0000	2.6180	1.2560					0.905		
	0.0000	2.6230	1.2660					0.905		
	0.0000	2.6200	1.2630					0.905		
	0.0180	2.5360	1.2160					0.938		
	0.0200	2.5450	1.2130					0.941		
	0.0210	2.5490	1.2170					0.942		
	0.0450	2.5190	1.2160					0.987		
	0.0440	2.5220	1.2070					0.984		
	0.0470	2.5050	1.2140					0.990		
	0.0520	2.5210	1.2170					0.998		
	0.0990	2.5040	1.2350					1.083		
	0.0960	2.5190	1.2380					1.077		
	0.1060	2.5140	1.2430					1.095		
	0.0890	2.5090	1.2220					1.065		
	0.0820	2.5270	1.2570					1.053		
	0.0760	2.5220	1.2600					1.041		
	0.0770	2.5240	1.2590					1.043		
	0.0820	2.5390	1.2500					1.053		
	0.1010	2.5450	1.2600					1.087		
	0.1200	2.5670	1.2720					1.121		
	0.1200	2.5660	1.2790					1.121		
	0.1210	2.5690	1.2710					1.123		
	0.1210	2.5580	1.2770					1.123		
	0.1660	2.5610	1.3060					1.207		
	0.1640	2.5550	1.3110					1.200		
	0.1620	2.5790	1.3050					1.196		
	0.2110	2.5970	1.3420					1.284		
	0.2150	2.6050	1.3370					1.290		
	0.2180	2.5970	1.3270					1.287		
	0.2110	2.6090	1.3460					1.284		
	0.2670	2.6360	1.3780					1.385		
	0.2720	2.6350	1.3740					1.394		
	0.2700	2.6480	1.3770					1.389		
	0.2550	2.6470	1.3760					1.363		
	0.3680	2.7090	1.3900					1.566		
	0.3670	2.7100	1.4040					1.564		
	0.3860	2.7310	1.4390					1.597		
	0.3760	2.7200	1.4370					1.580		
	0.3710	2.7430	1.4370					1.570		
	0.1930	2.5860	1.3000					1.251		
	0.1930	2.5890	1.3100					1.251		
	0.1930	2.5830	1.2950					1.252		
	0.2920	2.6470	1.3870					1.430		
	0.3010	2.6680	1.3740					1.445		
	0.2890	2.6400	1.3500					1.424		
	0.3440	2.7030	1.4330					1.522		
	0.3500	2.7090	1.4410					1.533		

Continuation: Table H-1: All artificial composite data sets.

Gomez et al. (2000)	0.4199	2.1370								
	0.4710	1.8630								
	0.4710	1.9178								
	0.4710	1.9863								
	0.4793	2.0616								
	0.5014	1.8973								
	0.5290	1.8699								
	0.5304	1.9178								
	0.5290	1.9863								
	0.5207	2.0616								
	0.5801	2.1370								
	0.6105	2.2055								
	0.6602	2.2123								
	0.6713	2.3630								
	0.7307	2.5274								
Piche and	0.0000	2.6670	1.3050					1.182		
Hammel (1986)	0.0340	2.4970	1.2460					1.392		
	0.0530	2.4350	1.2170					1.527		
	0.0720	2.3890	1.1940					1.667		
	0.0820	2.3580	1.1840					1.741		
	0.1220	2.2580	1.1550					1.996		
	0.1520	2.2270	1.1450					2.197		
	0.2210	2.1880	1.1440					2.641		
	0.3010	2.2170	1.1910					3.180		
	0.4000	2.3050	1.2690					3.838		
Piche	0.0000	2.6670	1.3050					1.182		
and Hammel (1987)	0.0336	2.5937	1.2716					1.348		
	0.0569	2.5323	1.2597					1.542		
FLAKES	0.0997	2.4160	1.2325					1.781		
	0.1227	2.3779	1.2310					1.936		
	0.1542	2.3333	1.2265					2.166		
	0.2010	2.2598	1.2552					2.484		
	0.2993	2.2533	1.3234					3.117		
Nguyen et al. (1996)	0.0200	2.2650	1.0510						0.5	
	0.0400	2.0650	0.9870						0.5	
	0.1700	1.8010	0.9320						0.5	
	0.1000	1.8700	0.9000						1.0	
	0.5000	2.0100	1.1170						1.0	
	0.1400	1.7320	0.8620						5.0	
	0.3700	1.6520	0.8670						5.0	
	0.4700	1.8740	1.0130						5.0	
	0.4300	1.7410	0.9370						10.0	
	0.5500	2.0230	1.2240						10.0	
	0.3600	1.6990	0.9070						14.0	
	0.5000	1.9420	1.0950						14.0	

Continuation: Table H-1: All artificial composite data sets.

Sugawara		2.5785						1.161	3.0	0.00
et al. (2005)		2.5785						1.249	3.0	0.05
		2.5575						1.315	3.0	0.10
		2.4287						1.403	3.0	0.20
		2.3179						1.601	3.0	0.30
		2.2341						1.757	3.0	0.40
		2.0874						2.001	3.0	0.50
		1.9378						2.401	3.0	0.60
		1.8151						3.070	3.0	0.70
		1.6774						4.139	3.0	0.80
		1.6474						6.080	3.0	0.90
Lees (1973)		2.0000						1.260		0.00
		1.5000						3.090		0.10
		1.3000						4.960		0.20
		1.0000						6.750		0.30
		0.8200						8.670		0.40
		0.9800						10.200		0.50
		1.2000						12.200		0.60
		1.9000						14.000		0.70
		2.7000						15.400		0.80
		2.7000						16.300		0.90
		5.3000						19.300		1.00
						E/Em				
Richard (1975)	0.0000					0.8998	0.45			
	0.0509					1.2215	0.46			
	0.1152					1.3824	0.43			
	0.1669					1.3491	0.43			
	0.2167					1.7152	0.42			
	0.3069					1.9148	0.40			
	0.3482					2.1589	0.38			
	0.3524					2.1866	0.39			
	0.4497					4.1113	0.33			
	0.4641					3.6842	0.35			
						E/Em				
Smith (1976)	0.0000					0.9901	0.39			
	0.0241					1.0168	0.41			
	0.0497					1.0815	0.39			
	0.0702					1.1192	0.40			
	0.0991					1.2273	0.38			
	0.1490					1.3730	0.37			
	0.2245					1.6704	0.39			
	0.3020					1.9949	0.38			
	0.3955					2.6287	0.35			
	0.5000					4.0173	0.33			
Doi et al. (1970)	0.0000			3.92	3.04	7.1400	0.19			0.00
	0.0180			3.96	2.94	7.0700	0.20			1.00
	0.0530			3.72	2.81	6.7320	0.20			3.10
	0.1030			3.62	2.67	6.4190	0.20			6.10
	0.1640			3.50	2.45	5.9530	0.22			10.00
	0.2500			3.17	2.18	5.3270	0.22			16.00
	0.3050			3.18	2.03	5.0130	0.24			20.00
	0.3050			3.14	2.02	4.9950	0.24			20.00
	0.3680			3.03	1.88	4.6770	0.24			24.80
	0.4400				0.00	4.2900				30.80
	0.4500				0.00	4.2700				32.20

Continuation: Table H-1: All artificial composite data sets.

Biwa (2001)	0.0000	2.7389	1.3773	5.91	2.25			1.189		
	0.2160	2.4717	1.2101	4.87	1.70			1.172		
	0.3720	2.3143	1.1160	4.28	1.45			1.158		
	0.5240	2.1727	1.0114	3.89	1.16			1.159		
	1.0000	1.7523	0.7053	2.71	0.56			1.126		
Ji and Wang (1999)	0.0000	8.0080	4.8350	104.60	74.20			3.174		
	0.2000	8.0400	4.8420	106.20	74.60			3.182		
	0.4000	8.0950	4.8380	109.50	74.70			3.191		
	0.5000	8.1700	4.8570	112.20	75.00			3.179		
	0.6000	8.2290	4.8900	114.10	76.10			3.183		
	0.8000	8.3720	4.9380	119.40	77.50			3.178		
	1.0000	8.5340	4.9980	126.30	79.80			3.195		
Pernot	0.0000					68.0000	0.18			
and Rogier (1993)	0.0350					72.0000	0.19			
	0.0600					72.0000	0.19			
	0.1000					74.0000	0.20			
	0.2000					79.0000	0.20			
	0.3000					88.0000	0.22			
	0.5000					102.0000	0.23			
Hasselman	0.0000					80.5000				
and Fulrath (1965a)	0.1000					92.4000				
	0.2000					107.1000				
	0.3000					122.8000				
	0.4000					144.7000				
	0.4500					158.5000				
	0.5000					167.8000				
	0.5500					137.2000				
	1.0000					411.0400				
Hasselman	0.0000					80.5000				
and Fulrath (1965b)	0.1000					90.9000				
	0.2000					105.5000				
	0.3000					118.0000				
	0.4000					137.5000				
	0.5000					159.9000				
	1.0000					355.5000				
						Epef	Epaf			
Hasselman	0.0000					68.8800	68.88			
and Fulrath (1963)	0.1960					40.3900	35.21			
	0.2540					33.7200	29.56			
	0.3440					25.8300	21.72			
	0.4110					21.5400	17.78			
	1.0000					1.5000	1.50			

Continuation: Table H-1: All artificial composite data sets.

Nishimatsu	0.0000					0.9936				
and Gurland (1960)	0.0994					1.0987				
	0.3479					1.5669				
	0.4982					1.8153				
	0.6284					2.0541				
	0.7787					2.4172				
	0.8982					2.9236				
Quesenberry	0.0000					2.4500		1.190		
et al. (2003)	0.0500					3.1300		1.210		
	0.1500					3.9000		1.340		
	0.2500					4.9900		1.490		
	0.2900					5.7000		1.550		
	0.4500					10.1000		1.790		
	0.5000					12.9000		1.840		
						Dynamic/Static				
Dunn and	0.1450			83.56	32.07	85.32/86.3				
Ledbetter (1995)	0.1520			83.94	32.27	85.77/86.75				
	0.1620			84.58	32.51	86.5/87.03				
	0.1860			86.79	34.08	90.37/91.42				
	0.2120			86.42	34.42	91.32/89.22				
	0.2400			88.77	35.71	94.63/96.14				
						E30/E130/E3.5				
Vollenberg and	0.0500					1.7505/1.7414/1.6459				
Heikens (1990)	0.1500					2.2768/2.232/2.2762				
	0.2500					3.0871/2.8074/2.9036				
	0.0500					1.6892/1.656/1.796				
	0.1000					2.0423/-/-				
	0.1500					2.3521/2.142/2.596				
	0.2000					2.6438/-1/2.994				
	0.2500					3.0835/2.605/3.5				
Gaudig et al. (2003)	0.0918					117.4184				
(Okamoto et al.,1983)	0.4003					141.9992				
	0.4550					146.6495				
	0.4944					156.8347				
	0.4396					170.1179				
	0.4352					176.9812				
	0.6847					169.2364				
	0.7416					167.2447				
	0.7875					174.3304				
	0.9145					174.3325				
(Speich et al., 1960)	0.0329					83.3210				
	0.0373					97.0480				
	0.0614					127.6015				
	0.0548					133.8007				
	0.9956					169.6679				
						Edyn/Estat				
Ledbetter	0.1450			83.56	32.07	85.32/86.3				
and Dunn (1995)	0.1520			83.94	32.27	85.77/86.75				
	0.1620			84.58	32.51	86.5/87.03				
	0.1860			86.79	34.08	90.37/91.42				
	0.2120			86.42	34.42	91.32/89.22				
	0.2400			88.77	35.71	94.63/96.14				

Appendix I

Carbonate data sets

This appendix contains the carbonate data sets used in Chapter 3. All data sets were collected from the literature.

Symbols used in the Tables:

AR-mean = mean aspect ratio
Class = Petrophysical classification
Cal = Calcite
Dry-Rhob = Bulk density at dry condition
k-feld = k-feldspar
kaol = Kaolinite
Minor Axis = Minor axis of grain or pores
Major Axis = Major axis of grain or pores
mbsf = Meters below sea floor
Por or Phi = Porosity
Pc = Confining pressure
Perm = Permeability
Vp-sat = P-wave velocity at full brine saturation condition
Vp-dry = P-wave velocity at dry condition
Vs-sat = S-wave velocity at full brine saturation condition
Vs-dry = S-wave velocity at dry condition
Vp-9 = P-wave velocity at 9 MPa differential pressure
Vp-30 = P-wave velocity at 30 MPa differential pressure
Vs-9 = S-wave velocity at 9 MPa differential pressure
Vs-30 = S-wave velocity at 30 MPa differential pressure
Rhog = Grain density
Sat-Rhob = Bulk density at full brine saturation condition

Table I-1: Carbonate data sets from Assefa et al. (2003).

Por	Dry-Rhob (g/cc)	Calcite (%)	Dolomite (%)	Quartz (%)	Vs-dry (km/s)	Vp-dry (km/s)	Vs-Sat (km/s)	Vp-Sat (km/s)
3.20	2.54	62.8	3.9	33.3	2.934	5.370	2.880	5.370
5.50	2.49	50.4	39.8	9.8	2.680	4.526	2.466	4.577
5.80	2.40	98.6	0.0	1.4	2.631	4.516	2.492	4.702
6.20	2.52	78.4	13.6	4.4	2.661	4.518	2.370	4.560
6.60	2.37	100.0	0.0	0.0	2.499	4.262	0.000	5.169
6.61	2.48	92.4	3.7	3.9	2.758	4.834	2.624	4.934
7.60	2.42	95.0	0.0	5.0	2.696	4.602	2.575	4.835
8.00	2.41	96.1	3.9	0.0	2.651	4.604	2.554	4.772
8.01	2.32	100.0	0.0	0.0	2.463	4.220	2.236	4.214
8.10	2.45	43.4	55.4	1.2	2.642	4.621	2.459	4.559
8.20	2.33	81.4	14.0	4.6	2.483	4.233	2.276	4.303
8.90	2.41	96.4	2.9	0.7	2.729	4.681	2.461	4.855
9.20	2.40	100.0	0.0	0.0	2.385	3.956	2.258	4.230
9.21	2.28	99.3	0.0	0.7	2.370	4.041	2.115	4.005
9.20	2.37	97.1	2.9	0.0	2.442	4.176	2.251	4.282
9.40	2.37	97.4	0.0	2.6	2.473	4.268	2.264	4.354
9.50	2.35	95.0	0.0	5.0	2.511	4.338	2.326	4.461
9.51	2.35	95.6	3.3	1.1	2.414	4.178	2.191	4.160
9.50	2.41	97.3	0.0	2.7	2.460	3.770	2.028	4.291
9.60	2.33	100.0	0.0	0.0	2.651	4.639	2.500	4.631
9.61	2.38	68.3	31.7	0.0	2.670	4.658	2.476	4.628
9.90	2.40	98.5	1.5	0.0	2.466	4.293	2.414	4.377
10.40	2.35	78.0	0.0	22.0	2.516	4.499	2.374	4.350
10.60	2.35	97.3	0.0	2.7	2.553	4.420	2.401	4.498
10.90	2.38	81.6	17.3	1.1	2.478	4.366	2.287	4.306
11.20	2.34	97.3	0.0	2.7	2.352	4.068	2.215	4.277
11.30	2.27	100.0	0.0	0.0	2.263	3.303	2.088	3.457
11.50	2.32	100.0	0.0	0.0	2.474	4.227	2.318	4.261
12.40	2.34	99.3	0.0	0.7	2.489	4.281	2.339	4.397
12.90	2.27	100.0	0.0	0.0	2.628	4.551	2.393	4.581
13.00	2.29	98.6	0.0	1.4	2.413	4.114	0.000	4.112
13.40	2.24	97.3	0.0	2.7	2.388	4.101	2.739	0.000
13.80	2.25	97.3	0.0	2.7	2.751	5.004	2.578	5.035
14.20	2.31	100.0	0.0	0.0	2.166	3.693	1.805	3.738
15.80	2.20	98.6	0.0	1.4	2.252	3.559	1.920	3.887
16.10	2.20	97.1	2.9	0.0	2.387	4.042	2.174	4.049
16.60	2.15	98.3	0.0	1.7	2.178	3.296	0.000	3.734
16.70	2.20	90.8	9.2	0.0	2.234	3.789	1.989	3.863

Continuation: Table I-1: Carbonate data sets from Assefa et al. (2003).

Por	Dry-Rhob (g/cc)	Calcite (%)	Dolomite (%)	Quartz (%)	Vs-dry (km/s)	Vp-dry (km/s)	Vs-sat (km/s)	Vp-sat (km/s)	AR-Mean	Menor Axis	Major Axis
3.2	2.54	62.8	3.9	33.3	2.934	5.370	2.880	5.370	0.300	60	200
5.8	2.40	98.6	0.0	1.4	2.631	4.516	2.492	4.702	0.357	50	140
8.0	2.41	96.1	3.9	0.0	2.651	4.604	2.554	4.772	0.100	20	200
8.9	2.41	96.4	2.9	0.7	2.729	4.681	2.461	4.855	0.199	27	136
9.2	2.40	100.0	0.0	0.0	2.385	3.956	2.258	4.230	0.143	20	140
9.2	2.28	99.3	0.0	0.7	2.370	4.041	2.115	4.005	0.061	20	330
9.5	2.35	95.6	3.3	1.1	2.414	4.178	2.191	4.160	0.231	30	130
10.6	2.35	97.3	0.0	2.7	2.553	4.420	2.401	4.498	0.588	100	170
11.2	2.34	97.3	0.0	2.7	2.352	4.068	2.215	4.277	0.146	60	410
11.5	2.32	100.0	0.0	0.0	2.474	4.227	2.318	4.261	0.095	20	210
12.4	2.34	99.3	0.0	0.7	2.489	4.281	2.339	4.397	0.357	50	140
13.0	2.29	98.6	0.0	1.4	2.413	4.114	0.000	4.112	0.258	80	310
15.8	2.20	98.6	0.0	1.4	2.252	3.559	1.920	3.887	0.400	60	150
16.7	2.20	90.8	9.2	0.0	2.234	3.789	1.989	3.863	0.143	20	140

Table I-2: Carbonate data sets from Fabricius et al. (2008).

Sample	Por (Fraction)	Vp-dry (km/s)	Vs-dry (km/s)	Vp-sat (km/s)	Vs-sat (km/s)	Rhog (g/cc)	Calcite (%)	Quartz (%)	Clay (%)
1	0.269	3.59	2.18	3.47	1.86	2.706	83.0	8.9	2.0
2	0.247	3.47	2.16	3.43	1.83	2.708	78.3	10.8	3.0
4	0.219	3.76	2.31	3.78	2.07	2.704	79.2	11.5	0.3
6	0.224	3.87	2.34	3.81	2.07	2.710	90.7	3.8	2.3
7	0.072	4.85	2.84	4.83	2.59	2.705	79.1	12.7	2.1
11	0.267	3.16	2.08	3.19	1.75	2.696	84.7	1.6	5.8
12	0.192	4.01	2.43	4.11	2.26	2.716	95.0	1.1	2.1
13	0.207	4.04	2.42	4.11	2.26	2.720	97.1	0.6	0.7
14	0.144	3.95	2.47	3.86	2.01	2.721	84.5	5.8	6.6
16	0.144	4.57	2.69	4.47	2.47	2.720	70.2	19.3	3.9
18	0.191	3.92	2.38	3.97	2.17	2.718	96.7	0.5	1.2
19	0.248	3.56	2.16	3.62	1.95	2.717	96.1	0.7	1.1
20	0.063	5.52	3.07	5.50	2.95	2.726	93.3	1.9	1.4
21	0.080	5.23	2.99	5.23	2.83	2.723	92.7	1.5	1.9
22	0.138	3.02	2.19	3.13	1.54	2.705	64.7	15.0	16.0
25	0.158	3.03	2.14	3.57	1.90	2.704	80.0	7.9	9.3
26	0.247	3.62	2.25	3.62	2.02	2.710	80.2	14.2	2.3
27	0.345	2.89	1.84	2.99	1.61	2.706	91.2	5.8	1.5
28	0.146	4.07	2.59	4.23	2.41	2.714	78.8	14.0	3.7
29	0.281	3.35	2.12	3.41	1.88	2.710	90.8	4.7	3.0
30	0.239	3.36	2.18	3.52	1.92	2.717	82.5	11.9	3.2
31	0.346	3.04	1.89	3.05	1.64	2.694	87.7	8.8	1.6
32	0.309	3.19	1.97	3.21	1.76	2.704	89.0	7.5	1.6
33	0.188	4.12	2.53	4.20	2.38	2.711	73.8	18.1	4.2
34	0.204	4.30	2.60	4.44	2.49	2.716	85.9	7.4	4.7
36	0.317	3.33	2.07	3.33	1.82	2.703	94.1	5.5	1.4
40	0.408	2.45	1.62	2.63	1.37	2.710	97.9	2.2	1.0
41	0.400	2.43	1.58	2.58	1.34	2.713	98.9	1.2	0.8
43	0.416	2.30	1.62	2.51	1.39	2.696	76.4	15.3	5.1
44	0.256	3.58	2.26	3.57	2.04	2.700	76.1	14.6	5.6
45	0.387	2.58	1.70	2.68	1.45	2.692	80.3	13.8	2.7
46	0.398	2.55	1.64	2.66	1.40	2.700	89.2	6.5	2.5
47	0.439	2.39	1.54	2.51	1.29	2.709	88.3	7.4	2.3
48	0.247	3.41	2.23	3.51	2.01	2.670	57.9	31.4	4.1
49	0.203	4.23	2.61	4.29	2.45	2.695	78.3	17.4	1.1
50	0.418	2.09	1.42	2.44	1.25	2.707	98.2	1.8	1.0
51	0.425	2.06	1.37	2.37	1.13	2.707	97.2	2.3	0.7
52	0.412	2.07	1.39	2.43	1.22	2.706	97.7	2.1	0.8
53	0.434	2.20	1.44	2.48	1.26	2.717	98.2	2.2	1.4
56	0.449	1.98	1.30	2.31	1.12	2.673	99.0	1.5	1.1
57	0.411	1.96	1.34	2.36	1.19	2.689	98.7	1.1	0.9
58	0.423	2.06	1.39	2.43	1.23	2.697	98.1	1.3	1.1
62	0.305	3.26	2.01	3.47	1.86	2.719	100.0	0.6	0.5

Table I-3: Carbonate data sets from Kenter et al. (1997).

Class	$CaCO_3$ (%)	K_2O (%)	Dol (%)	Cal (%)	Mica (%)	Kaol (%)	K-Feld (%)	Quartz (%)	Sat-Rhob (g/cc)	Rhog (g/cc)	Por	Vp-9 (km/s)	Vp-30 (km/s)	Vs-9 (km/s)	Vs-30 (km/s)
3	97.2	0.35	85.9	5.5	1.9	1.3	2.4	3.8	2.76	2.79	0.02	6.15	6.24	2.52	2.77
5	96.2	0.04	4.7	92.3	0.2	0.4	0.3	2.5	2.69	2.71	0.02	6.07	6.14	2.77	3.23
5	80.4	0.56	24.2	58.0	3.0	2.2	3.8	8.5	2.67	2.70	0.03	5.53	5.57	2.98	3.00
4	100.0	0.04	87.3	11.3	0.2	0.5	0.3	1.3	2.77	2.83	0.03	6.58	6.66	3.55	3.64
5	93.5	0.23	31.1	62.5	1.2	1.3	1.5	2.2	2.69	2.75	0.04	5.01	5.18	2.63	2.73
4	100.0	0.00	86.4	8.3	0.0	0.1	0.0	0.0	2.76	2.86	0.04	5.48	5.72	2.87	2.99
5	96.8	0.10	5.9	91.0	0.6	0.5	0.7	1.9	2.61	2.71	0.05	6.05	5.92	3.10	3.15
2	30.9	2.46	29.6	0.4	13.3	5.0	16.8	36.6	2.74	2.83	0.05	5.00	5.20	2.89	2.93
3	100.0	0.21	89.5	1.6	1.1	0.9	1.4	6.0	2.73	2.85	0.06	5.06	5.36	2.71	2.93
4	100.0	0.06	89.9	5.5	0.3	0.6	0.4	3.5	2.70	2.83	0.06	5.97	6.11	3.29	3.40
4	96.0	0.27	52.0	40.7	1.5	1.1	1.9	2.9	2.65	2.79	0.07	5.39	5.48	2.96	3.01
3	100.0	0.02	96.9	1.6	0.1	0.7	0.2	1.2	2.71	2.86	0.08	5.85	6.00	3.19	3.27
2	74.2	0.69	69.6	2.8	3.7	1.7	4.7	19.3	2.64	2.81	0.08	5.36	5.45	2.82	3.19
3	100.0	0.02	99.7	0.0	0.1	0.4	0.1	0.8	2.68	2.85	0.08	5.86	5.87	3.35	3.40
5	96.0	0.04	3.0	93.9	0.2	0.6	0.3	1.1	2.68	2.70	0.08	6.34	6.34	3.25	3.30
5	95.2	0.11	34.8	61.4	0.6	0.7	0.7	1.1	2.76	2.74	0.09	6.01	6.09	2.96	3.36
3	89.6	0.15	87.5	0.6	0.8	2.5	1.0	8.4	2.61	2.73	0.09	5.22	5.28	2.89	2.99
2	45.2	0.74	34.9	7.1	4.0	4.3	5.0	44.4	2.56	2.71	0.09	4.62	4.87	2.62	2.82
2	73.8	0.54	64.4	2.9	2.9	1.7	3.7	22.5	2.61	2.79	0.10	5.25	5.32	2.98	3.10
8	100.0	0.06	92.6	4.1	0.3	1.0	0.4	2.1	2.67	2.85	0.10	6.25	6.32	3.30	3.44
2	76.8	0.80	69.5	2.4	4.3	1.0	5.4	19.3	2.63	2.82	0.11	4.59	4.92	2.55	2.73
3	93.3	0.28	88.6	0.9	1.5	1.2	1.9	6.0	2.68	2.88	0.11	5.07	5.24	2.85	3.06
2	64.7	0.88	55.3	5.8	4.7	3.9	6.0	25.2	2.57	2.76	0.11	4.69	4.73	2.62	2.68
3	92.7	0.17	90.8	0.0	0.9	2.2	1.2	8.0	2.64	2.80	0.11	5.61	5.68	3.33	3.17
2	79.0	0.50	66.7	6.1	2.7	1.7	3.4	20.4	2.56	2.81	0.12	5.03	5.10	2.91	2.97
2	80.2	1.06	71.3	4.7	5.7	0.1	7.2	12.4	2.60	2.81	0.12	4.66	4.87	2.59	2.73
2	63.4	1.00	59.0	0.5	5.4	0.0	6.9	30.9	2.54	2.76	0.12	4.91	5.03	2.85	2.97
1	27.4	0.98	20.2	5.5	5.3	9.8	6.7	53.6	2.50	2.70	0.13	3.87	4.12	2.09	2.31
2	69.3	1.10	67.7	0.0	6.0	3.3	7.5	17.5	2.55	2.79	0.13	4.27	4.45	2.55	2.66
2	34.1	2.44	33.3	0.1	13.2	4.9	16.7	36.0	2.50	2.72	0.13	3.77	4.03	2.15	2.36
3	96.8	0.32	87.9	1.6	1.7	2.5	2.2	4.9	2.63	2.85	0.13	5.76	5.67	3.12	3.32
2	81.2	0.48	63.9	11.6	2.6	2.7	3.3	17.1	2.53	2.78	0.14	3.96	4.11	2.17	2.30
1	19.2	1.85	14.3	2.2	10.0	4.9	12.6	58.6	2.44	2.68	0.14	3.64	4.05	1.93	2.32
2	13.0	3.13	13.9	0.0	17.0	7.2	21.4	45.4	2.49	2.73	0.14	3.60	3.84	2.00	2.20
2	52.3	3.62	47.9	1.5	19.6	0.0	24.7	14.7	2.51	2.76	0.14	3.94	4.18	2.23	2.53
2	48.2	1.54	42.0	2.2	8.4	5.0	10.5	33.0	2.45	2.77	0.14	3.79	4.17	2.12	2.41
2	42.5	1.51	37.1	1.8	8.2	3.6	10.3	41.6	2.47	2.74	0.15	4.32	4.48	2.56	2.66
2	77.4	0.65	71.3	3.1	3.5	0.0	4.4	19.4	2.54	2.84	0.15	4.53	4.82	2.67	2.81
2	38.7	1.68	27.9	8.6	9.1	9.4	11.5	38.2	2.48	2.72	0.15	4.03	4.24	2.33	2.48
2	69.6	0.66	65.2	1.0	3.6	0.6	4.5	27.0	2.51	2.78	0.16	4.59	4.63	2.58	2.65
3	97.0	0.13	95.3	1.1	0.7	0.8	0.9	2.1	2.59	2.91	0.16	5.16	5.24	2.93	2.99
3	98.5	1.68	78.8	14.0	9.1	0.0	11.5	0.0	2.50	2.83	0.16	4.95	5.04	2.71	2.78
2	52.1	0.97	43.6	4.0	5.3	1.7	6.6	40.8	2.44	2.73	0.18	3.48	4.00	1.89	2.26
1	7.3	2.54	11.2	0.0	13.8	7.1	17.3	54.7	2.37	2.70	0.19	3.42	3.78	2.00	2.18
2	85.1	0.44	66.0	15.8	2.4	0.5	3.0	12.4	2.44	2.83	0.21	4.20	4.26	2.35	2.40
2	60.3	0.14	73.6	4.2	0.7	3.1	0.9	17.7	2.48	2.84	0.21	4.78	4.80	2.66	2.70
3	100.0	0.07	87.6	11.2	0.4	0.7	0.5	0.7	2.43	2.89	0.23	4.48	4.63	2.54	2.61

Table I-4: Carbonate data sets from Rafavich et al. (1984).

Facies	Depth (mbsf)	Perm (mD)	Phi (%)	Calcite (%)	Dolomite (%)	Anhydrite (%)	Celestite (%)	Quartz (%)
3	1218.1	0.0100	0.71	0	15	85	0	0
5	1218.3	0.0001	8.90	0	53	15	0	23
5	1221.9	0.0100	17.40	0	82	0	0	1
5	1222.4	0.0900	18.60	11	69	0	0	1
1	1222.7	0.0100	1.35	91	0	8	0	0
5	1223.3	1.1000	13.00	17	66	4	0	0
1	1223.9	0.0001	3.57	82	0	14	0	0
1	1224.1	0.0001	3.63	85	0	11	0	0
1	1224.5	0.0001	3.14	90	7	0	0	0
1	1225.3	0.0001	7.71	92	0	0	0	0
7	1226.5	0.0100	7.39	53	20	20	0	0
6	1227.4	0.0100	13.50	38	48	0	0	0
6	1228.0	0.0001	6.12	56	38	0	0	0
6	1229.3	0.0100	11.00	47	42	0	0	0
1	1229.9	6.3000	17.10	65	18	0	0	0
7	1230.1	0.0300	7.70	48	18	26	0	0
5	1230.2	0.0001	6.48	21	73	0	0	0
6	1230.5	0.0100	12.70	35	52	0	0	0
6	1231.7	0.0100	8.52	44	47	0	0	0
5	1232.0	0.0400	13.40	8	79	0	0	0
6	1232.2	0.7900	12.30	48	34	6	0	0
7	1232.5	2.4000	15.10	31	20	34	0	0
6	1232.6	6.9000	18.70	30	51	0	0	0
6	1232.9	7.2000	14.30	30	51	1	0	4
4	1233.5	0.4700	3.40	16	31	50	0	0
7	1234.1	0.0100	2.13	17	15	36	30	0
3	1234.4	0.0200	0.01	0	0	100	0	0
3	1235.2	0.0001	0.01	0	0	100	0	0

Continuation: Table I-4: Carbonate data sets from Rafavich et al. (1984).

Facies	Rhog (g/cc)	Sat-Rhob (g/cc)	Dry-Rhob (g/cc)	Vp-sat (km/s)	Vs-sat (km/s)	Vp-dry (km/s)	Vs-dry (km/s)	Major Axis	Menor Axis	Aspect Ratio
3	2.93	2.92	2.91	5.850	3.372	5.839	3.413	0.00	0.00	0.00
5	2.73	2.57	2.49	4.577	2.697	4.502	2.903	0.00	0.00	0.00
5	2.82	2.50	2.33	4.245	2.458	4.404	2.822	0.08	0.05	1.60
5	2.81	2.47	2.29	4.597	2.674	4.696	2.903	0.00	0.00	0.00
1	2.75	2.73	2.71	6.220	3.338	6.072	3.353	0.00	0.00	0.00
5	2.80	2.57	2.44	5.273	2.959	5.193	3.073	0.13	0.07	1.86
1	2.76	2.70	2.66	6.024	3.239	5.817	3.253	0.11	0.07	1.57
1	2.72	2.65	2.62	5.839	3.178	5.644	3.195	0.25	0.11	2.27
1	2.70	2.65	2.62	6.000	3.192	5.907	3.225	0.15	0.12	1.25
1	2.70	2.57	2.49	5.572	3.018	5.433	3.076	0.00	0.05	1.40
7	2.72	2.60	2.52	5.603	3.048	5.443	3.079	0.19	0.13	1.46
6	2.71	2.48	2.34	4.980	2.697	4.885	2.771	0.06	0.05	1.20
6	2.68	2.58	2.52	5.149	2.903	5.013	2.931	0.00	0.00	0.00
6	2.77	2.58	2.47	5.338	2.959	5.338	3.066	0.07	0.04	1.75
1	2.72	2.43	2.25	4.632	2.540	4.590	2.697	0.10	0.09	1.11
7	2.79	2.65	2.58	5.366	3.048	5.347	3.123	0.12	0.11	1.09
5	2.94	2.81	2.75	5.697	3.188	5.572	3.229	0.11	0.08	1.38
6	2.75	2.53	2.40	5.080	2.822	5.064	2.931	0.11	0.10	1.10
6	2.72	2.58	2.49	5.237	2.931	5.140	2.988	0.10	0.07	1.43
5	2.79	2.55	2.42	4.980	2.822	4.908	2.988	0.10	0.08	1.25
6	2.74	2.53	2.40	5.201	2.697	5.080	2.796	0.16	0.12	1.33
7	2.96	2.66	2.51	4.800	2.674	4.726	2.650	0.15	0.10	1.50
6	2.74	2.53	2.23	4.639	2.561	4.570	2.721	0.11	0.08	1.38
6	2.78	2.52	2.38	5.123	3.018	5.089	3.107	0.03	0.02	1.25
4	2.85	2.79	2.75	6.024	3.364	6.012	3.409	0.03	0.03	1.00
7	3.17	3.13	3.10	5.603	3.101	5.443	3.123	0.00	0.00	0.00
3	2.93	2.93	2.93	5.930	3.328	5.977	3.444	0.00	0.00	0.00
3	2.92	2.92	2.92	6.096	3.413	6.000	3.413	0.00	0.00	0.00

Table I-5: Carbonate data sets from Rafavich et al. (1984).

Facies	Depth (mbsf)	Rhog (g/cc)	Sat-Rhob (g/cc)	Dry-Rhob (g/cc)	Calcite (%)	Dolomite (%)	Anhydrite (%)	Celestite (%)	Quartz (%)
1	2976.8	2.72	2.70	2.70	86	7	6	0	0
1	2981.1	2.74	2.67	2.63	68	27	1	0	0
1	2983.2	2.68	2.63	2.59	96	1	0	0	0
1	2985.4	2.70	2.67	2.65	98	0	0	0	0
6	2990.2	2.75	2.72	2.70	52	45	1	0	0
5	2997.6	2.76	2.64	2.57	7	83	3	0	0
6	3000.3	2.74	2.65	2.60	41	54	0	0	0
5	3002.1	2.79	2.63	2.54	13	75	0	0	0
5	3004.3	2.83	2.71	2.64	0	93	0	0	0
5	3007.0	2.78	2.69	2.53	32	63	0	0	0
5	3010.7	3.20	3.10	3.06	2	92	0	2	0
6	3014.3	2.70	2.66	2.64	60	36	2	0	0
3	3016.8	2.81	2.69	2.62	1	92	0	0	0
5	3027.1	2.82	2.58	2.45	7	80	0	0	0
6	3028.3	2.71	2.69	2.67	36	62	0	0	0
5	3029.6	2.80	2.67	2.60	7	85	1	0	0
6	3031.1	2.75	2.73	2.71	36	63	0	0	0
5	3057.9	2.71	2.56	2.48	0	87	1	4	0
1	3071.3	2.69	2.64	2.61	95	2	0	0	0
5	3078.3	2.83	2.60	2.47	25	62	0	0	0
6	3085.6	2.72	2.69	2.67	64	34	0	0	0
6	3089.0	2.71	2.69	2.67	64	35	0	0	0
1	3099.1	2.72	2.65	2.62	74	22	0	0	0
1	3102.4	2.71	2.70	2.70	77	19	0	3	0
5	3038.4	2.77	2.48	2.31	0	78	1	4	0
6	3043.0	2.70	2.49	2.37	28	46	0	14	0
1	3061.9	2.67	2.55	2.48	93	0	0	0	0
6	3073.8	2.72	2.58	2.50	58	34	0	0	0

Continuation: Table I-5: Carbonate data sets from Rafavich et al. (1984).

Facies	Perm (mD)	Porosity	Vp-sat (km/s)	Vs-sat (km/s)	Vp-dry (km/s)	Vs-dry (km/s)
1	0.0001	0.72	6.2845	3.3348	5.9300	3.3059
1	0.0001	4.04	5.8842	3.1750	5.6444	3.2357
1	0.0100	3.34	6.0118	3.2254	5.8391	3.2495
1	0.0100	2.07	6.1328	3.2599	6.0717	3.2739
6	0.0001	1.78	6.1700	3.2704	5.5927	3.2739
5	0.0100	6.87	5.5217	3.1455	4.9885	3.1294
6	0.0100	5.03	5.6030	3.0913	5.1837	3.1165
5	0.0001	9.04	5.4235	3.0788	5.3287	3.2323
5	0.0001	6.75	5.9415	3.4056	6.0356	3.5075
5	0.0001	5.24	5.6972	3.1488	5.3947	3.2186
5	0.0001	4.37	6.0118	3.3605	5.5927	3.4519
6	0.0001	2.25	5.6760	3.1070	5.3662	3.1326
3	0.0001	6.89	5.7837	3.2774	5.5118	3.3642
5	0.3100	13.14	5.3474	3.0603	5.4820	3.2084
6	0.0001	1.66	5.9070	3.1651	5.6030	3.2880
5	0.0001	7.08	5.4043	3.0913	4.8535	3.1294
6	0.0001	1.24	6.1576	3.3202	5.7837	3.3642
5	0.0100	8.45	5.4043	3.3829	5.3662	3.4597
1	0.0001	3.15	5.6866	3.0757	5.1749	3.0572
5	0.1500	12.75	5.3757	3.0480	5.2825	3.1586
6	0.0001	1.93	5.9531	3.2194	5.6654	3.2529
6	0.0001	1.30	6.0596	3.2460	5.7727	3.2495
1	0.0001	3.56	5.6654	3.0757	5.5018	3.1684
1	0.0001	0.60	6.2331	3.3717	6.0960	3.3829
5	5.0000	16.77	4.8000	2.8755	4.8228	3.0178
6	0.2500	12.38	4.5835	2.7459	4.5357	2.9029
1	0.3600	7.42	5.2733	2.9029	5.0547	2.9308
6	1.0000	8.26	5.3009	2.9308	5.1574	3.0178

Table I-6: Carbonate data sets from Rafavich et al. (1984)

Facies	Depth (mbsf)	Rhog (g/cc)	Sat-Rhob (g/cc)	Dry-Rhob (g/cc)	Calcite (%)	Dolomite (%)	Anhydrite (%)	Celestite (%)	Quartz (%)
5	2954.3	2.79	2.61	2.50	0	88	0	0	2
4	2958.4	2.91	2.91	2.90	0	40	60	0	0
3	2966.5	2.94	2.94	2.94	0	19	81	0	0
2	2967.7	2.77	2.75	2.74	59	15	25	0	0
7	2974.8	2.83	2.82	2.82	31	19	50	0	0
1	2980.5	2.70	2.69	2.69	100	0	0	0	0
6	2985.2	2.72	2.56	2.71	55	32	4	0	0
5	2987.5	2.82	2.51	2.33	0	80	0	0	2
5	2991.8	2.73	2.58	2.49	0	91	0	0	0
5	2994.9	2.83	2.61	2.48	0	88	0	0	0
5	2998.3	2.81	2.72	2.67	0	95	0	0	0
5	3002.9	2.71	2.65	2.61	8	88	0	0	0
5	3004.7	2.72	2.62	2.56	4	90	0	0	0
5	3015.7	2.80	2.63	2.53	4	86	0	0	0
6	3019.3	2.72	2.70	2.69	40	53	2	0	4
5	3029.1	2.67	2.49	2.38	9	67	1	0	12
5	3033.1	2.81	2.66	2.57	17	75	0	0	0
5	3037.0	2.75	2.57	2.46	21	68	0	0	0
1	3038.6	2.69	2.67	2.65	96	0	3	0	0
1	3049.5	2.70	2.68	2.67	99	0	0	0	0
5	3059.5	2.83	2.60	2.47	0	87	0	0	0
1	3062.6	2.74	2.59	2.50	68	23	0	0	0
1	3067.1	2.71	2.62	2.57	81	14	0	0	0
1	3068.6	2.73	2.65	2.61	72	24	0	0	0
1	3076.7	2.70	2.64	2.60	70	26	0	0	0
1	3082.3	2.70	2.66	2.63	98	0	0	0	0

Continuation: Table I-6: Carbonate data sets from Rafavich et al. (1984)

Facies	Perm (mD)	Porosity	Vp-sat (km/s)	Vs-sat (km/s)	Vp-dry (km/s)	Vs-dry (km/s)
5	0.0001	10.27	4.8076	2.7214	4.6892	2.9308
4	0.0100	0.30	6.2459	3.4874	6.3368	3.5237
3	0.0100	0.20	6.0717	3.3239	6.0838	3.3131
2	0.0001	0.86	6.0838	3.2704	5.5824	3.2460
7	0.0100	0.39	6.2331	3.3202	5.6654	3.2774
1	0.0001	0.25	6.3500	3.3867	6.3632	3.3867
6	0.4300	9.35	4.9161	2.7214	4.8613	2.7459
5	0.4000	17.55	5.1400	3.0178	5.2014	3.1358
5	0.0100	8.87	5.1574	2.9308	5.2371	3.1390
5	1.0000	12.26	5.3194	3.0603	5.3194	3.1849
5	0.0001	5.07	6.0356	3.3867	6.0960	3.5156
5	3.9000	3.92	5.6236	3.1039	5.3662	3.1553
5	0.0100	6.04	5.4139	2.9882	5.2192	3.0480
5	0.0001	9.68	5.3380	3.0178	5.3474	3.2017
6	0.0001	1.07	6.0118	3.2357	5.5519	3.2669
5	0.0100	11.05	4.6463	2.7459	4.4824	2.8755
5	0.1000	8.43	5.6030	3.1455	5.6444	3.2774
5	0.4300	10.66	4.8846	2.7214	4.9400	2.9029
1	0.0001	1.29	5.9765	3.2152	5.6972	3.2152
1	0.0001	0.98	6.1082	3.2916	5.7293	3.2599
5	0.0100	12.53	5.3194	3.0480	5.3851	3.2017
1	1.1000	8.70	5.3009	2.9592	5.3662	3.0480
1	0.0100	4.99	5.3101	2.9308	5.1925	3.0178
1	0.0001	4.24	5.4139	2.9308	5.0464	2.9882
1	0.0001	3.96	5.4332	2.9308	5.0631	2.9882
1	0.0001	2.47	5.8956	3.1294	5.7401	3.1950

Table I-7: Carbonate data sets from Verwer et al. (2008).

Sample	Dry-Rhob (g/cc)	Sat-Rhob (g/cc)	Rhog (g/cc)	Por	Vp-dry (km/s)	Vs-dry (km/s)	Vp-sat (km/s)	Vs-sat (km/s)	Calcite (fraction)	Dolomite (fraction)	Perm (mD)
1	2.121	2.387	2.855	0.26	4.797	2.854	4.826	2.786	0.23	0.77	0.00
2	2.294	2.459	2.729	0.16	5.209	2.909	5.163	2.843	0.92	0.08	0.00
3	1.743	2.147	2.860	0.39	4.028	2.438	3.953	2.314	0.00	1.00	0.00
5	1.805	2.187	2.859	0.37	4.070	2.507	4.018	2.314	0.01	0.99	0.00
7	1.596	2.036	2.774	0.42	4.009	2.188	3.959	1.976	0.03	0.97	0.00
11	1.517	2.003	2.860	0.47	3.368	2.002	3.236	1.852	0.00	1.00	0.00
15	1.326	1.881	2.860	0.54	2.992	1.876	2.900	1.629	0.00	1.00	0.00
17	1.352	1.895	2.846	0.53	3.060	1.954	2.977	1.761	0.08	0.92	0.00
23	2.452	2.600	2.860	0.14	6.663	3.663	6.690	3.604	0.00	1.00	0.00
25	2.505	2.633	2.859	0.12	6.630	3.670	6.559	3.615	0.01	0.99	0.01
27	2.117	2.386	2.860	0.26	5.376	3.177	5.388	3.091	0.00	1.00	0.00
28	2.261	2.478	2.860	0.21	5.596	3.142	5.720	3.161	0.00	1.00	0.00
29	1.957	2.265	2.789	0.30	4.701	2.782	4.756	2.624	0.50	0.50	0.00
30	1.862	2.221	2.850	0.35	4.263	2.279	4.220	2.199	0.07	0.93	0.02
31	2.198	2.437	2.857	0.23	5.147	3.251	5.036	2.974	0.02	0.98	0.00
32	2.112	2.383	2.860	0.26	5.177	2.915	5.024	2.754	0.00	1.00	0.00
33	2.276	2.474	2.815	0.19	5.681	3.213	5.694	3.243	0.32	0.68	0.00
34	2.316	2.513	2.860	0.19	5.634	3.231	5.549	3.156	0.00	1.00	0.00
36	2.208	2.442	2.852	0.23	5.593	3.127	5.784	3.079	0.05	0.95	0.00
37	2.412	2.574	2.860	0.16	5.879	3.406	5.912	3.272	0.00	1.00	0.00
39	2.531	2.641	2.833	0.11	6.492	3.508	6.467	3.517	0.19	0.81	0.00
40	2.349	2.523	2.825	0.17	5.705	3.171	5.849	3.152	0.25	0.75	0.00
41	2.513	2.664	2.942	0.15	6.312	3.669	6.253	3.419	0.03	0.97	0.00
42	1.355	1.884	2.774	0.51	2.450	1.196	2.459	1.382	0.03	0.97	0.00
44	2.406	2.560	2.826	0.15	4.959	2.921	5.020	2.901	0.24	0.76	0.00
48	1.898	2.210	2.718	0.30	3.355	2.368	3.273	2.330	1.00	0.00	0.00
49	1.964	2.251	2.718	0.28	4.486	2.596	4.455	2.526	1.00	0.00	0.00
53	2.232	2.417	2.718	0.18	4.901	2.808	4.957	2.745	1.00	0.00	0.00
54	2.412	2.528	2.718	0.11	5.800	3.173	5.813	3.135	1.00	0.00	0.00
56	1.722	2.132	2.851	0.40	4.180	2.468	4.061	2.289	0.06	0.94	0.00
57	1.789	2.172	2.840	0.37	3.874	2.373	3.882	2.263	0.14	0.86	0.00
58	1.468	1.970	2.853	0.49	2.773	1.665	2.493	1.533	0.05	0.95	0.00
59	1.401	1.928	2.854	0.51	2.953	1.730	2.935	1.566	0.04	0.96	0.00
61	1.977	2.288	2.826	0.30	4.456	2.531	4.383	2.432	0.24	0.76	0.00
62	1.474	1.974	2.854	0.48	3.066	1.850	2.904	1.659	0.04	0.96	0.00
63	1.571	2.037	2.857	0.45	2.924	1.533	2.960	1.529	0.02	0.98	0.00
65	1.516	2.002	2.856	0.47	3.847	2.098	3.757	1.909	0.03	0.97	0.00
66	1.901	2.245	2.845	0.33	4.088	2.473	4.067	2.341	0.10	0.90	0.00
67	1.902	2.247	2.850	0.33	4.066	2.374	4.107	2.249	0.07	0.93	0.00
70	2.010	2.316	2.854	0.30	2.468	1.354	2.477	1.352	0.05	0.95	0.00

Continuation: Table I-7: Carbonate data sets from Verwer et al. (2008).

72	2.172	2.421	2.860	0.24	5.301	3.139	5.284	3.039	0.00	1.00	0.00
73	2.114	2.383	2.856	0.26	5.154	2.856	5.221	2.818	0.03	0.97	0.00
74	2.362	2.542	2.860	0.17	6.248	3.329	6.364	3.329	0.00	1.00	0.00
75	2.133	2.395	2.858	0.25	5.677	3.073	5.661	2.952	0.02	0.98	0.00
77	2.074	2.357	2.856	0.27	4.791	2.840	4.712	2.743	0.03	0.97	0.00
79	2.127	2.387	2.843	0.25	4.751	2.768	4.696	2.665	0.12	0.88	0.00
80	2.137	2.395	2.846	0.25	5.175	2.914	5.164	2.853	0.10	0.90	0.00
81	2.095	2.372	2.859	0.27	4.740	2.835	4.768	2.778	0.01	0.99	0.00
83	2.399	2.564	2.853	0.16	5.631	3.198	5.586	3.180	0.05	0.95	0.00
84	2.376	2.549	2.853	0.17	5.696	3.170	5.756	3.201	0.05	0.95	0.00
85	2.415	2.573	2.849	0.15	6.140	3.297	6.140	3.290	0.08	0.92	0.00
87	2.506	2.629	2.845	0.12	6.276	3.477	6.210	3.121	0.10	0.90	0.01
88	2.320	2.513	2.849	0.19	5.498	3.053	5.638	3.014	0.08	0.92	0.00
89	2.561	2.667	2.854	0.10	6.384	3.562	6.384	3.456	0.04	0.96	0.00
91	2.254	2.462	2.822	0.20	5.895	3.300	5.702	3.205	0.27	0.73	0.00
92	2.112	2.354	2.758	0.23	5.046	2.749	5.212	2.681	0.72	0.28	0.00
93	2.247	2.440	2.761	0.19	5.683	3.043	5.602	3.004	0.70	0.30	0.00
95	2.508	2.633	2.853	0.12	5.310	2.569	5.400	2.523	0.05	0.95	0.00
107	1.455	1.963	2.855	0.49	2.533	1.547	2.552	1.436	0.01	0.99	514.00
108	1.710	2.125	2.855	0.40	3.015	1.806	2.952	1.723	0.02	0.98	306.00
109	1.655	2.091	2.860	0.42	3.437	1.956	3.507	1.869	0.00	1.00	0.00
110	2.185	2.429	2.859	0.24	5.148	2.838	5.132	2.765	0.01	0.99	0.00
111	1.697	2.118	2.860	0.41	3.819	2.175	3.793	2.162	0.00	1.00	0.00
112	2.146	2.403	2.856	0.25	5.696	3.149	5.682	3.091	0.03	0.97	0.00
113	2.372	2.549	2.860	0.17	4.793	2.649	4.813	2.561	0.00	1.00	0.00
114	2.035	2.334	2.860	0.29	4.378	2.583	4.361	2.606	0.00	1.00	0.00
115	2.156	2.408	2.851	0.24	5.222	2.961	5.190	2.841	0.06	0.94	0.00
116	2.041	2.336	2.854	0.29	4.307	2.563	4.416	2.565	0.02	0.98	0.00
117	2.059	2.348	2.857	0.28	4.374	2.522	4.408	2.524	0.02	0.98	0.00
118	1.850	2.215	2.857	0.35	5.665	3.068	5.665	3.080	0.02	0.98	0.00
119	1.657	2.091	2.855	0.42	3.181	1.997	3.193	1.863	0.03	0.97	0.00
120	1.747	2.150	2.860	0.39	3.618	2.145	3.607	2.094	0.00	1.00	0.00
121	1.925	2.263	2.858	0.33	4.762	2.615	4.813	2.655	0.02	0.98	0.00
122	2.256	2.474	2.856	0.21	5.595	3.121	5.618	3.184	0.03	0.97	0.00
123	2.440	2.589	2.852	0.14	5.761	3.148	5.912	3.192	0.04	0.96	0.00
124	2.536	2.605	2.718	0.07	5.980	3.270	6.034	3.341	1.00	0.00	0.00
125	2.112	2.343	2.718	0.22	5.590	2.865	5.660	2.920	1.00	0.00	0.00
126	2.635	2.667	2.718	0.03	5.353	2.860	5.370	2.803	1.00	0.00	0.00
127	2.431	2.546	2.734	0.11	5.784	3.066	5.989	3.071	0.89	0.11	0.00
128	2.686	2.739	2.831	0.05	5.367	2.835	5.316	2.779	0.01	0.99	0.00
129	2.189	2.432	2.860	0.23	5.071	2.839	5.137	2.801	0.00	1.00	0.00
130	1.968	2.266	2.766	0.29	4.754	2.611	4.725	2.553	0.66	0.34	0.00
131	2.190	2.391	2.718	0.19	5.852	3.076	5.913	3.016	0.98	0.02	0.00
132	1.902	2.213	2.718	0.30	3.496	2.095	3.619	1.997	1.00	0.00	0.00

Continuation: Table I-7: Carbonate data sets from Verwer et al. (2008).

133	2.337	2.526	2.860	0.18	4.200	2.494	4.291	2.325	0.00	1.00	0.00
134	2.280	2.472	2.800	0.19	4.800	2.725	5.105	2.832	0.42	0.58	0.00
136	2.258	2.473	2.853	0.21	4.955	2.826	5.017	2.748	0.05	0.95	0.00
137	2.381	2.509	2.718	0.12	5.408	2.875	5.522	3.060	1.00	0.00	0.00
138	2.112	2.382	2.860	0.26	4.654	2.685	4.673	2.721	0.00	1.00	0.00
139	1.953	2.282	2.863	0.32	4.153	2.455	4.239	2.349	0.02	0.98	518.00
140	2.211	2.417	2.762	0.20	4.888	2.757	4.963	2.704	0.69	0.31	0.00
141	2.377	2.544	2.835	0.16	5.533	3.084	5.520	3.045	0.17	0.83	0.00
142	2.187	2.406	2.775	0.21	5.116	2.853	5.170	2.920	0.58	0.42	0.00
143	2.039	2.329	2.833	0.28	5.091	2.823	5.153	2.850	0.17	0.83	0.00
145	1.367	1.907	2.860	0.52	3.023	1.841	2.996	1.644	0.00	1.00	0.00
146	1.376	1.913	2.860	0.52	3.060	1.827	2.994	1.691	0.00	1.00	0.00
147	1.523	2.007	2.860	0.47	3.197	1.765	3.210	1.728	0.00	1.00	0.00
148	1.515	2.002	2.860	0.47	3.645	2.156	3.610	2.007	0.00	1.00	0.00
150	1.423	1.943	2.860	0.50	3.499	1.930	3.478	1.904	0.00	1.00	0.00
151	1.275	1.849	2.860	0.55	2.868	1.727	2.950	1.618	0.00	1.00	0.00
152	1.283	1.853	2.859	0.55	3.180	1.717	3.193	1.688	0.01	0.99	0.00
154	1.481	1.980	2.860	0.48	3.264	2.047	3.407	1.909	0.00	1.00	0.00
155	1.425	1.945	2.860	0.50	3.130	1.599	3.228	1.589	0.00	1.00	0.00
157	1.276	1.849	2.860	0.55	3.129	1.799	3.174	1.823	0.00	1.00	0.00
158	1.621	2.069	2.860	0.43	3.475	2.051	3.444	1.888	0.00	1.00	0.00
159	1.571	2.038	2.860	0.45	3.255	1.997	3.324	1.893	0.00	1.00	0.00
161	1.939	2.272	2.859	0.32	4.882	2.686	4.866	2.703	0.01	0.99	0.00
162	1.558	2.029	2.860	0.46	3.669	2.108	3.693	1.991	0.00	1.00	0.00
163	1.665	2.097	2.860	0.42	3.758	2.217	3.814	2.128	0.00	1.00	0.00
164	1.918	2.259	2.860	0.33	4.485	2.449	4.396	2.405	0.00	1.00	0.00
165	2.164	2.416	2.859	0.24	4.667	2.724	4.725	2.679	0.01	0.99	0.00
166	1.572	2.038	2.860	0.45	3.708	2.036	3.885	2.000	0.00	1.00	0.00
167	1.823	2.198	2.860	0.36	4.430	2.564	4.328	2.420	0.00	1.00	0.00
168	1.625	2.072	2.860	0.43	3.832	2.219	3.854	1.933	0.00	1.00	0.00
169	1.541	2.018	2.860	0.46	3.513	2.103	3.625	1.998	0.00	1.00	0.00
170	2.515	2.640	2.859	0.12	5.702	3.037	5.674	3.095	0.01	0.99	0.00
171	1.780	2.171	2.859	0.38	4.812	2.426	4.733	2.413	0.01	0.99	0.00
173	2.197	2.437	2.860	0.23	4.646	2.636	4.885	2.664	0.00	1.00	0.00
175	2.058	2.348	2.860	0.28	4.518	2.643	4.611	2.590	0.00	1.00	0.00
176	2.005	2.314	2.860	0.30	4.780	2.716	4.770	2.621	0.00	1.00	0.00
178	2.054	2.346	2.860	0.28	4.963	2.816	4.885	2.746	0.00	1.00	0.00
179	1.834	2.206	2.860	0.36	5.306	2.712	5.469	2.719	0.00	1.00	0.00
182	2.307	2.507	2.860	0.19	5.923	3.138	5.923	3.245	0.00	1.00	0.00
184	1.996	2.309	2.859	0.30	5.046	2.852	5.136	2.888	0.01	0.99	0.00
185	2.041	2.337	2.860	0.29	5.028	2.818	5.165	2.839	0.00	1.00	0.00
187	1.531	2.002	2.810	0.46	4.402	2.307	4.318	2.318	0.35	0.65	0.00
188	1.553	2.026	2.860	0.46	3.158	1.833	3.164	1.758	0.00	1.00	0.00
191	1.727	2.137	2.860	0.40	3.559	2.151	3.698	2.107	0.00	1.00	0.00

Continuation: Table I-7: Carbonate data sets from Verwer et al. (2008).

192	1.843	2.210	2.855	0.35	4.707	2.605	4.666	2.575	0.04	0.96	0.00
194	2.220	2.451	2.859	0.22	5.210	2.951	5.159	2.793	0.01	0.99	0.00
195	2.110	2.367	2.809	0.25	5.271	2.801	5.398	2.863	0.36	0.64	0.00
196	1.877	2.233	2.860	0.34	4.109	2.391	4.098	2.236	0.00	1.00	0.00
199	2.431	2.584	2.851	0.15	5.688	3.078	5.745	3.074	0.06	0.94	0.00
200	2.290	2.477	2.796	0.18	5.643	3.036	5.685	3.027	0.45	0.55	0.00
203	2.202	2.440	2.858	0.23	5.339	2.928	5.395	3.007	0.01	0.99	0.00
204	2.327	2.518	2.851	0.18	5.337	2.931	5.355	2.896	0.06	0.94	0.00
206	2.438	2.591	2.860	0.15	5.467	2.953	5.566	2.928	0.00	1.00	0.00
208	1.911	2.233	2.776	0.31	4.558	2.695	4.595	2.555	0.59	0.41	0.00
209	2.422	2.535	2.718	0.11	5.354	2.866	5.372	2.871	1.00	0.00	0.00
210	2.384	2.511	2.718	0.12	5.671	2.903	5.734	2.896	1.00	0.00	0.00
212	2.071	2.347	2.825	0.27	2.182	1.303	2.238	1.248	0.25	0.75	0.00
213	1.311	1.861	2.800	0.53	2.076	1.131	2.087	1.118	0.43	0.57	0.00
214	1.471	1.957	2.776	0.47	2.416	1.400	2.451	1.319	0.59	0.41	0.00
215	1.738	2.144	2.859	0.39	3.362	2.048	3.333	1.955	0.01	0.99	112.00
216	1.349	1.874	2.737	0.51	2.091	1.139	2.097	1.139	0.86	0.14	0.00
217	1.673	2.102	2.856	0.41	3.356	2.068	3.392	2.011	0.03	0.97	0.00
218	2.358	2.538	2.854	0.17	5.305	2.982	5.251	3.017	0.04	0.96	0.00
219	2.367	2.544	2.856	0.17	5.397	3.007	5.379	3.074	0.03	0.97	0.18
220	2.458	2.595	2.833	0.13	5.404	3.072	5.497	3.075	0.19	0.81	0.00
221	2.180	2.415	2.820	0.23	4.996	2.605	5.059	2.693	0.28	0.72	0.00
222	1.820	2.196	2.859	0.36	3.756	2.331	3.956	2.204	0.01	0.99	0.00
223	1.976	2.292	2.846	0.31	4.209	2.453	4.220	2.373	0.10	0.90	0.00
224	2.110	2.380	2.854	0.26	4.778	2.739	4.778	2.707	0.04	0.96	0.00
225	1.930	2.264	2.849	0.32	4.372	2.519	4.713	2.483	0.08	0.92	0.00
226	2.285	2.488	2.843	0.20	5.597	3.087	5.637	3.087	0.12	0.88	0.00
227	2.283	2.491	2.856	0.20	5.009	2.878	5.009	2.818	0.03	0.97	0.00
228	1.953	2.276	2.839	0.31	5.082	2.520	5.023	2.428	0.15	0.85	0.00
229	2.168	2.415	2.849	0.24	5.250	2.927	5.394	2.942	0.08	0.92	0.00
230	1.892	2.241	2.853	0.34	4.079	2.455	4.157	2.449	0.05	0.95	0.00
231	2.052	2.344	2.859	0.28	4.122	2.451	4.166	2.361	0.01	0.99	0.00
232	1.907	2.263	2.907	0.34	4.057	2.358	4.142	2.261	0.07	0.93	0.00
233	2.051	2.343	2.856	0.28	4.580	2.593	4.645	2.578	0.03	0.97	0.00
234	2.053	2.335	2.823	0.27	4.831	2.754	4.968	2.718	0.26	0.74	0.00
235	2.120	2.383	2.843	0.25	4.693	2.646	4.839	2.562	0.12	0.88	0.00
236	1.466	1.969	2.853	0.49	3.154	1.759	3.115	1.694	0.05	0.95	0.00
237	1.710	2.124	2.851	0.40	3.818	2.229	3.845	2.161	0.06	0.94	0.00
238	2.190	2.429	2.849	0.23	4.437	2.612	4.425	2.552	0.08	0.92	0.00
239	2.130	2.379	2.807	0.24	4.933	2.748	5.028	2.733	0.38	0.62	0.00
240	2.276	2.460	2.768	0.18	5.003	2.688	5.003	2.650	0.65	0.35	0.00
241	2.207	2.433	2.825	0.22	5.824	3.011	5.867	3.005	0.25	0.75	85.70
242	1.507	1.970	2.727	0.45	2.831	1.700	2.837	1.625	0.94	0.06	0.00
243	1.601	2.026	2.718	0.41	3.005	1.796	3.075	1.713	1.00	0.00	0.00

Continuation: Table I-7: Carbonate data sets from Verwer et al. (2008).

244	2.221	2.411	2.722	0.18	5.100	2.764	5.084	2.742	0.97	0.03	0.00
245	2.061	2.328	2.776	0.26	5.789	2.887	5.854	2.879	0.59	0.41	0.00
246	2.083	2.352	2.815	0.26	4.811	2.585	4.886	2.489	0.32	0.68	0.00
247	1.672	2.083	2.774	0.40	3.826	2.200	3.911	2.056	0.60	0.40	125.00
248	1.965	2.286	2.849	0.31	4.992	2.702	5.139	2.752	0.08	0.92	0.00
249	2.022	2.312	2.810	0.28	5.216	2.925	5.182	2.908	0.36	0.64	0.00
250	1.483	1.981	2.856	0.48	3.301	2.033	3.287	1.967	0.03	0.97	0.00
251	2.049	2.327	2.802	0.27	4.928	2.750	5.007	2.867	0.41	0.59	0.00

Table I-8: Carbonate data sets from Woodside et al. (1998).

Sample	Depth (mbsf)	Dry-Rhob (g/cc)	Sat-Rhob (g/cc)	Rhog (g/cc)	Por	Vp-sat (km/s)	Vs-sat (km/s)	CaCO3 (wt%)	Dolomite (wt%)
1	125.58	2.19	2.37	2.72	0.20	4.797	2.402	0.97	0.05
2	145.25	2.33	2.45	2.75	0.15	5.646	2.938	1.00	0.22
3	146.07	2.56	2.60	2.76	0.07	5.722	3.022	1.00	0.26
4	154.99	2.07	2.30	2.76	0.25	4.349	2.371	1.00	0.27
5	164.64	2.39	2.53	2.81	0.15	5.550	3.031	1.00	0.64
6	164.67	2.41	2.54	2.87	0.16	5.430	3.035	1.00	1.05
7	173.97	1.97	2.22	2.72	0.27	4.078	2.230	0.99	0.00
8	183.95	2.37	2.52	2.83	0.16	5.580	3.082	1.00	0.74
9	192.44	2.54	2.60	2.84	0.10	6.151	3.117	1.00	0.81
10	193.79	2.32	2.49	2.85	0.19	5.359	2.967	1.00	0.89
11	202.60	2.26	2.44	2.83	0.20	5.287	2.803	1.00	0.79
12	203.93	2.31	2.48	2.85	0.19	5.556	3.060	1.00	0.91
13	215.33	2.03	2.30	2.85	0.29	4.623	2.528	1.00	0.86
14	222.74	2.13	2.37	2.81	0.24	4.486	2.497	1.00	0.65
15	233.63	1.98	2.25	2.76	0.28	3.712	1.857	1.00	0.30
16	301.11	1.77	2.04	2.68	0.34	3.066	1.668	0.63	0.00
17	307.99	1.60	1.98	2.70	0.41	2.948	1.536	0.77	0.00
18	318.68	1.73	2.09	2.71	0.36	3.053	1.578	0.89	0.00
19	318.74	1.73	2.08	2.71	0.36	3.252	1.682	0.92	0.00
20	323.81	1.83	2.14	2.71	0.32	3.242	1.688	0.88	0.00
21	337.58	1.72	2.08	2.71	0.36	3.299	1.682	0.89	0.00
22	337.61	1.72	2.07	2.71	0.37	3.103	1.623	0.92	0.00
23	346.42	1.95	2.21	2.71	0.28	3.350	1.727	0.92	0.00
24	349.65	1.95	2.22	2.71	0.28	3.404	1.786	0.91	0.00
26	130.00	1.72	2.06	2.70	0.36	2.522	1.230	0.79	0.00
27	140.89	1.78	2.11	2.71	0.34	2.665	1.304	0.89	0.00
29	149.35	1.79	2.12	2.71	0.34	2.963	1.500	0.91	0.00
30	149.45	1.80	2.12	2.71	0.34	2.969	1.496	0.91	0.03
31	150.91	1.70	2.04	2.71	0.37	2.728	1.458	0.89	0.00
32	153.14	1.76	2.09	2.71	0.35	2.847	1.438	0.88	0.00
33	158.28	1.81	2.14	2.71	0.33	3.012	1.568	0.90	0.00
34	159.51	1.73	2.07	2.71	0.36	2.861	1.555	0.91	0.00
35	160.78	1.68	2.04	2.70	0.38	2.709	1.356	0.85	0.00
36	167.60	1.66	2.04	2.72	0.39	2.881	1.429	0.88	0.11
38	178.60	1.66	2.01	2.70	0.39	2.624	1.429	0.83	0.01
40	188.06	1.71	2.03	2.73	0.37	2.919	1.520	0.91	0.15
41	189.31	1.67	2.02	2.77	0.40	3.083	1.640	0.94	0.41
42	197.40	1.64	2.03	2.76	0.41	2.922	1.501	0.95	0.31
43	198.00	1.65	2.04	2.74	0.40	2.917	1.510	0.93	0.19

Continuation: Table I-8: Carbonate data sets from Woodside et al. (1998).

44	199.75	1.65	2.04	2.73	0.40	3.060	1.583	0.95	0.14
45	206.40	1.56	1.97	2.71	0.42	2.990	1.531	0.92	0.00
46	207.60	1.72	2.07	2.71	0.37	2.994	1.504	0.92	0.00
47	208.15	1.65	2.03	2.71	0.39	2.990	1.523	0.90	0.00
49	218.81	1.65	2.04	2.71	0.39	3.011	1.544	0.95	0.00
50	226.39	1.74	2.09	2.72	0.36	3.167	1.623	0.97	0.00
51	227.36	1.73	2.08	2.71	0.36	3.089	1.559	0.93	0.00
52	235.69	1.72	2.07	2.71	0.37	3.117	1.575	0.92	0.00
53	236.57	1.77	2.11	2.71	0.35	3.093	1.584	0.94	0.00
54	244.58	1.75	2.10	2.71	0.35	3.011	1.549	0.93	0.00
55	246.86	1.71	2.01	2.71	0.37	2.887	1.545	0.92	0.00
56	254.42	1.65	1.95	2.71	0.39	2.917	1.636	0.93	0.00
57	256.68	1.82	2.15	2.71	0.33	2.989	1.493	0.92	0.00
58	257.57	1.72	2.08	2.71	0.37	3.059	1.556	0.92	0.00
59	264.20	1.84	2.15	2.71	0.32	3.109	1.602	0.92	0.00
60	265.77	1.80	2.13	2.71	0.33	3.019	1.510	0.91	0.00
62	275.02	1.53	1.95	2.71	0.44	2.919	1.493	0.96	0.00
63	276.66	1.68	2.05	2.71	0.38	3.100	1.610	0.96	0.00
65	342.73	1.85	2.18	2.71	0.32	3.122	1.663	0.92	0.00
66	370.15	1.74	2.08	2.71	0.36	3.132	1.658	0.93	0.00
68	408.00	1.92	2.20	2.72	0.29	3.627	1.918	0.96	0.00

Glossary

Symbols used in this Thesis:

AR	Aspect ratio
α	Aspect ratio
ARp	Aspect ratio V_p velocity
ARs	Aspect ratio from V_s velocity
DEM-ARp	Aspect ratio from DEM needed to match V_p data
DEM-α_p	Aspect ratio from DEM needed to match V_p data
DEM-ARs	Aspect ratio from DEM needed to match V_s data
DEM-α_s	Aspect ratio from DEM needed to match V_s data
AR-mean	Mean aspect ratio
CPA- ARp	Aspect ratio from CPA needed to match V_p data
CPA-α_p	Aspect ratio from CPA needed to match V_p data
CPA- ARs	Aspect ratio from DEM needed to match V_s data
CPA-α_s	Aspect ratio from DEM needed to match V_s data
SC-AR	Aspect ratio from SC needed to match V_s data
Cal	Calcite
k-feld	k-feldspar
kaol	Kaolinite
mbsf	Meters below sea floor
Pc	Confining pressure

Pp	Pore pressure
Perm	Permeability
V_p -sat	*P*-wave velocity at full saturation condition
V_p -dry	*P*-wave velocity at dry condition
V_s -sat	*S*-wave velocity at full saturation condition
V_s -dry	*S*-wave velocity at dry condition
HS	Hashin-Shtrikman
HSA	Hashin-Shtrikman upper and lower bounds average
HS-	Hashin-Shtrikman lower bound
HS+	Hashin-Shtrikman upper bounds
DEM	Differential effective medium
CPA	Coherent potential approximation
MM	Mondescu and Muthukumar model
DL	Devaney and Levine model
CPSF	Compliant phase supported frame
SPSF	Stiff phase supported frame
TF	Transitional frame
TFC	Transitional frame continuous
TFD	Transitional frame discontinuous
MLHS	Modified lower Hashin-Shtrikman
MUHS	Modified upper Hashin-Shtrikman
MLHS-PG	Modified lower Hashin-Shtrikman bounds with porous grains
MUHS-PG	Modified upper Hashin-Shtrikman bounds with porous grains
CPG	Cementation theory with porous grains
WPG	Wood's model with porous grain
V_p	*P*-wave velocity
V_s	*S*-wave velocity
SC-*P*-wave velocity	*P*-wave velocity from SC
DEM-*P*-wave velocity	*P*-wave velocity from DEM